Rashba-type spin-split surface states: Heavy post transition metals on Ag(111)

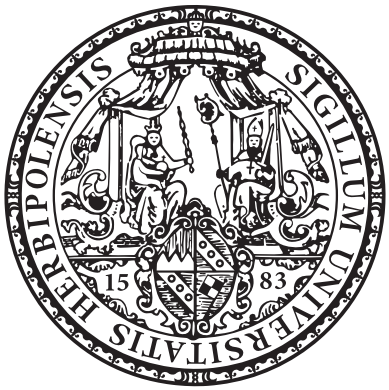

Dissertation

zur Erlangung des naturwissenschaftlichen Doktorgrades
der Julius-Maximilians-Universität Würzburg

vorgelegt von

Lydia El-Kareh

aus Altenburg

Würzburg 2014

Eingereicht am 16.12.2014
bei der Fakultät für Physik und Astronomie

1. Gutachter: Prof. Dr. Matthias Bode
2. Gutachter: Priv.-Doz. Dr. Jörg Schäfer
3. Gutachter:

der Dissertation

Vorsitzende(r):

1. Prüfer: Prof. Dr. Matthias Bode
2. Prüfer: Priv.-Doz. Dr. Jörg Schäfer
3. Prüfer: Prof. Dr. Giorgio Sangiovanni

im Promotionskolloquium

Tag des Promotionskolloquiums:
Doktorurkunde ausgehändigt am:

Die Natur verbirgt ihr Geheimnis
durch die Erhabenheit ihres Wesens,
aber nicht durch List.

Albert Einstein

Abstract

In the framework of this thesis, the structural and electronic properties of bismuth and lead deposited on Ag(111) have been investigated by means of low-temperature scanning tunneling microscopy (LT-STM) and spectroscopy (STS).
Prior to spectroscopic investigations the growth characteristics have been investigated by means of STM and low energy electron diffraction (LEED) measurements. Submonolayer coverages as well as thick films have been investigated for both systems.

Subsequently the quantum well characteristics of thick Pb films on Ag(111) have been analyzed and the quantum well character could be proved up to layer thicknesses of $N \approx 100\,\mathrm{ML}$. The observed characteristics in STS spectra were explained by a simple cosine Taylor expansion and an in-plane energy dispersion could be detected by means of quasi-particle interferences.

The main part of this work investigates the giant Rashba-type spin-split surface alloys of $(\sqrt{3} \times \sqrt{3})$Pb/Ag(111)$R30°$ and $(\sqrt{3} \times \sqrt{3})$Bi/Ag(111)$R30°$. With STS experiments the band positions and splitting strengths of the unoccupied $(\sqrt{3} \times \sqrt{3})$Pb/Ag(111)$R30°$ band dispersions could be resolved, which were unclear so far. The investigation by means of quasi-particle interferences resulted in the observation of several scattering events, which could be assigned as intra- and inter-band transitions.
The analysis of scattering channels within a simple spin-conservation–approach turned out to be incomplete and led to contradictions between experiment and theory. In this framework more sophisticated DFT calculations could resolve the apparent deviations by a complete treatment of scattering in spin-orbit–coupled materials, which allows for constructive interferences in spin-flip scattering processes as long as the total momentum $\vec{J}$ is conserved.
In a similar way the band dispersion of $(\sqrt{3} \times \sqrt{3})$Bi/Ag(111)$R30°$ was investigated. The STS spectra confirmed a hybridization gap opening between both Rashba-split bands and several intra- and inter-band scattering events could be observed in the complete energy range. The analysis within a spin-conservation–approach again turned out to be insufficient for explaining the observed scattering events in spin-orbit–coupled materials, which was confirmed by DFT calculations. Within these calculations an inter-band scattering event that has been identified as spin-conserving in the simple model could be assigned as a spin-flip scattering channel. This illustrates evidently how an incomplete description can lead to completely different indications.

The present work shows that different spectroscopic STM modes are able to shed light on Rashba-split surface states. Whereas STS allowed to determine band onsets and splitting strengths, quasi-particle interferences could shed light on the band dispersions. A very important finding of this work is that spin-flip scattering events may result in constructive interferences, an effect which has so far been overlooked in related publications. Additionally it has been found that STM measurements can not distinguish between spin-conserving scattering events or spin-flip scattering events, which prevents to give a definite conclusion on the spin polarization for systems with mixed orbital symmetries just from the observed scattering events.

Zusammenfassung

Im Rahmen dieser Arbeit wurden die strukturellen und elektronischen Eigenschaften von Bismut und Blei bedampften Ag(111) Oberflächen mittels Tieftemperatur-Rastertunnelmikroskopie und -spektroskopie untersucht.
Im Vorfeld zur Untersuchung der elektronischen Struktur wurde das Wachstumsverhalten sowohl von Bismut als auch Blei auf Ag(111) für Submonolagen und dicke Filme untersucht. Als komplementäre Messmethode wurden hierbei auch LEED Messungen herangezogen.

Im Anschluss an die strukturellen Untersuchungen wurden die elektronischen Eigenschaften von dicken Bleifilmen auf Ag(111) untersucht. Der Quantentrogcharakter konnte hierbei deutlich für sehr dicke Filme von bis zu 100 Monolagen nachgewiesen werden. Die beobachteten STS Spektren wurden im Rahmen einer Cosinus-Taylorentwicklung erläutert und erklärt. Eine Dispersion parallel zur Oberfläche konnte mittels Quasiteilcheninterferenz nachgewiesen werden.

Der Hauptteil dieser Arbeit beschäftigte sich mit den Legierungsoberflächen der $(\sqrt{3} \times \sqrt{3})$Pb/Ag(111)$R30°$ und $(\sqrt{3} \times \sqrt{3})$Bi/Ag(111)$R30°$ Strukturen, welche über eine außergewöhnlich starke Rashba Aufspaltung verfügen.
Zunächst wurde die Bandstruktur der $(\sqrt{3} \times \sqrt{3})$Pb/Ag(111)$R30°$ Oberfläche aufgeklärt, welche aufgrund ihrer energetischen Lage weit oberhalb des Ferminiveaus für ARPES Messungen nicht zugänglich ist und darum bisher ungeklärt blieb. Zur Untersuchung der Banddispersionen wurden Quasiteilcheninterferenzexperimente durchgeführt, durch die mehrere Intra- und Interbandstreuprozesse identifiziert werden konnten. Die Analyse der Streuprozesse hinsichtlich der Spinpolarisationen der beteiligten Bänder in einem einfachen spinerhaltenden Ansatz führte zu einem Widerspruch zwischen experimentell beobachteten Streuprozessen und theoretisch vorhergesagten Spinpolarisationen. In diesem Zusammenhang konnten neue DFT Rechnungen, die einen vollständigeren Ansatz verfolgten, zeigen, dass dieser Widerspruch gelöst werden konnte, indem anstelle eines spinerhaltenden Ansatzes die Erhaltung des Gesamtdrehimpulses $\vec{J}$ gefordert wurde.
Anschließend wurde die Banddispersion der isostrukturellen $(\sqrt{3} \times \sqrt{3})$Bi/Ag(111)$R30°$-Oberfläche in ähnlicher Weise untersucht. Die STS-Daten bestätigten die Existenz einer Hybridisierungslücke zwischen den beiden Rashba-aufgespaltenen sp_z und p_x, p_y Bändern. Die im gesamten Energiebereich der Bänder beobachteten Intra- und Interbandübergänge konnten ähnlich zur Untersuchung auf der $(\sqrt{3} \times \sqrt{3})$Pb/Ag(111)$R30°$ nicht im Rahmen eines spinerhaltenden Ansatz zufriedenstellend erklärt werden, sondern nur unter Erhaltung

des Gesamdtrehimpulses $\vec{J}$. Es konnte sogar gezeigt werden, dass ein Interbandübergang, der im vereinfachten Modell als spinerhaltend identifziert wurde, in der vollständigeren Betrachtung einem Spinflipstreuereignis zugeordnet werden konnte. Dies zeigt deutlich, dass eine unvollständige Betrachtung mitunter zu völlig verschiedenen Interpretationen führen kann.

Die vorliegende Arbeit konnte zeigen, dass es möglich ist Rashba-aufgespaltene Oberflächen mittels verschiedener spektroskopischer STM Messmodi zu untersuchen. Punktspektren erlauben aufgrund des charakteristischen Signals eines Rashba-aufgespaltenen Zustandes Aussagen über Bandmaxima und Aufspaltungen zu ermitteln. In günstigen Fällen ist es mittels Quasiteilcheninterferenz möglich die unverschobenen Banddispersionen abzubilden. Die Interpretation von Quasiteilcheninterferenzen wurde bisher stets im einfachen spinerhaltenden Bild durchgeführt und in diesem Zusammenhang ist ein sehr wichtiger Aspekt dieser Arbeit die Erkenntnis, dass auch Spinflip-Streuungen zu konstruktiven Interferenzen führen können. Zusätzlich wurde herausgefunden, dass es mittels Quasiteilcheninterferenz nicht möglich ist zu unterscheiden, ob der zugrunde liegende Streuvorgang einem spinerhaltenden oder Spinflip-Übergang zuzuordnen ist. Diese Tatsache verhindert, dass in Systemen mit gemischter orbitaler Symmetrie sichere Aussagen über Spinpolarisationen anhand der experimentell beobachteten Streuereignisse getroffen werden können.

Contents

1 Introduction

It is well known that the degeneracy of electronic states can be lifted intrinsically by structural inversion symmetry (Dresselhaus effect [1]) or by breaking the inversion symmetry of crystal lattices by the Rashba effect [2], which rises due to the introduction of surfaces or interfaces in spin-orbit–coupled materials. Appealingly, structure-inversion–induced spin-orbit coupling acts as an effective magnetic field in the rest frame of the moving electrons. Thus it potentially provides the possibility to control spin precession without an external magnetic field, which opens the gateway of utilization in the wide field of spintronics [3–5].

Indeed the spin-field transistor proposed by Datta and Das in 1989 makes explicit usage of the Rashba effect by a controlled spin precession in the gate electrode between two parallel polarized ferromagnetic source and drain electrodes [6]. Similar to conventional FETs or MOSFETS the gate electrode controls the conductance of the whole device: If the spins arrive with a parallel alignment on the drain, the channel conductance and accordingly the passed current are considerably enhanced. In the case of an antiparallel spin alignment the channel conductance and the passed current are reduced significantly. Since then several explicit suggestions for suitable materials for the Datta-Das transistor have been investigated [7–10]. Also other possible applications have been discussed, e.g. the usage for spin-filters [8, 11] and enhanced superconductivity [12] in the presence of the Rashba effect. The given potential for applications in spintronic devices motivated the research on spin-orbit–coupled materials in the presence of broken inversion symmetry since prior to utilization in modern electronics the underlying microscopic mechanisms have to be understood.

It turned out, that—although originally introduced for semiconductor interfaces—Rashba-split states arise also on metallic surfaces which allows for investigations with surface science methods. After the first successful proof of a Rashba splitting in the Au(111) surface state [13–16] several subsequent experimental and also theoretical studies showed that the exact mechanism for the observed splitting is a complex interplay of atomic spin-orbit coupling, potential gradients, and asymmetries of the involved electron wave functions [17–19]. It could be shown, that a controlled manipulation of the surface potential gradient influenced the observed splittings [16, 20–22]. After the reports about controlled manipulations due to a change of the potential gradient a class of isostructural surface alloys of heavy post transition metals on noble metal Cu(111) and Ag(111) surfaces has been discovered. They exhibit a distinct in-plane potential gradient, which leads to giant Rashba splittings [22–39]. Their splitting strengths can be tailored by choosing appropriate

substrate or adsorbate materials—Bi, Pb, or Sb—and also by controlling the stoichiometry of these adsorbates [33, 40].
Although several studies have been performed so far on these systems, open questions still remain regarding the unoccupied band structures and their spin polarizations. The present work mainly focuses on these aspects for the $(\sqrt{3} \times \sqrt{3})$Pb/Ag(111)$R30°$ and $(\sqrt{3} \times \sqrt{3})$Bi/Ag(111)$R30°$ surfaces. The used methods—STM—has the advantage to detect electronic properties on surfaces with high spatial resolution and additionally provides access to occupied as well as unoccupied states.

The present work is divided into eight chapters.
The following chapter describes the theoretical background of the used experimental methods, i.e. STM and LEED. A short overview of the experimental setup is given in chapter 3. Subsequently the concept of surface states is introduced in chapter 4. The detectability of surface states by means of scanning tunneling spectroscopy and quasi-particle interference mapping are explained and illustrated for the Ag(111) surface, which serves as substrate for the obtained data in the results chapter.
Chapter 5 describes the theory of spin-orbit coupling on surfaces, starting with an intuitive derivation of the spin-orbit coupling as an effective magnetic field in the rest frame of the moving electron. The spin-orbit coupling is then adapted for structural inversion asymmetry on interfaces or surfaces, which directly yields the Rashba-type splitting. In this context the origin of the observed splitting strength is further explained and the isostructural class of 1/3 ML heavy post transition metals deposited on fcc(111) noble metal substrates is introduced. The current experimental and theoretical findings are summarized for the specific systems of Pb/Ag(111) and Bi/Ag(111). This chapter ends with a detailed inspection of the detectability of Rashba-split states by means of scanning tunneling modes.
The next chapter gives a theoretical description of quantum-well states, which form as result of finite film thicknesses. Within this frame actual findings of Pb/Ag(111) films are given.
Chapter 7 presents all results of this work starting with a preliminary growth study of lead and bismuth deposited on Ag(111) in the submonolayer range up to thick films in section 7.1. The electronic properties of lead films on Ag(111) are presented in section 7.2. The results could confirm quantized states for very thick films and the observed spectra are explained within a simple model for the electron dispersion. Subsequently layer-dependent parallel dispersions on the surface could be detected with quasi-particle interferences for exemplary quantum well states.
The main content of this work—the Rashba-type spin-split surfaces of Pb and Bi on Ag(111)—is presented in sections 7.3 and 7.4, starting with the case of Pb/Ag(111). Section 7.3 initially starts with a clarification of the band structure, which was unclear so far. Subsequently the electronic properties were investigated by means of quasi-particle interferences and the unshifted band dispersions could be extracted. The observed scattering channels could be interpreted within extended DFT calculations, that allowed for constructive

spin-flip interferences under the assumption of the conservation of the total momentum $\vec{J}$. The Bi/Ag(111) Rashba surface was investigated in a similar way in section 7.4. A hybridization between both bands could be confirmed by STS and the observed quasi-particle interferences proved the fact, that a treatment of scattering events within a spin-conservation model is incomplete for spin-orbit–coupled materials and led to totally different indications. The most important comprehensive finding of this work is the fact that constructive spin-flip scattering events can indeed occur which has been abnegated so far in similar scattering experiments in spin-orbit–coupled materials. In addition the present work shows, that STM measurements are insensitive to recognize the underlying nature—either spin-flip or spin-conserving—of an observed scattering in spin-orbit–coupled systems exhibiting mixed orbital symmetries.

2 Theory

2.1 Scanning tunneling microscopy

The scanning tunneling microscope (STM) has been invented by G. Binning, H. Rohrer, C.G. Gerber, and E. Weibel in the early 1980's [41–43], based on the purely quantum mechanic tunneling effect. In the tunneling process electrons are, contrary to classical physics, able to penetrate finite potential barriers, even if their energy E is smaller than the potential barrier height V_0. The following sections will describe two different mathematical models. The first model, presented in section 2.1.1, is based on the time-independent Schrödinger equation and wave matching in the case of a simple 1D square potential, which can already show the high spatial resolution of STM measurements [44]. The second model, proposed by Bardeen in 1961, will be described in section 2.1.2 and treats the tunneling effect as a time-dependent perturbation between two independent systems, i.e. sample and tip [45]. It has been further developed by Tersoff and Hamann in order to adapt the tunneling process directly to a tunneling between sample and tip in the STM [46, 47].
Following there will be a description of an STM setup and the measuring technique in section 2.1.3, focusing on the spectroscopic modes of an STM and its theory in section 2.1.4 [48–50]. In this framework the lock-in–technique is explained, which improves the signal-to-noise ratio (SNR) in spectroscopic experiments considerably [51, 52]. Subsequently the different spectroscopic modes are described. Eventually the energy resolution of scanning tunneling spectroscopy (STS) is discussed in section 2.1.5 [48, 51, 53].

2.1.1 1D square potential

The most simple approach for the tunneling barrier is a one-dimensional square potential, sketched in Fig. 2.1 with height V_0 and width d. The stationary Schrödinger equation

$$\left(-\frac{\hbar^2}{2m}\frac{\mathrm{d}^2}{\mathrm{d}z^2}+V_0\right)\Psi(z)=E\Psi(z) \tag{2.1.1}$$

can be solved in all regions by three different wave functions

$$\Psi_1(z)=\mathrm{e}^{ikz}+A\,\mathrm{e}^{-ikz} \qquad z<0 \tag{2.1.2}$$

$$\Psi_2(z)=B\,\mathrm{e}^{-\kappa z}+C\,\mathrm{e}^{\kappa z} \quad 0<z<d \tag{2.1.3}$$

$$\Psi_3(z)=D\,\mathrm{e}^{ikz} \qquad z>d, \tag{2.1.4}$$

with the wave vector

$$k^2 \;=\; \frac{2mE}{\hbar^2} \tag{2.1.5}$$

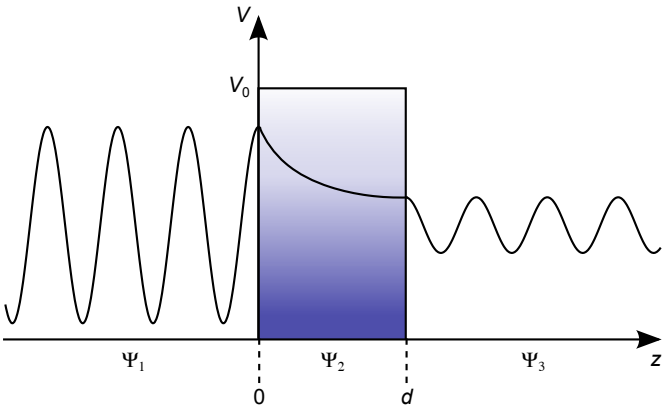

Figure 2.1: The quantum mechanic tunneling process on a square-shaped barrier with width d and finite height V_0. The wave function with $E < V_0$ enters the barrier, is damped exponentially within the barrier and has a finite transmission probability to penetrate the barrier.

and the decay length

$$\kappa^2 = \frac{2m(V_0 - E)}{\hbar^2}. \tag{2.1.6}$$

The Amplitudes A, B, C and D can be derived considering the continuity conditions at $z = 0$ and $z = d$ for Ψ and Ψ'. The tunneling probability T depends only on the transmitted amplitude D or the ratio between initial and final probability current.

$$T = |D|^2 \tag{2.1.7}$$

$$= \frac{j_3}{j_1}$$

$$= \frac{1}{1 + \frac{(k^2+\kappa^2)^2}{4k^2\kappa^2 \sinh^2(\kappa d)}} \tag{2.1.8}$$

with the probability current j_n

$$j_n = \frac{\hbar}{2m}\left(\Psi_n^* \frac{\partial \Psi_n}{\partial z} - \frac{\partial \Psi_n^*}{\partial z}\Psi_n\right). \tag{2.1.9}$$

For strongly attenuating potential barriers ($\kappa d \gg 1$) Eq. (2.1.8) simplifies to

$$T \approx \frac{16k^2\kappa^2}{(k^2+\kappa^2)^2}\, \mathrm{e}^{-2\kappa d}. \tag{2.1.10}$$

The simple 1D square potential model already illustrates the strong exponential dependency between tunneling probability, barrier width, and potential height. For typical work functions of $\phi \approx 4\,\mathrm{eV}$ and barrier widths of several Ångström a variation of 1 Å influences the tunneling current by one order of magnitude, thus demonstrating the high spatial resolution of STM measurements.

2.1.2 Bardeen's perturbation theory and expansion by Tersoff-Hamann

The model proposed by Bardeen is based on Fermi's golden rule describing the tunneling effect as a time-dependent perturbation between two independent systems [45–47]. In this formalism the tunneling current for elastic tunneling can be written as

$$I = \frac{2\pi e}{\hbar} \sum_{\mathrm{t,s}} \underbrace{f(E_\mathrm{t})(1 - f(E_\mathrm{s} + eU))}_{\text{(i)}} - \underbrace{f(E_\mathrm{s} + eU)(1 - f(E_\mathrm{t}))}_{\text{(ii)}} \cdot |M_\mathrm{ts}|^2 \delta(E_\mathrm{t} - E_\mathrm{s}) \quad (2.1.11)$$

with the Fermi function $f(E)$ of the unperturbated states $|\Psi_\mathrm{t}\rangle$ of the tip und $|\Psi_\mathrm{s}\rangle$ of the sample, the applied voltage U between both electrodes, and the transfer matrix element

$$M_\mathrm{ts} = -\frac{\hbar^2}{2m} \int_S \mathrm{d}\vec{S}\,(\Psi_\mathrm{t}^* \nabla \Psi_\mathrm{s} - \Psi_\mathrm{s} \nabla \Psi_\mathrm{t}^*). \quad (2.1.12)$$

It is integrated over any surface S in the vacuum barrier dividing sample and tip entirely. The factor $f(E_\mathrm{t})(1 - f(E_\mathrm{s} + eU))$ in (i) describes tunneling between filled sample and empty tip states, whereas (ii) describes a reverse tunneling from filled tip to empty sample states, which can be set to zero in the limit of low temperatures. Assuming also the limit of low voltages[1] ($eU \ll k_\mathrm{B}T$), Eq. (2.1.11) turns into

$$I = \frac{2\pi e^2 U}{\hbar} \sum_{\mathrm{t,s}} |M_\mathrm{ts}|^2 \delta(E_\mathrm{s} - E_\mathrm{F}) \delta(E_\mathrm{t} - E_\mathrm{F}). \quad (2.1.13)$$

For the evaluation of M_ts Tersoff and Hamann applied a periodic semi-infinite crystal for the surface and expressed the surface wave function Ψ_s as a Fourier expansion

$$\Psi_\mathrm{s} = \frac{1}{\sqrt{\Omega_\mathrm{s}}} \sum_G a_G \, \mathrm{e}^{-\sqrt{\kappa^2 + |\vec{k}_{||} + \vec{G}|^2} z} \, \mathrm{e}^{i(\vec{k}_{||} + \vec{G})\vec{x}}. \quad (2.1.14)$$

Here Ω_s is the sample volume, $\vec{k}_{||}$ the surface Bloch wave vector of the state, $\vec{G}$ is a surface reciprocal-lattice vector, and $\kappa = \sqrt{\frac{2m\phi}{\hbar^2}}$ the inverse decay length with the work function ϕ which is defined as energy difference between the Fermi level and vacuum level $\phi = E_\mathrm{vac} - E_\mathrm{F}$.
Since the tip wave function Ψ_t was unknown, they chose the most simple mathematic approach and modeled it as spherical on its apex (see Fig. 2.2(a)) with a s-wave character

$$\Psi_\mathrm{t} = \frac{c_\mathrm{t} \kappa R \, \mathrm{e}^{\kappa R}}{\sqrt{\Omega_\mathrm{t}}} \cdot \frac{\mathrm{e}^{-\kappa |\vec{r} - \vec{r}_0|}}{\kappa |\vec{r} - \vec{r}_0|} \quad (2.1.15)$$

with the tip volume Ω_t and the local radius of curvature R centered at $\vec{r}_0$. The factor c_t is determined by the geometric and electronic tip properties and the boundary conditions between probe and vacuum.

[1] Finite bias voltages are described in Sec. 2.1.4

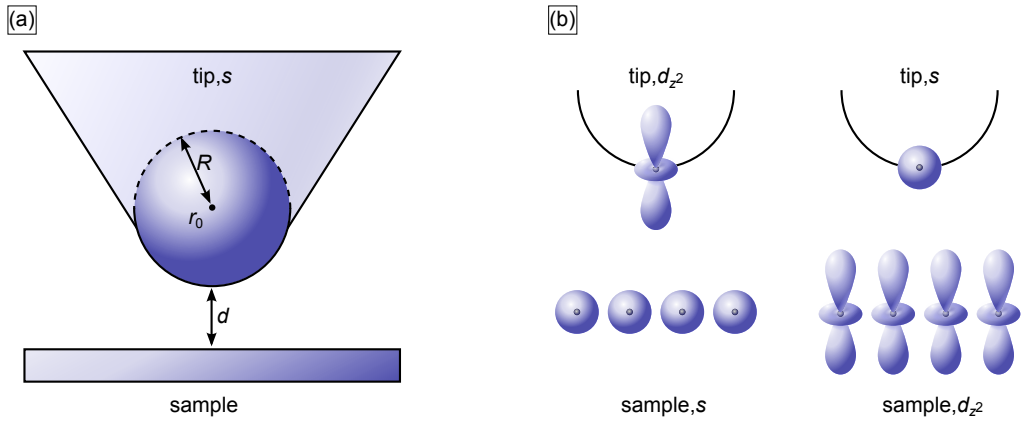

Figure 2.2: Panel (a) shows the tip model proposed by Tersoff and Hamann exhibiting a spherical shape with radius R located around r_0 and the distance d between sample and probe. The tip wave functions are assumed as spherical in this model. Panel (b) shows the tip wave function model proposed by Chen in order to explain the lateral resolution of STM measurements. The tip wave functions are modeled with a d_{z^2} character instead of spherical character. In the reciprocity principle the tip and surface wave functions have been interchanged for the calculation.

For simplification the work functions for tip and sample are set equal and the tunneling current can be expressed as

$$I = \frac{32\pi^3}{\hbar} e^2 U \phi^2 D_\mathrm{t}(E_\mathrm{F}) \frac{R^2\, \mathrm{e}^{2\kappa R}}{\kappa^4} \cdot \underbrace{\sum_\mathrm{s} |\Psi_\mathrm{s}(\vec{r}_0)|^2 \delta(E_\mathrm{s} - E_\mathrm{F})}_{\rho_\mathrm{s}(\vec{r_0}, E_\mathrm{F})} \tag{2.1.16}$$

Here $\rho_\mathrm{t}(E_\mathrm{F})$ is the density of states (DOS) of the tip per unit volume on the Fermi level and $\rho(\vec{r_0}, E_\mathrm{F})$ the local DOS (LDOS) of the sample as sum over all wave functions Ψ_s on the tip curvature center $\vec{r_0}$ at the Fermi level. Following expression (2.1.16) the STM probes contours of constant $\rho(\vec{r}, E_\mathrm{F})$ if the tunneling current is held constant. Due to the exponential decay of Ψ_s in the vacuum region

$$|\Psi_\mathrm{s}(\vec{r_0})|^2 \propto \mathrm{e}^{-2\kappa(R+d)}\,. \tag{2.1.17}$$

follows

$$I \propto \mathrm{e}^{-2\kappa d} \tag{2.1.18}$$

for the tunneling current. This reproduces the simple case of the 1D square potential and confirms the exponential dependency between tunneling current and barrier width. The Tersoff-Hamann model reveals also the influence of tip and sample DOS on the current, both have an impact on the observed tunneling current. Even with the assumption of a constant tips DOS STM measurements are still difficult to interpret since they are always a convolution of topographic and electronic features of the surface.
Within the spherical tip approximation the lateral resolution of STM measurements has

been calculated to approximately 5 Å, which has been experimentally confirmed on the Au(110) surface [47, 54]. Later on much better lateral resolutions could be observed on closed packed surfaces like Au(111), Al(111), and Cu(100) with lattice parameters of $a = 2.5 - 3$ Å [55–57]. These results can not be explained in the framework of spherical tip wave functions since it provides a resolution limit of 5 Å. Instead C. Chen suggested d_{z^2}-wave tip states for the d-band metals Pt, Ir, and W, that are mainly used for tips [58]. The d_{z^2} orbital provides a lobe-shaped charge distribution, pointing into z-direction, as shown in Fig. 2.2(b). The overlap of s- and d_{z^2}-orbitals results in a much stronger atomic corrugation compared to the overlap of two s-orbitals and can thus explain the improved lateral resolution of STM measurements.

2.1.3 Basic working principles

The basic working principle of an STM is shown schematically in Fig. 2.3. In order to maintain the current in the tunneling regime a bias voltage is applied between sample and tip (see also Fig. 2.4.). All acquired signals are amplified and then transferred to the control electronics, which controls all piezo movements via a feedback circuit. The tip is approached to the sample by piezo stacks using the slip stick technique [59]. Each coarse

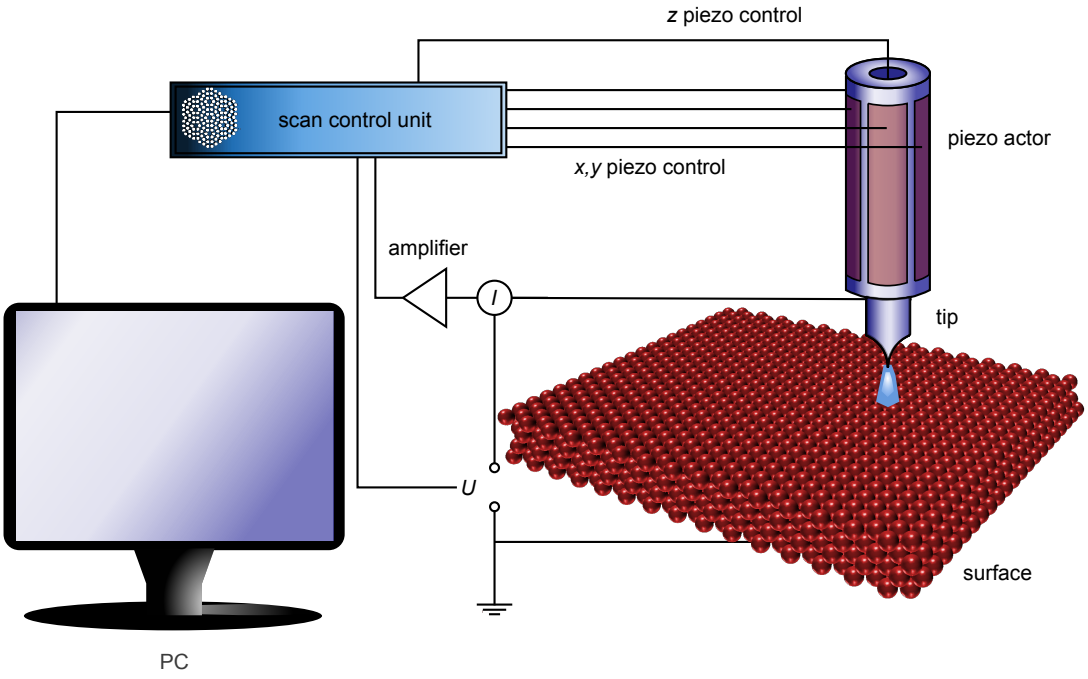

Figure 2.3: The basic working principle of an STM. A bias U is applied between sample and tip in order to maintain the tunneling current. A tubular piezo actor performs the tip movement during the measurement in x, y, and z direction. The collected tunneling current I is amplified and then transferred to the control electronics. The z-piezo movement is controlled by means of a feedback loop during the scan.

motion step is followed by an elongation of the tube piezo actor along its z-axis in order to test whether a tunneling current can be detected or not. In the latter case the piezo tube is retracted and the entire procedure is repeated. In the first case the elongation movement is stopped immediately which avoids tip damages due to physical contacts between tip and sample. During all measurements the tube piezo actor executes the high precision tip movement in the x, y in-plane and the out-of–plane z sample directions. Typical applied bias voltages are in the order of several mV up to some V, the tunneling current can be set between some pA up to $\approx 300\,\mathrm{nA}$. A complete image of the surface is measured by linewise scanning, resulting in a forward and backward scan with fast scan direction along the lines and slow scan direction perpendicular to them.
The most commonly used mode for STM measurements is the constant-current mode (CCM). In this mode the tunneling current is hold stable and the piezo is moved in z-direction during the scan. This considerably minimizes the risk of a physical contact between sample and tip, which may damage the tip as well as the sample area. The measure in the CCM mode is a map of constant DOS as long as the surface DOS is homogeneous in the scan frame. For inhomogeneous samples the interpretation of z height differences in the piezo position can have chemical origin, i.e. different work functions or different DOS (topographic effect see Ref. [44]).

2.1.4 Scanning tunneling spectroscopy

As a result of the nature of the tunneling process STM opens the possibility to obtain information about local electronic properties below and above the Fermi level. Since the very beginning of STM various different spectroscopic modes have been developed, which are all employing the same basic principle, but allow manifold points of view on a given sample. For the understanding of scanning tunneling spectroscopy (STS) an extension of Bardeen's model in section 2.1.2 to finite bias voltages is necessary [50, 59]. For finite bias voltages and a tunneling direction from occupied tip states to unoccupied sample states the tunneling current can be written as

$$I = \frac{4\pi e}{\hbar} \int_{-\infty}^{\infty} [f_\mathrm{t}(E - eU) - f_\mathrm{s}(E)] \cdot \rho_\mathrm{t}(E - eU)\rho_\mathrm{s}(E)|M_\mathrm{ts}|^2 \mathrm{d}E \tag{2.1.19}$$

with the tunneling matrix element $|M_\mathrm{ts}|^2$, that describes the tunneling probability T [44,50,59]. Within the WKB approximation and for trapezoidal barriers it can be estimated to

$$|M_\mathrm{ts}|^2 = T = \mathrm{e}^{-2z\sqrt{\frac{2m}{\hbar^2}\left(\frac{\phi_\mathrm{t}+\phi_\mathrm{s}}{2} + \frac{eU}{2} - (E - E_{||})\right)}} \tag{2.1.20}$$

with the work functions $\phi_{\mathrm{t,s}}$ of tip and sample, and the parallel energy component $E_{||} = \frac{\hbar^2 k^2}{2m}$. States in the center of the 2D Brillouin zone with parallel momentum $k_{||} = 0$ have the strongest impact on the tunneling current, whereas states with $k_{||} \neq 0$ have an additional exponential damping. However, it is possible to detect states with finite momentum as

long as the signal is not buried in a much stronger signal originating from states in the center of the 2D Brillouin zone.
The first derivative of the tunneling current integral with respect of the applied voltage U allows to achieve information about the sample DOS. Assuming $\frac{\mathrm{d}T}{\mathrm{d}U} = 0$ and $\frac{\mathrm{d}\rho_t}{\mathrm{d}U} = 0$ the first derivative of equation 2.1.20 can be written as

$$\frac{\mathrm{d}I}{\mathrm{d}U} = \frac{4\pi e}{\hbar}\int_{-\infty}^{\infty}\frac{\mathrm{d}f_\mathrm{t}(E-eU)}{\mathrm{d}U}\cdot\rho_\mathrm{t}(E-eU)\rho_\mathrm{s}(E)T\mathrm{d}E \tag{2.1.21}$$

with the first derivative of the Fermi function $f(E)$

$$\frac{\mathrm{d}f_\mathrm{t}(E)}{\mathrm{d}U} = \underbrace{\frac{\partial E}{\partial U}}_{e}\cdot\frac{\partial f(E)}{\partial E} = -e\frac{1}{k_\mathrm{B}T}\frac{\mathrm{e}^{\frac{E}{k_\mathrm{B}T}}}{\left(1+\mathrm{e}^{\frac{E}{k_\mathrm{B}T}}\right)^2} = \frac{-e}{2k_\mathrm{B}T}\mathrm{sech}^2\left(\frac{E}{k_\mathrm{B}T}\right). \tag{2.1.22}$$

For low temperatures ($k_\mathrm{B}T \ll E$) the Fermi function collapses to a step function and its derivative is simply the delta distribution

$$\lim_{T\to 0}\frac{\partial f(E)}{\partial E} = \delta(E). \tag{2.1.23}$$

The final result for equation 2.1.21 is then

$$\frac{\mathrm{d}I}{\mathrm{d}U} = \frac{4\pi e^2}{\hbar}\int_{-\infty}^{\infty}\rho_\mathrm{t}(E-eU)\rho_\mathrm{s}(E)T\cdot\delta(E-eU)\mathrm{d}E \tag{2.1.24}$$

$$= \frac{4\pi e^2}{\hbar}\rho_\mathrm{t}(E_\mathrm{F})\rho_\mathrm{s}(eU)T. \tag{2.1.25}$$

Equation (2.1.25) shows, that at a given bias voltage U the simplified differential conductance in Eq. (2.1.25) probes the unoccupied sample DOS $\rho_\mathrm{s}(eU)$ as if the tip DOS was concentrated at the Fermi level ($\rho_\mathrm{t}(E_\mathrm{F})$). For an inverted tunneling direction from occupied sample states to unoccupied tip states, the tip and sample electrode are interchanged in the whole calculation, which results in probing the unoccupied tip DOS $\rho_\mathrm{t}(eU)$ with the sample DOS concentrated at the Fermi level ($\rho_\mathrm{t}(E_\mathrm{F})$). This implies, that a flat tip DOS is absolutely essential for reliable spectra of the occupied sample states. This derivation, where only tunneling from $\rho_\mathrm{t}(E_\mathrm{F})$ to $\rho_\mathrm{s}(eU)$ or from $\rho_\mathrm{t}(E_\mathrm{F})$ to $\rho_\mathrm{s}(eU)$ (for switched tunneling direction) is possible, is only an approximation. Generally, tunneling processes take place in the whole energy integral, as shown in Fig. 2.4. The states on the Fermi level of the energetically higher electrode have the strongest impact on the tunneling current, as they feel the lowest potential barrier. Moreover, also states below the Fermi level contribute to the tunneling current, but they are damped exponentially due to the higher tunneling barrier. This damping is included in the tunneling process by the tunneling probability T in Eq. (2.1.19).
To record a differential conductance the tip is positioned above the desired sample area at setpoint U_set and I_set and then the feedback loop is opened. The simplest way is a measurement of the current $I(U)$, while the bias U is ramped from the initial bias to the

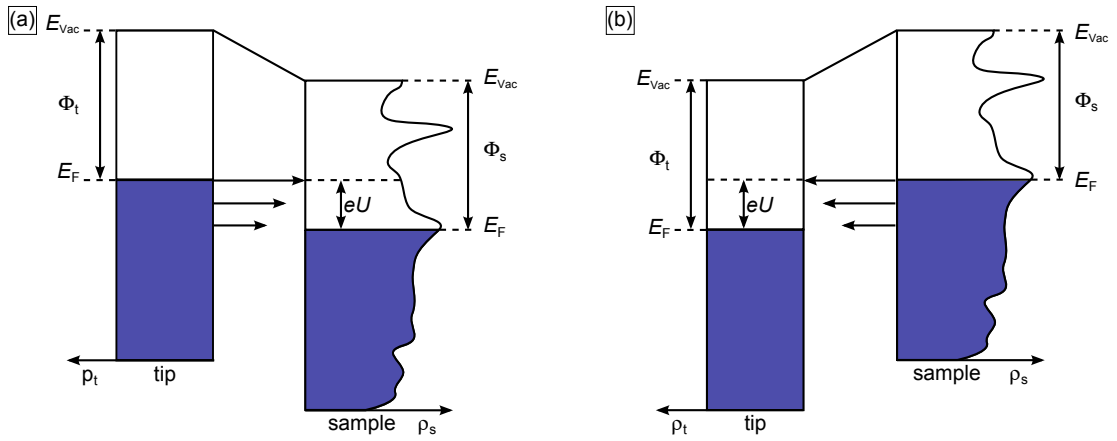

Figure 2.4: The tunneling process for finite applied bias voltages, the tip DOS is set as constant for panel (a) and (b). The applied bias shifts the Fermi levels against each other by eU, which maintains the tunneling current stable. Without a bias the tunneling current leads to an equalization of both Fermi levels and the tunneling current is crudely vanishing. Panel (a) shows tunneling from occupied tip states to unoccupied sample states. The arrows depict the tunneling process from tip to sample, their length represents their impact on the tunneling current. States on the Fermi level (long arrow) of the tip feel the lowest potential barrier and therefore contribute stronger to the tunneling signal than energetically lower states (shorter arrows). Panel (b) shows the tunneling for switched tunneling direction from occupied sample states to unoccupied tip states. Again the states on the Fermi level have the highest tunneling probability.

final bias. Numerical differentiation of $I(U)$ then yields directly the differential conductance $\frac{\mathrm{d}I}{\mathrm{d}U}$, which is shown as blue curve in Fig. 2.5. The spectrum shows the L-gap Shockley-type surface state of Ag(111). The fingerprint of a parabolic 2D state is a steplike rise in the DOS on the band onset and can be seen in the spectrum with an energy onset of about $E_0 = -60\,\mathrm{meV}$ (the concept of surface states will be discussed in details in section 4).
However, ramping the applied bias U and collecting the tunneling current I allows already insight into the sample DOS, but offers only a very poor signal to noise ratio (SNR).
The SNR can be improved significantly by the use of the Lock-In–technique. Thereby the bias voltage is modulated with a sine function during the bias ramp. Assuming an energy-independent tip DOS, a constant transmission probability, and low temperatures the modulated tunneling current can be written as

$$I(U + U_{\mathrm{mod}}\sin(\omega t)) = \frac{4\pi e}{\hbar} T\rho_{\mathrm{t}} \int_0^{eU+eU_{\mathrm{mod}}\sin(\omega t)} \rho_{\mathrm{s}}(E)\mathrm{d}E \tag{2.1.26}$$

A Taylor expansion then yields

$$I(U+U_{\mathrm{mod}}\sin(\omega t)) = \underbrace{\frac{4\pi e}{\hbar} T\rho_{\mathrm{t}} \int_0^{eU} \rho_{\mathrm{s}}(E)\mathrm{d}E}_{I(U)} + \underbrace{\frac{4\pi e^2}{\hbar} T\rho_{\mathrm{t}}\rho_{\mathrm{s}}(eU)}_{\frac{\mathrm{d}I}{\mathrm{d}U}} U_{\mathrm{mod}}\sin(\omega t)+.... \tag{2.1.27}$$

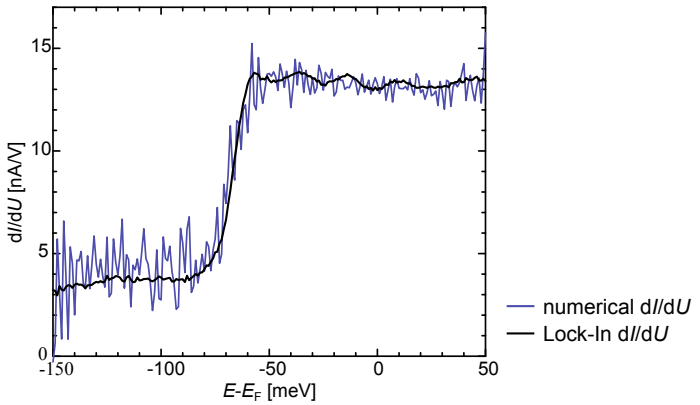

Figure 2.5: The spectroscopic fingerprint of the L-gap Shockley-type Ag(111) surface state with a band onset of $E - E_\mathrm{F} \approx -60\,\mathrm{meV}$. The blue curve shows the numerical derivative of $I(U)$ as average of 3 single spectra. The steplike rise of the surface state is indeed visible, but the noise level is rather high. The Lock-In signal (black curve) shows a significantly improved signal. The parameters were $I_\mathrm{set} = 1\,\mathrm{nA}$, $U_\mathrm{set} = -150\,\mathrm{mV}$, and for the Lock-In signal $U_\mathrm{mod,rms} = 5\,\mathrm{mV}$ and $\nu = 789\,\mathrm{Hz}$.

The first term reproduces the tunneling current without a bias modulation, whereas the second term contains the differential conductance multiplied with the modulation bias $U_\mathrm{mod}\sin(\omega t)$. The Lock-In is now used to determine the differential conductance. With this technique it is possible to increase the SNR significantly as it is able to suppress noise, that is usually spread over a wide band of frequencies. In order to achieve this, the collected signal is first amplified and then mixed with a reference signal from the Lock-In in a phase sensitive multiplier. The modulation and reference frequency ω_mod are equal, but phase shifted. The mixed output is

$$I_\mathrm{out} \propto \sin(\omega t + \varphi)\left[\underbrace{I(U) + \frac{\mathrm{d}I}{\mathrm{d}U}U_\mathrm{mod}\sin(\omega t + \varphi_0)}_{\text{signal}} + \underbrace{\int_0^\infty a_{\omega'}\sin(\omega' t + \varphi_{\omega'})\mathrm{d}\omega'}_{\text{noise}}\right] \tag{2.1.28}$$

$$= \underbrace{\sin(\omega t + \varphi)}_{\text{AC signal}} I(U) + \frac{1}{2}\frac{\mathrm{d}I}{\mathrm{d}U}U_\mathrm{mod}[\underbrace{\cos(2\omega t + \varphi + \varphi_0)}_{\text{AC signal}} + \underbrace{\cos(\varphi - \varphi_0)}_{\text{DC signal}}] + \ldots \tag{2.1.29}$$

The multiplier output contains AC as well as DC components. Low-pass filtering picks the DC components [52]. This component depends on the phase difference $\varphi - \varphi_0$ and linearly on the desired differential conductance signal.
Lock-In technique is able to suppress the broadband noise in Eq. (2.1.28) very effectively. Noise signals at frequencies far from the reference are attenuated by the low-pass filter. Only noise frequencies very close to the reference frequency can pass the low-pass filter and contribute to the Lock-In signal. This removes effectively $\frac{1}{f}$ noise and by the usage of high reference frequencies of $\approx 1\,\mathrm{kHz}$ the contribution of the $\frac{1}{f}$ noise close to the reference frequency is minimized considerably. Notably, although removed by the Lock-In, electronic

noise radio frequencies lead to an overall signal-broadening, which can not be suppressed by the Lock-In filtering (see Sec. 2.1.5).
A Lock-In measurement of the Ag(111) surface state is shown as black curve in Fig. 2.5. It can be directly seen, that the SNR has been improved significantly compared to the numerical derivative of the $I(U)$ signal (blue curve). Due to the phase shift $\cos(\varphi - \varphi_0)$ the Lock-In signal can be reduced. In order to maximize the Lock-In signal the phase difference should be adjusted to $(\varphi - \varphi_0) \approx 0$.

$\mathrm{d}I/\mathrm{d}U$ maps

The spectroscopic mode of $\mathrm{d}I/\mathrm{d}U$ mapping combines local and electronic sample information. During the measurement the applied bias is kept constant and the scanning stays active with an active feedback loop at I_{set} and U_{set}. The bias setpoint is then again modulated with U_{mod} in order to use the Lock-In–technique. Since the feedback loop is active, the modulation frequency has to be set higher than the feedback but lower than the cutoff frequency of the preamplifier. In order to match these conditions the used frequencies in this work are $\nu = 789\,\mathrm{Hz}$ or $\nu = 1333\,\mathrm{Hz}$.
A recorded $\mathrm{d}I/\mathrm{d}U$ map corresponds to a LDOS map at a given energy $E = eU$. It allows to investigate e.g. chemical contrasts of surfaces or—much more attractive—quasi-particle interferences of two dimensional nearly free electron gas states on surfaces. The latter one has been first applied by the IBM research division in 1993 on the surface state of Cu(111) [60] (for the concept of quasi-particle interferences see section 4).

Full spectroscopy

This mode combines topographic resolution and single spectra. Instead of continuous scanning at constant bias, a complete STS spectrum of the surface is recorded on each grid point with a given coordinate (x_i, y_j). This results in a three-dimensional data set $(x_i, y_j, \rho(E))$. The data can be analyzed by viewing the single spectra in dependency of (x_i, y_j) or by viewing all coordinates as a two-dimensional map in dependency of $\rho(E)$ at a certain energy, the latter one results in slices of single $\mathrm{d}I/\mathrm{d}U(\mathrm{E})$ maps. This scan mode is very time consuming, 24 h even for comparably low grid resolutions of $128 \times 128\,\mathrm{px}$ are not unusual. Since the cryostat lifetime of $\approx 50\,\mathrm{h}$ limits the resolution full spectroscopy is not used for quasi-particle interference maps, which are recorded usually with $512 \times 512\,\mathrm{px}$.

2.1.5 Energy resolution

The energy resolution in STS measurements is besides mechanical stability influenced by thermal broadening, the bias modulation, and electronic noise, e.g. due to radio frequencies. The influence of thermal broadening and bias modulation will be discussed in the following, starting with the bias modulation.
The bias modulation broadens the applied bias and therefore limits the energy resolution

intrinsically. The first harmonic component of the current measured by the Lock-In is [51, 59, 61]

$$I_\omega = \frac{\omega}{\pi}\int_{-\frac{\pi}{\omega}}^{\frac{\pi}{\omega}} I(eU + eU_{\mathrm{mod}}\sin(\omega t))\cdot\cos(\omega t)\mathrm{d}t. \tag{2.1.30}$$

Partial integration and substitution leads to

$$I_\omega = \frac{2}{\pi}\int_{-eU_{\mathrm{mod}}}^{eU_{\mathrm{mod}}} \frac{\mathrm{d}I(eU+E)}{\mathrm{d}U}\frac{\sqrt{e^2U_{\mathrm{mod}}^2 - E^2}}{e^2U_{\mathrm{mod}}^2}\mathrm{d}E. \tag{2.1.31}$$

This term can be understood as a convolution of the measured $\frac{\mathrm{d}I}{\mathrm{d}U}$ with a modulation-induced instrumental resolution function Φ_{mod}

$$\Phi_{\mathrm{mod}} = \begin{cases} \frac{2}{\pi}\frac{\sqrt{e^2U_{\mathrm{mod}}^2 - E^2}}{e^2U_{\mathrm{mod}}^2} & ,|E| < eU_{\mathrm{mod}} \\ 0 & ,|E| > eU_{\mathrm{mod}}, \end{cases} \tag{2.1.32}$$

which broadens all STS signals due to the convolution integral in Eq. (2.1.31). The instrumental resolution function is shown in Fig. 2.6(a). It has a half-sphere shape with a base width of $2\,eU_{\mathrm{mod}}$ scaled with the prefactor $\frac{2}{\pi U_{\mathrm{mod}}^2}$. The full width at half maximum (FWHM) of this sphere is $\Delta_{\mathrm{mod}} = 1.73\,eU_{\mathrm{mod}}$. To consider the fact that the Lock-In displays the modulation bias as root means square value (rms), the modulation broadening can be written in terms of $U_{\mathrm{mod,rms}} = \frac{U_{\mathrm{mod}}}{\sqrt{2}}$ to

$$\Delta_{\mathrm{mod}} = 2.45\,eU_{\mathrm{mod,rms}}. \tag{2.1.33}$$

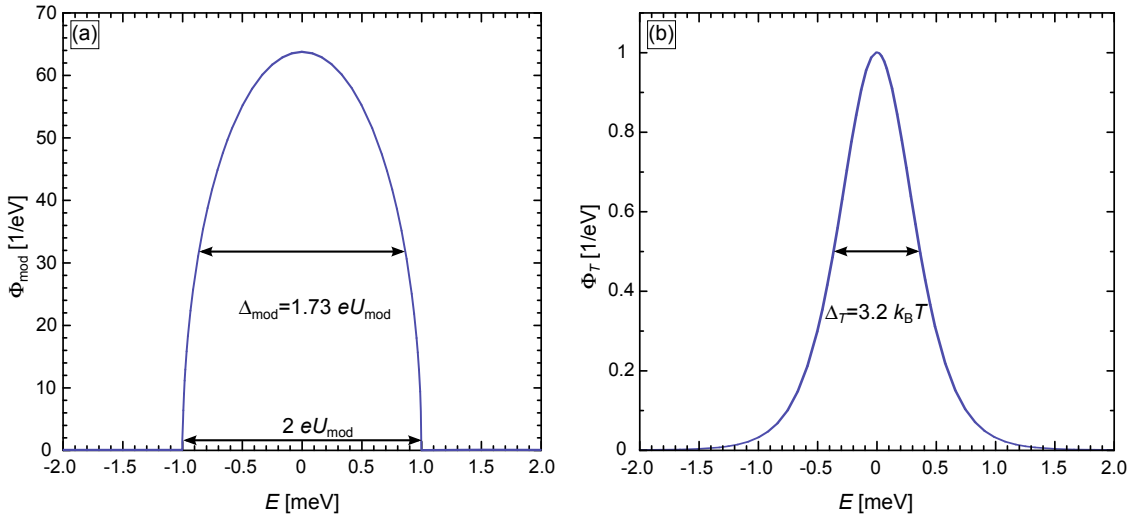

Figure 2.6: (a) Instrumental work function shown for $U_{\mathrm{mod}} = 1\,\mathrm{mV}$. The FWHM is determined to $\Delta_{\mathrm{mod}} = 1.73\,eU_{\mathrm{mod}}$ (b) Thermal broadening shown for $T = 4.8\,\mathrm{K}$. It shows a Gaussian like broadening with a FWHM of $\Delta_T = 3.2\,k_{\mathrm{B}}\mathrm{T}$.

The influence of finite temperatures can be extracted out of Eq. (2.1.21). Inserting Eq. (2.1.22) and assuming an energy independent tunneling probability T and tip DOS ρ_t Eq. (2.1.21) can be written as

$$\frac{\mathrm{d}I}{\mathrm{d}U} = \frac{4\pi e^2}{\hbar}\rho_t T \int_{-\infty}^{\infty} -\frac{1}{2k_B T}\mathrm{sech}^2\left(\frac{E}{k_B T}\right) \cdot \rho_s(E+eU)\mathrm{d}E. \tag{2.1.34}$$

This can be interpreted as a convolution of the sample DOS with a hyperbolic secant function. The thermal broadening is shown in Fig. 2.6(b), it shows a Gaussian like broadening with a FWHM of

$$\Delta_T = 3.2\, k_B T.^2 \tag{2.1.35}$$

Summarizing the energy resolution ΔE is determined by the broadening due to the Lock-In technique and finite temperatures

$$\Delta E(T, U_{\mathrm{mod}}) = \sqrt{(3.2\, k_B T)^2 + (2.45\, eU_{\mathrm{mod,rms}})^2}. \tag{2.1.36}$$

For room temperature, the thermal broadening is the limiting factor for the energy resolution with $\Delta_T(300\,\mathrm{K}) = 83\,\mathrm{meV}$. In the low temperature regime the modulation broadening becomes more and more important. At $T = 4.8\,\mathrm{K}$ the thermal broadening accounts to $\Delta_T(4.8\,\mathrm{K}) = 1.3\,\mathrm{meV}$. Figure 2.7 shows STS data obtained at the surface state of Ag(111) for different modulation bias. For a modulation of 10 meV the surface state shows a width of $\Delta = 24\,\mathrm{meV}$ (determined by the FWHM of $\frac{\mathrm{dI}^2}{\mathrm{dU}^2}$), which is far above the width of $\Delta = 8\,\mathrm{meV}$ reported in literature [62]. Reducing the modulation amplitude to 8, 5, 2, 1 mV leads

[2] This formulation does only account the thermal broadening of one electrode. It threads the sample at a given temperature T with a given temperature dependent characteristic, that would be even measured with a tip at $T = 0\,\mathrm{K}$. The thermal broadening of the second electrode is simply the same Gaussian like term and leads to an energy resolution of $\Delta E(T, U_{\mathrm{mod}}) = \sqrt{(4.5\, k_B T)^2 + (2.45 eU_{\mathrm{mod,rms}})^2}$.

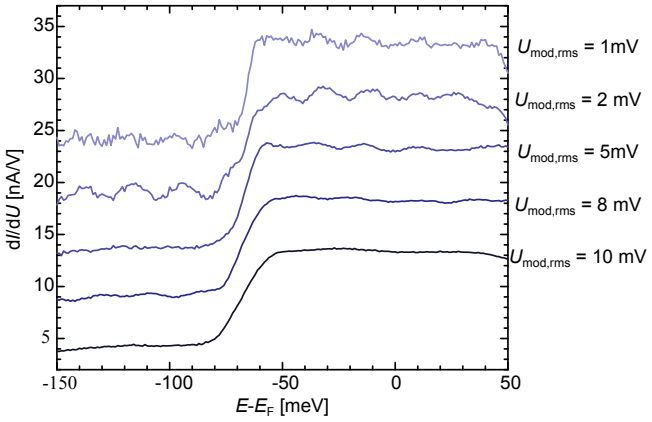

Figure 2.7: The modulation induced broadening of the Ag(111) surface state. The width of the onset is broadened to $\Delta = 24\,\mathrm{meV}$ for $U_{\mathrm{mod,rms}} = 10\,\mathrm{mV}$ and reduces to $\Delta = 19, 12, 8, 7\,\mathrm{meV}$ for $U_{\mathrm{mod,rms}} = 8, 5, 2, 1\,\mathrm{mV}$. Scanning parameters were $I_{\mathrm{set}} = 1\,\mathrm{nA}$, $U_{\mathrm{set}} = -150\,\mathrm{mV}$, and $\nu = 789\,\mathrm{Hz}$.

to widths of $\Delta = 19, 12, 8, 7\,\mathrm{meV}$, respectively. For the modulation of 1 mV the width of $\Delta = 7\,\mathrm{meV}$ seems to be even smaller than reported by Kliewer *et al.* [62]. The discrepancy originates from the fact that the authors of Ref. [62] evaluated Δ directly from the $\frac{\mathrm{dI}}{\mathrm{dU}}$ signal. Applying this method for the lowest STS spectrum in Fig. 2.7 yields—in good agreement to literature—also a value of $\Delta = 8\,\mathrm{meV}$.

As mentioned in the beginning of the section also electronic noise broadens the energy resolution. During this work it turned out that the electronic noise was the limiting factor leading to an energy resolution of approx. 10-15 meV. A careful low-pass filtering and grounding of the electronic feedthroughs on the STM chamber could improve the energy resolution significantly down to several meV. The spectra shown in Fig. 2.7 have been performed after the filtering, but most data in chapter 7 have been taken before the filtering.

2.2 Low energy electron diffraction

Low energy electron diffraction (LEED) is a reciprocal space method to obtain surface structures by means of elastically diffracted electrons on crystalline surfaces. It has been experimentally confirmed for the first time by C. Davison and L.H. Germer in 1927 on a nickel crystal [63]. In LEED experiments a low energy electron beam (E=20..500 eV) is focused on the sample and the diffracted electrons are visualized by a fluorescent screen. A 4-Grid LEED instrument is shown schematically in Fig. 2.8(a). An electron gun with a LaB_6 filament provides free electrons, which are accelerated by an anode and focused by a Wehnelt cylinder and four electronic lenses. The electron beam impinges perpendicularly onto the sample surface under normal incidence and is reflected to the fluorescent screen. The grids filter inelastically reflected electrons and shield the electric fields. The sample is grounded to avoid charging effects. A typical LEED pattern of a clean Ag(111) crystal is shown in Fig. 2.8(b). It shows spots of enhanced intensity that directly correspond to the reciprocal surface lattice.
For a constructive interference the incident ($\vec{k}_\mathrm{i}$) and reflected ($\vec{k}_\mathrm{f}$) electron wave vectors must fulfil the Bragg conditions, graphically shown in the Ewald sphere construction for surfaces in Fig. 2.9(a). Due to the missing Laue constraint for the z-component, the Bragg condition can always be fulfilled as soon as the Ewald sphere sweeps two neighbouring Bragg rods (indicated by vertical lines along the z-direction) and can be connected by $\Delta\vec{k}$.

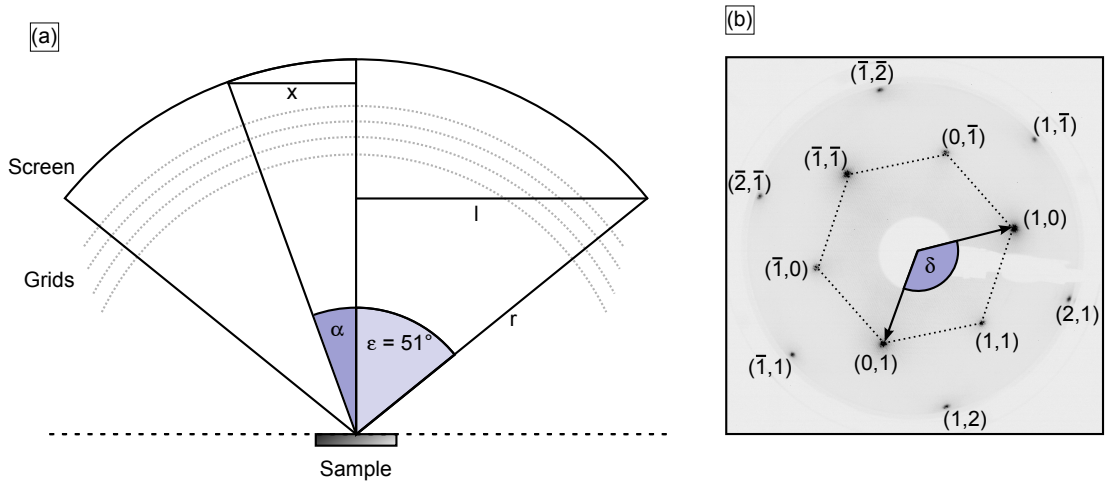

Figure 2.8: (a) Schematic of a 4-grid LEED optic. The sample is positioned in the center of the screen sphere. The low energy electrons hit the sample under normal incidence and are then diffracted to the screen. The angle between the incident electron beam and an intensity maximum is α. Panel (b) shows a LEED pattern of a clean Ag(111) surface. The electron gun is visible in the center of the image. The intensity maxima show directly a hexagonal surface structure with a threefold symmetry. The reciprocal lattice vectors are indicated by the arrows with an angle of $\delta = 120°$. The spots are labeled with miller indices (h, k), the (0,0) spot is not visible due to the electron gun.

This means

$$\Delta\vec{k} = \vec{k}_\mathrm{i} - \vec{k}_\mathrm{f} = G_{||} \tag{2.2.1}$$

with a reciprocal 2D surface lattice vector

$$G_{||} = h\vec{b_1} + k\vec{b_2} \tag{2.2.2}$$

with miller indices h, k.
For determination of lattice vectors $\vec{a_1}, \vec{a_2}$, the absolute value of $|\Delta k|$ can be written as

$$|\Delta k| = |G_{||}| = \sqrt{h^2|\vec{b_1}|^2 + k^2|\vec{b_2}|^2 + 2hk|\vec{b_1}||\vec{b_2}|\cos\delta}, \tag{2.2.3}$$

whereas δ is the angle between $\vec{b_1}$ and $\vec{b_2}$ as shown in Fig. 2.9(b) and can be read out of the LEED pattern as shown in Fig. 2.8(b). Using the relations $\vec{a_1}\vec{b_1} = 2\pi = |\vec{a_1}| \cdot |\vec{b_1}|\cos\gamma$ with $\cos\gamma = \sin\delta$ and $\vec{a_2}\vec{b_2} = 2\pi = |\vec{a_2}| \cdot |\vec{b_2}|\cos(\delta - \beta - \gamma)$ with $\cos(\delta - \beta - \gamma) = \sin\delta$ Eq. (2.2.3) can be written as

$$|\Delta k| = |G_{||}| = \sqrt{\left(\frac{2\pi}{\sin\delta}\right)^2 \left(\frac{h}{|\vec{a_1}|}\right)^2 + \left(\frac{2\pi}{\sin\delta}\right)^2 \left(\frac{k}{|\vec{a_2}|}\right)^2 + \left(\frac{2\pi}{\sin\delta}\right)^2 \frac{2hk\cos\delta}{|\vec{a_1}||\vec{a_2}|}}. \tag{2.2.4}$$

With $|\vec{a_1}| = b \cdot |\vec{a_2}|$ follows

$$|\vec{a_1}| = \frac{2\pi}{|\Delta\vec{k}|\sin\delta}\sqrt{h^2 + \left(\frac{k^2}{b}\right)^2 + \frac{2hk\cos\delta}{b}} \tag{2.2.5}$$

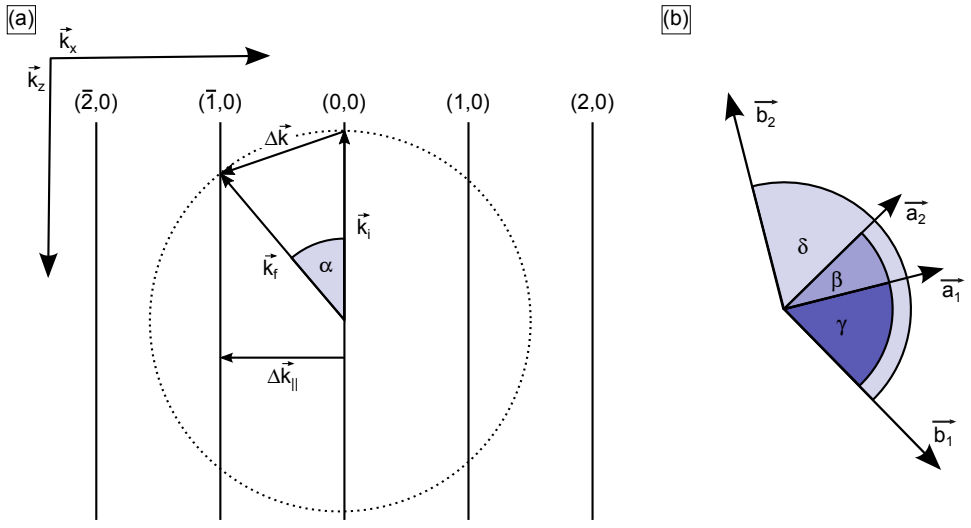

Figure 2.9: (a) The 2D Ewald construction. Due to the missing Laue constraint for the z-direction the construction shows Bragg rods instead of distinct reciprocal lattice sites. As soon as the Ewald sphere sweeps two neighbouring Bragg rods, the diffraction fulfils the Bragg conditions in 2D and leads to constructive interferences in the LEED pattern. For increasing energy, the Ewald sphere is getting larger and the angle α is shrinking, which leads to a migration of the spots towards the center of the screen. Panel (b) shows the relation between lattice vectors and reciprocal lattice vectors.

and $|\Delta\vec{k}|$ can be expressed as

$$\sin\alpha = \frac{x}{r} = \frac{|\Delta\vec{k}|}{|\vec{k_\mathrm{f}}|}. \tag{2.2.6}$$

With $|\vec{k_f}| = |\vec{k_i}| = \frac{2\pi}{\lambda}$ and the de Broglie wave length $\lambda = \frac{h}{\sqrt{2mE_\mathrm{kin}}}$ follows then

$$|\Delta\vec{k}| = \frac{2\pi\sqrt{2mE_{kin}}}{h_P} \cdot \frac{x}{r}. \tag{2.2.7}$$

Replacing the screen radius r by $\sin\varepsilon = \frac{l}{r}$ yields

$$|\Delta\vec{k}| = \frac{2\pi\sqrt{2mE_\mathrm{kin}}}{h} \cdot \frac{x}{l}\sin\varepsilon. \tag{2.2.8}$$

The opening angle of the instrument used in this thesis amounts to $\varepsilon = 51°$ (Omicron 4-Grid SpectaLEED). Replacing $|\Delta\vec{k}|$ in Eq. (2.2.5) yields to the following expression which allows to determine the real space lattice constant from LEED measurements

$$|\vec{a_1}| = \frac{h_P}{\sqrt{2mE_{kin}}} \cdot \frac{l}{x\sin\varepsilon\sin\delta}\sqrt{h^2 + \left(\frac{k^2}{b}\right)^2 + \frac{2hk\cos\delta}{b}}. \tag{2.2.9}$$

3 Experimental setup

The experimental setup is an ultra-high vacuum (UHV) chamber, which is shown in Fig. 3.1. It is separated into a preparation and cryostat chamber, which can be separated from each other by a gate valve. In order to keep the UHV conditions of $p < 2 \cdot 10^{-10}$ mbar both chambers are equipped each with a turbomolecular pump with power controlled membrane rough pump, a ion getter pump, and a titan sublimation pump. The important functional units of the chamber are coloured for better visibility in Fig. 3.1.
The samples can be transferred inside the vacuum system with the manipulator (salmon), which exhibits a boralectric heating element directly under the sample slot for the sample preparation. It allows also for direct current heating for semiconducting samples.
For the cleaning of samples a sputter gun is attached operating with argon gas (turquoise), that can be provided via a high precision gas inlet and is then ionized in the sputter gun. A

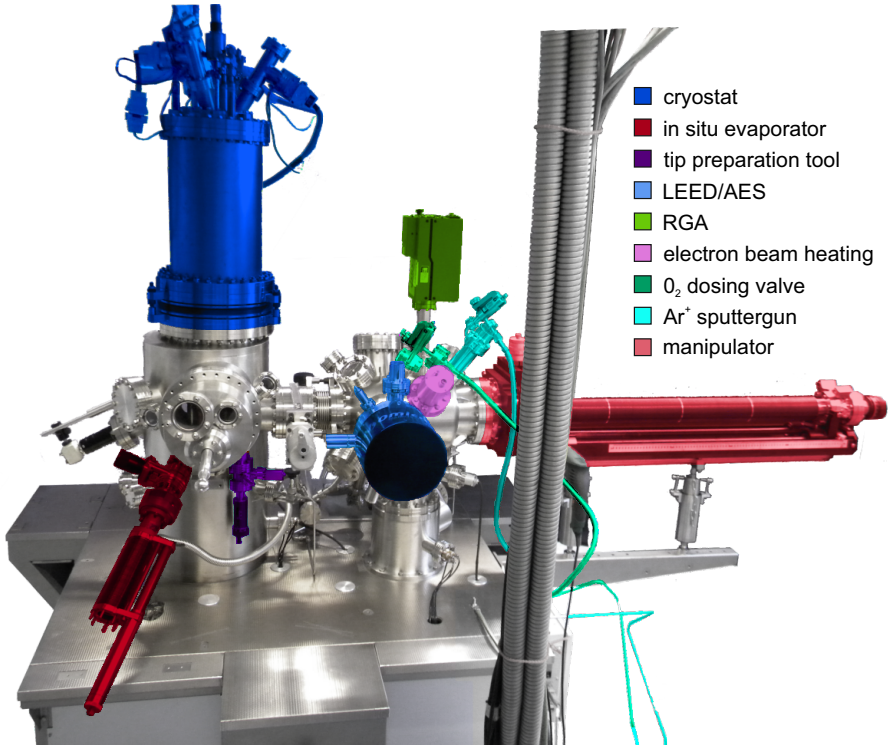

Figure 3.1: The experimental UHV setup. The important functional units are coloured for better visibility. The system consists of two separable chambers—the preparation chamber with LEED/AES optics (blue) and the cryostat chamber with the LT-STM (dark blue).

second high precision gas inlet provides oxygen (green), which is required for samples, that mainly suffer from carbon contaminations intrinsically, e.g. W and Ir crystals. For those high melting substrates an additional electron beam (e-beam) sample heating is attached on the preparation chamber (rose).
For the deposition of high melting materials (e.g. Co, Ni, Fe, Cr, ..) the chamber exhibits two e-beam evaporators on the back side of the preparation chamber and one attached on the cryostat chamber (dark red), which enables for in-situ deposition directly into the STM.
For the deposition of Bi and Pb a home-built triple-cell water-cooled Knudsen Cell evaporator is attached on the back side of the preparation chamber. The special evaporator design allows in principle for co-evaporation of up to three materials at once providing evaporation temperatures up to 1000°C. Furthermore, the preparation chamber is equipped with a quadrupol mass spectrometer (RGA, olivine) and commercial 4 Grid LEED/AES optics from Omicron Nanotechnology (blue).
The cryostat chamber contains the cryostat (dark blue) with the commercial Omicron low temperature STM (LT-STM), a sample storage, and a tip preparation tool (purple), which allows for controlled tip melting preparation procedures. The LT-STM feedthroughs are on the top part of the bath cryostat, the microscope itself is mounted directly under the bottom part of the cryostat. The STM stage is shown in Fig. 3.2. In the measurement position it hangs free on springs and is damped via an eddy current damping. Cooled down to LHe it operates at $T = 4.8\,\mathrm{K}$.

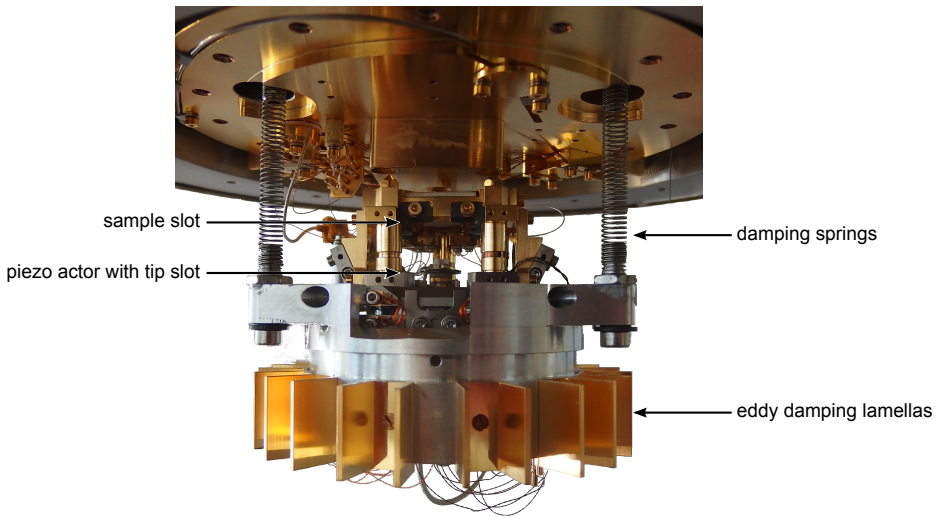

Figure 3.2: The STM stage is directly mounted on the bottom of the cryostat. The whole stage is hanging free on springs during the measurement. The damping lamellas of the eddy current system are visible at the bottom of the stage. The sample and tip position are visible, the tip is magnetically clamped onto the tubular piezo actor and the sample is mechanically clamped with two molybdenum flat springs.

4 The concept of surface states and quasi-particle interferences

The following sections will treat surface states, starting with a theoretical description of Shockley surface states in section 4.1. Section 4.2 continues with the characteristics of the Ag(111) surface state, that verifies the theoretical model discussed in section 4.1. In this framework the detectability of surface states by means of STM and the phenomenon of quasi-particle interferences are described and explained. The section ends with a short comment on 2D fast Fourier transformation (2D-FFT) data evaluation as valuable method for the detection of periodic signals.

4.1 Theoretical description of surface states

The existence of a surface, i.e. a perturbation to the perfect infinite crystal, can enable states with a strong localization on the surface—the so-called surface states. In a theoretical work in 1939 Shockley demonstrated, that surface states can evolve within bulk band gaps based on strongly overlapping orbitals [64]. The evolution of a surface state in dependency of the lattice constant a is shown in Fig. 4.1. Decreasing the atomic distance a leads to a broadening of the s- and p-type orbitals to bands, until they cross each other and the band gap gets inverted with p-like bands at lower and s-like bands at higher energy. (marked with the vertical line in Fig. 4.1). In the range of the inverted band gap a spin degenerate surface state develops out of the p and s bulk bands, respectively.
A 1D crystal model of the crystal close to the surface is shown in Fig. 4.2(a). The periodic crystal potential is interrupted at the surface ($z = \frac{a}{2}$) and connected to the vacuum potential V_0. In a 1D nearly free electron (NFE) model, suitable for a metallic surface [65], the potential $V(z)$ of the screened ion cores in the stationary Schrödinger equation

$$\left(-\frac{\hbar^2}{2m}\frac{\mathrm{d}^2}{\mathrm{d}z^2} + V(z)\right)\Psi(z) = E\Psi(z) \tag{4.1.1}$$

can be modeled with a weak periodic pseudopotential

$$V(z) = -V_0 + 2V_\mathrm{g}\cos(gz) \tag{4.1.2}$$

with the shortest reciprocal lattice vector $g = \frac{2\pi}{a}$. For the solution of Eq. (4.1.1) a linear combination of plane wave functions can be applied

$$\Psi_k(z) = \alpha\,\mathrm{e}^{ikz} + \beta\,\mathrm{e}^{i(k-g)z}\,. \tag{4.1.3}$$

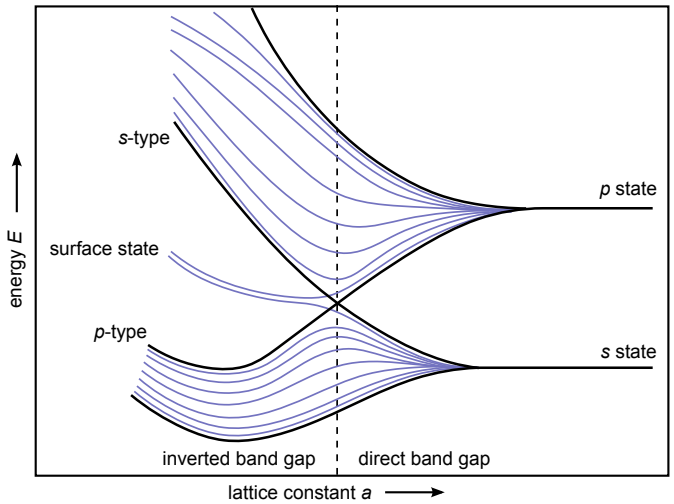

Figure 4.1: The evolution of bands out of atomic s and p orbitals. With decreasing lattice constant a the s and p orbitals broaden to bands and come closer until they cross (marked with the vertical line). For even smaller lattice constants the gap inverts with a p-type character on the bottom and s-type character on the top. In the range of the inverted gap a spin degenerate surface state develops out of the s- and p-band located energetically in the gap. Adapted from Ref. [64].

Solving the Eigenvalues of Eq. (4.1.1) with Eq. (4.1.3) leads to

$$E = -V_0 + \left(\frac{1}{2}g\right)^2 + \kappa^2 \pm \sqrt{g^2\kappa^2 + V_\mathrm{g}^2} \tag{4.1.4}$$

$$\Psi_k = \mathrm{e}^{ikz}\cos\left(\frac{1}{2}gz + \delta\right) \tag{4.1.5}$$

with $\hbar = m = 1$, the substitution $\mathrm{e}^{i2\delta} = \frac{(E-k^2)}{V_\mathrm{g}}$, and the wave vector k written as $k = \frac{g}{2} + \kappa$. A plot of $E(\kappa^2)$ in Fig. 4.2(b) shows a continuous function with solutions also for complex values of κ ($\kappa^2 < 0$). These solutions are not valid in the bulk, since their wave functions would become infinite with $|z| \to \infty$ and consequently they can not be normalized. In the energy range of complex κ values the bulk forms bulk gaps. However, the existence of a surface allows to normalize these solutions due to the fact that the wave function $\Psi(z)$ in the crystal is matched to an exponentially decaying wave function in the vacuum ($z > \frac{a}{2}$)

$$\Psi(z) = \begin{cases} \mathrm{e}^{\widetilde{\kappa}z}\cos\left(\frac{1}{2}gz + \delta\right) & , z < \frac{a}{2} \\ \mathrm{e}^{-qz} & , z > \frac{a}{2} \end{cases} \tag{4.1.6}$$

with real $\widetilde{\kappa} = i\kappa$ and the decay length $q^2 = V_0 - E$ in the vacuum. The sign of V_g influences the slope of Ψ for $z < \frac{a}{2}$ and matching both wave function parts is only successful for positive values of V_g [65, 66]. An exemplary surface state wave function for positive V_g is shown as blue line in Fig. 4.2(a). The Bloch-type oscillation of Ψ is damped exponentially into the crystal bulk as well as into the vacuum area, which results in a strong localization of Ψ on the surface. Although Shockley surface states require the surface, they are not

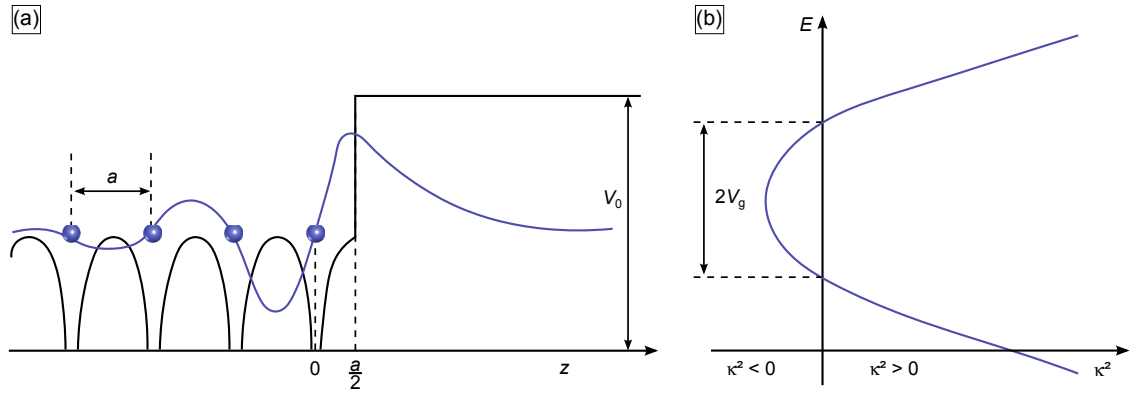

Figure 4.2: (a) The crystal potential close to the surface. The periodic lattice potential is connected to the vacuum potential V_0 at $z = \frac{a}{2}$. An exemplary surface state is represented by the blue curve. Inside the crystal ($z < \frac{a}{2}$) it features a Bloch-type oscillation with a superimposed exponential damping and beyond the surface into the vacuum ($z > \frac{a}{2}$) it is matched to an exponential decaying part. Panel (b) shows $E(\kappa^2)$ which results from a 1D nearly free electron approach. The energy range of imaginary κ values, that span the bulk band gap, gives rise to the existence of surface states. Both figures are adapted from Ref. [65].

induced by the potential change that accompanies with the existence of a surface. States, that arise from the potential change on the surface are so-called Tamm states. Tamm showed their existence 1932 in a tight binding approach within in the Kronig-Penney model [67].

4.2 The Ag(111) surface state and quasi-particle interference

Due to the required strong overlap of the atomic orbitals in Shockley-type surface states (see Fig. 4.1) they appear particularly for strongly delocalized states, e.g. in the inverted *sp*-type L-gap of Cu(111), Ag(111), and Au(111) surfaces [68, 69]. Figure 4.3 shows an angle-resolved photoemission (ARPES) measurement of a Ag(111) single crystal [15]. Panel (a) shows the dispersion of the surface state as a function of $k_{||}$, the surface state is visible as enhanced intensity (bright) in the measurement. It is energetically located in the L-gap of Ag(111) and shows a parabolic dispersion with a band minimum in the center of the 2D Brillouin zone ($\overline{\Gamma}$, $k_{||} = 0$). It can be described by a parabolic 2D NFE gas dispersion

$$E(k_{||}) = E_0 + \frac{\hbar^2 \vec{k}_{||}^2}{2m^*} \tag{4.2.1}$$

with an effective mass of $m^* = 0.397\, m_e$ (unfortunately without an error bar) and an energy onset $E_0 = -(63 \pm 1)\,\mathrm{meV}$ [14, 15]. A constant energy cut (CEC) at the Fermi level in Fig. 4.3(b) demonstrates, that the surface state features an isotropic dispersion around $\overline{\Gamma}$ resulting in a ring-like structure with $k_\mathrm{F} = 0.8\,\mathrm{nm}^{-1}$ [14, 15]. The same characteristics have

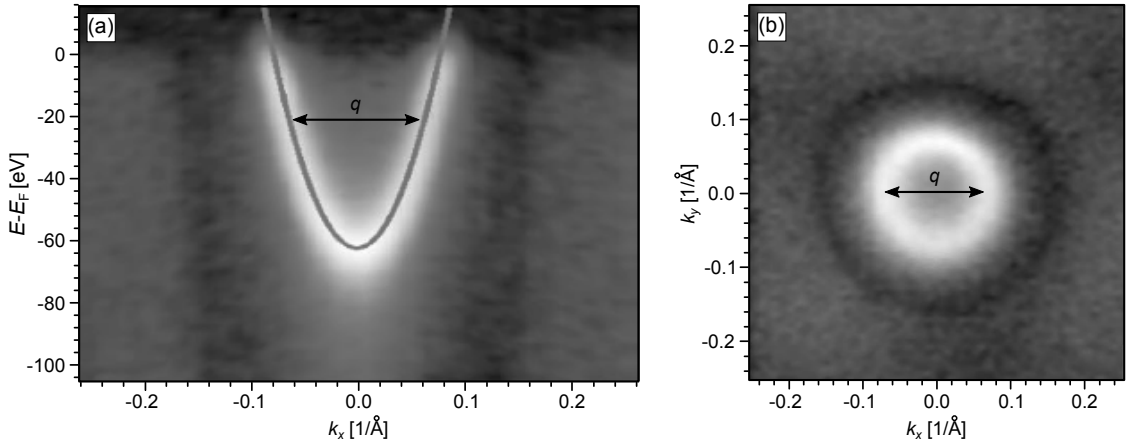

Figure 4.3: An ARPES measurement of the Ag(111) surface state, taken from Ref. [15]. Panel (a) shows its electron-like parabolic dispersion $E(k_{||})$ located in the projected bulk band gap. Panel (b) shows the constant energy cut (CEC) at the Fermi level. The Ag(111) surface state exhibits an isotropic dispersion in momentum space resulting in a ring-like structure. The arrows in (a) and (b) indicate an elastic backscattering process between $\vec{k}_{||}$ and $-\vec{k}_{||}$ resulting in a scattering vector $\vec{q}(E) = 2\vec{k}_{||}(E)$.

been found also on Cu(111) and Au(111), which additionally exhibit a spin-orbit–induced Rashba-type splitting [14, 70] (this effect will be further discussed in section 5).
Parabolic surface states can be observed in STS spectra due to their characteristic fingerprint in the DOS. The DOS for a 2D parabolic state can be calculated within the following expression

$$\rho(E) = \sum_j \frac{1}{(2\pi)^2} \int_{BZ \bigcap S} \mathrm{d}S \frac{1}{|\vec{\nabla}_{\vec{k}} E(\vec{k})|_{E=E_j}}, \tag{4.2.2}$$

where $\mathrm{d}S$ depicts a surface integral over the surface Brillouin zone for E =const[1]. With the given 2D parabolic dispersion in Eq. (4.2.1) the energy gradient is calculated by

$$|\vec{\nabla}_{\vec{k}} E(\vec{k})|_{\vec{k}} = \frac{\hbar^2 |\vec{k}_{||}|}{m^*} \tag{4.2.3}$$

and Eq. (4.2.2) turns into

$$\rho(E) = 2 \cdot \frac{1}{(2\pi)^2} \frac{m^*}{\hbar^2 |\vec{k}_{||}|} \int_{BZ \bigcap S} \mathrm{d}S. \tag{4.2.4}$$

The factor 2 accounts for the spin degeneracy and the surface integral yields the circumference of a ring with $2\pi|\vec{k}_{||}|$. The DOS is then determined to

$$\rho(E) = \begin{cases} 0 & , E < E_0, \\ \frac{m^*}{2\pi\hbar^2} = \text{const.} & , E > E_0. \end{cases} \tag{4.2.5}$$

[1]The complete derivation of this formulation is shown in the appendix

The DOS of a 2D parabolic surface state shows a steplike behaviour at the band onset and remains then constant. Indeed the steplike rise in the DOS, which is broadened by its lifetime [62], temperature, and experimental resolution limit, is visible in Fig. 2.5 (see section 2.1.5). Besides the spectroscopic fingerprint in STS measurements, the existence of a 2D electron gas on a surface leads to a fascinating phenomenon—quasi-particle interferences—that can be observed by means of STM and allows insight into the electronic properties of surfaces. The first quasi-particle interferences of surface states have been reported in 1993 at the IBM research division by Crommie and Eigler on Cu(111) [60]. Since then it has been used in several studies on many different surfaces [71–79], which feature delocalized states on the surface.
An STM measurement on clean Ag(111) close to the Fermi level is shown in Fig. 4.4(a) at $U_{\mathrm{set}} = -2\,\mathrm{mV}$. An intense pattern is visible on the surface, that stems from quasi-particle interferences. The surface defects act as scattering centers for the 2D electron gas on the surface and thus the surface exhibits a complicated pattern that is the result of superpositions of ring-like oscillations.
These oscillations can be understood under the assumption of a 2D electron gas and energy conservation (elastic scattering with E =const.). The wave functions around the surface defects can be described by a linear combination of spherical waves

$$\Psi(E = \mathrm{const.}) = \sum_{k_i} A_i \frac{1}{\sqrt{r}}\, \mathrm{e}^{i\vec{k}_i\vec{r}}. \tag{4.2.6}$$

They propagate on the surface with their Bloch wave vector $\vec{k}_i$ and are scattered on surface defects and step edges[2]. Since STM maps the DOS, $|\Psi|^2 = \Psi \cdot \Psi^*$ has to be evaluated for the interference pattern. Neglecting the degenerate spin character the wave functions for the Ag(111) surface state can be described as

$$\Psi(E = \mathrm{const.}) = A\frac{1}{\sqrt{r}}\, \mathrm{e}^{i\vec{k}\vec{r}} + B\frac{1}{\sqrt{r}}\, \mathrm{e}^{-i\vec{k}\vec{r}} \tag{4.2.7}$$

leading to

$$|\Psi|^2 = \mathrm{const.} + \frac{1}{r}\left(A^* \cdot B\, \mathrm{e}^{-i\vec{q}\vec{r}} + \mathrm{c.c.}\right) \tag{4.2.8}$$

with the scattering vector $\vec{q} = 2\vec{k}$, that connects the parabolic energy dispersion between $\vec{k}$ and $-\vec{k}$ as sketched by the arrows in Fig. 4.3(a-b). A visualization of Eq. (4.2.8) is presented schematically in Fig. 4.4(c) showing the spherical wave with a wavelength of $\lambda = \frac{2\pi}{|\vec{q}|}$ around the point-like scattering center and its $\frac{1}{r}$ decreasing amplitude. Generally the scattering vector $\vec{q}$ connects final and initial states with

$$\vec{q}(E) = \vec{k}_{\mathrm{f}}(E) - \vec{k}_{\mathrm{i}}(E). \tag{4.2.9}$$

In order to extract the scattering vector $\vec{q}$ from the interference patterns, 2D-FFT is a suitable method. The symmetrized 2D-FFT of Fig. 4.4(a) is shown in Fig. 4.4(b). It

[2]The wave vectors $\vec{k}_i$ are all 2D in-plane wave vectors, the subscript is here omitted for more clarity.

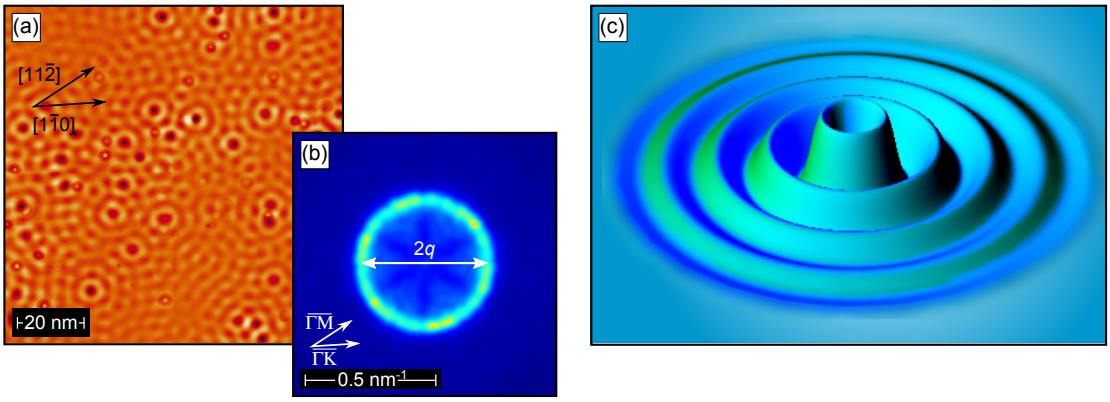

Figure 4.4: (a) Quasi-particle interferences on the Ag(111) surface. The scan shows a $100 \times 100\,\mathrm{nm}^2$ surface area ($U_{\mathrm{set}} = -2\,\mathrm{mV}, \mathrm{I}_{\mathrm{set}} = 1\,\mathrm{nA}$) . Each defect scatters the incoming waves on the surface and gives rise to oscillations with characteristic ring-like interference patterns. (b) The corresponding 2D-FFT reveals an isotropic scattering event with scattering vector $\vec{q}$, which equals the radius of the ring. Panel (c) shows a schematic of quasi-particle interference on a point-like defect showing the descending amplitude with increasing distance from the defect. Corresponding to the observed scattering on Ag(111) in (a) the scattering center exhibits a minimum in amplitude.

exhibits a ring with enhanced intensity (bright turquoise) around the center of the 2D-FFT indicating one scattering event, that occurs equally distributed with almost the same intensity for all directions. Its diameter corresponds to $2\vec{q}$ as indicated by the arrow and its circular shape denotes an isotropic dispersion for the Ag(111) surface state (compare to the CEC in Fig. 4.3(b)). The slightly enhanced sixfold intensity within the ring originates from the symmetrization where the threefold symmetry of the Ag(111) has been used to significantly increase the SNR. For this purpose the 2D-FFT is rotated by 60° and 120° around its center. Subsequently the original and rotated 2D-FFT maps are averaged. Since the 2D-FFT itself exhibits a 180° symmetry a threefold symmetrization directly leads to a sixfold symmetry in the 2D-FFT. In this context it is also important to note, that scattering maps derive from CECs, but they can not be set equal. A scattering map will only display allowed scattering events (which of course reflect the symmetry of the underlying CEC, e.g. anisotropic dispersions). For instance, in the case of topological insulators (TIs) backscattering through $\overline{\Gamma}$ is forbidden due to their peculiar electronic band structure and the resulting scattering maps look rather different from their corresponding CECs [75, 76, 79].

However, the scattering of the Ag(111) surface state is a simple intra-band backscattering event with $\vec{q} = 2\vec{k}$ and allows to unambiguously extract the surface state's dispersion relation $E(k_{||})$. The wave vectors obtained from an entire $\mathrm{d}I/\mathrm{d}U$ map series in an energy range between $(E - E_{\mathrm{F}}) = -100\,\mathrm{meV}$ and $(E - E_{\mathrm{F}}) = +200\,\mathrm{meV}$ are shown in Fig. 4.5. The data show a parabolic evolution and a fit (blue line) to the data points yields a band onset of $E_0 = (-63 \pm 2)\,\mathrm{meV}$ and an effective mass of $\mathrm{m}^* = (0.40 \pm 0.01)\,\mathrm{m_e}$, which is in a very good agreement to the parameters obtained by ARPES. The excellent agreement between

ARPES and STM data demonstrates, that STM is not only bound to real space but can also be utilized to determine reciprocal properties, such as the dispersion of a surface state band. Additionally, the advantage of STM is spatially resolved access to occupied as well as unoccupied sample states.

2D-FFT data evaluation

The evaluation of periodic signals by means of 2D-FFT is very useful in STM measurements, all scattering vectors in Fig. 4.5 have been extracted out of 2D-FFT maps. Especially for more complicated band structures the real space quasi-particle interference pattern may consist of multiple scattering channels which can also be anisotropic. While the detection of such details in real space is extremely difficult, the transformation into momentum space through 2D-FFT offers the advantage to reveal more than one scattering channel or anisotropic dispersions easily. The momentum space resolution of a 2D-FFT depends on the real space measurement as described in the following. The size K of the 2D-FFT is determined by the real space resolution δx

$$\delta x = \frac{L}{\#\mathrm{px}} \tag{4.2.10}$$

with the real space length L and the number of pixel #px.

$$K = \frac{1}{\delta x} \tag{4.2.11}$$

In this definition the common factor 2π is missing in the numerator, which allows to determine atomic distances out of the FFT directly by the inverse values. For the evaluation

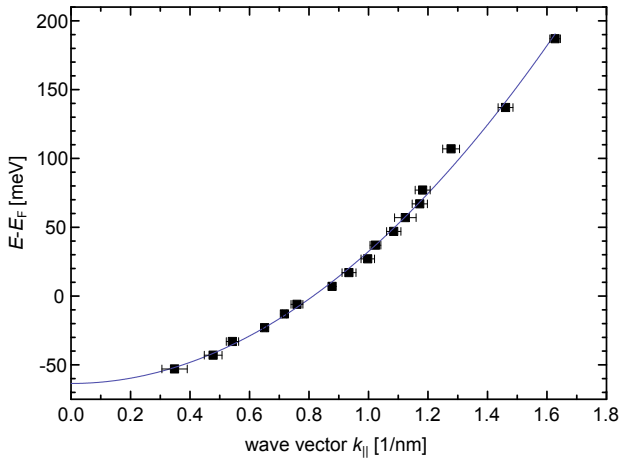

Figure 4.5: Extracted k values for a series of $\mathrm{d}I/\mathrm{d}U$ maps on the Ag(111) surface. Each data point represents an elastic backscattering event within the surface state from $+k$ to $-k$. The blue line represents a parabolic fit to the data points with a band minimum of $E_0 = (-63 \pm 2)\,\mathrm{meV}$ and an effective mass of $m^* = (0.40 \pm 0.01)\,m_e$.

of scattering vectors all readout values have to be multiplied with 2π. The momentum space resolution δk can be determined by

$$\delta k = \frac{K}{\#\mathrm{px}}, \tag{4.2.12}$$

with equal numbers of pixel in real and momentum space. Inserting Eq. (4.2.11) in Eq.(4.2.12) yields

$$\delta k = \frac{1}{\# \cdot \mathrm{px}\ \delta x} = \frac{1}{L} \tag{4.2.13}$$

An image with 100 nm scan size and 512 pixel resolution leads to a 2D-FFT with $5.12\,\frac{1}{\mathrm{nm}}$ size and resolution of $0.01\,\frac{1}{\mathrm{nm}}$. The 2D-FFT is symmetric around the center and its values are distributed equally to positive and negative k values.

5 Theory of spin-orbit coupling on surfaces

The spin-orbit coupling (SOC) is a relativistic correction to the Schroedinger equation [80], which gives rise to several phenomena, e.g. the complex chiral magnetic orders on surfaces due to the Dzyaloshinskii-Moriya interaction [81, 82], topological insulators [75, 83–87], and the Rashba effect [2, 17–19]. Section 5.1 gives a short introduction to the SOC and gives an intuitive explanation as an effective magnetic field in the rest frame of the moving electron. Yu. A. Rashba and É . I. Bychkov applied the SOC to a 2D NFE gas at an interface or surface [2, 17–19], which is presented in Sec. 5.2. It creates a momentum-split energy dispersion of the NFEs with in-plane polarized states. As a result of the broken inversion symmetry—that accompanies naturally with an interface or surface—the Kramers degeneracy is lifted. Section 5.3 describes experimental findings on the Rashba-split Au(111) surface state [13–16] and discusses the origin and strength of the observed splitting in comparison to the simple Rashba model [17–19]. Section 5.4 presents isostructural alloy surfaces of heavy post-transition metals on Ag(111) and Cu(111), which have been recently reported to exhibit giant Rashba-split states and illustrates the current experimental and theoretical findings for the special cases of Pb and Bi deposited on Ag(111). The last section of this chapter discusses the detectability of Rashba-split states by means of STM using STS spectroscopy [25, 88] and quasi-particle interference mapping [17].

5.1 Spin-orbit interaction

The spin-orbit interaction is a relativistic correction that can be derived from the Dirac equation [80, 89]

$$H_{\mathrm{SOC}} = \frac{\hbar}{4m_e^2c^2}\vec{\sigma}\cdot\left(\vec{\nabla}V\times\vec{p}\right) \tag{5.1.1}$$

with the electron mass m_e, the Pauli matrices vector $\vec{\sigma}$, the potential V, and the momentum operator $\vec{p}$.
The SOC Hamiltonian can be understood in the rest frame of the moving electron, where the electron feels the static electric field $\vec{E} = -\frac{\vec{\nabla}V}{e}$ as an effective magnetic field [90]

$$\vec{B} = -\frac{1}{c^2}(\vec{v}\times\vec{E}) = -\frac{1}{em_ec^2}(\vec{\nabla}V\times\vec{p}). \tag{5.1.2}$$

The energy E of the electron in this effective field is

$$E = -\frac{e}{m_e} \cdot \frac{\hbar}{2}\vec{\sigma} \cdot \vec{B} \tag{5.1.3}$$

$$= \frac{\hbar}{2m_e^2c^2}\vec{\sigma} \cdot (\vec{\nabla}V \times \vec{p}) \tag{5.1.4}$$

This is besides a factor of $\frac{1}{2}$ exactly the SOC Hamiltonian - the missing factor stems from the fact that the electron's rest frame is a rotating coordinate system. Considering the so-called Thomas precession [91] for Eq. (5.1.4) yields a factor of $\frac{1}{2}$ resulting in the same expression as given in Eq. (5.1.1).
The coupling between spin $\vec{S}$ and orbital angular momentum $\vec{L} = \vec{r} \times \vec{p}$ is not directly visible in the formulation of Eq. (5.1.1), but assuming a spherically symmetric potential $\vec{\nabla}V = \frac{\vec{r}}{r}\frac{\mathrm{d}V}{\mathrm{d}r}$ and using $\vec{S} = \frac{\hbar}{2}\vec{\sigma}$ Eq. (5.1.1) can be written as

$$H_{\mathrm{SOC}} = \frac{1}{2m_e^2c^2}\frac{1}{r}\frac{\mathrm{d}V}{\mathrm{d}r}\left(\vec{S} \cdot \vec{L}\right). \tag{5.1.5}$$

Equation (5.1.5) describes the atomic SOC and shows directly the coupling between the electron spin $\vec{S}$ and its orbital angular momentum $\vec{L}$. The SOC scales with the atomic number Z^4 for hydrogen-like atoms [90, 92] and is therefore important for heavy elements, e.g. the heavy post transition elements Pb ($Z = 82$) and Bi ($Z = 83$)[1]. The SOC is the driving force for several phenomena, e.g. the chiral magnetic orders on surfaces due to Dzyaloshinskii-Moriya interaction [81,82], topological insulators [75,83–87], and the Rashba effect [2, 17–19], which will be discussed in the next section.

5.2 The Rashba effect

The Rashba effect describes a 2D NFE gas at an interface ($\vec{p} = (p_x, p_y, 0)$) with an at least threefold symmetry and a potential gradient along the interface normal, $\vec{\nabla}V = \frac{\mathrm{d}V}{\mathrm{d}z}\vec{e}_z$ [2, 17–19]. Under these assumptions Eq. (5.1.1) reduces to

$$H_{\mathrm{R}} = -\frac{\alpha}{\hbar}\vec{\sigma} \cdot (\vec{e}_z \times \vec{p}) \tag{5.2.1}$$

with $\alpha = -\frac{\hbar^2}{4m^2c^2} \cdot \frac{\mathrm{d}V}{\mathrm{d}z}$ that contains the surface potential gradient and quantifies the strength of the coupling. The complete Hamiltonian including the NFE Hamiltonian can be written as 2D matrix

$$H_{\mathrm{R}} = \begin{pmatrix} \frac{p^2}{2m^*} & \frac{\alpha}{\hbar}(ip_x + p_y) \\ \frac{\alpha}{\hbar}(-ip_x + p_y) & \frac{p^2}{2m^*} \end{pmatrix}. \tag{5.2.2}$$

For the solution a superposition of plane waves can be applied

$$\Psi = \mathrm{e}^{ikr}(a\,|\uparrow\rangle + b\,|\downarrow\rangle) \tag{5.2.3}$$

[1] Bi is the heaviest non-radioactive element in the periodic table of elements.

where the spin states $|\uparrow\rangle = (1,0)$ and $|\downarrow\rangle = (0,1)$ are quantized along the z-axis. The plane wave character of Ψ yields $p_i = \hbar k_i$ and with polar coordinates $k_x + ik_y = |\vec{k}_{||}|\,\mathrm{e}^{i\varphi}$ follows

$$H_{\mathrm{R}} = \begin{pmatrix} \frac{\hbar^2\vec{k}_{||}^2}{2m^*} & i\alpha|\vec{k}_{||}|\,\mathrm{e}^{-i\varphi} \\ -i\alpha|\vec{k}_{||}|\,\mathrm{e}^{i\varphi} & \frac{\hbar^2\vec{k}_{||}^2}{2m^*} \end{pmatrix}. \tag{5.2.4}$$

The Eigenvalues of Eq. 5.2.4 are solved by $\mathrm{Det}(H_{\mathrm{R}} - E\mathbb{1}) \stackrel{!}{=} 0$ to

$$E_{+/-}(\vec{k}_{||}) \;=\; \frac{\hbar^2\vec{k}_{||}^2}{2m^*} \pm \alpha|\vec{k}_{||}|. \tag{5.2.5}$$

The first term describes a parabolic NFE gas dispersion, which is energy-split by the second term $\pm\alpha|\vec{k}_{||}|$. Thus the energy splitting is linear in $|\vec{k}_{||}|$ and its splitting strength is determined by α which contains the potential gradient.[2] To show the momentum splitting Eq.(5.2.5) can be brought into the form

$$E_{+/-}(\vec{k}_{||}) \;=\; \frac{\hbar^2}{2m^*}(k_{||} \pm k_0)^2 - \Delta_{\mathrm{SO}} \tag{5.2.6}$$

$$\tag{5.2.7}$$

with the momentum splitting $k_0 = \frac{\alpha m^*}{\hbar^2}$ and an overall SOC-induced reduction of the energy $\Delta_{\mathrm{SOC}} = \frac{m^*\alpha^2}{2\hbar^2}$ [19].
Figure 5.1(a) shows the resulting dispersion of the Rashba Hamiltonian for a positive effective mass m^*. The dispersion is cut along the k_x-axis through $\overline{\Gamma}$ to illustrate the $\pm k_0$ shifted parabolas in the silhouette of the cut. The inner (upper) part of the dispersion represents the E_+ and the outer (lower) shell the E_- solution. The overall momentum shift between both parabolas in the contour is $2k_0$. The crossing of both parabolas at $k = 0$ is labeled E_{R} in this work. The term ΔE_{R} describes the energy splitting between E_{R} and the band minima E_0

$$\Delta E_{\mathrm{R}} = E(k=0) - E_-(k=+k_0) = \frac{\hbar^2 k_0^2}{2m^*}.^{3} \tag{5.2.8}$$

The Eigenstates $\Psi_{+/-}$ can be solved by $\mathrm{Det}(H_{\mathrm{R}} - E_{+/-}\mathbb{1}) \cdot \Psi_{+/-} = 0$, which results in

$$\Psi_{+/-} \propto \left(i\,|\uparrow\rangle \pm \mathrm{e}^{i\varphi}\,|\downarrow\rangle\right). \tag{5.2.9}$$

Finally the spin polarization is evaluated by $\sigma_{i,+/-} = \langle\Psi_{+/-}|\sigma_i|\Psi_{+/-}\rangle\,(i = x,y,z)$ to

$$\vec{\sigma}_{+/-} = \pm\mathrm{sgn}\alpha \begin{pmatrix} \sin\phi \\ -\cos\phi \\ 0 \end{pmatrix}. \tag{5.2.10}$$

[2] From now on vector symbols are omitted for more clarity.
[3] Some studies define E_{R} as the energetic splitting, that is labeled ΔE_{R} in this work. Also the factor 2 in the denominator is missing in some definitions.

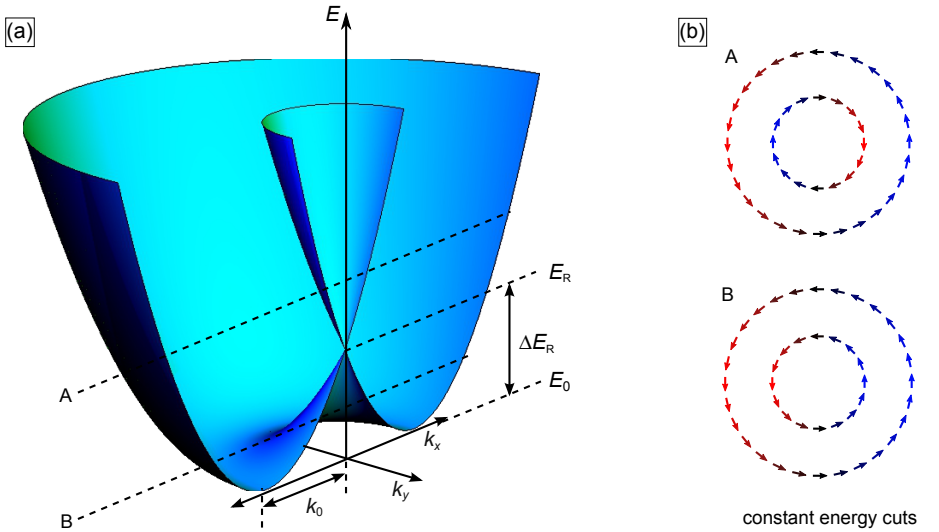

Figure 5.1: Panel (a) shows the dispersion of a Rashba-split 2D NFE state. The cut profile shows two parabolas shifted by $\pm k_0$ away from the center of the 2D Brillouin zone. The energy of their crossing at $k = 0$ is called Rashba energy E_R and the energetic distance between E_R and the band onsets E_0 defines the quantity ΔE_R. Panel (b) shows two CECs at the intersection lines A and B in panel (a). Both CECs show two concentric rings. Above E_R the in-plane spin polarizations of the inner and outer ring (indicated by the arrows and blue/red colour) rotate against each other (A). Between E_R and E_0 both rings belong to E_- leading to the same sense of rotation (B).

The spin polarization rotates in the k_x, k_y plane and is locked perpendicular to $\vec{k}_{||}$ with a vanishing z-component, therefore both states are fully in-plane polarized and the sign of α determines the overall sense of rotation. The spin polarizations of E_+ and E_- solution are counter-rotating as pointed out by Eq. (5.2.10). This leads to two qualitatively different spin polarizations in CECs, as shown in Fig. 5.1(b). Both exhibit two concentric rings, but the spin polarization rotates differently above and below E_R. The outer ring and inner ring have opposite senses of rotation above E_R (Fig. 5.1(b), top) but between E_R and E_0 both rings exhibit the same sense of rotation (Fig. 5.1(b), bottom), since their origin is in both cases E_-.

Remarkably, the Rashba Hamiltonian lifts the Kramers degeneracy and leads to fully spin-polarized states in momentum space, but the net magnetization remains zero as time reversal symmetry still holds with $E(k, \uparrow) = E(-k, \downarrow)$.

5.3 Rashba-split surface states

While originally introduced for interfaces of semiconductor heterostructures, the Rashba-Bychkov effect on metallic surfaces consisting of high-Z elements has recently attracted considerable interest. The first successful observation of a Rashba-split surface state was reported by La Schell *et al.* [13] in 1996 for the Au(111) surface state, which features an electron-like NFE band dispersion similar to Ag(111) [93] with a band onset of $E_0 = -(487 \pm 6)\,\text{meV}$ [14]. The band dispersion of an Au(111) single crystal as obtained by ARPES is presented in Fig. 5.1(a) [15]. Two clearly distinguishable parabolas are visible, which are shifted by $2k_0 = 0.025\mathring{A}^{-1}$ [15] away from each other, which corresponds to an energy splitting of $\Delta E_\text{R} = 2.1\,\text{meV}$ [94]. A CEC at the Fermi level is presented in Fig. 5.1(b). It exhibits two concentric isotropic rings centered around $\overline{\Gamma}$. The qualitative agreement between the theoretical model developed in Sec. 5.1 and the experimentally observed band structure is striking. Nevertheless, the authors of Ref. [13] already realized, that the splitting strength can not originate from the surface induced potential gradient that has been used in the simple Rashba model (for the simple Rashba model see Sec. 5.2). Within this model the resulting splitting for Au(111) amounts to approximately $10^{-6}\,\text{eV}$ [13, 19, 24], which is numbers of magnitudes smaller than the observed energy splitting of $\approx 100\,\text{meV}$ at the Fermi level [13][4]. Searching for an origin of the observed splitting they

[4]In this study the splitting is described as the energy splitting at E_F

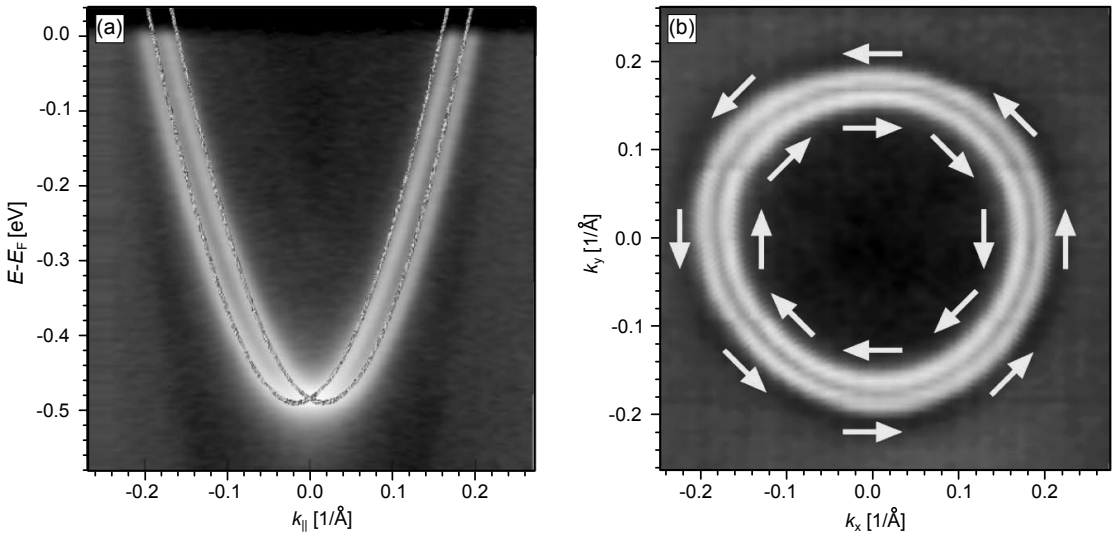

Figure 5.2: An ARPES measurement of the Au(111) surface state, taken from Ref. [15]. Panel (a) shows its electron-like parabolic dispersion $E(k_{||})$ very similar to the Ag(111) case in Fig. 4.3, but a momentum splitting of the parabolic surface state into two branches with $2k_0 = 0.025\frac{1}{\mathring{A}}$ is clearly visible. Panel (b) shows the constant energy cut (CEC) at the Fermi level. The Au(111) surface state exhibits two concentric isotropic rings, which is in a perfect agreement to the model of Fig. 5.1. The arrows indicate the counter-rotating in-plane spin polarizations.

considered the strong potential gradients close to the ion cores, which are totally neglected in the NFE model. Within this approach they estimated a value of $\approx 150\,\mathrm{meV}$ which is in a good agreement to the observed splitting.
In the following several theoretical studies were performed in order to resolve the mechanism of Rashba-split surface states more in detail [17–19]. Peterson and Hedegård developed a tight binding model for the *sp*-derived surface state of Au(111) [17] and demonstrated, that the Rashba splitting is proportional to the product of the atomic spin-orbit coupling and an asymmetry parameter γ, which represents the surface potential gradient. In other words, the inversion asymmetry is necessary for the appearance of Rashba-split states, but the atomic-spin orbit coupling determines its magnitude.
References [18, 19] showed by means of DFT calculations, that more than 90% of the Rashba-splitting of the Au(111) surface state originates from a very narrow sphere with $r = 0.25 \cdot a_0 \approx 0.2\,\text{Å}$ around the ion cores[5]. They pointed out, that the potential gradient in this area is of an almost ideal *s*-type character, which is not expected to result in any spin-orbit splitting. However, the potential gradient of the cores enters the spin-orbit coupling since the wave functions in the core region are asymmetric. Thus, the required asymmetry is provided by the wave functions. According to that the orbital mixture of $l : (l \pm 1)$ states is responsible for the splitting strength in analogy to the asymmetry parameter γ [17] and gives quantitatively the correct splitting strength. In this context it can also be understood why DFT calculations predict a 20 times stronger momentum splitting for Au(111) than for Ag(111) where it amounts to only $2k_0 = 0.0013\,\text{Å}^{-1}$ [16]. The ratio of $p : d$ (for $m = 0$) for Au(111) amounts to 3.3 but $p : d = 9.5$ for Ag(111) [18, 19]. Thus the Au(111) surface state has a stronger admixture of d_{z^2} character, which enhances the splitting considerably. The authors of Ref. [18] also mentioned that the surface potential gradient influences the orbital character of surface states and consequently the splitting strength is affected by manipulations of the electric field on the surface, which they showed in DFT calculations for Lu(0001). Also experimental works reported about splitting strength manipulations due to adsorbates, e.g. Xe,Ar/Au(111) [16, 21] O/Gd(0001) [20] Na,Xe/Bi/Cu(111) [22]. The experimental findings in these studies are addressed to adsorbate-induced surface potential changes which affected the asymmetry of the involved surface state wave functions.
Interestingly, the surface state of Cu(111) has been reported recently as Rashba-split in a laser excited ARPES experiment [70]. The authors reported about a momentum splitting of $2k_0 = 0.0114\,\text{Å}^{-1}$, which results in an energy splitting of $\Delta E_\mathrm{R} = 0.3\,\mathrm{meV}$ for an effective mass of $m^* = 0.41\,m_e$. Interestingly the momentum splitting is about nine times larger than the one predicted for Ag(111), although Cu features actually a smaller atomic mass than Ag—in contrast to the simple picture where heavier elements should provide stronger Rashba splittings due to the enhanced atomic spin-orbit coupling. The authors point out that the simple consideration of atomic spin-orbit coupling fails to estimate correct splitting strengths and assign the stronger splitting in the Cu(111) surface state to the asymmetry

[5] Bohr radius $a_0 = 0.529\,\text{Å}$ [95]

of the involved wave functions.
All these aspects show, that the simple NFE gas model in Sec. 5.2 gives qualitatively a correct model but fails to characterize the Rashba splitting on surfaces quantitatively since numerous aspects have to be reconsidered for correct splittings.

5.4 Model systems: Giant Rashba splittings on isostructural surface alloys

After the discovery of Rashba-split surface states on Au(111) [13] and manipulating the out-of–plane surface potential gradient by adsorbates [16, 20–22] Ast *et al.* introduced 2007 the idea of enhancing the in-plane surface potential gradient [23]. The authors proposed the idea of surface alloying with heavy elements, which could create new electronic states due to the resulting modification of the in-plane hybridization. They deposited Bi atoms on Ag(111) and created an ordered $(\sqrt{3} \times \sqrt{3})$ Bi/Ag(111)$R30°$ surface, which was found to exhibit a fully occupied Rashba-split surface state with an enormously large energy splitting of $\Delta E_\mathrm{R} = 200\,\mathrm{meV}$. They mentioned that an isostructural $(\sqrt{3} \times \sqrt{3})$ Sb/Ag(111)$R30°$ surface alloy has been found earlier in an $I(V)$ LEED study, which already indicated, that an isostructural class of surface alloys with similar Rashba band characteristics and splitting strengths could exist.
Indeed in the following years giant Rashba-type splittings have been experimentally observed and theoretically predicted for the deposition of $1/3\,\mathrm{ML}_{\mathrm{fcc}(111)}$[6] of heavy post transition metals on the noble metal surfaces of Ag(111) and Cu(111) such as Bi/Ag(111) [23–31, 33], Bi/Cu(111) [22, 31, 32, 34, 35], Pb/Ag(111) [24–28, 36, 37], Sb/Ag(111) [28, 33, 38, 39], and Sb/Cu(111) [34]. The strongest splittings have been observed on the Bi/Ag(111) surface with $\Delta E_\mathrm{R} = 200\,\mathrm{meV}$ [25] followed by Pb/Ag(111) with $\Delta E_\mathrm{R} = 67\,\mathrm{meV}$ [25], Bi/Cu(111) with $\Delta E_\mathrm{R} = 15\,\mathrm{meV}$ [34], Sb/Ag(111) with $\Delta E_\mathrm{R} = 5.7\,\mathrm{meV}$ [28] and almost vanishing for Sb/Cu(111) with an estimated value $\Delta E_\mathrm{R} \approx 3\,\mathrm{meV}$ [28]. Obviously the alloys containing Bi atoms split stronger than Pb alloys and the weakest splittings are provided by Sb alloys for the same substrate. Since Bi is the heaviest and Sb the lightest atom, the decreased splitting strength can be assigned to the atomic spin-orbit coupling. Generally, alloys with Ag(111) substrates provide stronger splittings than the Cu(111) alloys, although the situation is reversed for the pure substrates. The origin of this behaviour can be explained with the wave function asymmetry, since small variations of that value lead to large changes in the splitting strength [24]. Interestingly, so far no Rashba-split 1/3 ML surface alloys have been reported for the Au(111) surface. A possible reason might be the fact that Au(111) exhibits the characteristic herringbone reconstruction [96–99] in contrast to the unreconstructed Cu(111) and Ag(111) surfaces.
Figure 5.3(a) shows a structural model of the isostructural surface alloys. The deposited atoms—Bi, Pb or Sb—replace every third Ag or Cu atom in the surface and form

[6] The subscript indicates the reference lattice, e.g. $1\,\mathrm{ML}_{\mathrm{Ag}(111)} \neq 1\,\mathrm{ML}_{\mathrm{Pb}(111)}$

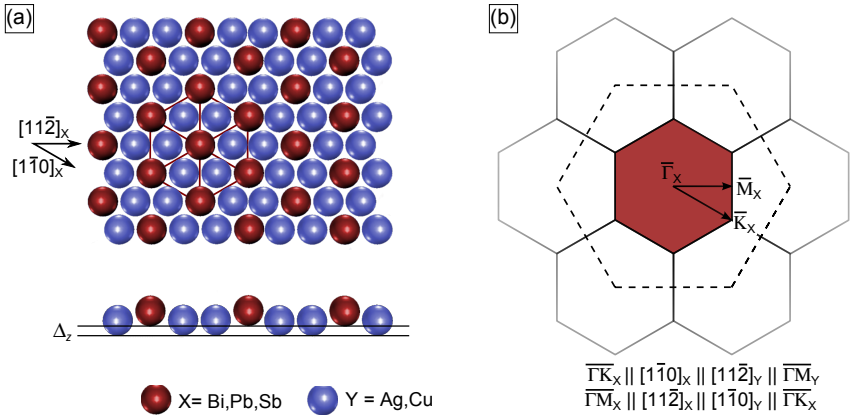

Figure 5.3: (a) Top and side view of the isostructural $(\sqrt{3} \times \sqrt{3})$ X/Y(111)$R30°$ alloy surfaces with relaxation Δ_z of the adsorbed atoms. The adsorbate atoms X=Bi,Pb,Sb (red atoms) replace every third atom of the Y=Ag,Cu surface (blue atoms). The unit cell of the surface alloy is therefore rotated by 30° with respect to the substrate, resulting in a nearest neighbour direction of the X atoms (illustrated with the arrows) which corresponds to the next nearest neighbours of the substrate atoms and vice versa: $[1\bar{1}0]_X||[11\bar{2}]_Y$ and $[11\bar{2}]_X||[1\bar{1}0]_Y$. (b) The first surface Brillouin zone of the alloy structure (marked red) features a hexagonal shape with the center $\overline{\Gamma}$ of the 2D Brillouin zone. The high symmetry points $\overline{M}$ and $\overline{K}$ on the borders of the first Brillouin zone and $\overline{\Gamma}$ span the reciprocal space directions $\overline{\Gamma K}_X$ and $\overline{\Gamma M}_X$. The first Brillouin zone of the substrate (dashed line) is rotated by 30° with respect to the alloy structure leading to the relation $\overline{\Gamma K}_X||\overline{\Gamma M}_Y$ and $\overline{\Gamma M}_X||\overline{\Gamma K}_Y$. The real space directions can also be connected to the reciprocal space directions with $\overline{\Gamma K}_X||[1\bar{1}0]_X$ and $\overline{\Gamma M}_X||[11\bar{2}]_X$.

$(\sqrt{3} \times \sqrt{3})R30°$ alloy structures with a hexagonal surface (top view). The adsorbed atoms stick out of the surface, shown in Figure 5.3(a) (side view) by the outward relaxation Δ_z, which differs for the specific adsorbate-substrate systems [94]. Figure 5.3(b) illustrates the hexagonal 2D Brillouin zones (solid line) of the surface alloy structure which is rotated by 30° with respect to the Ag(111) Brillouin zone (dashed line). The first Brillouin zone is coloured red and the momentum space directions are indicated by the arrows that connect the center of the Brillouin zone ($\overline{\Gamma}$) with the high symmetry points $\overline{M}$ and $\overline{K}$.

5.4.1 Pb/Ag(111)

The first experimental evidence for a Rashba-split Pb/Ag(111) surface has been reported in Ref. [36], an ARPES measurement is presented in Fig. 5.4(a). It indicates the tails of two hole-like states which are shifted in k and exhibit band onsets that are far above the Fermi level. The authors of Ref. [36] assigned the observed bands to a Rashba-split hole-like band with an effective mass of $m^* = -0.15\, m_e$, a splitting of $2k_0 = 0.06\,\text{Å}^{-1}$ and a band onset located at $(E - E_F) = 0.66\,\text{eV}$.

A DFT study found that the band positions of these Rashba states critically depend on the vertical relaxation Δ_z of the Pb atoms relative to the Ag atoms, [24]. The authors

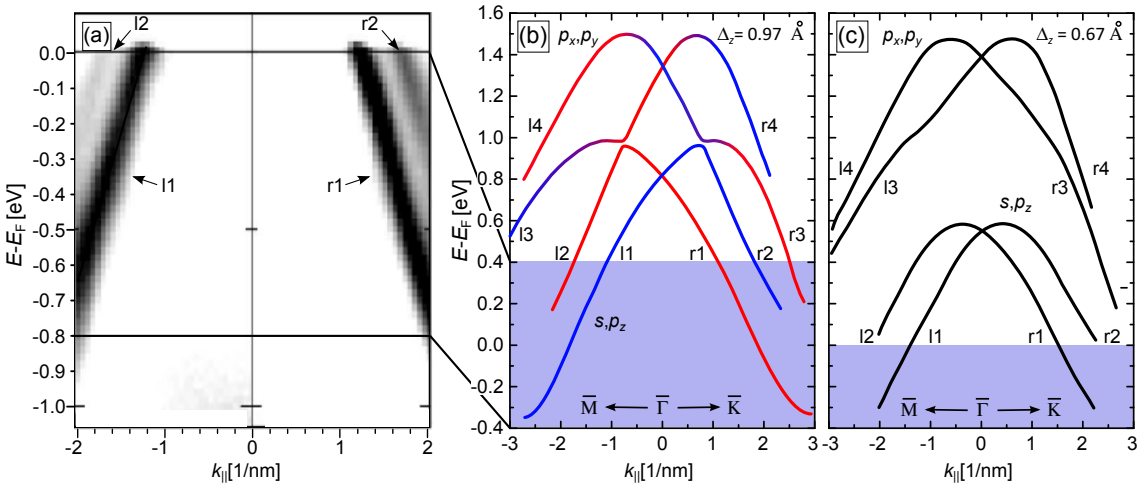

Figure 5.4: (a) An ARPES measurement of $(\sqrt{3}\times\sqrt{3})$Pb/Ag(111)$R30°$ surface alloy, adapted from Ref. [36]. Two hole-like dispersions are visible which are momentum-shifted by $\pm k_0 = 0.03\mathring{A}^{-1}$. The band onsets of these branches are located in the unoccupied states, therefore it is not clear whether the two branches belong to one Rashba-split state or to two Rashba-split states. Panel (b) and (c) show DFT calculations for two different relaxations of the Pb atoms in the surface with $\Delta_z = 0.97$ Å and $\Delta_z = 0.67$ Å, respectively. Panels (b) and (c) are adapted from Ref. [24]. Both band dispersions exhibit a p_x, p_y-derived state (upper) and s, p_z- derived state (lower). For $\Delta_z = 0.97$ Å the observed band dispersion in (a) would belong to two different surface states with a strong momentum splitting. In order to match the DFT calculations to the experimental data, the Fermi level had to be shifted by 400 meV indicated by the blue shaded area. For the second case in (c) with $\Delta_z = 0.67$ Å the lower Rashba band shifts down in energy, thereby increasing the energy separation between the two bands. In this case, the experimental data would belong to one surface state with a weak momentum splitting (see text for more details).

considered two distinct scenarios in their calculations as schematically represented in Fig. 5.4(b) and (c). While qualitatively both dispersions are composed of momentum split p_x, p_y- and s, p_z-derived bands, the particular splitting strengths, band positions and characteristics differ considerably for both models.

In the first case, at the self-consistent relaxation value of $\Delta_z = 0.97$ Å (Fig. 5.4(b)), the band dispersion exhibits a hybridization of the s, p_z and p_x, p_y bands close to the onset of the lower Rashba band (s, p_z) at about $(E - E_F) = 1$ eV. However, this band position disagrees with ARPES measurements in Ref. [36], which differs by ≈ 400 meV from the DFT result. This offset is indicated by the blue shaded area in Fig. 5.4(b). In order to improve the agreement between the experimentally observed band positions and the calculated surface electronic structure the relaxation value was subsequently tuned to $\Delta_z = 0.67$ Å [24]. The resulting band structure is shown in Fig. 5.4(c). It agrees well with ARPES data [36] and the characteristically shaped van-Hove–like singularity which appears in STS spectra at 654 meV above the Fermi level [25].

The calculations in Ref. [24] also presented a quite complicated spin polarization for

the dispersion which is indicated by red and blue colours in Fig. 5.4(b). It features an unconventional spin polarization for the p_x, p_y-derived band with a sign change of spin polarization at both band maxima. Around the hybridization gap the spin polarizations of the p_x, p_y-derived bands change sign again, whereas a conventional polarization was found for the s, p_z-derived band. Spin-resolved ARPES (SARPES) experiments could qualitatively confirm the theoretically predicted spin texture in the occupied energy range [27], but so far nothing is known about the unoccupied energy range. Unfortunately, Ref. [24] does not indicate the spin polarization of the second model in Fig. 5.4(c), therefore the bands are coloured black.
Obviously, the smaller relaxation of the Pb atoms results in a larger inter-band spacing and the absence of any hybridization between the upper and the lower band. Since both models result in a very similar dispersion below the Fermi-level, it is virtually impossible to verify one of the two models by ARPES measurements. In the case of Fig. 5.4(b) the branches observed below E_F would belong to two different surface states with a strong momentum splitting, in the case of Fig. 5.4(c) both branches would originate from the same Rashba-split surface state with a smaller splitting. Experimentally even smaller outward relaxations of $\Delta_z = (0.46 \pm 0.06)\,\text{Å}$ have been reported [28], pointing towards the model presented in Fig. 5.4(c). However, the exact band structure remains unclear so far due to their highly unoccupied nature.

5.4.2 Bi/Ag(111)

Shortly after the experimental detection of the Rashba-split $(\sqrt{3} \times \sqrt{3})$Pb/Ag(111)$R30°$ surface also the case of $(\sqrt{3}\times\sqrt{3})$Bi/Ag(111)$R30°$ has been confirmed as Rashba-split [23,25]. Since Bi has one p electron more than Pb, the bands shift downwards with respect to the Fermi level, which allows ARPES measurements to detect a larger range of the bands. An ARPES measurement of a Bi/Ag(111) surface is presented in Fig. 5.5(a) [100]. Two downwards dispersing (effective electron mass $m^* < 0$) surface states can be seen, a fully occupied s, p_z-like band and a mostly unoccupied p_x, p_y-derived band [24]. The splittings have been determined to $2k_0 = 0.26\,\text{Å}^{-1}$, $\Delta E_\mathrm{R} = 200\,\text{meV}$ [23] for the s, p_z-like band and $2k_0 = 0.14\,\text{Å}^{-1}$ for the p_x, p_y-derived band [31].
A calculated band structure is presented in Fig. 5.5(b) [24], which shows good consensus between experiment and theory regarding the band positions and splitting strengths. Figure 5.5(b) indicates a complicated spin topology [24] similar to Fig. 5.4(b) with an unconventional spin polarization of the upper (empty) Rashba bands, that change sign at the band maxima (Fig. 5.5(b)). Furthermore, it has been predicted [24] and experimentally verified [30] that the upper and the lower Rashba band avoid hybridization due to spin-orbit–induced inter-band spin-mixing. DFT calculations have predicted that both bands switch polarization around the hybridization gap similar to the Pb/Ag(111) model in Fig. 5.4(b).
Similar band dispersions without any hybridization have been also observed and predicted for

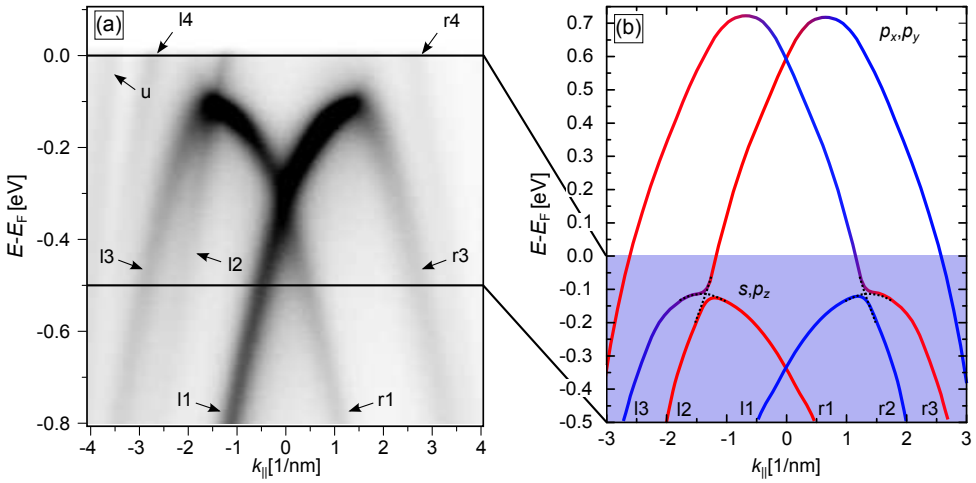

Figure 5.5: (a) An ARPES measurement of $(\sqrt{3} \times \sqrt{3})$Bi/Ag(111)$R30°$ surface alloy, adapted from Ref. [100]. The s, p_z- derived band lies completely in the occupied energy range with an onset of $E_0 = -135\,\text{meV}$ and an effective mass of $m^* = -0.35\,m_e$ [23]. The p_x, p_y-derived state is mostly unoccupied and one of its branches intersects the s, p_z- derived band approximately at its band maximum. Panel (b) shows a DFT calculation of the $(\sqrt{3} \times \sqrt{3})$Bi/Ag(111)$R30°$ surface alloy, adapted from Ref. [24]. The calculations show a very good agreement with the experimental data (see text for more details).

Bi/Cu(111) [32]. Although the band structures of Bi/Ag(111), Pb/Ag(111) and Bi/Cu(111) differ qualitatively—hybridization Vs. non-hybridization—the unconventional spin texture for the p_x, p_y-derived bands has been predicted coincident for all three surfaces. This indicates that the unconventional spin polarization is a general feature in the p_x, p_y-derived bands.

5.4.3 Hexagonal warping

The existence of a distinct in-plane potential gradient, which is the origin of the very strong splittings, significantly modifies the band structure. This has been experimentally confirmed in ARPES measurements where snowflake-shaped CECs have been observed. A CEC of the Bi/Ag(111) surface at $(E - E_\text{F}) = -600\,\text{meV}$ is presented in Fig. 5.6(a) [100]. Comparison with the data presented in Fig. 5.5 leads to the identification of the branches l1/r1, l2/r2, l3/r3 and a Ag(111) bulk band u. The latter one is backfolded due to the $(\sqrt{3} \times \sqrt{3})$ surface reconstruction and the l4/r4 bands are not visible at $(E - E_\text{F}) = -600\,\text{meV}$ (see Fig. 5.5(a)). Focusing on the visible Rashba bands it is evident that the inner contour l1/r1 features a circular shape, whereas the l2/r2 and l3/r3 bands show snowflake-shaped contours, which is quite different from the simple Rashba model and the observed Au(111) surface state in Fig. 5.2(b). Whereas the l2/r2 branch features cusps pointing into $\overline{\Gamma\text{K}}$ directions, the cusps of the l3/r3 branches are rotated by 30° and point into $\overline{\Gamma\text{M}}$ directions. A schematic model of a CEC at $(E - E_\text{F}) = -900\,\text{meV}$ [27, 102] is presented in Fig. 5.6(b).

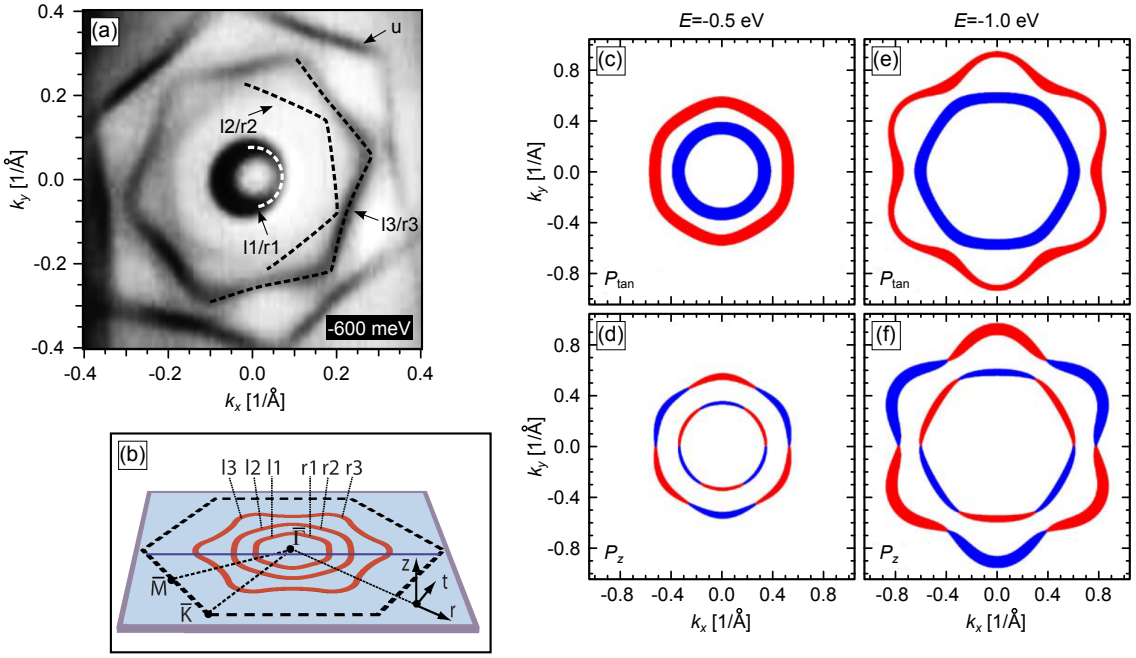

Figure 5.6: (a) ARPES CEC measurement on $(\sqrt{3}\times\sqrt{3})$Bi/Ag(111)$R30°$ at $(E-E_F) = -600\,\text{meV}$, adapted from Ref. [100]. The branches are labeled according to Ref. [27]. The inclusion of an in-plane potential gradient mediated by the crystal lattice leads to a hexagonal warping of the Rashba paraboloids. Due to the k^3 dependence the outer shells are distorted much stronger than the inner shells. Panel (b) illustrates a schematic CEC at $(E-E_F) = -0.9\,\text{eV}$, adapted from Ref. [27]. Panels (c-f) present DFT CECs for the s, p_z-derived band calculated with an effective mass of $m^* = 0.4\,m_e$ at $(E-E_F) = -0.5\,\text{eV}$ (c-d) and $(E-E_F) = -1.0\,\text{eV}$ (e-f) (the presented bands correspond to l1/r1 and l3/r3). The line thickness indicates the degree of spin polarization. Whereas the in-plane spin polarization P_{tan} remains unchanged in (c) and (e) compared to the simple Rashba model, the distinct in-plane potential gradient gives rise to a finite P_z polarization with a threefold symmetry, shown in (d) and (f). The out-of–plane polarization amounts to $0.00 \leq |P_z| \leq 0.41$ for (d) and $|P_z| \leq 0.88$ in (f). Panels (c-f) and the corresponding values are adapted from Ref. [101].

Since the energy is lowered by 300 meV compared to Fig. 5.6(a) a slight hexagonal warping is visible for the l1/r1 branches with cusps pointing into $\overline{\Gamma K}$ directions. The l2/r2 branches show the same orientation, but the l3/r3 branches point into $\overline{\Gamma M}$ directions which is in good agreement to ARPES CEC presented in Fig. 5.6(a).
The hexagonal warping can be explained by the in-plane potential gradient. It can be expressed as [103]

$$H_{3\nu} = \lambda |k|^3 \cos(3\varphi) \cdot \sigma_z, \tag{5.4.1}$$

within a $C_{3\nu}$ symmetry, which is valid for the surface alloys (and also for the pure fcc(111) substrates) [85, 103]. The Eigenvalues are solved by $\text{Det}(H_R + H_{3\nu} - E\mathbb{1}) \stackrel{!}{=} 0$ which leads

to a modified band dispersion

$$\widetilde{E}_{+/-} = \frac{\hbar^2 \vec{k}_{||}^2}{2m^*} \pm \sqrt{\alpha^2 |\vec{k}_{||}|^2 + \underbrace{\lambda^2 |\vec{k}_{||}|^6 \cos^2(3\varphi)}_{\text{warping term}}}. \tag{5.4.2}$$

Exemplary CECs with the modified band structure $\widetilde{E}_{+/-}$ are presented in Fig. 5.6(c-f) for the s, p_z-derived band of Bi/Ag(111). The authors of Ref. [101] didn't include the p_x, p_y-derived band, therefore the outer and inner contour of (c-f) correspond to the l1/r1 and l3/r3 branches of Fig. 5.6(a-b), respectively. The qualitative agreement between the calculated and experimentally CECs is clearly visible.

The k^3 dependency in Eq. (5.4.2) explains the fact that the warping occurs much stronger for larger k values. Although the warping term possesses a threefold symmetry in Eq. (5.4.1), the dispersion features a sixfold symmetry, which is forced by the time reversal symmetry. Remarkably, the same mechanism leads to characteristic snowflake shaped CECs far away from $\overline{\Gamma}$ for topological insulators, which are likewise spin-orbit–coupled materials and belong to the $C_{3\nu}$ space group [75, 76, 78, 79, 84, 85].

Up to that point any discussion of modifications of the spin texture has been avoided. As already mentioned in Ref. [23], an in-plane potential gradient induces a non-zero out-of–plane spin polarization P_z and decreases the in-plane polarization $P_{\text{tan}} < 1$ [23, 101]. The CECs in Fig. 5.6 show the tangential in-plane polarizations P_{tan} in (c) and (e) and the respective P_z polarizations in (d) and (f). The line widths in (c-f) indicate the degree of spin polarization and it is clearly visible that the P_z polarization exhibits a threefold symmetry $\propto \cos(3\varphi)$ [104] with alternating spin orientations for neighbouring lobes in (d) and (f). The in-plane polarization for the outer l3/r3 branch is still dominant at $(E - E_{\text{F}}) = -0.5\,\text{eV}$ (c) with $0.80 \leq |P_{\text{tan}}| \leq 0.97$ but the z-polarization already reaches values of $0.00 \leq |\text{P}_z| \leq 0.41$. The maximum and minimum values of $|P_z|$ and $|P_{\text{tan}}|$ are located at the cusps of the hexagons, which are the points where the warping term in Eq. (5.4.2) is maximal. Further increased k-values at $(E - E_{\text{F}}) = -1.0\,\text{eV}$ yield even larger z-polarization values $|\text{P}_z| \leq 0.88$ in (f) for the outer branch. Similar values for the l3/r3 branch of the Bi/Ag(111) surface have been reported in an experimental SARPES study with maximum values of $|\text{P}_z| = 0.84$ at $(E - E_{\text{F}}) = -0.4\,\text{eV}$ and $|\text{P}_z| = 0.93$ at $(E - E_{\text{F}}) = -0.9\,\text{eV}$ [27]. The maximum z-polarizations for the l2/r2 and l1/r1 branches are found to be much smaller with $|\text{P}_z| \leq 0.1$.

At this point the hexagonal warping can be reconsidered for the Rashba-type Au(111) surface state and the circular contours in Fig. 5.2(b) for Au(111) indicate a very small in-plane potential. Consequently, the hexagonal warping is very small and DFT calculations predicted a very small out-of–plane polarization $|\text{P}_z| = 1.4\%$ [104], which could not be detected experimentally [105, 106].

In summary, the in-plane potential gradient, which is the driving force for very strong Rashba splittings, causes an apparent hexagonal warping proportional to k^3 and at the

same time a threefold non-zero P_z polarization. Notably, all these aspects occur very similar also for topological insulators, which indicates the similarity of both material classes.

5.5 Detectability of Rashba-split surface states by means of STM/STS

The Rashba-split parabola gives rise to a characteristic asymmetric peak shape in STS spectra [25, 88] as a result of the momentum-split band structure. The DOS can be calculated starting with the same expression as in Sec. 4.2 for the Ag(111) surface state

$$\rho(E) = \sum_j \frac{1}{(2\pi)^2} \int_{BZ \bigcap S} \mathrm{d}^{d-1} S \frac{1}{|\vec{\nabla}_{\vec{k}} E(\vec{k})|_{E=E_j}}. \tag{5.5.1}$$

The integral must be solved separately for the energy range II ($E > E_0 + \Delta E_\mathrm{R}$) and I ($E_0 < E < E_0 + \Delta E_\mathrm{R}$), since in polar coordinates a constant energy cut intersects once the E_+ and E_- branches in energy range II but twice the E_- branch in I (compare to Fig. 5.7(a)). The intersections for energy range II are located at $k - k_0$ und $k + k_0$ for E_+ and E_-, respectively. All k values denote in-plane vectors, the subscript and vector symbols have been omitted for more clarity.
Using the dispersion from Eq. (5.2.7) for E_+ (at $k - k_0$) results in

$$|\vec{\nabla}_k E_+(k)|_{k-k_0} = \frac{\hbar^2 k}{m^*} \tag{5.5.2}$$

$$= \hbar\sqrt{\frac{2E}{m^*}}, \tag{5.5.3}$$

for energy range II with the unshifted parabola

$$E = \frac{\hbar^2 k^2}{2m^*}. \tag{5.5.4}$$

The energy gradient for $E_-(k)$ at $k + k_0$ yields accordingly

$$|\vec{\nabla}_k E_-(k)|_{k+k_0} = \frac{\hbar^2 k}{m^*} \tag{5.5.5}$$

$$= \hbar\sqrt{\frac{2E}{m^*}}. \tag{5.5.6}$$

The surface integral in Eq. (5.5.1) covers two rings with radii $k - k_0$ and $k + k_0$ for the E_+ and E_- branches, respectively. In this energy range the DOS is then determined to

$$\rho(E) = \frac{1}{(2\pi)^2\hbar}\sqrt{\frac{m^*}{2E}} 2\pi(k - k_0 + k + k_0) \tag{5.5.7}$$

$$= \frac{1}{\pi\hbar} k \sqrt{\frac{m^*}{2E}}. \tag{5.5.8}$$

Substituting $k = \sqrt{\frac{2m^*E}{\hbar^2}}$ yields

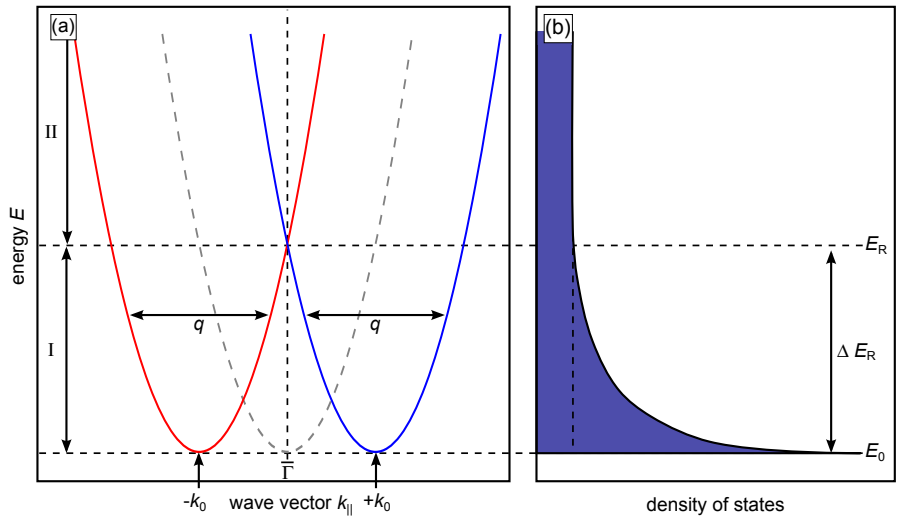

Figure 5.7: Panel (a) shows a 1D cut through the Rashba-split dispersion. The spin polarizations of both parabolas are rotated by 180° with respect to each other, indicated by the red and blue colour. Panel (b) shows the corresponding DOS. Above E_R it is constant but between E_R and E_0 it follows a $\frac{1}{\sqrt{E}}$ behaviour with a singularity at the band minimum E_0.

$$\rho(E) = \frac{m^*}{\pi\hbar^2} = \text{const.} \tag{5.5.9}$$

The DOS in energy range II is therefore identic to the DOS of an unshifted Kramers degenerate parabola (see Eq. (4.2.5)).
In energy range I the CEC exhibits two intersections located at $k + k_0$ and $-(k - k_0)$. The energy gradient remains unchanged with $\hbar\sqrt{\frac{2E}{m^*}}$, but the surface integral covers rings with radii $k + k_0$ and$-(k - k_0)$ (which belong both to the E_- branch). This modifies the DOS to

$$\rho(E) = \frac{1}{(2\pi)^2\hbar}\sqrt{\frac{m^*}{2E}}2\pi(k + k_0 - k + k_0) \tag{5.5.10}$$

$$= \frac{1}{\pi\hbar}k_0\sqrt{\frac{m^*}{2E}}. \tag{5.5.11}$$

With the substitution $k_0 = \sqrt{\frac{2m^*\Delta E_R}{\hbar^2}}$ follows

$$\rho(E) = \frac{m^*}{\pi\hbar^2}\sqrt{\frac{\Delta E_R}{E}} \tag{5.5.12}$$

for energy range I. Considering a non-zero band onset E_0 the DOS of an electron-like band can be described by

$$\rho(E) = \begin{cases} \frac{|m^*|}{\pi\hbar^2}\sqrt{\frac{\Delta E_\mathrm{R}}{E-E_0}} & , E_0 < E < E_0 + \Delta E_\mathrm{R} \\ \frac{|m^*|}{\pi\hbar^2} = \text{const.} & , E > E_0 + \Delta E_\mathrm{R} \\ 0 & , \text{else.} \end{cases} \tag{5.5.13}$$

The DOS follows a $\frac{1}{\sqrt{E}}$ behaviour between E_0 and E_R and then it remains constant as shown in Fig. 5.7(b). It results in strong asymmetric peak shapes in the DOS which show up as characteristical fingerprints in STS spectra of Rashba-split surfaces (see Ref. [25,35,107,108] and this work).

Notably, although Au(111) and Cu(111) have been proved to feature a Rashba-split surface state corresponding STS spectra do not provide peak shapes at all (see Ref. [62]). The absence of a peak-like signal can be assigned to the very small energy splitting of $\Delta E_{\mathrm{R,Au(111)}} = 2.1\,\mathrm{meV}$ and $\Delta E_{\mathrm{R,Cu(111)}} = 0.3\,\mathrm{meV}$. These values are much smaller than the lifetime broadenings of $\Gamma_{\mathrm{Au(111)}} = 18\,\mathrm{meV}$ and $\Gamma_{\mathrm{Cu(111)}} = 24\,\mathrm{meV}$ [62] on the respectively band onsets and therefore the Rashba-type fingerprint is concealed in STS measurements.

The issue of quasi-particle interferences within Rashba-split states has been discussed by Peterson and Hedegård [17] in order to resolve the question whether or not the momentum splitting can be observed by quasi-particle interferences. They used the spin Eigenstates as given in Eq. (5.2.9) combined with spherical waves and assumed a single Rashba-split state with wave vectors $k_1 = k + k_0$, $k_2 = k - k_0$ and the corresponding time-reversed partners $-k_1$ and $-k_2$

$$\begin{aligned}
\Psi_+(k_1) &= \tfrac{1}{\sqrt{r}}\,\mathrm{e}^{i\vec{k_1}\vec{r}}\left(i\,|\uparrow\rangle + \mathrm{e}^{i\theta}\,|\downarrow\rangle\right)\\
\Psi_-(k_2) &= \tfrac{1}{\sqrt{r}}\,\mathrm{e}^{i\vec{k_2}\vec{r}}\left(i\,|\uparrow\rangle - \mathrm{e}^{i\theta}\,|\downarrow\rangle\right)\\
\Psi_+(-k_1) &= \tfrac{1}{\sqrt{r}}\,\mathrm{e}^{i-\vec{k}_1\vec{r}}\left(i\,|\uparrow\rangle - \mathrm{e}^{i\theta}\,|\downarrow\rangle\right)\\
\Psi_-(-k_2) &= \tfrac{1}{\sqrt{r}}\,\mathrm{e}^{i-\vec{k}_2\vec{r}}\left(i\,|\uparrow\rangle + \mathrm{e}^{i\theta}\,|\downarrow\rangle\right).
\end{aligned} \tag{5.5.14}$$

The time reversal operator induces a transition from $k \to -k$ and flips the spin character of $\Psi_+(-k_1)$ and $\Psi_-(-k_2)$ as compared to their time-reversed partners $\Psi_+(k_1)$ and $\Psi_-(k_2)$ [109].

The complete wave function Φ is a linear combination of the individual wave functions

$$\Phi = A\Psi_+(k_1) + B\Psi_-(k_2) + C\Psi_+(-k_1) + D\Psi_-(-k_2). \tag{5.5.15}$$

According to Sec. 4.2 $|\Phi|^2 = \Phi\Phi^*$ has to be evaluated for the interference pattern leading to

$$|\Phi|^2 = \text{const.} + \frac{2}{r}\left[(A^*D + B^*C)\,\mathrm{e}^{-i(k_1+k_2)r} + \text{c.c.}\right]. \tag{5.5.16}$$

This directly leads to the conclusion, that the momentum splitting k_0 of Rashba-split parabolas can not be observed in quasi-particle interferences since $k_1 = k+k_0$ and $k_2 = k-k_0$ and consequently

$$q = k_1 + k_2 = 2k. \tag{5.5.17}$$

The scattering vector $q = 2k$ denotes intra-band scattering processes for both parabolas as indicated by black arrows in Fig. 5.7(a). Both vectors are equal and consequently only one wavelength is observed in quasi-particle interferences [29]. In this case the dispersion characteristics can be mapped by simple backscattering $q = 2k$ but the momentum shift k_0 is inacessible for quasi-particle interference experiments.

However, this model is simplified and just accounts for one single Rashba-split state with a

conventional spin polarization. More complicated band structures can yield to different results, e.g. a very recent experimental STM study performed on $(\sqrt{3}\times\sqrt{3})$ Bi/Cu(111)$R30°$ was able to determine the momentum splitting of the s, p_z-derived bands [35]. This was possible due to coexisting intra-band and inter-band scattering events between the s, p_z- and p_x, p_y-derived Rashba states.

In summary, scanning tunneling modes are able to shed light on the electronic properties of Rashba-split surface states. Whereas STS spectra are able to determine band onsets E_0 and energy splittings ΔE_R, quasi-particle interferences can trace the dispersion characteristics in the case of simple backscattering $q = 2k$.

6 Quantum Well States Theory

An infinite crystal exhibits continuous band structures, but a reduction to finite thicknesses, e.g. by deposition of thin films on a bulk crystal, leads to a different situation. Perpendicular to the surface, the thickness of the film is finite and consequently discrete energy levels arise along $k_\perp$, whereas parallel to the film the band structures are still continuous.
The valence electrons in the film can be consequently treated as waves trapped in a 1D quantum well between the bulk crystal and the surface barrier. They can be described with an adapted phase accumulation model that has been developed by Echenique and Pendry for image potential states [110].
A potential barrier reflects an incoming wave function and the strength of reflection is determined by the reflectivity r. Additionally the reflected wave function picks up a phase shift $\mathrm{e}^{i\Phi}$. Within the film the electrons can be reflected on the surface barrier to the vacuum with $r_\mathrm{B}\,\mathrm{e}^{i\Phi_\mathrm{B}}$ (barrier-induced) and on the barrier between film and substrate with $r_\mathrm{C}\,\mathrm{e}^{i\Phi_\mathrm{C}}$ (crystal-induced), which is shown schematically in Fig. 6.1. Since it bounces back and forth between both barriers the amplitude A of the wave function can be described as geometric sum

$$A = \sum_{n=0}^{\infty} r_\mathrm{B} r_\mathrm{C}\,\mathrm{e}^{i(\Phi_\mathrm{B}+\Phi_\mathrm{C})} = \frac{1}{1 - r_\mathrm{B} r_\mathrm{C}\,\mathrm{e}^{i(\Phi_\mathrm{B}+\Phi_\mathrm{C})}}. \tag{6.0.1}$$

A bound state is characterized by a singularity in Eq. (6.0.1). Correspondingly there are two conditions for a bound state:

$$r_\mathrm{B} r_\mathrm{C} = 1 \tag{6.0.2}$$

$$\Phi_\mathrm{B} + \Phi_\mathrm{C} = 2\pi n, \quad n \in \mathbb{N}_0 \tag{6.0.3}$$

In order to satisfy Eq. (6.0.1), both reflectivities have to be unity, $r_\mathrm{B} = r_\mathrm{C} = 1$ and both phase shifts have to be integer multiples of 2π. So far these conditions describe a surface [110] or consequently a film with vanishing film thickness. To include a finite film thicknesses $d = Na$ with single layer height a and number of layers $N \in \mathbb{N}$ the perpendicular propagation of the wave function through the film has to be considered. This changes the phase condition to

$$\Phi_\mathrm{B} + \Phi_\mathrm{C} + 2k_\perp(E) \cdot d = 2\pi n, \quad n \in \mathbb{N}_0. \tag{6.0.4}$$

Within the WKB approximation and the assumption of an image potential on the surface the barrier-induced phase shift can be expressed as [111, 112]

$$\Phi_\mathrm{B}(E) = \pi \sqrt{\frac{3.4\,\mathrm{eV}}{E_\mathrm{vac} - E}} - \pi \tag{6.0.5}$$

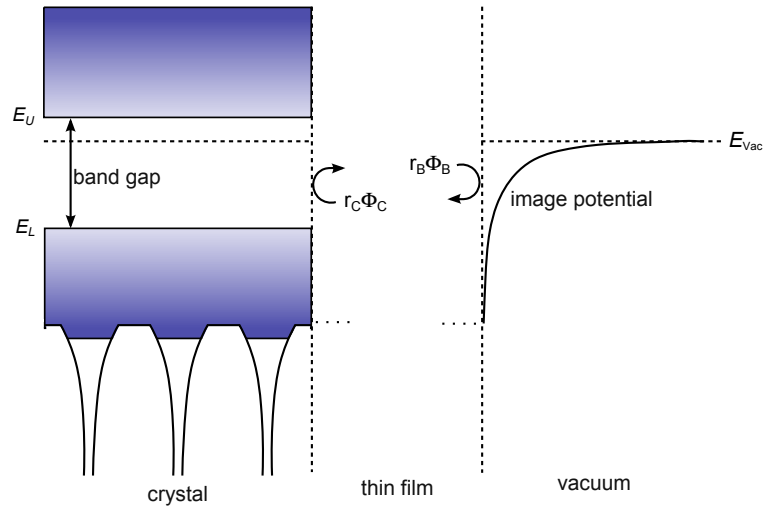

Figure 6.1: Quantum well states in a thin film deposited on a crystal. For energies between E_{vac} and inside the bulk band gap of the substrate, the wave function is trapped inside the film. It is reflected on the crystal-induced barrier with reflectivity r_{C} and the surface-induced barrier with r_{B}. Bouncing back and forth it picks up a phase shift $\mathrm{e}^{i\Phi_{\mathrm{C,B}}}$ with each reflection.

and for the crystal-induced phase shift the empirical term

$$\Phi_{\mathrm{C}}(E) = 2\arcsin\sqrt{\frac{E-E_L}{E_U-E_L}} - \pi \tag{6.0.6}$$

is used. Here $E_{L,U}$ denote the lower and upper values of the substrate's energy gap. Both phase shift functions are shown in Fig. 6.2(a) as functions of energy.

The thickness-dependent phase shift can be derived from the tight binding model for a linear chain [112]

$$2k_\perp(E)Na = 2\arccos\left(1-\frac{2E}{E'_U-E'_L}\right)N \tag{6.0.7}$$

with the upper and lower band edges $E'_{U,L}$ of the thin film. With the given expressions for the phase shifts solutions of Eq. (6.0.4) can be solved only with numerical methods or by graphical analysis. The latter one is shown in Fig. 6.2(b) as separate plots of $2\pi n - \Phi_{\mathrm{B}} - \Phi_{\mathrm{C}}$ with a variation of $0 \le n \le 5$ and $2k_\perp(E)Na$ with $1 \le N \le 10$. Each intersection between both sets of curves represents a solution of the phase condition in Eq. (6.0.4). With increasing layer thickness N, the number of quantum well states (QWSs) increases. Simultaneously, the energetic distance between QWSs decreases and in the limit of $N \to \infty$ the continuous band structure $E(k_\perp)$ is restored.

Thin films and their QWS characteristics can be used to extract the perpendicular energy dispersion $E(k_\perp)$ of the corresponding bulk crystal [113–115]. The analysis of thin film QWSs allows to determine the $E(k_\perp)$ band structures and, vice versa, the existence of QWSs allows to determine film thicknesses with high accuracy [114] (see Sec. 7.1.1 and 7.2) if $E(k_\perp)$ and all relevant phase shifts are known.

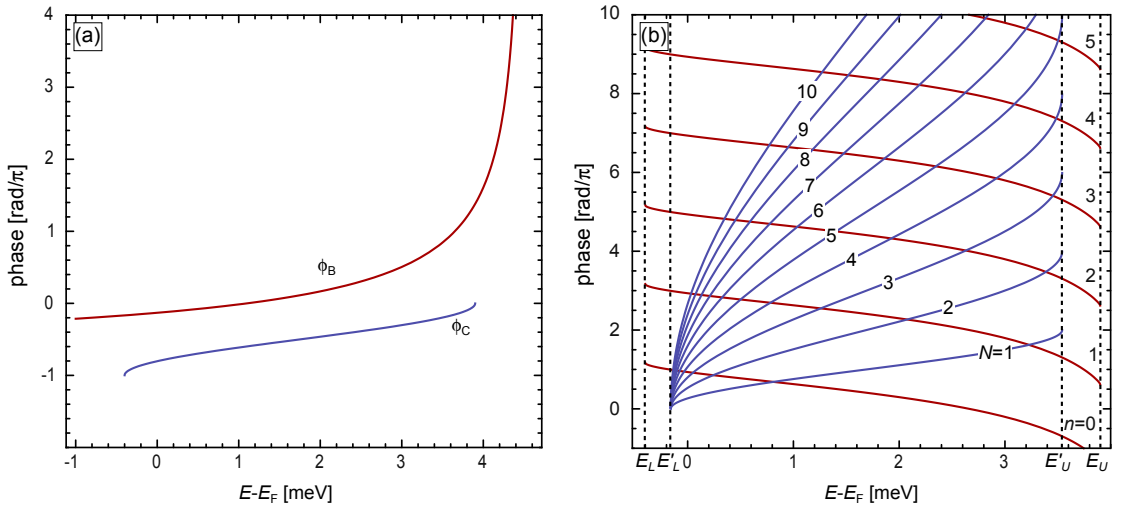

Figure 6.2: (a) The crystal- (blue line) and barrier-induced (red line) phase shifts. Φ_C has only solutions within the substrate bandgap between E_U and E_L. Panel (b) shows the graphical solutions of Eq. (6.0.4). The red curves are $2\pi n - \Phi_B - \Phi_C$ and the blue curves denote the thickness dependent phase shift for layer thicknesses between one and ten layers. Each intersection of both sets of curves depicts a solution of the phase condition in a thin film. With increasing film thickness, the number of solutions increases and consequently the energetic distance between adjacent QWSs decreases.

The quantum well character of thin films can strongly influence their properties, such as the growth mode [116–119], conductivity [120], superconductivity [121–123], electron-phonon-coupling [124], work functions [125], and Kondo physics [126]. A quantum well character of thin films is observed if the wavelength of the electron has approximately the same dimension as the film thickness [127]. In this frame a very peculiar quantum well system is formed by thin Pb layers deposited on various substrates, e.g. Pb/Si(111) [120, 128–133], Pb/Cu(111) [134, 135], Pb/Ag(111) [114, 136]. It has been experimentally shown, that the quantum well resonances in Pb(111) layers persist up to thicknesses of 37 ML on Ag(111) [114, 136]. A reason for this very unusual behaviour has been discussed in literature [137] by Jia *et al.* They found that the Friedel oscillations (FO) decay with $\frac{1}{z}$ for Pb(111) films, which is in contrast to the usual $\frac{1}{z^2}$ decay for other metal films. They addressed the much slower $\frac{1}{z}$ decay to Fermi nesting of two sheets of the Fermi surface along the [111] direction, which enhances the quantum well resonances significantly compared to other metal films.

In STS experiments the QWSs of thin Pb films on different substrates show very sharp and strong peak-like signals [128, 134, 136], thereby allowing their easy detection. In ARPES measurements and DFT calculations the QWSs have been found to additionally feature a band dispersion along $k_{||}$ [120, 129–131] as illustrated exemplary for 24 ML Pb/Si(111) in Fig. 6.3(a). All visible bands show an m-shaped dispersion with the 2π phase condition of Eq. (6.0.4) fulfilled at each band minimum at $k_{||} = 0$. An exemplary m-shaped dispersion is sketched in Fig. 6.3(b) exhibiting a free electron-like parabola close to $\overline{\Gamma}$. The value

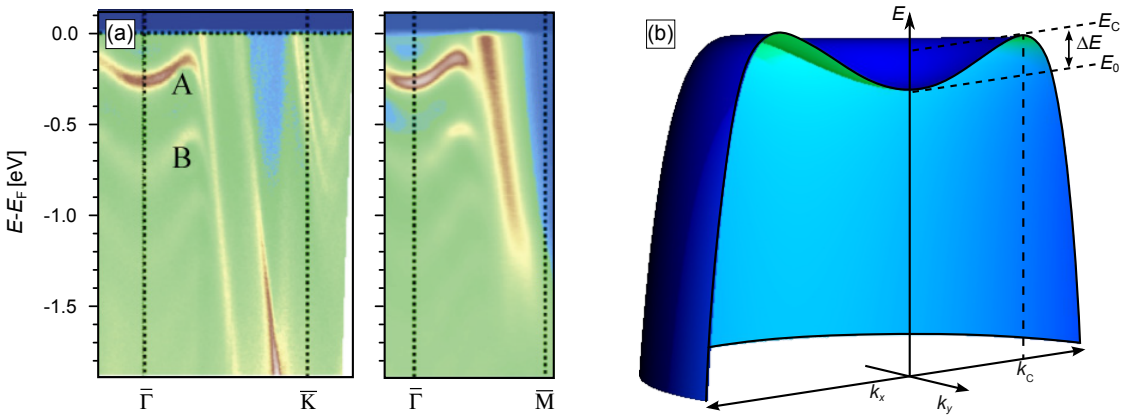

Figure 6.3: (a) An ARPES measurement of a 24 ML thick Pb film deposited on Si(111) along $\overline{\Gamma K}$ (left panel) and $\overline{\Gamma M}$ (right panel), adapted from Ref. [131]. Each observed band fulfils one QWS solution at $\overline{\Gamma}$. The energy dispersions of all states $E(k_{||})$ feature m-shaped contours in both directions, whereas the m-shape flattens out for higher numbered QWS solutions. Panel (b) shows a schematic of the band dispersion. Starting at the band onset E_0 at $\overline{\Gamma}$ the dispersion follows an electron-like parabolic character, for higher k-values the slope lowers until the band bends down at k_c. The energy distance between the band maximum E_c and E_0 is labeled with ΔE.

ΔE is defined by the energy distance between the band minimum E_0 at $\overline{\Gamma}$ and the band maximum E_c at k_c. As can be seen in Fig. 6.3(a) ΔE becomes smaller for higher QWSs. Thereby, the band dispersion around $\overline{\Gamma}$ gets more flat, until it is more reminiscent of a plateau than an m-shape [120, 129–132].
The authors in Ref. [129, 131] discuss that the observed QWS bands originate from the Pb bulk band structure. The authors of Ref. [131] further specify the m-shaped feature to the p_z bulk band, which is transferred to the QWSs. This indicates, that the m-shape dispersion is related to the Pb film itself and should appear likewise for other substrates. The high compliance in STS measurements of Pb films deposited on Si(111) [128], Ag(111) [136], and Cu(111) [134] indeed points into the same direction.

7 Results

In this chapter the results of this work are presented, interpreted and discussed.

Section 7.1 starts with a description of the growth characteristics of Pb and Bi deposited on Ag(111). The Pb/Ag(111) growth is presented in Sec.7.1.1 from the submonolayer regime up to thicknesses of $\approx 100\,\mathrm{ML}$. For a Pb deposition of $\leq 1/3\,\mathrm{ML}_{\mathrm{Ag(111)}}$ the adsorbed Pb forms a $(\sqrt{3}\times\sqrt{3})\mathrm{Pb/Ag}R30°$ surface alloy [138, 139]. Exceeding the $1/3\,\mathrm{ML}_{\mathrm{Ag(111)}}$ coverage leads to a dealloying process on the surface and patches of a pure Pb(111) wetting layer arise, which feature a characteristical moiré pattern [139, 140]. At even higher coverages the complete surface dealloys and a smooth Pb(111) film grows on top of the Ag(111) substrate [140]. They feature a strong contrast between odd and even layer thicknesses and domains of coexisting rotational equivalent Pb(111) films. The wetting layer moiré pattern is detected on a layer thicknesses of 74 ML.
Section 7.1.2 describes the growth of Bi on Ag(111) in analogy to the Pb growth in Sec.7.1.2 beginning at submonolayer coverages and rising the coverage up to thicknesses of $\approx 30\,\mathrm{ML}$ Bi. Isostructural to the Pb/Ag(111) case a $(\sqrt{3}\times\sqrt{3})\mathrm{Bi/Ag}R30°$ surface alloy forms for coverages of $\leq \frac{1}{3}\,\mathrm{ML}_{\mathrm{Ag(111)}}$ [25, 141, 142]. For coverages of $\geq 1/3\,\mathrm{ML}_{\mathrm{Ag(111)}}$ the surface dealloys and a rectangular striped phase of pure Bi atoms develops [141, 142], reminiscent of the Bi(110) surface, but slightly larger. Exceeding the coverage of $\geq 1\mathrm{Bi(110)}\,\mathrm{ML}$ leads to a phase transition from the striped phase to a pure Bi(110) film on the surface [142, 143]. The observed pure Bi(110) film provides high ribbon-like islands with edge lengths up to $1\,\mu\mathrm{m}$ and step edge heights corresponding to Bi bilayers. Concluding from STM and LEED measurements the Bi(110) domains appear in six different domains.

Section 7.2 illustrates QWS of thick Pb films on Ag(111), which are the origin of the observed odd-even effect in Sec.7.1.1. In this work it is verified, that the quantum character of the Pb film survives very intensely up to layer thicknesses of $\approx 100\,\mathrm{ML}$. The observed spectroscopic features show an evolution from plateau-like to peak-like shapes for each layer thickness. This characteristic is explained by a model based on m-shaped dispersions. The free electron character of the m-shaped dispersion has been subsequently observed by means of quasi-particle interferences for exemplary layer thicknesses of $N = 32, 34\,\mathrm{ML}$.

Sections 7.3 and 7.4 describe the Rashba-type spin-split surface states of $(\sqrt{3}\times\sqrt{3})\mathrm{Pb/Ag}R30°$ and $(\sqrt{3}\times\sqrt{3})\mathrm{Bi/Ag}R30°$ surface alloy.
Sec. 7.3 starts with a clarification of the $(\sqrt{3}\times\sqrt{3})\mathrm{Pb/Ag}R30°$ band structure by means

of STS indicating two hole-like Rashba-split bands in the unoccupied energy range, since the band structure is highly unoccupied and so far unclear (see Fig.5.4). Subsequently the band dispersions are investigated by means of quantum interference maps in the energy range of both bands. The unambiguous assignment of scattering vectors is achieved by comparison to ARPES measurements. While intra-band scattering is found for both Rashba bands, inter-band scattering is only observed in the occupied energy range. Considering the explanation of the observed scattering channels two different interpretations are given. The spin-conserving interpretation leads to the indication of conventional Rashba states in contradiction to DFT calculations for this class of materials [24, 32]. Spin- and orbitally-resolved band structures were then obtained by DFT calculations. Considering the spin-orbit coupling in the scattering between states of different spin and orbital character, can resolve the apparent deviation between experimentally observed scattering events and the theoretically predicted spin polarization. This section ends with a comparison of step edge scattering compared to defect scattering, that legitimates the use of step edges in scattering events for this sample system.
Sec. 7.4 starts similarly with the determination of band onsets and splitting strengths of the $(\sqrt{3} \times \sqrt{3})$Bi/Ag(111)$R30°$ surface alloy indicating two hole-like Rashba-split states in good agreement to the theoretically predicted band structure [24]. The deviation of the STS spectra is assigned to a hybridization gap opening at the band onset of the occupied Rashba state, which is in good agreement to DFT calculations. A series of quasi-particle interference maps reveals scattering within the whole energy range of those bands. The analysis of the observed scattering channels reveals intra-band scattering for the p_x, p_y-derived state as well as inter-band scattering between the sp_z- and p_x, p_y-derived states in the occupied energy range. The assignment of scattering vectors is achieved by comparison to ARPES measurements. In the framework of spin-conserving scattering the inter-band scattering in the occupied energy range is in agreement with the predicted hybridization gap opening. In the unoccupied energy range it leads to the indication of a conventional Rashba state in contradiction to DFT calculations [24, 32]. Again spin and orbitally-resolved band structures were obtained by DFT calculations that can explain all observed scattering events in occupied as well as unoccupied states and thus closes the gap between theory and experiment.

7.1 Growth of Lead and Bismuth on Ag(111)

7.1.1 Growth characteristics of Pb/Ag(111)

Thin Films

It has been reported, that the deposition of Pb on Ag(111) for coverages $\leq 1/3\,\mathrm{ML}_{\mathrm{Ag(111)}}$ leads to the formation of a $(\sqrt{3}\times\sqrt{3})\mathrm{Pb/Ag(111)}R30°$ reconstruction [144, 145]. This structure has been later identified as a surface alloy, where every third Ag surface atom is replaced by Pb [138, 139].
The Ag(111) substrate was held at elevated temperature $T = 250°\mathrm{C}$ during growth for all images in this section. Unless otherwise indicated the given directions refer to the $(\sqrt{3}\times\sqrt{3})\mathrm{Pb/Ag(111)}R30°$ reconstruction on the surface (see Fig. 5.3(b) for the corresponding substrate and momentum space directions).
Figure 7.1 shows three different submonolayer coverages of Pb deposited on Ag(111) beginning at very low coverages of 0.2 ML in Fig. 7.1(a). The Pb atoms (partially indicated with red atoms) arrange in small close-packed triangular or less dense rectangular clusters

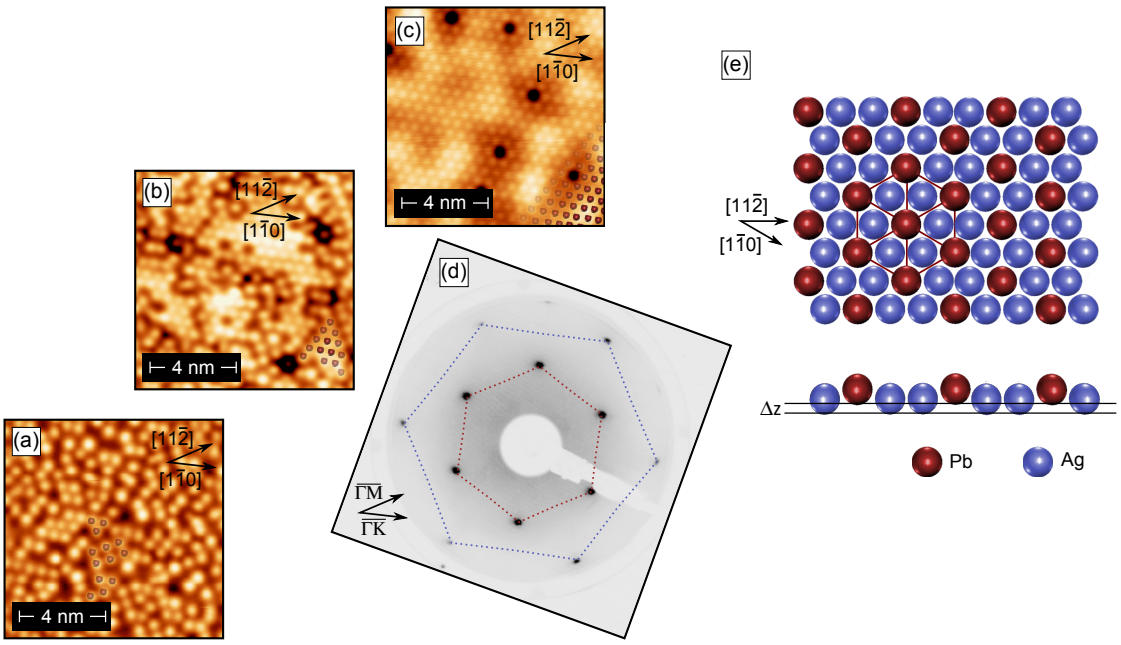

Figure 7.1: Panel (a)-(c) show the evolution of the $(\sqrt{3}\times\sqrt{3})$ $\mathrm{Pb/Ag(111)}R30°$ surface alloy. Initially at a coverage of 0.2 ML the deposited Pb atoms arrange arbitrary on the surface (a). The increased coverage of 0.25 ML (b) shows already small patches of the $(\sqrt{3}\times\sqrt{3})$ reconstruction. Eventually at a coverage of 1/3 ML the $(\sqrt{3}\times\sqrt{3})\mathrm{Pb/Ag(111)}R30°$ structure has fully evolved. The corresponding LEED pattern is shown in (d) at an energy of $E = 60\,\mathrm{eV}$. The blue hexagon represents the Ag unit cell, the inner red hexagon, originates from the $(\sqrt{3}\times\sqrt{3})R30°$ reconstruction. The structural model of the $(\sqrt{3}\times\sqrt{3})\mathrm{Pb/Ag(111)}R30°$ surface alloy is shown in (e) as top and side view with the relaxation Δ_z of the Pb atoms.

(indicated by the red atoms), a well-defined structure is not visible. At increased coverage of $0.25\,\mathrm{ML}_{\mathrm{Ag(111)}}$ in Fig. 7.1(b) small patches of the $(\sqrt{3}\times\sqrt{3})R30°$ surface alloy are already visible. The largest patch in this scan covers an area of about $16\,\mathrm{nm}^2$, but the surface still lacks a long range order. The $(\sqrt{3}\times\sqrt{3})R30°$ reconstruction has fully evolved for $1/3\,\mathrm{ML}_{\mathrm{Ag(111)}}$. The lattice constant is determined to $a = (5.0\pm0.1)\,\text{Å} = \sqrt{3}a_{\mathrm{Ag(111)}}$. In this scan frame the surface already exhibits seven defects, that show up as circular depressions. Interestingly they can not be suppressed by further Pb deposition and the most probable origin are Ag atoms, that have not been replaced by Pb atoms. The defect density amounts to $\approx 70/1000\mathrm{nm}^2$ (for comparison see Fig. 7.24(a)). Compared to the growth of Bi on Ag(111) (see Fig. 7.7(a)) the defect density of $(\sqrt{3}\times\sqrt{3})\mathrm{Pb/Ag}R30°$ is considerably higher (for comparison see also Ref. [139]). Notably, only Pb atoms are visible in the atomically resolved images in Fig. 7.1(a-c), the Ag atoms are entirely hidden [138].
The corresponding LEED pattern of Fig. 7.1(c) is presented in Fig. 7.1(d). It consists of an outer hexagon (red) that belongs to the underlying Ag(111) substrate and an inner hexagon (blue) which reflects the $(\sqrt{3}\times\sqrt{3})R30°$ symmetry of the surface alloy. The lattice constant determined by LEED amounts to $a = (5.0\pm0.1)\,\text{Å}$ which is in compliance with the STM value.
A top and side view model of the surface is shown in Fig. 7.1(e). In the top view every

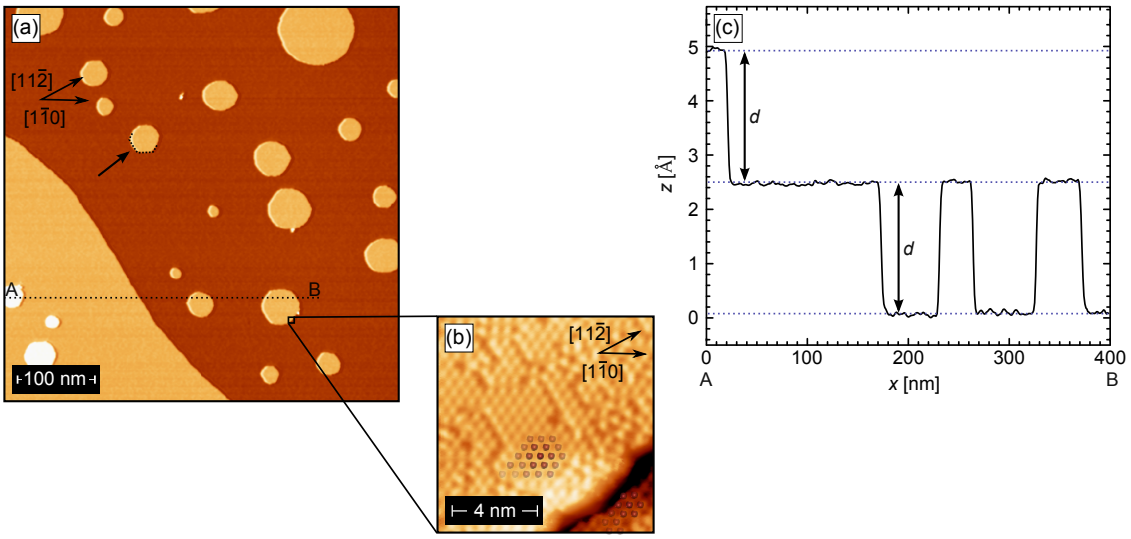

Figure 7.2: A $500\times500\,\mathrm{nm}^2$ surface area with a deposition of slightly less than 1/3 ML with 0.29 ML and a substrate temperature of $T = 250°\mathrm{C}$ during the growth. The surface shows islands that originate from the alloying process. The replaced Ag atoms which excess the surface form the islands on top of the terraces. The islands are approximately circular shaped, but some of them exhibit edges along the $[1\bar{1}0]$ directions (indicated by the dotted hexagonal frame and arrow). (b) $10\times10\,\mathrm{nm}^2$ atomically resolved scan on an island edge. Terraces as well as islands surfaces are found to exhibit the $(\sqrt{3}\times\sqrt{3})$ $\mathrm{Pb/Ag(111)}R30°$ surface alloy. (c) A line profile crossing a step edge and some islands proves that the islands originate from monoatomic Ag islands.

third Ag atom (blue) within the surface layer has been replaced by Pb (red). The resulting hexagonal unit cell is by a factor of $\sqrt{3}$ larger and rotated by $\nu = 30°$ with respect to the Ag(111) unit cell. The surface is buckled due to a relaxation Δ_z of Pb atoms perpendicular to the surface plane (side view). The relaxation has been experimentally observed by means of STM to $\Delta_z = 0.8\,\text{Å}$ [138], but a smaller value $\Delta_z = 0.46\,\text{Å}$ has been found in an $I(V)$-LEED study [28].

The smaller value determined with $I(V)$-LEED is more plausible due to the fact that the determination of atomic corrugation with STM, especially for an atomically inhomogeneous surface, is practically impossible without theory. As first aspect atomic corrugations in STM measurements are strongly influenced by the orbital character of tip and sample (see Fig. 2.2 in Sec. 2.1.2 and Ref. [58]). As second aspect, also the DOS is inhomogeneous in the $(\sqrt{3} \times \sqrt{3})\text{Pb/Ag(111)}R30°$ surface as all Pb atoms are surrounded by Ag atoms. Hence a value for Δ_z is not given in this work.

The intensity modulations around the defects in Fig. 7.1(c) originate from standing wave patterns of the 2D Rashba-split surface states on the $(\sqrt{3} \times \sqrt{3})\text{Pb/Ag(111)}R30°$ surface and will be discussed in section 7.3.

By comparison of $500 \times 500\,\text{nm}^2$ large sample areas with different local miscuts it is clearly visible that the surface morphology depends on the terrace widths. Figure 7.2(a) shows a surface area with a Pb deposition of $0.29\,\text{ML}_{\text{Ag(111)}}$. Only one step edge and a terrace of several hundred nm in width are visible in this scan frame. Both terraces feature randomly distributed islands, at which the smallest observed island is only 10 nm in diameter and the largest island holds a diameter of 90 nm. They are approximately circular shaped, but some island edges are oriented along $[1\bar{1}0]$ directions (indicated with the dashed line and arrow). As can be seen in Fig. 7.2(b) the $(\sqrt{3} \times \sqrt{3})\text{Pb/Ag(111)}R30°$ exists on the terrace as well as on the island. This indicates, that the islands descend from monoatomic Ag islands. Indeed the step height of the islands in Fig. 7.2(a) show exactly the same height of $d = (2.4 \pm 0.1)\,\text{Å}$ in the line profile Fig. 7.2(c), that corresponds very well to the Ag(111) step edge height of $d_{\text{Lit.}} = 2.36\,\text{Å}$. The interpretation of the line profile as pure topographic information is only possible since the entire surface is covered with the same surface reconstruction.

The formation of the monoatomic Ag(111) islands, which are again alloyed with Pb, can be understood by the following explanation: As a result of the alloying process Ag atoms, which have been replaced by Pb, diffuse on the surface. On large terraces they form small clusters rather than merging to a step edge. Every extra incoming Ag atom further increases the island sizes and during their formation the Ag islands are also alloyed with Pb atoms.

For smaller terraces the situation is different as shown in Fig. 7.3(a) with $500 \times 500\,\text{nm}^2$ size. The widest terrace is visible on the right-hand side of the scan frame with a width $w \geq 150\,\text{nm}$, the others exhibit widths $w \leq 100\,\text{nm}$. Only two islands are visible on this surface indicated by the black arrows. In the case of smaller terraces the diffusing Ag atoms have the possibility to reach Ag step edges, which leads to a uniform and smooth

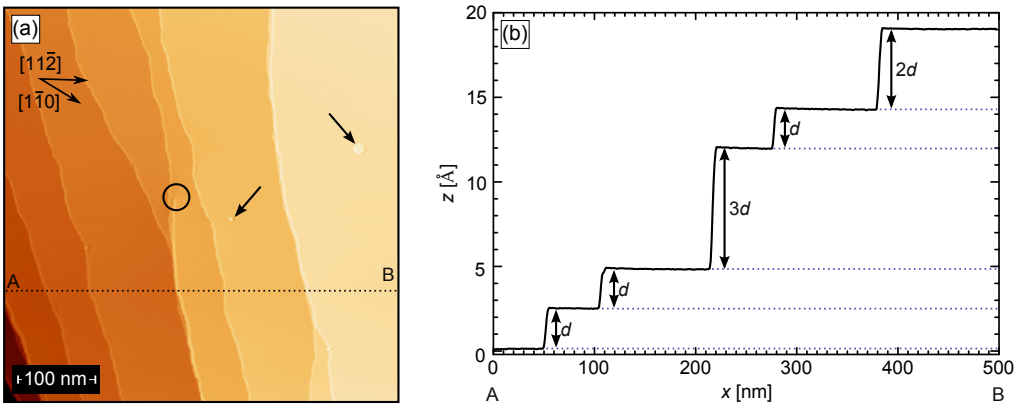

Figure 7.3: (a) A $500 \times 500\,\mathrm{nm}^2$ surface area. Due to the more densely stepped surface with terrace widths of $w \leq 100\,\mathrm{nm}$, the extracted Ag atoms were able to merge to step edges during the growth. Only two very small islands can be seen on the surface (indicted by the arrows). The dotted line in (a) indicates the line profile in (b). The $(\sqrt{3} \times \sqrt{3})$ Pb/Ag(111)$R30°$ surface exhibits frequently multiple steps as can be seen in the line profile.

surface. An interlayer material transport of the Ag atoms is indicated by the appearance of step edges with multiple Ag(111) step edge heights[1]. They occur rather often on the $(\sqrt{3} \times \sqrt{3})$Pb/Ag(111)$R30°$ surface and can be also seen in the line profile in Fig. 7.3(b), with the single Ag(111) step height determined to $d = (2.37 \pm 0.05)\,\text{Å}$. Besides three monoatomic steps it shows two step edges with respectively twice or triple step edge heights. However, the $3d$ high step edge is caused by a screw dislocation, which stems from the substrate (marked with circle in Fig. 7.3(a)). Without the substrate induced screw dislocation it would probably be only a double step. The appearance of double height step edges can be understood under the assumption that the Ag atoms may drop down step edges (i.e. interlayer mass transport) during their random diffusion movement. Consequently, a larger terrace statistically drops more Ag atoms than a smaller one. If a larger (and one monoatomic higher) terrace is situated next to a smaller terrace, the interlayer mass transport simultaneously decreases and increases the size of the smaller and larger terrace, respectively. Finally, the smaller terrace vanishes completely and instead of two monoatomic terraces one terrace with a double step edge height evolved. Similar effects have been reported for Ag islands deposited on Ag(111) where large islands grew larger and smaller islands disappeared due to Oswald ripening on the surface [146].

Increasing the coverage $\geq 1/3\,\mathrm{ML}_{\mathrm{Ag(111)}}$ leads to a dealloying process in the surface layer [114, 139]. Figure 7.4(a) shows the sample surface of Pb/Ag(111) at a Pb coverage of $0.46\,\mathrm{ML}_{\mathrm{Ag(111)}}$. Coexisting domains of the $(\sqrt{3} \times \sqrt{3})$ Pb/Ag(111)$R30°$ surface alloy (A) and a close packed hexagonal structure (B) are visible. The atomically resolved scan of structure B in Fig. 7.4(b) shows a hexagonal arrangement of atoms with a lattice constant

[1]The Ag(111) crystal barely showed multiple step edge heights which where mostly induced by screw dislocations.

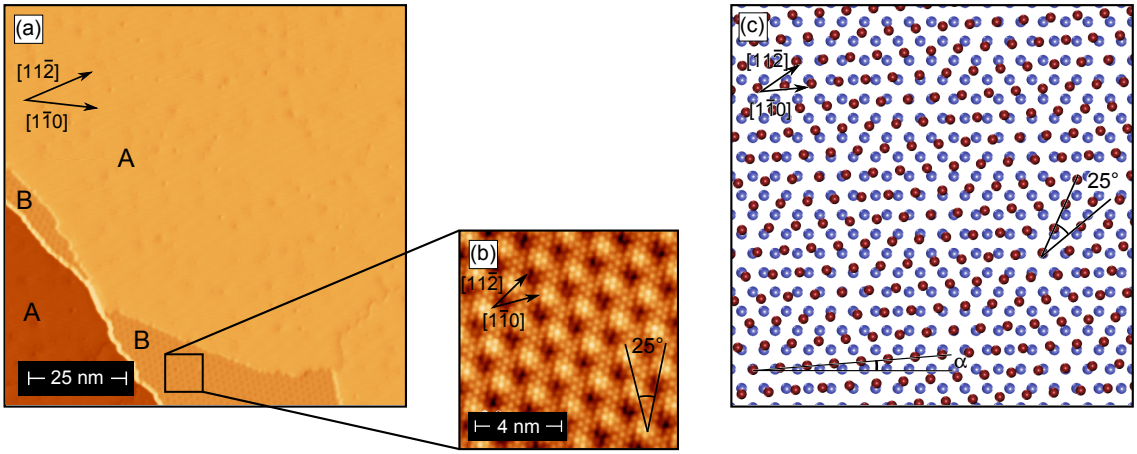

Figure 7.4: (a) Overcoming 1/3 ML leads to a dealloying process of the Pb atoms and pure patches of the Pb(111) wetting layer with a superimposed moiré modulation arises on the surface. $(\sqrt{3}\times\sqrt{3})$Pb/Ag(111)$R30°$ (A) and Pb(111) (B) surfaces coexist in neighbouring domains, whereas the wetting layer prefers the step edges. An atomically resolved scan (b) shows the Pb(111) surface with its additional moiré pattern. The indicated directions refer here to the Pb(111) wetting layer. The $[1\bar{1}0]$ directions of the Pb(111) and moiré are rotated by $\beta = (25 \pm 1)°$, a corresponding structural model of the moiré is shown in (c). The angle $\alpha = 4.6°$ depicts the rotation between Pb(111) overlayer and Ag(111) substrate.

of $a = (3.5 \pm 0.1)$ Å and is therefore identified as pure Pb(111) wetting layer [139, 140, 145] (the lattice directions in this image refer to the Pb(111) wetting layer). The formation of pure Pb(111) has also been reported for Cu(111) [147], and Au(111) [148]. The Pb(111) patches are preferentially found at step edges and show a characteristic moiré pattern that forms as consequence of the lattice mismatch between Ag(111) and Pb(111). The appearance on step edges indicates, that the dealloying process starts at step edges in agreement to previous studies [139] and similar to the dealloying process of Bi/Ag(111) discussed in Sec. 7.1.2. The moiré pattern has a periodicity of $\lambda = (1.6 \pm 0.1)$ nm and the $[1\bar{1}0]$ directions of the Pb(111) wetting layer and the moiré pattern are rotated by $\beta = (25 \pm 0.2)°$ with respect to each other. This allows to conclude on the rotation angle α between the Pb(111) wetting layer and the Ag(111) substrate [149, 150]. Using the relation [150]

$$\tan\beta = -\frac{|g_{\mathrm{Ag(111)}}|\sin\alpha}{|g_{\mathrm{Pb(111)}}| - |g_{\mathrm{Ag(111)}}|\cos\alpha} \tag{7.1.1}$$

leads to an rotation angle of $\alpha = (4.6 \pm 0.2)°$, which is in good agreement with previous studies [114, 139]. Although the origin of a moiré periodicity in STM measurements is a mixture of electronic and structural modulation a geometric superposition of a Ag(111) and Pb(111) layer is capable to model the observed moiré pattern as shown in Fig. 7.4(c). The Pb(111) layer has been rotated by $\alpha = 4.6°$ with respect to the Ag(111) layer in the schematic and the resulting moiré periodicity shows up as intensity modulation. The experimentally observed angle $\beta = 25°$ between the $[1\bar{1}0]$ directions of the Pb(111) layer

and the moiré can be reproduced in the moiré model, indicated with the angle.
In summary Pb deposited on Ag(111) initially leads to an alloying process on the surface for coverages $\leq 1/3\,\mathrm{ML}_{\mathrm{Ag(111)}}$ forming a $(\sqrt{3} \times \sqrt{3})$ Pb/Ag(111)$R30°$ surface alloy, where every third Ag atom is replaced by a Pb atom. The extracted Ag atoms diffuse on the surface and form monoatomic islands on large terraces, whereas on small terraces they merge to existing step edges. An interlayer mass transport of Ag is indicated by frequently appearing multiple steps. Exceeding the coverage of $1/3\,\mathrm{ML}_{\mathrm{Ag(111)}}$ leads to a dealloying process and patches of pure Pb(111) with a characteristical moiré modulation, which arise preferentially on step edges and coexist with the $(\sqrt{3} \times \sqrt{3})$ Pb/Ag(111)$R30°$ phase.

Thick Pb Films on Ag(111)

After the completion of the Pb(111) wetting layer on Ag(111), further Pb deposition leads to the growth of a Pb(111) film [114,136]. All crystallographic directions in this section refer to the Pb(111) overlayer. Fig. 7.5(a) shows a $500 \times 500\,\mathrm{nm}^2$ large sample area which exhibits Pb thicknesses between 40 and 60 Pb layers on Ag(111). The surface features smooth terraces with widths in the order of 100 nm as well as a densely stepped area. An atomically resolved scan of the Pb(111) surface is visible in Fig. 7.5(b) with a next neighbour distance of $a = (3.5 \pm 0.1)$ Å in good agreement to the Pb(111) wetting layer and Pb(111) bulk value. Additionally the surface features a bright hexagonally shaped moiré-type modulation with a periodicity of $\lambda = (1.6 \pm 0.1)$ nm with a rotation of $\beta = (25 \pm 1)^\circ$ between the $[1\bar{1}0]$ moiré and atomic directions (see black angle in Fig. 7.5(b)). Obviously, these moiré parameters are identical to those of the wetting layer discussed in the previous subsection.
Figure 7.5(c) shows a $100 \times 100\,\mathrm{nm}^2$ large area with three Pb step edges crossing the image vertically. The step edge height between different Pb thicknesses is $d = (2.8 \pm 0.1)$ Å corresponding to the layer distance of single Pb(111) step edges ($d = 2.86$ Å).
Fig. 7.5 (d) and (e) show the corresponding $\mathrm{d}I/\mathrm{d}U$ maps of (c) with setpoints $U_{\mathrm{set}} = 680$ mV for (d) and $U_{\mathrm{set}} = 560$ mV for (e). Both $\mathrm{d}I/\mathrm{d}U$ maps reveal a buried Ag(111) step edge that crosses the image diagonally along a $[11\bar{2}]$ direction leading to different Pb thicknesses as indicated. The different Pb thicknesses show a strong contrast between odd and even film thicknesses in both maps. Even thicknesses ($N = 50, 52$) appear bright and the odd thickness ($N = 51$) dark in Fig. 7.5(d) indicating a high and low DOS, respectively. Decreasing the energy by 120 meV completely inverts the contrast to high intensities for the odd film thickness ($N = 51$) and low intensities for even thicknesses (N=50, 52) in Fig. 7.5(e). This behaviour can be explained by the STS spectra in Fig. 7.5(f), showing layer dependent oscillations. The energies of Fig. 7.5(d) and (e) are marked with dashed lines within the spectra. The spectra for $N = 50, 52$ show a maximum and a minimum for $N = 51$ at 680 mV, whereas the situation is inverted at 560 mV. The oscillating behaviour of the DOS is addressed to quantum well states perpendicular to the Pb film. They allow the precise determination of Pb film thicknesses and will be further discussed in section 7.2.
Figure 7.6(a) shows the topography of a $300 \times 300\,\mathrm{nm}^2$ area of a Pb film on Ag(111) with coverages of 42 to 100 Pb layers, although the Pb surface itself shows only three atomically smooth terraces. The high number of different Pb layer thicknesses has its origin in buried silver step edges. They show up as a very faint zebra-like pattern in Fig. 7.6(a) crossing the image diagonally and lead to a wavy impression (for comparison see Fig. 7.13(a)). Interestingly, the moiré pattern from the Pb wetting layer is still visible in Fig. 7.6(b) for a 74 ML thick Pb film. The amplitude of the moiré pattern became considerably weaker as compared to the 1 ML wetting layer, but it is still clearly detectable. The surface features a periodic seam-like dislocation pattern (indicated by the black arrows in (a)) that crosses the Pb as well as the buried Ag step edges and follows the $[11\bar{2}]$ and $[1\bar{1}0]$ directions of the Pb(111) overlayer. The perpendicular distance between neighbouring dislocations amounts

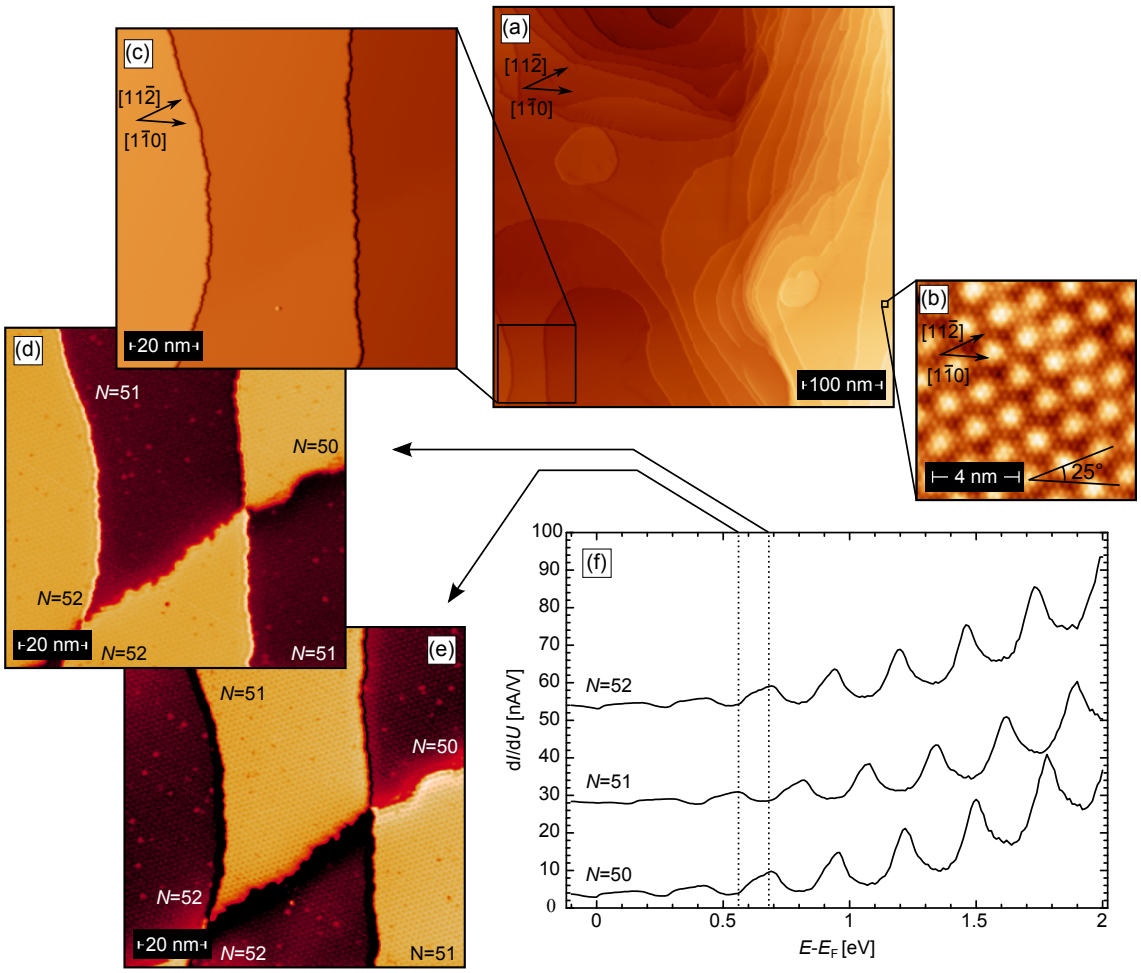

Figure 7.5: (a) $500 \times 500\,\mathrm{nm}^2$ large area of the sample with Pb coverages of 40-60 layers on Ag(111) ($U_{\mathrm{set}} = 2\,\mathrm{V}, I_{\mathrm{set}} = 50\,\mathrm{pA}$). The atomically resolved Pb(111) surface is shown in (b) with a superimposed moiré modulation, image size is $10 \times 10\,\mathrm{nm}^2$ ($U_{\mathrm{set}} = 100\,\mathrm{mV}, I_{\mathrm{set}} = 250\,\mathrm{nA}$). Panel (c) shows a $100 \times 100\,\mathrm{nm}^2$ large area with three vertically aligned Pb step edges ($U_{\mathrm{set}} = 250\,\mathrm{mV}, \mathrm{I_{set}} = 50\,\mathrm{pA}$). Panel (d) and (e) represent $\mathrm{d}I/\mathrm{d}U$ maps of (c) at setpoints $U_{\mathrm{set}} = 680\,\mathrm{mV}$ and $U_{\mathrm{set}} = 560\,\mathrm{mV}$, respectively ($I_{\mathrm{set}} = 50\,\mathrm{pA}, \mathrm{U_{mod,rms}} = 20\,\mathrm{mV}, \nu = 789\,\mathrm{Hz}$). Panel (f) shows STS spectra for the different Pb thicknesses of (c-e), spectra have been shifted by $50\,\mathrm{nA/V}$ for better visibility ($U_{\mathrm{set}} = -100\,\mathrm{mV}, \mathrm{I_{set}} = 2\,\mathrm{nA}, \mathrm{U_{mod,rms}} = 5\,\mathrm{mV}, \nu = 789\,\mathrm{Hz}$).
Lattice directions refer to the Pb(111) surface for (a-e).

to $b = (3.9 \pm 0.1)\,\mathrm{nm}$. A zoom on the dislocation line in Fig 7.6(c) reveals that the moiré patterns on the left and right side of the dislocation are rotated by an angle of $\gamma \approx 20°$ (red and black arrows represent the [1$\bar{1}$0] moiré directions of both domains). The 2D-FFT of Fig. 7.6(c), represented in Fig. 7.6(d), features 12 spots, that correspond to both moiré orientations. The angle of $\gamma = 20°$ can be found between the two coexisting domains, which are indicated by the red and black hexagon. The red hexagon belongs to the moiré on the right side and the black hexagon to the moiré on the left side of the dislocation line.

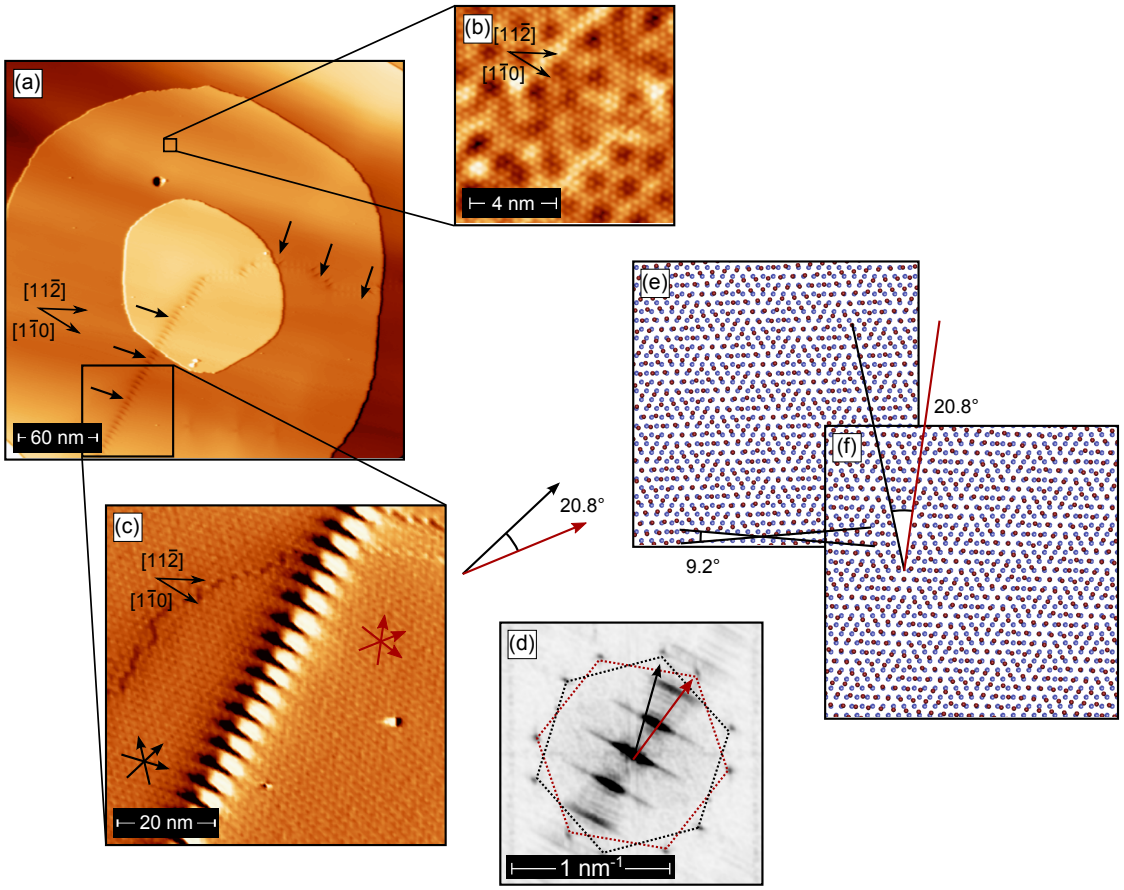

Figure 7.6: Panel (a) shows a $300 \times 300\,\mathrm{nm}^2$ area of the sample after 15 min Pb deposition time ($U_{\mathrm{set}} = -100\,\mathrm{mV}, \mathrm{I}_{\mathrm{set}} = 0.3\,\mathrm{nA}$). The surface shows a smooth Pb film with 3 Pb step edges. Buried silver edges lead to Pb layer thicknesses variation of 42 to 100 layers. An atomically resolved zoom on 74 ML thickness (b) reveals, that the moiré pattern is still visible, but attenuated ($U_{\mathrm{set}} = -50\,\mathrm{mV}, \mathrm{I}_{\mathrm{set}} = 1\,\mathrm{nA}$). Panel (c) shows a $70 \times 70\,\mathrm{nm}^2$ magnification of the seam-like dislocation pattern ($U_{\mathrm{set}} = -100\,\mathrm{mV}, \mathrm{I}_{\mathrm{set}} = 0.3\,\mathrm{nA}$). The moiré pattern on both sides of the dislocation line are rotated by $\gamma \approx 20°$ as indicated with the red and black arrows. A 2D-FFT ($1.7 \times 1.7\,\mathrm{nm}^{-2}$) of (c) reflects the two rotated domains—the black and red hexagon belong to the left and right side of (b), respectively. The rotation angle γ is found again as indicated with the red and black arrow. Panel (e) and (f) show models for both possible moiré patterns of Pb(111) on Ag(111). The angle between both Pb(111) surfaces is $2\alpha = 9.2°$ as indicated with the black angle and the moiré modulations are rotated by $\gamma = 20.8°$ with respect to each other as indicated with the red and black arrow.

This rotation can be understand by the growth of the first Pb wetting layer, which has in principal the possibility to grow in two crystallographic equivalent structures rotated by $\alpha = \pm 4.6°$ with respect to the substrate. Both resulting moiré structures are sketched in Fig. 7.6(e) and (f). The Pb(111) domains show an angle of $2\alpha = 9.2°$ and the moiré [1$\bar{1}$0] directions are rotated by $\gamma = 20.8°$ as indicated. This angle is in good agreement with the experimentally observed value, which confirms the existence of the two rotational Pb(111)

domains in Fig. 7.6(a) and (c).
In summary, thick films of Pb overlap Ag(111) step edges leading to a high variation of Pb layer thicknesses even if the Pb(111) surface itself is smooth. The buried Ag step edges can be made visible due to strong odd-even layer contrasts in $\mathrm{d}I/\mathrm{d}U$ maps in the film. Two crystallographic equivalent Pb(111) orientations coexist in the film with a rotation of $\alpha = \pm 4.6°$ referring to the Ag(111) surface and the moiré modulation remains detectable up to 74 ML. This indicates, that the electronic properties of the wetting layer are transferred through the film without a significant loss of coherence.

7.1.2 Growth characteristics of Bi/Ag(111)

Thin Films

The deposition of Bi on Ag(111) has been reported to lead to an alloying process for coverages $\leq 1/3\,\mathrm{ML}_{\mathrm{Ag(111)}}$ [23, 25, 141, 142] followed by a dealloying for higher coverages [141, 142]. Unless otherwise indicated the given directions refer to the $(\sqrt{3}\times\sqrt{3})$ Bi/Ag(111)$R30°$ reconstruction on the surface in this section (see Fig. 5.3(b) for the corresponding substrate and momentum space directions) and the substrate has been at elevated temperature $T = 200°\mathrm{C}$ during the growth.

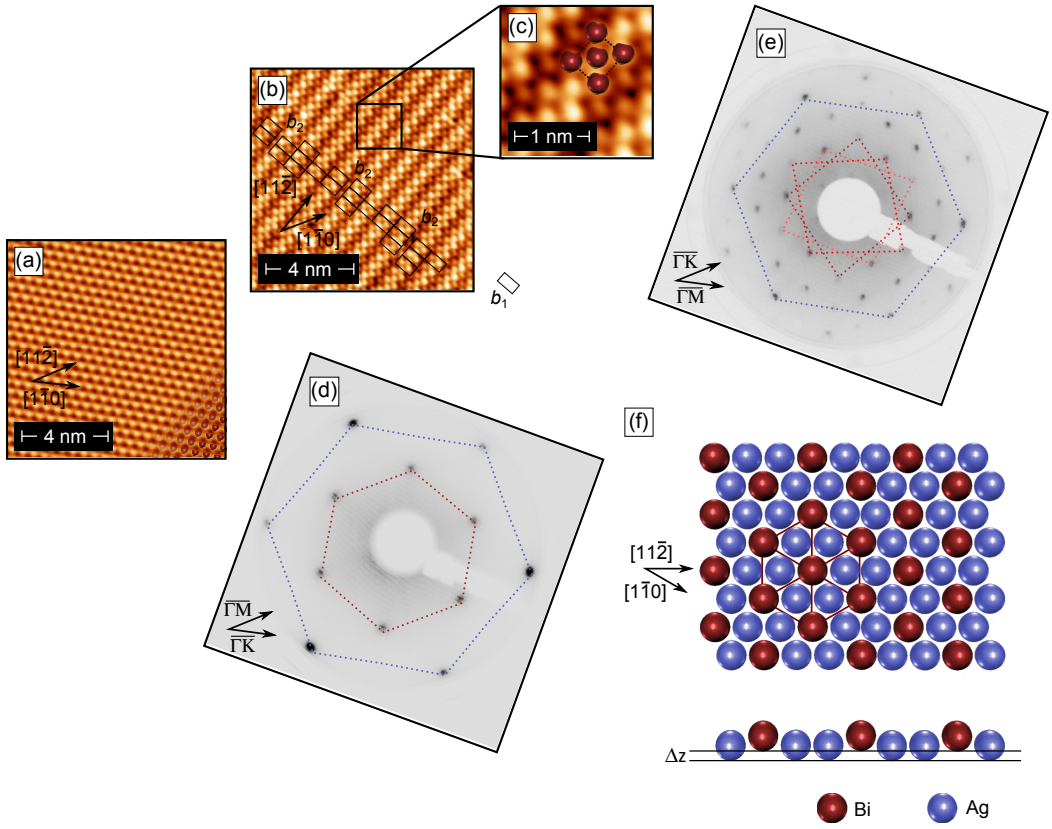

Figure 7.7: Atomically resolved $10\times 10\mathrm{nm}^2$ scans of the $(\sqrt{3}\times\sqrt{3})$ Bi/Ag(111)$R30°$ surface alloy (a) and the dealloyed ribbon structure of Bi/Ag(111) (b), which features a rectangular unit cell indicated by the red atoms in the inset (c). The corresponding LEED patterns of both structures are shown in (d) at $E = 48\,\mathrm{eV}$ and (e) with $E = 60\,\mathrm{eV}$, respectively. Panel (d) exhibits an inner hexagon (red), that corresponds to the $(\sqrt{3}\times\sqrt{3})$Bi/Ag(111)$R30°$ surface with a hexagonal unit cell of $a = (5.0\pm 0.1)\,\text{Å}$ and a larger hexagon (blue), that stems from the Ag(111) substrate. The LEED pattern of the dealloyed Bi ribbon structure indicates a rectangular unit cell on top of the Ag(111) with unit cell size $a_1 = (5.1\pm 0.2)\,\text{Å}$ and $a_2 = (4.5\pm 0.2)\,\text{Å}$ and threefold symmetry in the LEED pattern (indicated by the dark red, bright red and salmon unit cells). For (b) and (e) the given directions refer to the Ag(111) substrate. (f) The structural model of $(\sqrt{3}\times\sqrt{3})$Bi/Ag(111)$R30°$ as top and side view with the relaxation Δ_z of the Bi atoms.

Figure 7.7(a) and (b) show $1/3\,\mathrm{ML}_{\mathrm{Ag(111)}}$ and $0.6_{\mathrm{Ag(111)}}\,\mathrm{ML}$ coverages of Bi deposited on Ag(111), respectively. The coverage of $1/3_{\mathrm{Ag(111)}}\,\mathrm{ML}$ forms the $\sqrt{3}\times\sqrt{3}\mathrm{Bi/Ag(111)}R30°$ hexagonal alloy reconstruction, isostructural to the $\sqrt{3}\times\sqrt{3}\mathrm{Pb/Ag(111)}R30°$ alloy in Fig. 7.1(c). It features a lattice constant of $a = (5.0 \pm 0.1)\,\text{Å}$ determined by STM. The surface shown in this scan frame is defect-free indicating a higher surface quality than for the Pb/Ag(111) alloy. Indeed the very low defect density $\leq 10/10000\mathrm{nm}^{-2}$ can be seen in the $\mathrm{d}I/\mathrm{d}U$ map series in Fig. 7.27.

The corresponding LEED pattern of (a) is shown in Fig. 7.7(d). It consists of an outer hexagon (blue) that belongs to the underlying Ag(111) substrate and an inner hexagon (red) which is rotated by 30° and reflects the $\sqrt{3}\times\sqrt{3}R30°$ symmetry of the surface alloy. The structural model of the $\sqrt{3}\times\sqrt{3}\mathrm{Bi/Ag(111)}R30°$ surface alloy is given in Fig. 7.7(f). In accordance to Fig. 7.1(e) blue atoms represent the Ag(111) substrate and red atoms depict the embedded Bi atoms which buckle out of the surface by the relaxation Δ_z.

At a coverage of $0.6_{\mathrm{Ag(111)}}\,\mathrm{ML}$ in Fig. 7.7(b) the surface shows a ribbon-like densely packed structure with stripes extending into a $[11\overline{2}]_{\mathrm{Ag}}$ direction[2]. The surface features a rectangular unit cell that contains two atoms (marked in the zoom in Fig. 7.7(c)). The lattice constant along $[11\overline{2}]_{\mathrm{Ag}}$ directions is determined to $a_1 = (5.1 \pm 0.1)\,\text{Å}$, which corresponds very well to the nearest next neighbour distance $\sqrt{3}a_{\mathrm{Ag(111)}} = 5.0\,\text{Å}$ and is in good agreement to previous studies [141, 142]. Perpendicular to the stripe orientation (along $[1\overline{1}0]_{\mathrm{Ag}}$) $a_2 = (4.4 \pm 0.1)\,\text{Å}$ is determined, which is in between the reported values of $(4.0 \pm 0.1)\,\text{Å}$ [141] and 4.7 Å [142]. The corresponding LEED pattern of the ribbon structure is shown in Fig. 7.7(e). It indicates a rectangular surface structure with threefold symmetry (dark red, red, and rose) with lattice constants of $(a_1 = 5.1 \pm 0.2)\,\text{Å}$ and $a_2 = (4.5 \pm 0.2)\,\text{Å}$, which is in a good agreement to the STM data in this work.

The stripes, that are superimposed to the atomic structure, feature different stripe to stripe distances on the surface. The smallest observed spacing amounts to $b_1 = (9.0 \pm 0.2)\,\text{Å} \approx 2a_2$, but also spacings of about $b_2 = (10.4 \pm 0.4)\,\text{Å}$ and $b_3 = (11.8 \pm 0.3)\,\text{Å}$ are found (see also Ref. [141]). The spacings b_1 and b_2 can be seen in Fig. 7.7(b). The black rectangles have the length b_1 along $[1\overline{1}0]_{\mathrm{Ag}}$ and a_1 along $[11\overline{2}]_{\mathrm{Ag}}$. The three visible gaps in between the rectangles denote the b_2 spacings and at that positions the rectangles are shifted by $\frac{a_1}{2}$ against each other along a $[11\overline{2}]_{\mathrm{Ag}}$ direction.

The rectangular phase is discussed controversely in literature either as commensurate (3012) phase with a 4-atomic unit cell [141] or as incommensurate $(p \times \sqrt{3})$ rect. phase [142].

Within the interpretation as incommensurate structure the stripes are interpreted as moiré modulation. Due to the $\sqrt{3}$ periodicity along the $[11\overline{2}]_{\mathrm{Ag}}$ directions a moiré-type modulation should posess a 1D nature consistent with the observed stripe pattern. In a 1D model the reciprocal vector of the moiré periodicity $g_{\mathrm{moiré}}$ is described by

$$|g_{\mathrm{moiré}}| = |g_{\mathrm{Ag(111)}}| - |g_{\mathrm{Bi}}| \tag{7.1.2}$$

[2]The lattice directions in Fig. 7.7(b) and (e) refer to the Ag(111) substrate.

with the reciprocal lattice vectors $g_{\mathrm{Ag}(111)} = \frac{2\pi}{a_{\mathrm{Ag}(111)}}$ and $g_{\mathrm{Bi}} = \frac{2\pi}{a_2}$. This gives

$$a_{\text{moiré}} = \frac{a_{\mathrm{Ag}(111)} a_{\mathrm{Bi}}}{g_{\mathrm{Bi}} - d_{\mathrm{Ag}(111)}}. \tag{7.1.3}$$

With the lattice constant $a_2 = (4.4 \pm 0.1)\,\text{Å}$ the moiré periodicity is determined to $a_{\text{moiré}} = (8.4 \pm 0.9)\,\text{Å}$. The uncertainty of 0.9 Å is quite large since Eq. (7.1.3) is very sensitive to small changes of the involved lattice constants. Within the accuracy of the data it agrees with the experimentally observed smallest spacing. Assuming a lattice constant of 4.7 Å of Ref. [142] and estimating an uncertainty of 0.1 Å leads to a $a_{\text{moiré}} = (7.5 \pm 0.9)\,\text{Å}$, which is far smaller than the stripe distances of $\approx 1.2\,\text{nm}$ observed in that study[3]. However, it can be seen in Fig. 7.7(b-c) and very clear in Ref. [141] (Fig. 2), that the lattice constant $a_2 = (4.5 \pm 0.2)\,\text{Å}$ of the adsorbed Bi layer does not change its value even for the larger stripe spacings. Consequently also the moiré periodicity should remain constant as it follows the rigid relation in Eq. (7.1.3). At this point I conclude, that the striped structure can not be explained at all in a moiré interpretation since it is not possible to change the moiré modulation without a change of the involved lattice constants.

Instead the authors of Ref. [141] introduced a 4-atomic larger (3012) phase model. Along $[1\bar{1}0]_{\mathrm{Ag}}$ directions this gives a unit cell size of $3a_{\mathrm{Ag}(111)} = 8.67\,\text{Å}$, which corresponds very well to observed smallest stripe spacing b_1. As already indicated by the rectangles in Fig. 7.7(b) larger stripe spacings rise at domain boundaries. The b_3 spacing can be also explained in this model for neighbouring domains consisting of only one stripe. Hence, the (3012) phase model is able to explain all observed aspects of the observed surface features.

Similar to the Pb/Ag(111) case in Sec. 7.1.1 the surface appears different depending on the terrace size. A $500 \times 500\,\text{nm}^2$ large scan of a sample with a Bi coverage of $\approx 0.46\,\text{ML}$ that was prepared on Ag(111) held at room temperature is shown in Fig. 7.8(a). It features one large terrace with a width of $\geq 200\,\text{nm}$ and small terraces $\leq 100\,\text{nm}$ widths on the left side. Whereas the small terraces feature a smooth appearance, a network-like island structure is visible on the large terrace. The two surface structures are shown at higher magnification in Fig. 7.8(b) and (c). On the network structure in Fig. 7.8(b) two different phases coexist, which can be identified as $(\sqrt{3} \times \sqrt{3})\text{Bi/Ag}(111)R30°$ (A) and the ribbon phase (B). In agreement with the LEED pattern in Fig 7.7(e) the ribbon phase shows orientations along all three equivalent symmetry directions. The bright islands (A) stem from underlying monoatomic Ag islands with a height of $d = (2.34 \pm 0.05)\,\text{Å}$. Apparently the Bi/Ag(111) surface shows the same island forming mechanism as Pb/Ag(111) as a result of the alloying process where Ag atoms are extracted from the surface and assemble to islands on large terraces.

Interestingly, almost all $(\sqrt{3} \times \sqrt{3})\text{Bi/Ag}(111)R30°$ islands are connected to each other with a network of the ribbon phase (B). This indicates that the dealloying process leading to the striped phase starts on step edges of the completed $(\sqrt{3} \times \sqrt{3})\text{Bi/Ag}(111)R30°$ surface. The situation on the smaller terraces in Fig. 7.8(c) confirms this behaviour. The striped

[3]The value has been readout by means of the sketched unit cell in Ref. [142].

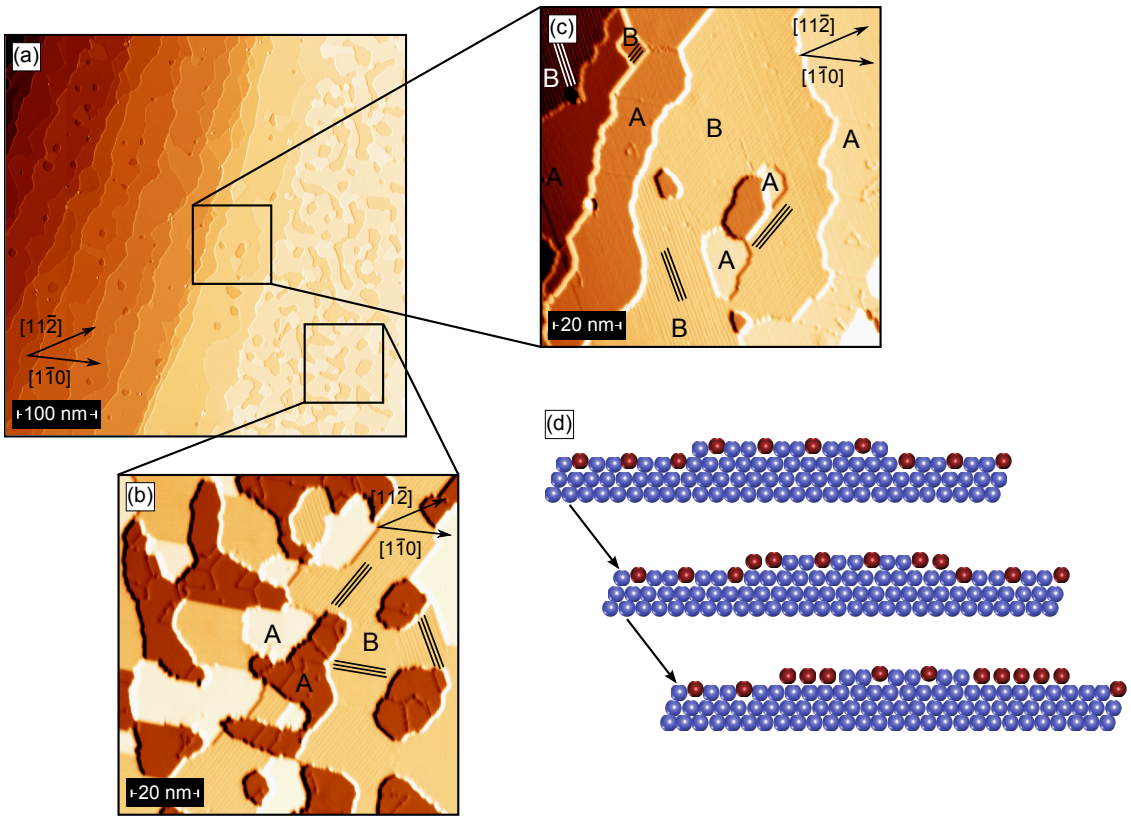

Figure 7.8: (a) $500 \times 500\,\mathrm{nm}^2$ scan of $0.46\,\mathrm{ML}_{\mathrm{Ag(111)}}$ Bi/Ag(111) held at room temperature during the growth. The surface features a large terrace on the right side and small terraces of $\leq 100\,\mathrm{nm}$ width on the the left side of the image. Whereas the large terrace holds a network-like pattern with three different contrasts, the smaller terraces are smooth in appearance. $100 \times 100\,\mathrm{nm}^2$ zooms of both textures are shown in (b) and (c). The contrasts in (b) are identified as $(\sqrt{3} \times \sqrt{3})$ Bi/Ag(111)$R30°$ with monoatomic Ag islands (A) (darkest and brightest contrast), which are connected by a network of the ribbon phase (B). The smooth surface in (c) exhibits only two Ag islands and the ribbon phase is preferentially found on step edges. (d) A schematic of the growth mode. After the completion of the $(\sqrt{3} \times \sqrt{3})$ Bi/Ag(111)$R30°$ surface alloy (top image) the additional Bi atoms adsorb on Ag step egdes and replace Ag atoms forming a pure Bi layer with pure Ag(111) underneath (centered image). The Bi atoms in the lower terrace can be replaced by the released Ag atoms and the pure Bi patch can further extend (bottom image)Figure (d) is based on a description in Ref. [142].

phase (B) is preferentially found at step edges forming very broad step edge decorations, which implies that the dealloying process starts on step edges. A network structure is not visible on the small terraces due to the fact that almost all diffusing Ag atoms merged to Ag(111) step edges.

A schematic of this growth mode is shown in 7.8(d) based on a description in Ref. [142], starting with the completed $(\sqrt{3} \times \sqrt{3})$Bi/Ag(111)$R30°$ surface (top image). An incoming Bi atom replaces a Ag atom on a step edge (centered image), the Ag atom is released then.

In the next step a Bi atom in the lower terrace can be replaced by the diffusing Ag atom and a patch of pure Bi develops (bottom image), the Ag(111) surface is now dealloyed in this area. By further deposition of Bi atoms the pure Bi patches grow until the surface is dealloyed completely and covered with the pure Bi phase.
In summary the deposition of Bi/Ag(111) initially forms the alloyed $(\sqrt{3}\times\sqrt{3})$ Pb/Ag(111)$R30°$ phase isostructural to the case of Pb/Ag(111), but with a much higher surface quality. The surface dealloys for Bi coverages above $1/3\,\mathrm{ML}_{\mathrm{Ag(111)}}$ and patches of a striped phase rise, which coexist with the alloy phase. Its unit cell resembles the Bi(110) surface though it exhibits a larger unit cell. In this context it is important to note that Bi exhibits a rhombohedral crystal structure and the indexing in this work refers to its rhombohedral structure. Bismuth surfaces might also be indexed pseudocubic or even hexagonal in literature, therefore the rhombohedral Bi(110) surface may appear as pseudocubic Bi(100) or hexagonal Bi(00$\bar{1}$2) surface. The transfer of all different indexings can be found in Refs. [151, 152]. However, the appearance of three rotated orientations of the striped Bi phase reflects the threefold symmetry of the substrate and the stripe origin could be addressed to a four-atomic unit cell with different atomic positions of the Bi atoms on top of the substrate rather than a moiré modulation.

Thick Films

A phase transition from the striped Bi/Ag(111) phase to Bi(110) for further Bi deposition has been reported previously [142, 143] but no studies for films ≥ 2 ML are available so far. Data from this range of coverages of Bi/Ag(111) will be presented in the following section. A structural model of Bi(110) is given in Fig. 7.9(a-b). Every Bi(110) layer is composed of a bilayer as shown in top view (a). The Bi(110) bilayer features a rectangular two-atomic unit cell with $a_1 = 4.75\,\text{Å}$ along $[1\bar{1}0]_{\text{Bi}}$ and $a_2 = 4.54\,\text{Å}$ along $[001]_{\text{Bi}}$ direction. The embedded atom is off-centered and located in the second layer (bright red). The zigzag lines indicate chains of covalent surface bonds along the $[1\bar{1}0]_{\text{Bi}}$ direction. The dashed vertical line indicates the mirror plane symmetry of Bi(110). A side view of Bi(110) in Fig. 7.9(b) illustrates its bilayer structure with $d = 3.27\,\text{Å}$ between adjacent bilayers. The red lobes denote dangling bonds of the first layer atoms. The mirror plane symmetry in Fig. 7.9(a) appears also in the LEED pattern ($E = 139\,\text{eV}$) in Fig. 7.9(c) (horizontal line). Therefore the LEED spot intensities are symmetric for a reflection on the horizontal line. In contrast, for a reflection on a vertical line it can be seen that the $(0, \bar{1})$ and $(0, \bar{2})$ spots show a weak intensity, but $(0, 1)$ and $(0, 2)$ feature a high intensity.
Figure 7.10(a) shows an $1 \times 1\,\mu\text{m}^2$ overview of nominally $(28 \pm 2)\,\text{ML}_{\text{Bi(110)}}$[4] calibrated with LEED and STM. The surface exhibits a strongly stepped surface with about 13 different

[4] One Bi(110) layer accounts to $9.24 \cdot 10^{14}\text{atoms/cm}^2$, an Ag(111) layer contains $13.8 \cdot 10^{14}\text{atoms/cm}^2$

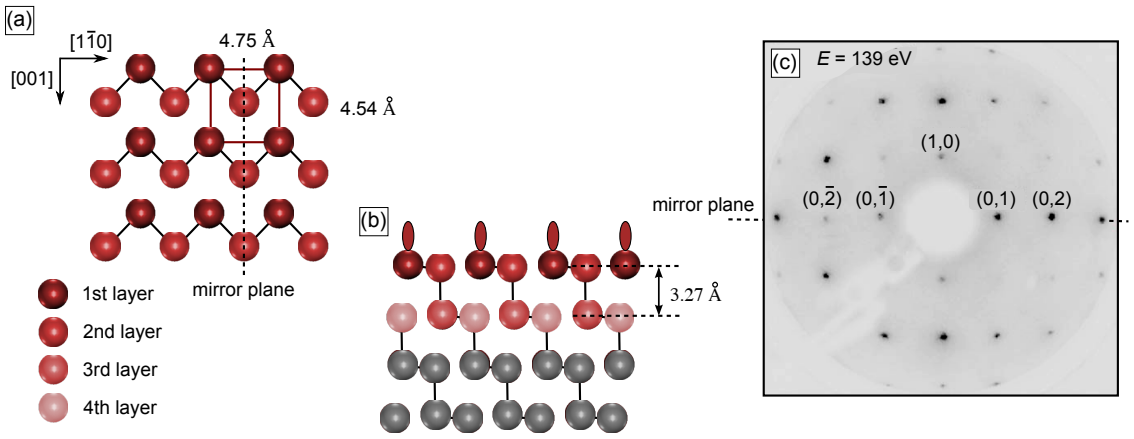

Figure 7.9: (a) Top view of the first Bi(110) bilayer surface. The dark red atoms (1st layer) span a rectangular unit cell with $a_1 = 4.75\,\text{Å}$ along $[1\bar{1}0]_{\text{Bi}}$ and $a_2 = 4.54\,\text{Å}$ along $[001]_{\text{Bi}}$. The centered atom (off-center, bright red) is located in the second layer and completes the Bi(110) bilayer. The zigzag lines along $[1\bar{1}0]_{\text{Bi}}$ direction indicate covalent bonds. The Bi(110) surface exhibits a mirror plane indicated with the dashed vertical line. A side view is visible in (b), the distance between adjacent bilayers amounts to $d = 3.27\,\text{Å}$. The red lobes indicate the dangling bonds in the first layer. (c) A LEED measurement of a Bi(110) single crystal at $E = 139\,\text{eV}$. The spot intensities reflect the structural mirror plane of (a), it is indicated by the horizontal line in the LEED measurement. Figures (a)-(c) are adapted from Ref. [153].

terrace heights observable in this scan. The terraces itself show a strong ribbon-like growth along two of the three crystallographic equivalent $[1\bar{1}0]_{\mathrm{Ag(111)}}$ directions (the third direction was visible in other scans). The elongated growth of Bi has been reported already after the completion of the first Bi(110) layer on Ag(111) [142, 143]. It has been addressed to the semimetallic character of Bi(110) [153, 154] that leads to the formation of chains of covalent bonds along $[1\bar{1}0]_{\mathrm{Bi}}$ (see Fig. 7.9(a)). As a result of the weaker bonding along the $[001]_{\mathrm{Bi}}$ direction Bi atoms preferentially adsorb on already existing chains rather than forming a new chain. The ribbons reach lengths up to $1\,\mu$m and the widths of the respectively top layer islands amount to $10 - 30\,$nm. For more details a $500 \times 500\,\mathrm{nm}^2$ scan is shown in Fig. 7.10(b). The surface shows a striped pattern with protrusions of $\approx 5 - 6\,$pm. The stripes exhibit spacing variations between $5.2 - 6.2\,$nm and rotations of up to 20° with respect to each other for the same Bi(110) domain (see left bottom part of the image and the right top corner). However, all three crystallographic orientations for the stripes can be seen in the frame which indicates a structural connection between stripe directions and Bi(110) domains. This is more clearly visible in Fig. 7.10(c) that shows a domain boundary between two rotated Bi domains. The scan frame already exhibits atomic resolution and the different Bi directions for both domains are indicated. It is visible that the stripes (black arrows) rotate together with the domains.

The stripes potentially originate from a 1D moiré, a charge density wave or stress in the film. A moiré modulation between substrate and film can be excluded as possible origin, since the resulting moiré pattern should possess a two-dimensional pattern as both directions of the Bi unit cell are incommensurable to the Ag(111) periodicity. Also a charge density wave can not be the origin, as charge density waves appear likely close to the Fermi level [155] but the stripes remain largely unchanged for a wide range of bias voltages far away from the Fermi level between $U_{\mathrm{set}} = 0.1 - 2\,$V. Therefore the most probable origin is a one-dimensional stress-induced relaxation in the film.

In Fig. 7.10(d) atomic resolution is presented, a one-atomic rectangular unit cell is visible, zoomed-in for more clarity in Fig. 7.10(e). It features lattice constants of $a_1 = (4.76 \pm 0.06)\,$Å along the $[1\bar{1}0]_{\mathrm{Bi}}$ direction and $a_2 = (4.55 \pm 0.04)\,$Å along $[001]_{\mathrm{Bi}}$ direction, which are in good agreement to the unit cell of the Bi(110) surface (see Fig. 7.9(a)).

Only the atoms of the first atomic layer are observed in the atomic resolution in Fig. 7.10(d-e), the centered atoms from the second layer are entirely missing. This has also been reported for a Bi(110) single crystal [74] and was explained in terms of the semimetallic character of Bi. Only atoms in the first layer possess dangling bonds that point into the vacuum, whereas the atoms in the second layer are fully bound to the subjacent layers (see Fig. 7.9(b)). The observation of a Bi(110) film on Ag(111) at such a high coverages is different from Bi deposited on Si(111) where a phase transition from a Bi(110) to a Bi(111) film above a coverage of 4 ML has been reported [156][5]. Thus, the choice of the substrate

[5] The authors of Ref. [156] follow a different notation for the Bi surfaces. However, the surfaces have been transferred to rhombohedral indexing here.

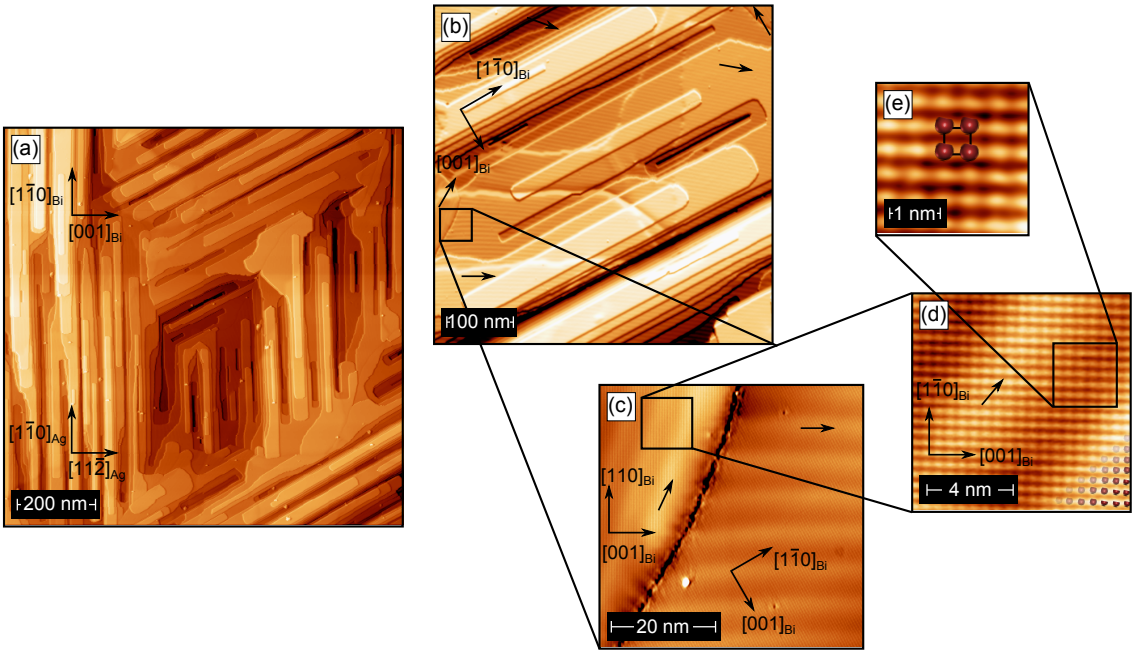

Figure 7.10: (a) $1 \times 1\,\mu m^2$ scan of nominally (28 ± 2) ML Bi(110) layers deposited on Ag(111). The surface features long extended islands with lenghts up to $1\,\mu m$ along $[1\bar{1}0]_{Bi}$ and short edges along $[001]_{Bi}$ directions. The lattice directions of the substrate and overlayer are indicated with $[1\bar{1}0]_{Bi}||[1\bar{1}0]_{Ag}$ and $[001]_{Bi}||[11\bar{2}]_{Ag}$. The visible stripe directions correspond to two 60° rotated Bi(110) domains and reflect the threefold symmetry of the substrate. (b) A $500 \times 500\,nm^2$ scan reveals a striped pattern on the surface (indicated by the black arrows). (c) A $50 \times 50\,nm^2$ scan frame with two different Bi domains and atomic resolution. The stripe modulation (indicated with black arrows) rotates together with the Bi(110) domain orientations. (d) A $10 \times 10\,nm^2$ atomically resolved scan, the surface exhibits a rectangular structure overlayed with the striped pattern. For more clarity the rectangular unit cell is indicated in the zoom in (d) with a lattice constant of $a_1 = (4.76 \pm 0.06)$ Å along $[1\bar{1}0]_{Bi}$ and $a_2 = (4.55 \pm 0.04)$ Å along $[001]_{Bi}$ direction.

considerably influences the Bi growth mode.

In order to further verify that the observed film is indeed a Bi(110) film, step edge heights and the LEED pattern are checked, starting with step edge heights in Fig. 7.11. The topography in Fig. 7.11(a) shows three different terrace heights exhibiting atomic resolution as well as the striped modulation (almost vertical in the frame). The dashed line indicates the position where the line profile shown in Fig. 7.11(b) has been obtained. All steps feature the same height $d = (3.3 \pm 0.2)$ Å. This value is in very good agreement to the height expected for a single Bi(110) bilayer as illustrated in Fig. 7.9(b). The observation of single bilayers for thick Bi films stands in contrast to the observations for coverages ≤ 2 ML. The authors in Ref. [143] report about Bi ribbons with 6.6 Å and 13.2 Å heights corresponding to double and quadruple bilayers, respectively. They argued that 50% of the Bi atoms in a single Bi bilayer exhibit dangling bonds, which makes them energetically unstable. In their argumentation double bilayers would saturate those dangling bonds, therefore

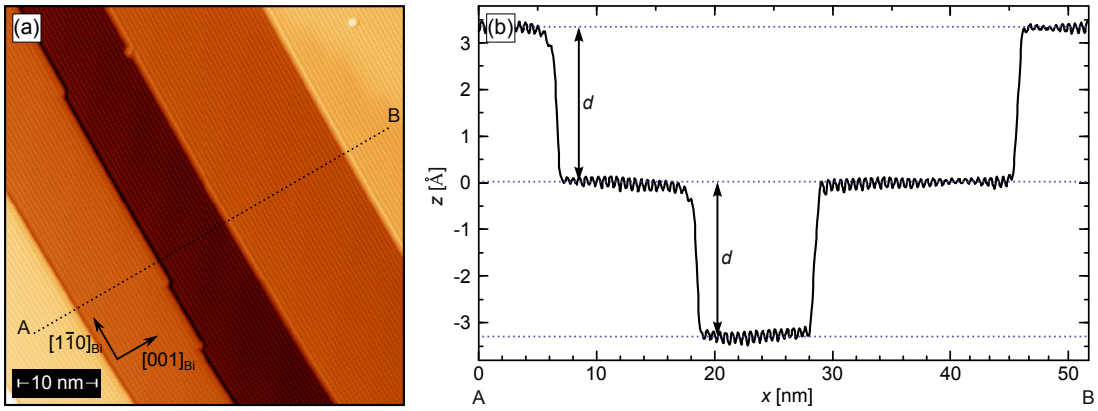

Figure 7.11: (a) $50 \times 50\,\mathrm{nm}^2$ scan with three different terrace heights and underlying atomic resolution. All step edges follow a $[1\bar{1}0]_{\mathrm{Bi}}$ direction, the dashed line indicates a line profile, that is presented in (b). All steps have the same height $d = (3.3 \pm 0.2)$Å, which corresponds to a Bi(110) bilayer.

integer multiples of Bi bilayers should be favoured in the growth. The same argumentation has also been given for Bi/Si(111) in Ref. [156]. Since this has been assigned to the intrinsical Bi(110) film properties double bilayers should show up entirely independent from the Bi coverage as well as from the substrate choice. Following that explanation single bilayer step edges should not—or rarely—be found on thicker films. However, the clear existence of single bilayer step edges in this work completely disagrees with that explanation. Furthermore, Bi double bilayers were completely absent in a study about Bi deposited on quasicrystalline substrates [157]. Instead they reported about integer thicknesses of quadruple bilayers. Therefore I consider that quantum size effects in thin Bi films might be the driving force for the observed thicknesses in [143, 156] which is consistent with the finding of single bilayer heights in this work as the quantum character decreases with increasing film thickness. Generally, the existence of quantum-driven "magic" island heights in thin films, that differ for the exact substrate choice, is not unusual and has been also reported for thin Pb films [118, 158].

A LEED measurement of the sample presented in Fig. 7.10 is shown in Fig. 7.12. The black hexagon indicates the Ag(111) substrate in Fig. 7.10(a-b) and the Bi(110) unit cell can be also identified, marked in bright red in Fig. 7.10(a). The two rectangles connect (1,0) and (1,1) spots, respectively. The remaining spots in Fig. 7.10(a) can be assigned by introducing rotated Bi domains, which reflect the threefold symmetry of the Ag(111) substrate. By a rotation of 60° (dark red) and 120° (salmon) all spots can be identified in Fig. 7.12(b). Apparently the mirror plane symmetry of Fig. 7.9(c) is missing completely within each domain, all spots feature similar intensities. This can be interpreted by an additional degree of freedom leading to 180° rotated Bi domains. Concerning the spot intensities in the LEED pattern this causes an averaging of the LEED spots in Fig. 7.9(c). Exemplary the (1,0) and (0,-1) spots average, as well as the (1,-1) and (-1,1) spots, which

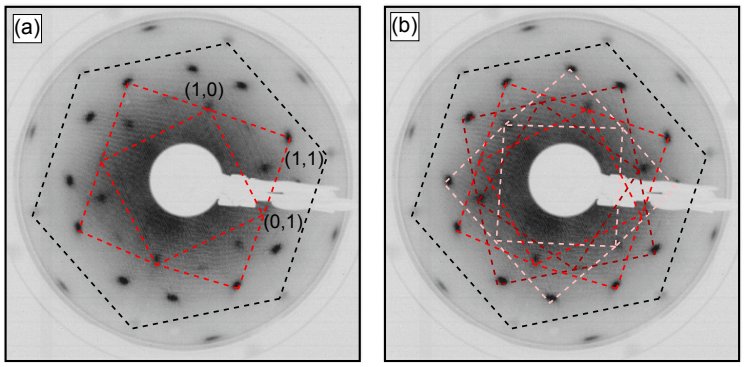

Figure 7.12: LEED measurement at $E = 60\,\text{eV}$ (a-b). (a) red rectangles connect (1,0) and (1,1) spots of the rectangular Bi(110) unit cell, the black hexagon represents the Ag(111) unit cell. The unit cell size determined by LEED accounts to $(4.6 \pm 0.2)\,\text{Å}$ and $(4.4 \pm 0.2)\,\text{Å}$ To pick up all LEED spots the Bi(110) unit cell is then rotated by 60° (dark red) and 120° (salmon) in (b) for all three Bi domains, which reflects the threefold symmetry of the Ag(111) substrate.

vanishes the mirror symmetry in Fig. 7.12. As the Bi atom in the second layer is not visible in the topography 180° rotational domains can not be distinguished by STM.
In summary thick Bi films deposited on Ag(111) form a Bi(110) structure and feature a ribbon growth with six different orientations on the Ag(111) substrate. The ribbons extend up to $1\,\mu\text{m}$ and adjacent step edge heights account to single Bi(110) bilayers. The whole surface exhibits a striped pattern, which most probably originates from a one-dimensional stress-induced relaxation in the film.
Compared to thick Pb/Ag(111) layers QWS are not observed spectroscopically for Bi/Ag(111) films. This could be addressed to the semimetallic character of Bi(110), that might prevent a free electron gas character for such thick films along the z-direction and thus prohibits pronounced QWSs.

7.2 Quantum Well States of Pb/Ag(111)

As already discussed in Sec. 6 and denoted in Sec. 7.1.1, Pb films exhibit a characteristic odd-even behaviour in film thickness, that influences e.g. the growth mode [116–119], conductivity [120], superconductivity [121–123], electron-phonon-coupling [124], work functions [125], and Kondo physics [126]. In the literature QWSs have been reported for Pb layer thicknesses up to 37 ML [114]. So far most studies of Pb QWSs have been carried out on Si(111), which has the disadvantage, that the interface between Si(111) and Pb film can be either a Si(111)(1×1) or a Si(111)(7×7) reconstruction, which shifts the QWSs in energy [128, 159]. This problem is avoided by the usage of Ag(111) in this section, since its surface does not reconstruct and also the low coverage $(\sqrt{3} \times \sqrt{3})$Pb/Ag(111)$R30°$ reconstruction completely disappears as soon as the Pb coverage amounts to $1\,\mathrm{ML}_{\mathrm{Pb(111)}}$ (see Sec. 7.1.1). Thus, the Ag(111) surface provides a stable interface.

Figure 7.13(a) shows a slice of a full grid spectroscopy at $U_{\mathrm{set}} = 810\,\mathrm{meV}$ from the same sample location, that was already presented in the topographic image of Fig. 7.6(a). The contrast between odd and even layer thicknesses is very strong at this bias setpoint, revealing the buried Ag step edges clearly. Even layer thicknesses show a decreased (orange) DOS, whereas odd layer thicknesses provide a strongly enhanced DOS (yellow). The existence of two different rotational Pb(111) domains separated by the dislocation pattern does not influence the observed contrast. The spectra in Fig. 7.13(b) are in a good agreement to the observed DOS contrasts, showing spectra for $N = 93\,\mathrm{ML}$ and $N = 94\,\mathrm{ML}$ (the arrows mark the spectra areas). The bias setpoint of Fig. 7.13(a) is indicated with the dashed line. It intersects a minimum between two oscillations for the even thickness $N = 94\,\mathrm{ML}$ and a

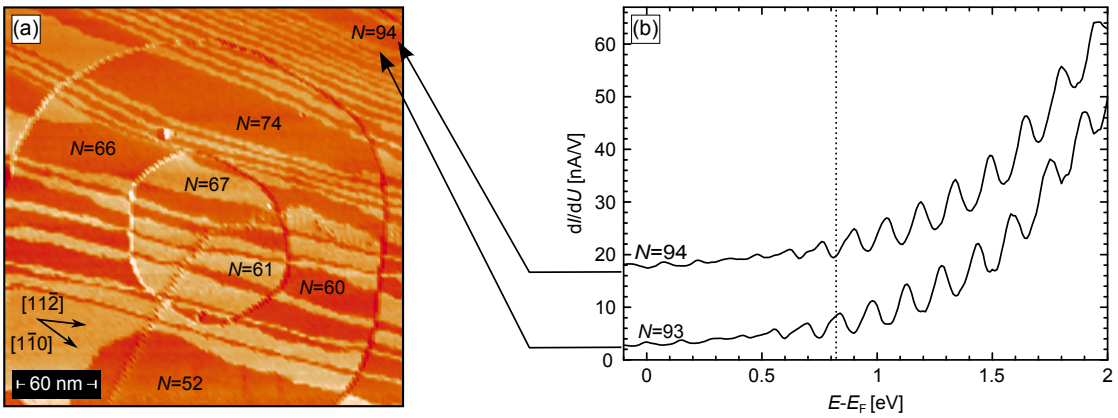

Figure 7.13: (a) A slice of full grid spectroscopy at $U_{\mathrm{set}} = 810\,\mathrm{mV}$ with $128 \times 128\,\mathrm{px}$ (the corresponding topography is shown in Fig. 7.6(a)). The dark (orange) contrast for even Pb layer thicknesses and bright (yellow) for odd layers reveals the buried Ag step edges. Panel (b) shows STS spectra taken on $N = 93, 94\,\mathrm{ML}$ Pb layer thicknesses. The peaks of the quantum well states in the spectra are despite the high number of layers still distinct in both layers. The bias setpoint of panel (a) is marked with a dashed line, indicating a high DOS for $N = 93\,\mathrm{ML}$ and low DOS for $N = 94\,\mathrm{ML}$ in a very good agreement to the observed $\mathrm{d}I/\mathrm{d}U$ map in (a).

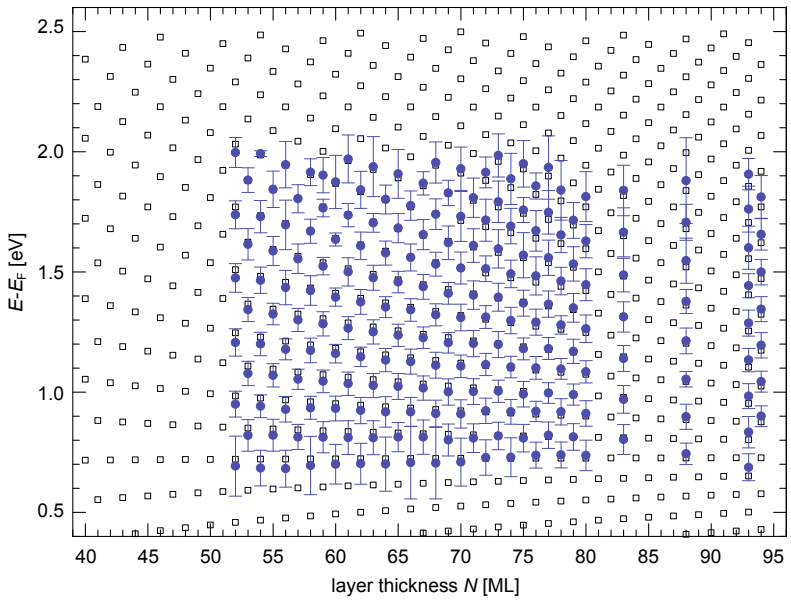

Figure 7.14: Quantum-well states extracted from a full grid spectroscopy of the scan area in Fig. 7.13(a). The blue points depict the data points, the empty squares are numerical solutions of Eq. (6.0.4). The best match between experimental and theoretical data is achieved by the presented assignment. Some layer thicknesses have been left out due to the diminutive size of the corresponding terrace sizes.

maximum for the odd thickness $N = 93\,\mathrm{ML}$. Remarkably, the layer thicknesses of almost 100 ML still provide very strong intensities for the observed QWSs.
For the determination of layer thickness the QWSs energies have been extracted out of the full grid spectroscopy, which allows to assign the single STS spectra directly to the topographic information. The results are presented in Fig. 7.14. Only peaks with energies $(E - E_\mathrm{F}) \geq 0.7\,\mathrm{eV}$ have been used and fit with a Lorentzian. Some layer thicknesses have been left out due to the diminutive sizes of the corresponding terraces.

The blue circles represent the experimental values, whereas empty squares were obtained by numerical solutions of the phase condition in Eq. (6.0.4). For the calculations the substrate band gap, work function of the film and the film band gap values are needed, the Ag(111) band gap values have been taken from Ref. [160] with $E_L = -0.4\,\mathrm{eV}$ and $E_U = -3.9\,\mathrm{eV}$. The work function for Pb(111) films has been determined to $E_\mathrm{vac} = 3.9\,\mathrm{eV}$ in Ref. [114]. Additionally the energy dispersion $E(k_\perp)$ has been found to follow an approximately linear relation $E(k_\perp) = E_0 + v \cdot k$ in Ref. [114] with the values $v = 13.19\,\mathrm{eV\AA}$ and the Fermi wave vector $k_F = 1.592\,\mathrm{\AA}^{-1}$. It can be used alternatively to the 1D tight binding approach in Eq. 6.0.7, which allows to dispense the Pb(111) band gap values in Eq. (6.0.7).
The best match between the experimental data and the theoretical solutions is achieved for the presented assignment, leading to the conclusion that the QWS character of Pb films on Ag(111) preserve distinctly up to very large thicknesses of $\approx 100\,\mathrm{ML}$.

7.2.1 Quasi-particle interferences

As pointed out in Ref. [114] QWSs in the STS spectra below $(E - E_F) \approx 1\,\text{eV}$ exhibit more a plateau-shape than a peak-like feature. Since the m-shape of $E(k_{||})$ in Pb/Si(111) films has been addressed to Pb [129, 131] bulk bands it seems likely, that an m-shape dispersion is also the origin of the broad features in the spectra in Pb/Ag(111) films.
In order to investigate the band structure by means of quasi-particle interferences a sample has been prepared with layer thicknesses of $30 - 40\,\text{ML}$. Figure 7.15(a) shows the topography of the investigated area, featuring several terraces. In the corresponding $\mathrm{d}I/\mathrm{d}U$ map in Fig. 7.15(b) ($U_{\text{set}} = 150\,\text{meV}$) 5 different Pb layer thicknesses are identified by their different contrasts. The STS spectra of all thicknesses are represented in Fig. 7.15(c), the vertical dashed line indicates the $\mathrm{d}I/\mathrm{d}U$ map setpoint in Fig. 7.15(b). The spectra show a good agreement to the observed intensities in Fig. 7.15(b). The QWS solutions have

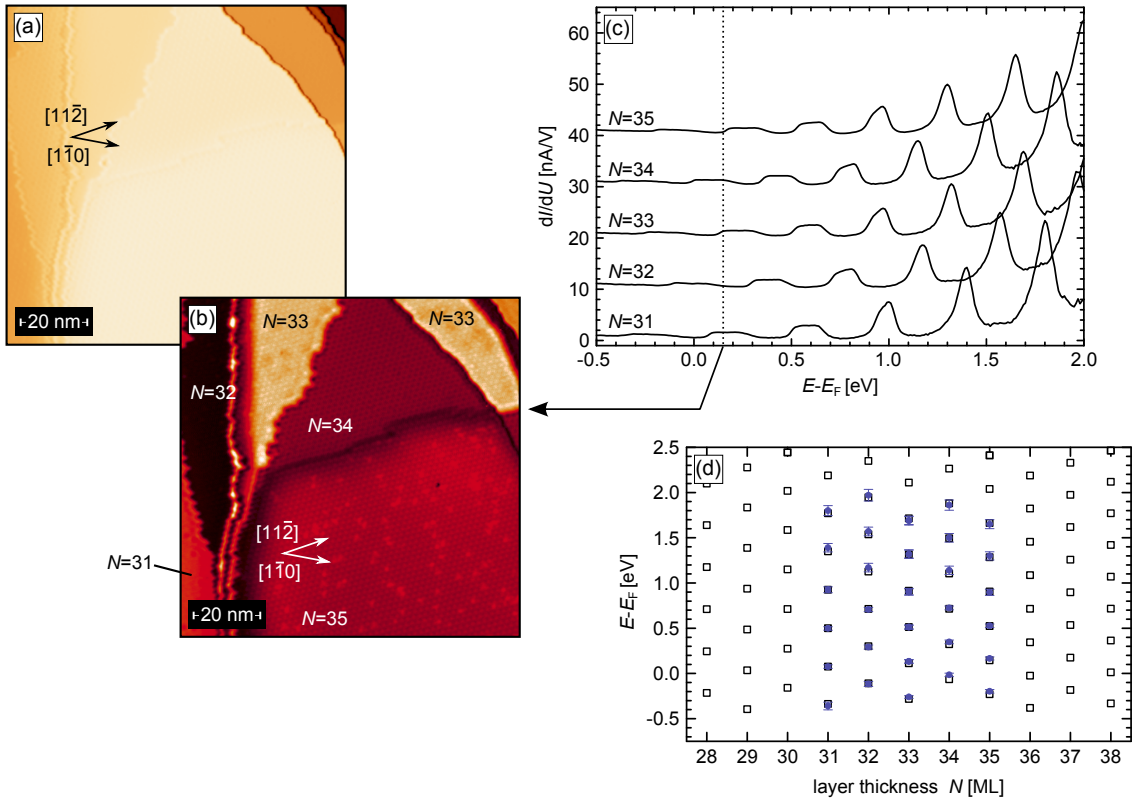

Figure 7.15: (a) A $100 \times 100\,\text{nm}^2$ area of Pb deposited on Ag(111). (b) The corresponding $\mathrm{d}I/\mathrm{d}U$ at $U = +150\,\text{mV}$ map shows different contrasts for different Pb layer thicknesses, revealing a buried Ag step edge. The dashed line in the STS spectra in (c) represents the energy of (b). The spectra do not provide the sharp peak-like structures at energies below $(E - E_F) \approx 1\,\text{eV}$, but resemble a plateau-shape with a steplike onset and descent. The layer thickness is determined again by the experimentally observed solutions (blue data points) in comparison to numerically solved values (open squares) in (d), that shows the best match between experiment and theory (see text for details).

been extracted out of the spectra and plot in Fig. 7.15(d) in order to determine the layer thicknesses. The peak-like solutions have been fit with Lorentzian profiles in analogy to the solutions in Fig. 7.14. The solutions for the plateau-type features have been extracted from their steplike onsets (the rising flank of the plateaus) [114]. For this purpose the numerical $\mathrm{d}^2I/\mathrm{d}U^2$ were calculated for the onset and the maxima in $\mathrm{d}^2I/\mathrm{d}U^2$ have been fit with Lorentzian. The assignment of the experimental data (blue circles) and the theoretical values (open squares) gives the best agreement with layer thicknesses between $N = 31 - 35$ (labeled in Fig. 7.15(a)).
The different appearances in STS, i.e. plateau-shape vs. peak-like, are discussed in the following. The dispersion $E(k_{||})$ can be modeled very well with the approach of

$$E_{\mathrm{QWS}}(k_{||}) = \alpha k_{||}^2 - \beta k_{||}^4 \tag{7.2.1}$$

with $\mathrm{sgn}\alpha = \mathrm{sgn}\beta$[6]. This approach can be understood as a Taylor expansion of a cosine function taking terms up to $k_{||}^4$ into account, since the inclusion of a term $\propto k_{||}^4$ can model the downward dispersing branch. Rewriting the formula similar to the Rashba case in Sec. 5 leads to

$$E_{\mathrm{QWS}}(k_{||}) = -\beta \left(k_{||}^2 - k_c^2\right)^2 + \frac{\alpha^2}{4\beta} \tag{7.2.2}$$

with the momentum vectors of E_{c} at $k_{\mathrm{c}} = \pm\sqrt{\frac{\alpha}{2\beta}}$. In contrast to the Rashba case, there is an additional exponent 2 within the brackets. Calculating $\mathrm{d}E_{\mathrm{QWS}}/\mathrm{d}k$ leads to:

$$\frac{\mathrm{d}E_{\mathrm{QWS}}}{\mathrm{d}k} = -2\beta \left(k_{||}^2 - k_c^2\right) \cdot k_{||}, \tag{7.2.3}$$

hence the derivative contains a $k_{||}^3$ and $k_{||}$ dependent term.
In the band dispersion in Fig. 6.3(a) the downward dispersing branches lie far away from the center of the Brillouin zone, so neglecting large $k_{||}$ values is reasonable due to the exponential damping in $k_{||}$(see Eq. (2.1.20)). Therefore only the inner shell of the dispersion with the parabolic character is considered in Eq. (7.2.3), which yields

$$\frac{\mathrm{d}E}{\mathrm{d}k_{||}} = \frac{\hbar^2}{m^*}k. \tag{7.2.4}$$

Finally this results in $\rho = \frac{m^*}{2\pi\hbar^2} = \text{const.}$ reminiscent of the parabolic Ag(111) surface state discussed in Sec. 4.2. Qualitatively for energies higher than E_{c} no further states can be observed, leading to a drop-off at the band maximum. Combining both features for the QWS leads to plateau-shaped signals in STS, whereas their energetic widths are assigned to the respective ΔE values. This model reproduces indeed the observed plateau-like QWSs for energies $E \leq 1\,\mathrm{eV}$ with widths up to 200 meV. However, it is visible in all spectra, that the plateaus get narrower in energy ($\Delta E \approx 50 - 100\,\mathrm{meV}$) for higher QWS solutions at energies between $E = 0.7 - 1.0\,\mathrm{eV}$ and at the same time a shoulder evolves at the upper

[6] α is the usual parabolic electron dispersion part with $\alpha = \frac{\hbar^2}{2m^*}$.

drop-off, which is associated to E_c. For energies $E \geq 1.0\,\mathrm{eV}$ the QWS solutions show a clear peak-shape.
The origin of the peak-shapes in the spectra have been assigned to Van-Hove like singularities by the authors of Ref. [131] with the assumption of $E(k_{||}) \approx (k - k_c)^2$ around E_c, which deviates from the description in Eq. (7.2.2). The $(k - k_c)^2$ approximation yields the E_- branch solution of a Rashba-split parabola and should accordingly generate asymmetric peaks for all QWS solutions without exception (see Eq. (5.5.13)). This is however definitely not the case in the observed spectra of Pb thin films in this work and other studies [114,136], since plateau-shaped features exist for lower QWS solutions and also the peak-like QWS solutions do not feature asymmetric peak-shapes.
An explanation for the peak-like appearance is addressed to the flattening of the m-shape dispersion in energy with increasing quantum number. A flattening leads to a reduced slope in $E(k_{||})$ and subsequently to a strong enhancement of the DOS since $\rho \propto (\frac{\mathrm{d}E}{\mathrm{d}k_{||}})^{-1}$. Due to the flattening the value of ΔE diminishes gradually leading to an energetic narrowing of the QWS in STS until finally the steplike band onset is buried completely under the peak. This model is able to describe the experimentally observed spectra in Fig. 7.15(c) very well. The interpretation as Van Hove-like singularities in Ref. [131] is not able to explain the plateau-shaped signals and thus it is not a suitable description.
The dispersion is now investigated by means of quasi-particle interference. If the bands provide a delocalized character it should be possible to detect scattering events. Therefore a series of $\mathrm{d}I/\mathrm{d}U$ maps has been performed in the energy range between $E = -70\,\mathrm{meV}$ and $E = 150\,\mathrm{meV}$ on the surface area of Fig. 7.15(a). Figure 7.16(a) shows zoomed spectra of $N = 32, 34$, both layers exhibit one QWS in this energy range with a steplike rise. If the free-electron approach is valid quasi-particle interferences are expected in the whole observed energy range for $N = 32$ which provides a band onset of $E_{0,\mathrm{STS}} = -(116 \pm 28)\,\mathrm{meV}$ and interferences should arise for $N = 34$ above its band onset $E_{0,\mathrm{STS}} - (15 \pm 19)\,\mathrm{meV}$. The setpoints of the displayed $\mathrm{d}I/\mathrm{d}U$ maps in Fig. 7.16(b-g) are marked with dashed lines in Fig. 7.16(a), the black arrows are pointing to the corresponding $\mathrm{d}I/\mathrm{d}U$ maps.
Indeed the layer thickness of $N = 32$ shows quasi-particle interferences for all energies with decreasing wavelength. Sweeping the energies up indicates larger scattering vectors q for higher energies. The trigonal domain with $N = 34$ gives the faint impression of a beginning interference at $(E - E_F) = -30\,\mathrm{meV}$ (Fig. 7.16(d)). Compared to the STS spectrum in (Fig. 7.16(a), upper spectrum) this is on the very onset of QWS. Increasing the energy in Fig. 7.16(e-g) clearly reveals quasi-particle interferences on the trigonal terrace. The characteristic shows shrinking wave lengths with increasing energy. Assuming simple backscattering with $q = 2k_{||}$ the wave vectors $k_{||}$ have been extracted by means of a real space analysis. A 2D-FFT evaluation was not possible due to the comparably weak scattering. The obtained wave vectors $k_{||}$ are plot in Fig. 7.17(a) for both QWSs (black circles). The observed scattering channels are assigned to a scattering within the free electron-like part of the dispersions as indicated with the arrows in Fig. 7.17(b), which represents a schematic band dispersion. The blue lines in Fig. 7.17(a) depict parabolic fits

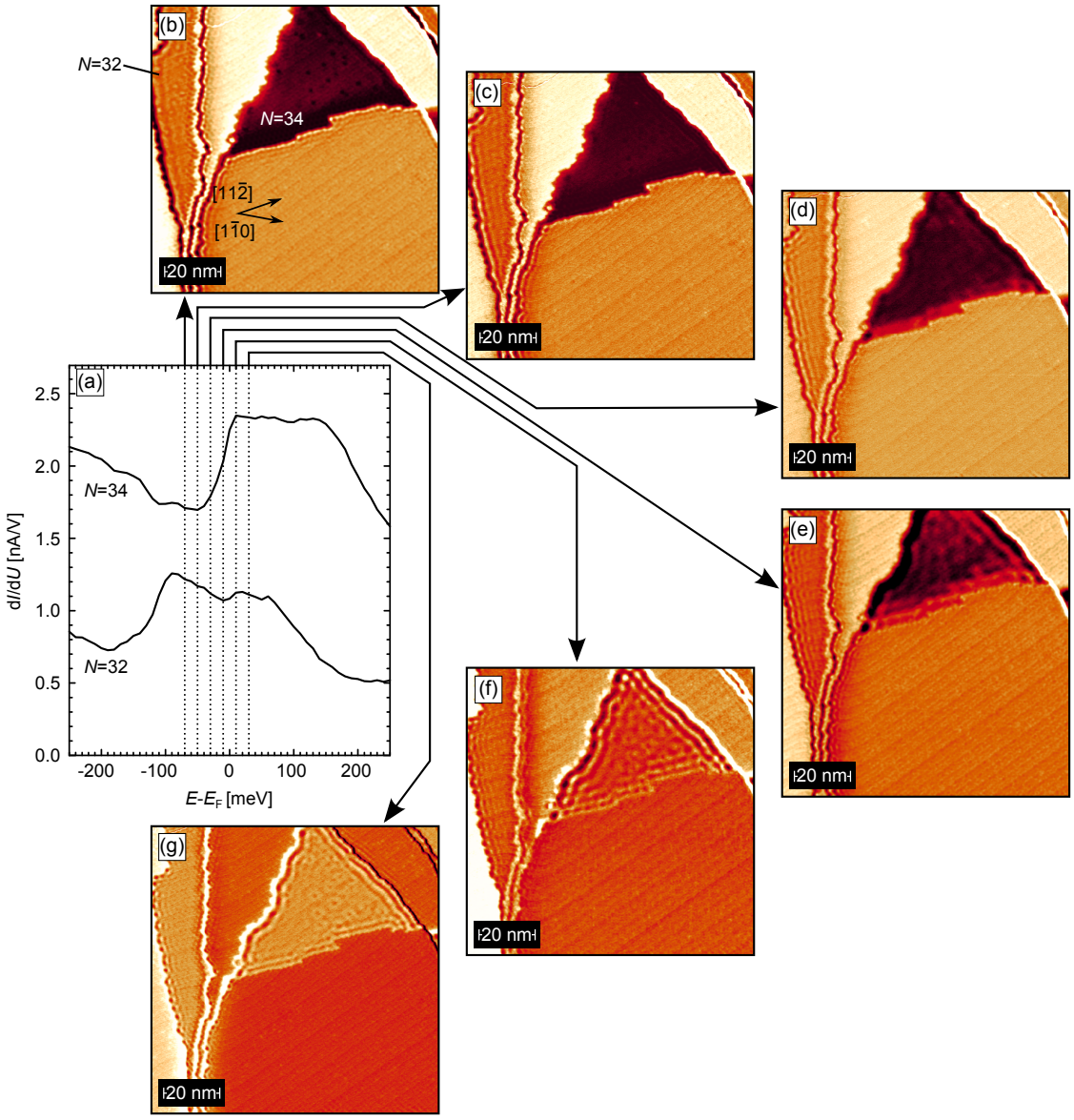

Figure 7.16: (a) Close-up STS spectra of $N = 32$ and $N = 34$, the steplike onset of each QWS is clearly visible. The dashed lines mark energies of $\mathrm{d}I/\mathrm{d}U$ maps in (b) at $U_{\mathrm{set}} = -70\,\mathrm{mV}$, (c) at $U_{\mathrm{set}} = -50\,\mathrm{mV}$,(d) at $U_{\mathrm{set}} = -30\,\mathrm{mV}$,(e) at $U_{\mathrm{set}} = -10\,\mathrm{mV}$, (f) at $U_{\mathrm{set}} = +10\,\mathrm{mV}$, and (g) at $U_{\mathrm{set}} = +30\,\mathrm{mV}$. The $\mathrm{d}I/\mathrm{d}U$ maps reveal quasi-particle interferences on the respectively surfaces, that follow a NFE character - whereas $N = 32$ exhibits interferences in the whole energy range in agreement with the spectrum in (a), quasi-particle interferences for $N = 34$ start in (d), which is barely on the onset of the QWS in the corresponding spectrum (see text for details).

to the data and yield band onsets of $E_{0,32} = (-145 \pm 12)\,\mathrm{meV}$, $E_{0,34} = (-15 \pm 4)\,\mathrm{meV}$ and effective electron masses of $m^*_{32} = (0.75 \pm 0.07)\,m_e$ and $m^*_{34} = (1.23 \pm 0.08)\,m_e$. Within the accuracy of the data the band onsets determined by STS and quasi-particle interferences agree very well, confirming the approach of $q = 2k_{||}$.

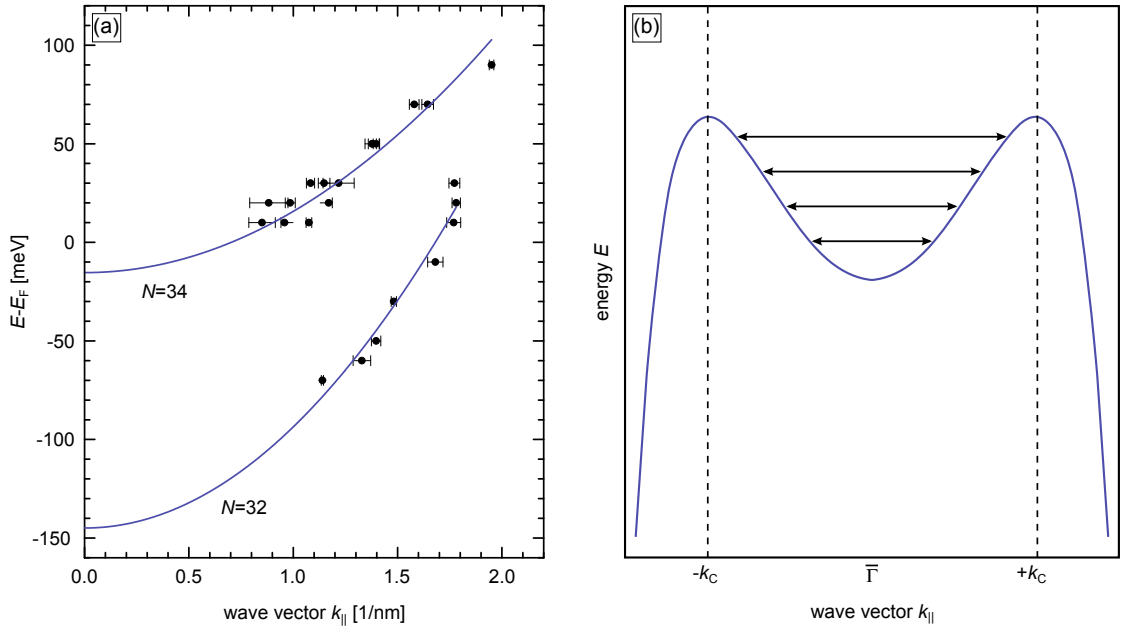

Figure 7.17: (a) Dispersion of wave vectors $k_{||}$ as extracted from the series of quasi-particle interference maps shown in Fig. 7.16 for the even layer thicknesses $N = 32, 34$. The blue lines represent parabolic fits to the data with $E_{0,32} = -(145 \pm 12)\,\text{meV}$, $E_{0,34} = -(15 \pm 4)\,\text{meV}$ with effective masses of $m^*_{32} = (0.75 \pm 0.07)\,m_e$ and $m^*_{32} = (1.23 \pm 0.08)\,m_e$. (b) The scattering events can be assigned to a scattering within the free electron-like part of the m-shape dispersion as indicated with the black arrows. Scattering between the downwards dispersing branches could not be observed.

Hence QWSs feature indeed a delocalized 2D character on the surface. Remarkably, scattering from the downward dispersing branches has not been observed. This can be explained in the context of the exponential damping of $k_{||}$ as the downward dispersing branches are located much further away from $\overline{\Gamma}$ than the free electron like branch, which can conceal any possible scattering from the downward dispersing branches. Also, as already mentioned, the scattering was evaluated in real space and therefore a second wave vector can also be missed.

Summarizing, the strong quantum character of Pb films on Ag(111) could be observed up to layer thicknesses of $\approx 100\,\text{ML}$. The shape evolution of the QWSs in the spectra could be explained by the inclusion of a $\propto k^4$ dependent term to the band dispersion $E(k_{||})$ and the flattening of the dispersion in the central parabolic part for higher solutions. Quasi-particle interference maps revealed that indeed the Pb/Ag QWSs feature a 2D parabolic dispersion on the surface with a delocalized nearly free electron-like character near $\overline{\Gamma}$.

7.3 The Rashba type spin-split surface of Pb/Ag(111)

As discussed in Sec. 5.4 the $(\sqrt{3} \times \sqrt{3})$Pb/Ag(111)$R30°$ surface, which structurally forms the same alloy as Bi/Ag(111) [138], has been studied to a far lesser extent. Since Pb has one p electron less than Bi, the bands are shifted upwards with respect to the Fermi level and DFT calculations predicted two spin-split states above the Fermi level [24] (see Fig. 5.4). As a result the bands relevant for the surface Rashba effect are mostly unoccupied and thereby largely inaccessible by ARPES [25, 27, 36, 37]. The positions of these Rashba states was found to critically depend on the vertical relaxation of the Pb atoms relative to the Ag atoms, leading to two distinct scenarios (see Fig. 5.4). In the first case with $\Delta_z = 0.97\,\text{Å}$ (Fig. 5.4(b)), the band dispersion exhibits a hybridization of both bands close to the onset of the lower Rashba band at about 1 eV above the Fermi level. However, this band position disagrees with ARPES measurements [36], where the extrapolated binding onset differs by $\approx 400\,\text{meV}$ from the DFT result. This offset is indicated by the blue shaded area in Fig. 5.4(b).
In order to improve the agreement between experiment and theory the relaxation value was tuned to $\Delta_z = 0.67\,\text{Å}$ [24] (see Fig. 5.4(c)). Under these conditions, the band structures obtained from constraint DFT calculations agree well with ARPES data [36] and the characteristically shaped van-Hove–like singularity which appears in STS spectra at 654 meV above the Fermi level [25]. The smaller relaxation of the Pb atoms results in a larger inter-band spacing and the absence of any hybridization between the upper and the lower band. Since both models result in a very similar dispersion below the Fermi-level the two different models can not be distinguished by ARPES measurements. In the case of Fig. 5.4(b) the branches observed below E_F in Fig. 5.4(a) would belong to two different surface states with a strong spin splitting, in the case of Fig. 5.4(c) both branches would originate from the same Rashba-split surface state with a smaller splitting. Experimentally even smaller outward relaxations of $\Delta_z = (0.46 \pm 0.06)\,\text{Å}$ have been reported [28], pointing towards the model presented in Fig. 5.4(c). Thus, the exact band positions, splitting strengths and electronic properties will be investigated in the following.

7.3.1 Spectroscopy

In order to illuminate the so far unclear band dispersion, an averaged STS spectrum (black dots) of the crucial energy range is presented in Fig. 7.18, the blue lines represent fits to the data. The $(\sqrt{3} \times \sqrt{3})$ Pb/Ag(111)$R30°$ surface alloy was prepared as described in Sec. 7.1.1. The spectrum shows two asymmetric peaks in the unoccupied energy range which are assigned as spectroscopic fingerprints of two Rashba-split surface states as discussed in Sec. 5.5 [25].
In order to achieve information about E_0 and ΔE_R, the spectra are simulated within the

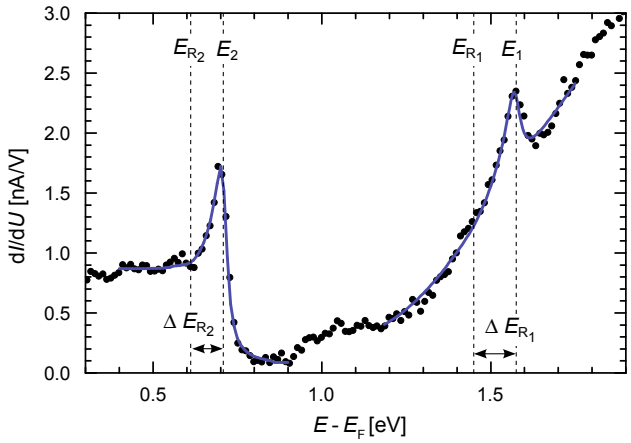

Figure 7.18: Tunneling spectrum (black dots) of the $(\sqrt{3}\times\sqrt{3})$ Pb/Ag(111)$R30°$ surface alloy. Two Rashba-type peaks are identified at $E_1 = (1580 \pm 5)$ meV with $\Delta E_{\mathrm{R}_1} = (130 \pm 10)$ meV and $E_2 = (710 \pm 5)$ meV with $\Delta E_{\mathrm{R}_2} = (80 \pm 10)$ meV (set point: $I_{\mathrm{set}} = 1$ nA, $U_{\mathrm{set}} = -1$ V, $\nu = 789$ kHz). The blue lines represent fits to the peaks (see text for details).

Tersoff-Hamann model [25, 47, 161] using the tunneling current integral

$$I \propto \int_{E_\mathrm{F}}^{E_\mathrm{F}+V} \rho_\mathrm{t}(E-V)\rho_\mathrm{s}(E)T(E)\,dE. \tag{7.3.1}$$

The transmission probability T and tip DOS ρ_t have been set constant. For ρ_s the Rashba DOS from Eq. (5.5.13) has been used slightly modified for a hole-like downbending Rashba-split state

$$\rho(E) = \begin{cases} \frac{|m^*|}{\pi\hbar^2}\sqrt{\frac{\Delta E_\mathrm{R}}{E_0-E}} & , E_0 - \Delta E_\mathrm{R} < E < E_0 \\ \frac{|m^*|}{\pi\hbar^2} = \mathrm{const} & , E < E_0 - \Delta E_\mathrm{R}, \\ 0 & , \mathrm{else}. \end{cases} \tag{7.3.2}$$

The tunneling current integral was solved numerically and afterwards the numerical derivative $\mathrm{d}I/\mathrm{d}U$ was computed. Subsequently this expression was convoluted with a Lorentzian to include finite lifetimes and experimental broadening. Due to the fact that the energy resolution is limited by electronic noise (see Sec. 2.1.5) the used Lorentzian broadening was never smaller than 10 meV. However, this does not influence the interpretation of the results, since the Rashba splittings in the investigated sample systems $(\sqrt{3}\times\sqrt{3})$Pb/Ag(111)$R30°$ and $(\sqrt{3}\times\sqrt{3})$Bi/Ag(111)$R30°$ are in the range of about 100-200 meV, i.e. an order of magnitude larger than the energy resolution limit.

Following the described fitting procedure both peaks are very well described by the fits. For the p_x, p_y-derived state the fit results in $E_1 = (1580 \pm 5)$ meV and $\Delta E_{\mathrm{R}_1} = (130 \pm 10)$ meV. For the s, p_z- derived band $E_2 = (710 \pm 5)$ meV and $\Delta E_{\mathrm{R}_2} = (80 \pm 10)$ meV is obtained, i.e. slightly further away from the Fermi level than reported previously [25].

The energetic distance of both band onsets of $\Delta = 870$ meV leads to the conclusion that

the scenario in Fig. 5.4(b) with $\Delta_z = 0.97\,\text{Å}$ where both bands hybridize can be excluded as the energetic distance amounts to $\approx 520\,\text{meV}$ in the DFT dispersion, which is far to small compared to the experimentally observed value. Comparing the Rashba energy splittings one can find, that the p_x, p_y-derived state shows a rather good agreement between the experimental value of $\Delta E_{\text{R}_1} = (130 \pm 10)\,\text{meV}$ and $\Delta E_{\text{R}_1,\text{DFT}} \approx 140\,\text{meV}$ but the experimentally observed s, p_z splitting $\Delta E_{\text{R}_2} = (80 \pm 10)\,\text{meV}$ is considerably overestimated with $\Delta E_{\text{R}_2,\text{DFT}} \approx 170\,\text{meV}$.
Furthermore a hybridization gap should yield a shoulder in the spectrum around the energy where the hybridization gap opens. As has been pointed out in Ref. [107] a shoulder is ascribed to the opening of a hybridization gap which—as a result of the flat energy dispersion around the gap—leads to an enhanced DOS. Based on these observations the spectrum in Fig. 7.18 does not show any hint for hybridization of the two Rashba-split surface states on Pb/Ag(111).
On the other hand the band dispersion scenario for the reduced relaxation of the Pb atom $\Delta_z = 0.67\,\text{Å}$ in Fig. 5.4(c) is in qualitatively good agreement to the experimental data. The energetic distance between both band onsets amounts to $\approx 900\,\text{meV}$ in very good compliance to the observed value of $\Delta = 870\,\text{meV}$. Although the splitting strengths in the calculated band structure are slightly smaller than the experimentally observed values with $E_{\text{R}_1,\text{DFT}} \approx 90\,\text{meV}$ and $E_{\text{R}_2,\text{DFT}} \approx 50\,\text{meV}$, they give qualitatively the correct relation with a stronger splitting within the p_x, p_y-derived states compared to the s, p_z-derived bands.
Summing up the features observed by STS strongly support a band structure as proposed in Fig. 5.4(c) where both branches in the observed ARPES measurements in Fig. 5.4(a) originate from the s, p_z-derived Rashba-split surface state with a smaller splitting.

7.3.2 Quasi-particle interferences on step edges and ARPES

In this section the dispersion is investigated by means of quasi-particle interference in the bias range between $-900\,\text{meV}$ (occupied states) and $1600\,\text{meV}$ (empty states) with an increment of $50\,\text{meV}$. Fig. 7.19(a) shows the topography of the first sample area. Arrows indicate the crystallographic directions relative to the Pb overlayer, which are rotated by 30° with respect to the Ag(111) substrate, i.e. $\overline{\Gamma\text{K}}_{\text{Pb}} \parallel \overline{\Gamma\text{M}}_{\text{Ag}}$ and $\overline{\Gamma\text{M}}_{\text{Pb}} \parallel \overline{\Gamma\text{K}}_{\text{Ag}}$. The surface features atomically flat terraces which are separated by two step edges oriented along different crystallographic directions. Small domains of the Pb wetting layer on Ag(111) are visible on the step edges. Figures 7.19(b-f) show the interference patterns measured at this location at (b) $U = +387\,\text{mV}$, (c) $U = +187\,\text{mV}$,(d) $U = -163\,\text{mV}$,(e) $U = -263\,\text{mV}$, and (f) $U = -463\,\text{mV}$, respectively. In this energy range the p_x, p_y-and s, p_z- derived bands coexist. Standing waves parallel to step edges and around defects are clearly visible for all energies. It can be clearly seen, that the wavelengths of the observed scattering events decrease with decreasing energy, indicating a hole-like band.

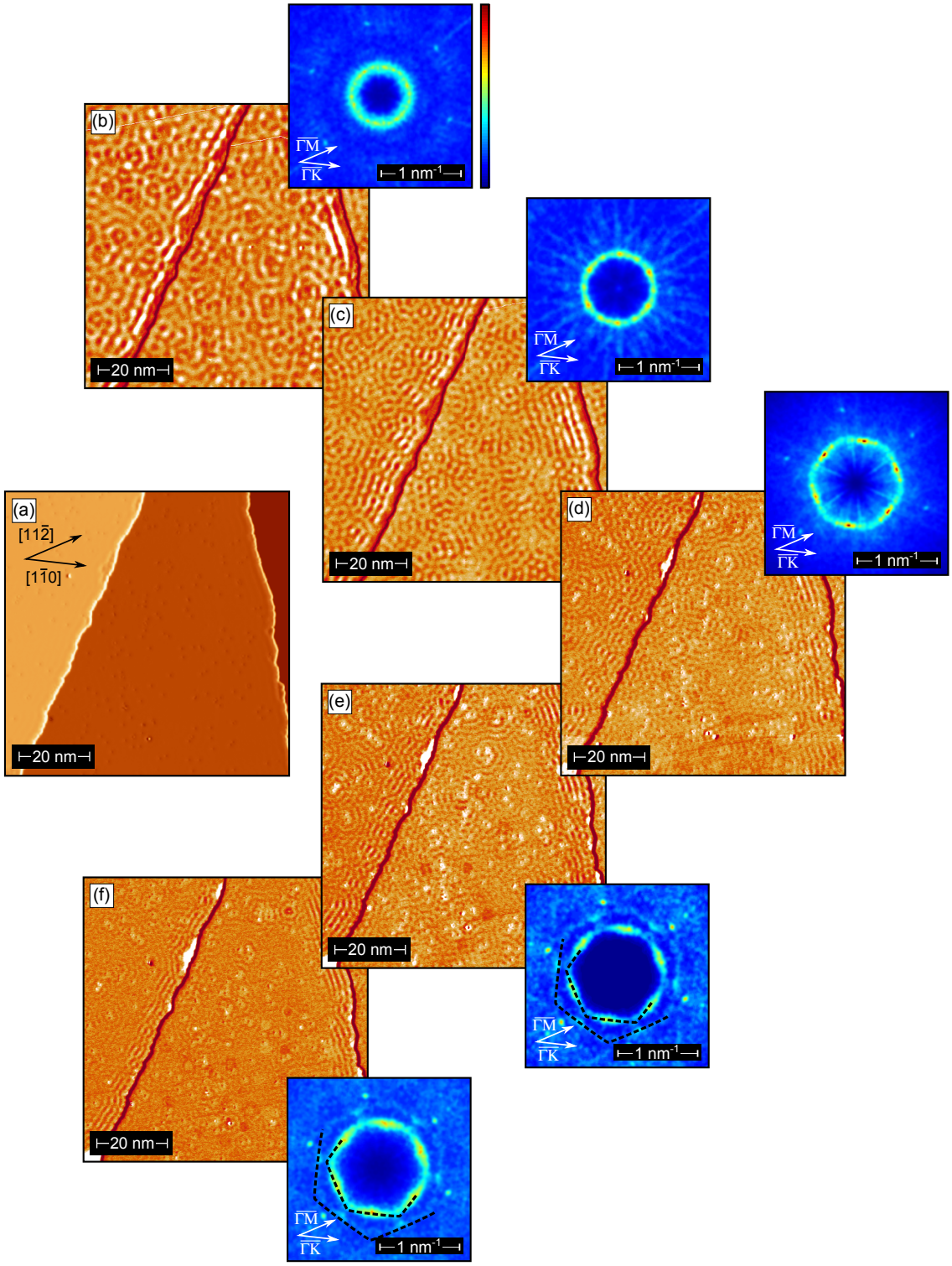

Figure 7.19: (a) $80 \times 80\,\mathrm{nm}^2$ constant-current image of the $(\sqrt{3} \times \sqrt{3})$ Pb/Ag(111)$R30°$ surface alloy. (b) $\mathrm{d}I/\mathrm{d}U$ map measured at $U = +387\,\mathrm{mV}$, (c) $U = +187\,\mathrm{mV}$,(d) $U = -163\,\mathrm{mV}$,(e) $U = -263\,\mathrm{mV}$, and (f) $U = -463\,\mathrm{mV}$. The insets of (b)-(f) show the corresponding symmetrized 2D-FFTs (see text for details).

The corresponding symmetrized 2D-FFT maps of the presented $\mathrm{d}I/\mathrm{d}U$ maps are shown in the insets[7]. The confinement of scattering events perpendicular to step edges consequently leads to higher intensities along those directions in the 2D-FFTs. Due to the symmetrization the higher intensities appear with a sixfold symmetry in the maps, which is a processing artefact and does not allow any conclusions about preferred or suppressed scattering directions as it is done e.g. for topological insulators [75, 76, 78, 79]. However, the benefit of symmetrized scattering maps is the considerably enhanced SNR (see Ref. [108] for the unsymmetrized 2D-FFT maps). Corresponding to the strong quasi-particle interferences in the $\mathrm{d}I/\mathrm{d}U$ maps all 2D-FFTs provide strong scattering events (bright turquoise frames). Starting at the highest setpoint ($U = +387\,\mathrm{mV}$) in Fig. 7.19(b) the 2D-FFT map reveals a circularly shaped frame. Decreasing the setpoint by 200 meV to $U = +187\,\mathrm{mV}$ yields the 2D-FFT in (c) which gives the impression of a slight but still rather vague deviation from a circular shape. A clear deviation from the circular shape is visible in (d) ($U = -163\,\mathrm{mV}$). The scattering event provides a hexagonally shaped frame with cusps pointing into $\overline{\Gamma\mathrm{K}}$ directions, which indicates an anisotropic dispersion induced by the hexagonal warping term discussed in Sec. 5.4. Besides a distinct dispersion of the scattering vector (q increases) the same scattering event with further enhanced hexagonal warping can be clearly observed in (e) and (f). Close inspection of the 2D-FFT maps in (e) and (f) reveals a second hexagon in both maps, which is slightly larger but much less pronounced. The latter hexagon is rotated by 30° with respect to the former, consequently pointing into $\overline{\Gamma\mathrm{M}}$ directions.

Due to a tip change the quasi-particle maps for determining the electronic properties of the p_x, p_y-derived state had to be measured on a different, second area of the same sample. In order to ensure that both areas exhibit the same electronic properties, both data sets overlap in energy. In fact, the dispersion relations are consistent. The constant-current STM topography of this area is shown in Fig. 7.20(a). Again, the surface features atomically flat terraces which are separated by two step edges. The patterns observed in Fig. 7.20(b-d) are not as strong and pronounced as the interference patterns in Figs. 7.19(b-f). The weaker interference patterns could be addressed to a reduced lifetime of electronic states which are energetically further away from the Fermi level [72, 73, 162, 163]. However, all three maps provide distinct scattering events, which can be clearly seen in the corresponding 2D FFTs (insets of Fig. 7.20(b-d)). The scattering vectors increase with decreasing energy, indicating a hole-like band. The highest setpoint at $U = 1237\,\mathrm{mV}$ in (b) exhibits a roughly circular shape, whereas a hexagonally shaped frame with cusps pointing into the $\overline{\Gamma\mathrm{M}}$ directions can be seen for (c)($U = 1137\,\mathrm{mV}$) and (d) ($U = 1037\,\mathrm{mV}$).
In addition to the observed quasi-particle interferences the step edges in Fig. 7.20(b-d) appear with an enhanced contrast (bright). A possible origin could be a scan artefact due to the finite time constant of the feedback loop. This results in a slight approach or withdraw of the tip to the sample when step edges are scanned upwards or downwards,

[7] The maps were symmetrized assuming a threefold symmetry for the substrate, which leads directly to a sixfold symmetry in the 2D-FFT as they are are rotational invariant under 180° rotations

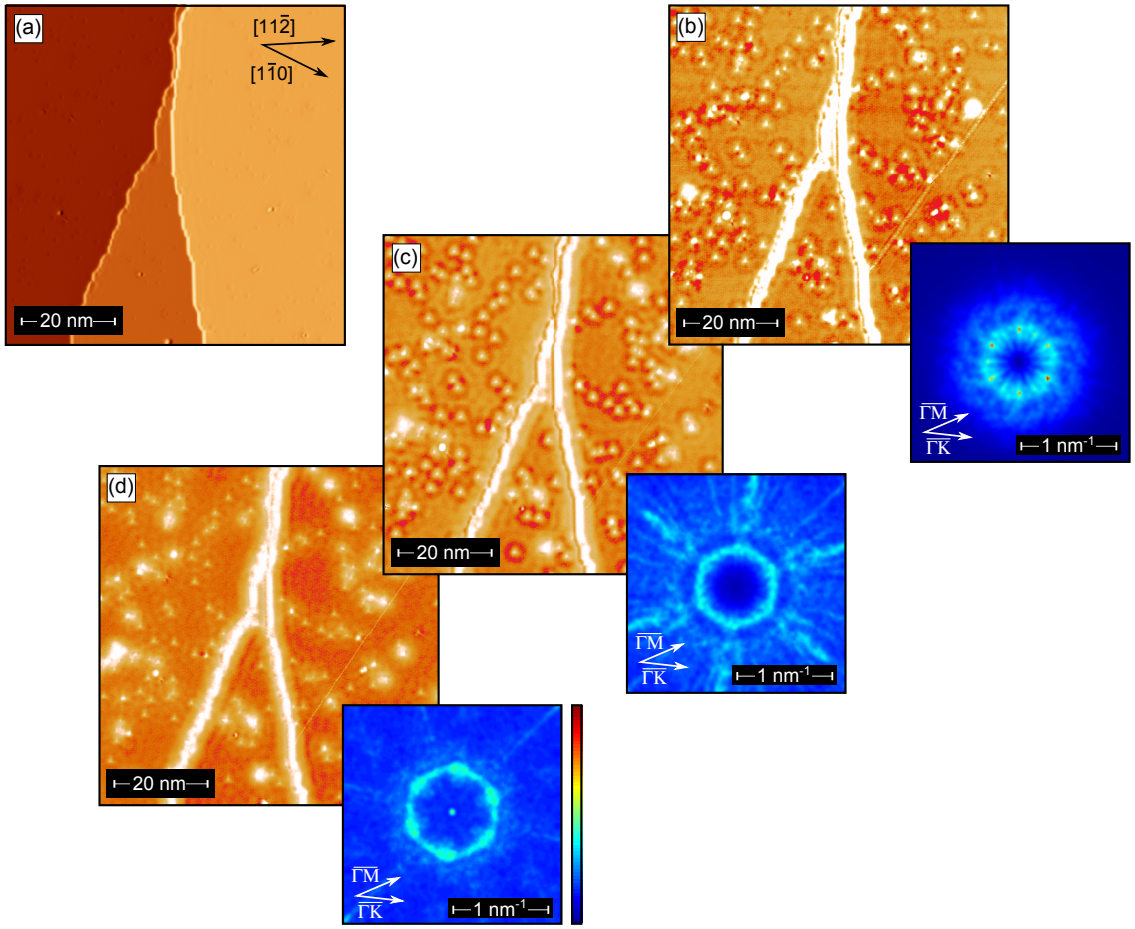

Figure 7.20: (a) $70 \times 70\,\mathrm{nm}^2$ Constant-current image of the $(\sqrt{3} \times \sqrt{3})$ Pb/Ag(111)$R30°$ surface alloy. Step edges as well as surface defects serve as scattering potentials. (b) $\mathrm{d}I/\mathrm{d}U$ map measured at $U = +1237\,\mathrm{mV}$, (c) $U = +1137\,\mathrm{mV}$, and (d) $U = +1037\,\mathrm{mV}$. The interferences appear considerably weaker compared to Fig. 7.19, which is justified by the larger damping due to energetic distance from the Fermi level. The insets of (b)-(d) show the corresponding symmetrized 2D-FFTs. Again the 2D-FFTs depict an anisotropic dispersion along $\overline{\Gamma K}$ and $\overline{\Gamma M}$ directions as result of the hexagonal warping (see text for details).

respectively. According to that the signal in the Lock-In channel is considerably enhanced or decreased and thus step edges appear brighter scanned upwards and darker scanned downwards in $\mathrm{d}I/\mathrm{d}U$ maps. A feedback artefact during the scanning procedure can be excluded since all presented images were scanned with fast direction from the higher to the lower terraces and should therefore lead to a dark appearance for the step edges (compare to Fig. 7.19(b-f)). Thus the bright step edge appearance indicates an edge charging effect at the presented energies.

The detailed analysis of the quasi-particle interference maps recorded over a wide range of bias voltages results in the extracted scattering vector $q(E)$ displayed in Fig. 7.21(a). Clearly, an energy dispersion of $q(E)$ can be observed for both Rashba bands. Four

different scattering channels can be identified, labeled D_1, D_2, D_3, and D_4, respectively. The illustrated hexagons represent the shapes of the scattering events as observed in the quasi-particle maps. The data measured along the $\overline{\Gamma K}$ and $\overline{\Gamma M}$ directions are plotted in red and black, respectively. Red and black lines depict corresponding fits to the data. Scattering within the p_x, p_y-derived band (labeled D_1 in Fig. 7.21) starts at about 1500 meV. The characteristic evolution of scattering vectors confirms the dominant role of intra-band scattering in this energy range indicating $q = 2k$ in this case. The dispersion was fitted with a cosine since it yields the best agreement to the experimentally observed scattering vectors (red and black lines in Fig. 7.21(a)). The band onset of the p_x, p_y-derived state is determined to $E_1 = (1556 \pm 44)$ meV and effective masses of $m^*_{\overline{\Gamma K}} = (-0.14 \pm 0.01) m_e$ and $m^*_{\overline{\Gamma M}} = (-0.15 \pm 0.001) m_e$ along the two high-symmetry directions. The effective masses have been determined by the parabolic contribution—extracted from a Taylor expansion—of the cosine function. The observed band onset is in good agreement with

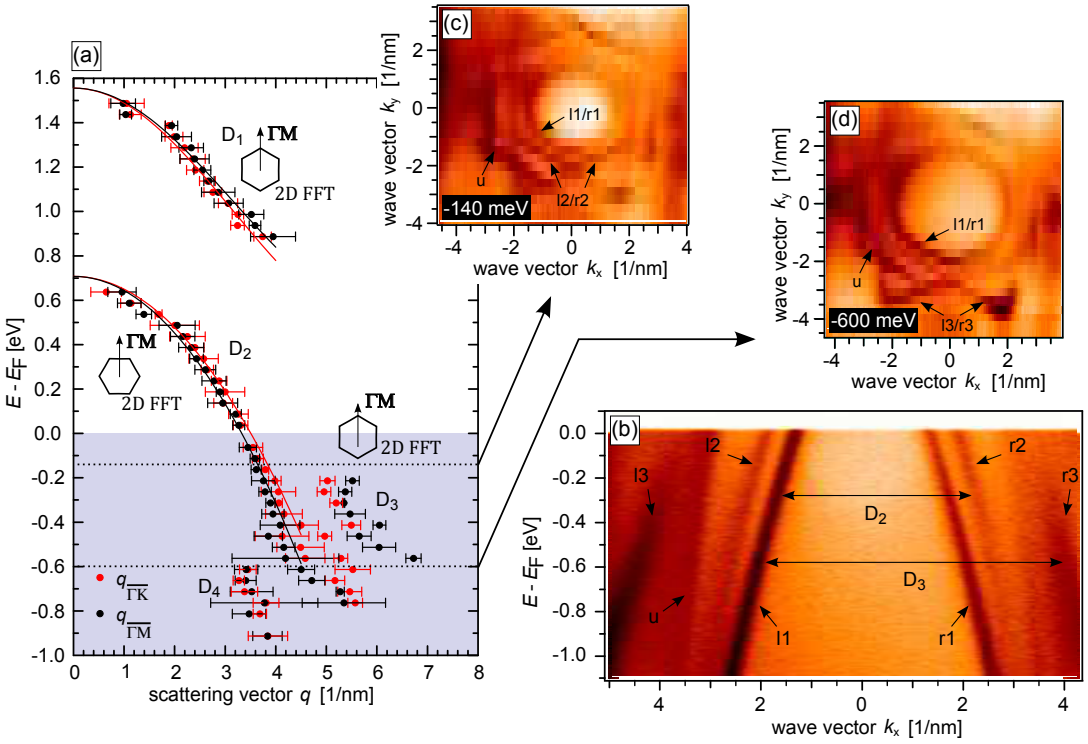

Figure 7.21: (a) Dispersion of scattering vectors q as extracted from two series of quasi-particle interference maps shown in Figs. 7.19 and 7.20. Data measured along the $\overline{\Gamma K}$ and $\overline{\Gamma M}$ directions are plotted in red and black, respectively. Respective lines are the results of fits of intra-band scattering events. (b) Electronic structure of $(\sqrt{3} \times \sqrt{3})$ Pb/Ag(111)$R30°$ as determined by ARPES. The measured band structure along $\overline{\Gamma M}$ consists of three surface bands labeled by r1-r3 (l1-l3) at positive (negative) wave vectors and a Ag(111) umklapp bulk band u. Panels (c) and (d) show CECs of the band structure at −140 meV and −600 meV as a function of both wave vector components k_x ($\overline{\Gamma M}$) and k_y ($\overline{\Gamma K}$) .

the STS spectrum presented in Fig. 7.18, thereby further confirming the model given in Fig. 5.4(c).

The analysis of the quasi-particle interference maps taken in the energy range of the s, p_z-derived bands turned out to be not as straightforward. Surprisingly, two and at some bias voltages even three scattering vectors appear (D_2, D_3, and D_4 in Fig. 7.21(a)). The shorter scattering vector D_2 can be assigned to intra-band scattering events within the s, p_z-branches. Fitting D_2 with a parabolic function leads to $E_2 = (708 \pm 22)\,\mathrm{meV}$, which is again in a good agreement with the STS data presented in Fig. 7.18. The effective masses are obtained to $m^*_{\overline{\Gamma K}} = (-0.166 \pm 0.005)\, m_e$ and $m^*_{\overline{\Gamma M}} = (-0.149 \pm 0.004)\, m_e$, which are slightly different from data obtained in Ref. [25]. The signal D_3 in the coexistence area shows the same anisotropy as the scattering events labeled D_1 for the p_x, p_y-derived state, indicating, that they are involved in the scattering. In order to compare the scattering vectors D_2–D_4 in the occupied electronic band structure of Pb/Ag(111) ARPES measurements are shown in Figs. 7.21(b)-(d)[8]. The ARPES data were collected with a hemispherical electron analyzer (Scienta R4000) and a monochromated He discharge lamp (MB Scientific) operating at an excitation energy of 21.22 eV (He Iα). The energy and angular resolutions were 7 meV and 0.3 °, respectively. The spectrum in Fig. 7.21(b) shows the band dispersion along the $\overline{\Gamma M}$ direction. In agreement with previous works [27, 36] three surface bands are identified with negative effective mass m^* which are labeled following the notation of Ref. [27]. In addition a bulk band u is visible which is back-folded due to the surface reconstruction [36]. The two inner bands originate from one Rashba-split surface band of mainly s, p_z orbital character with a momentum splitting of $2k_0 = 0.06(1)\,\text{Å}^{-1}$.

The momentum separation between r1 and l2 and the corresponding r2 and l1 branches is indeed in good agreement with the scattering vectors D_2 determined by STM and verifies the intra-band scattering fit above. The outer branches r3 and l3 correspond to another surface band of p_x, p_y character. For this band the ARPES data do not allow to deduce a finite momentum-splitting. Within the measured energy window the splitting $2k_0$ of the p_x, p_y-band is smaller than $\sim 0.04\,\text{Å}^{-1}$ and thus considerably reduced compared to the s, p_z-band. This finding is in line with DFT calculations (see Fig. 5.4(c) or Fig. 7.22(c)) which indicate only a very small splitting of the p_x, p_y-band below E_F. The scattering vectors labeled D_3 can then be assigned to scattering events between the bands l3 and r1 or between the corresponding bands r1 and l3. The origin of D_4 remains unclear, as no potential scattering vector from the ARPES data can be extracted that would quantitatively fit the periodicities observed in the quasi-particle interference experiments. A scattering between l1 and r1 can be excluded as D_4 is too small and also does not show a pronounced dispersion.

More detailed information about the dispersion of the surface bands within the full k-plane is obtained from the constant energy cuts in Fig. 7.21(c) and (d) that depict the photoe-

[8] The ARPES measurements have been performed by A. Buchter and Dr. H. Bentmann, Physikalisches Institut, Experimentelle Physik VII, Universität Würzburg, Am Hubland, D-97074 Würzburg, Germany

mission intensity at certain energies as a function of both wave vector components parallel to the surface, k_x and k_y. In Fig. 7.21(c) two inner contours are visible that correspond to the split s, p_z-band. Note that the contour originating from the branches l2 and r2 shows a hexagonal deformation. The cusps of the hexagonal contour point along the $\overline{\Gamma\mathrm{K}}$ direction, implying $m^*_{\overline{\Gamma\mathrm{K}}} > m^*_{\overline{\Gamma\mathrm{M}}}$ for the branches l2 and r2. The contour corresponding to the p_x, p_y-band (branches l3 and r3) is best visible in Fig. 7.21(d). Also in this case a significant hexagonal warping with cusps of the contour pointing along the $\overline{\Gamma\mathrm{M}}$ direction is visible. Hence, for the p_x, p_y-band one has $m^*_{\overline{\Gamma\mathrm{M}}} > m^*_{\overline{\Gamma\mathrm{K}}}$.
Obviously, ARPES finds anisotropies of the s, p_z- and the p_x, p_y-band which are rotated by 30° with respect to each other. This finding is in line with the STM results and DFT calculations [24]. Qualitatively, the same situation has also been found for other isostructural surface alloys, such as Bi/Cu(111) [31, 34], Sb/Cu(111) [34] and Sb/Ag(111) [38]. Within a tight-binding picture the rotated anisotropy of the two bands can be qualitatively understood under the assumption that a smaller effective mass corresponds to a larger orbital overlap. The orbital overlap for the p_x, p_y-band is then maximal along the direction connecting two neighbouring Pb atoms ($[1\bar{1}0]$ corresponding to $\overline{\Gamma\mathrm{K}}$). On the other hand, in the case of the s, p_z-band the orbital overlap is largest along the direction connecting a Pb atom with its neighbouring Ag atoms ($[11\bar{2}]$ corresponding to $\overline{\Gamma\mathrm{M}}$). Hence, for the p_x, p_y-band and the s, p_z-band the lateral atomic bonding appears to be dominated by Pb–Pb and Pb–Ag nearest neighbour interaction, respectively. With all parameters being determined the band model schematically represented in Fig. 5.4(b) can be excluded. Instead, the data are consistent with the smaller relaxation model sketched in Fig. 5.4(c), where no hybridization between the two Rashba bands takes part.

7.3.3 Spin polarization and DFT calculations

Up to this point the spin polarization of the involved bands has not been taken into account. By doing this two completely different interpretations are given and both may explain the observed scattering events.
The first interpretation, sketched in Fig. 7.22 (a-b) assumes that electronic states with opposite spin polarization are orthogonal and can not interfere (Fig. 7.22 (a)). Quantum interference patterns can only be observed if the spin polarizations of the involved states are parallel aligned (Fig. 7.22 (b)). Within this model the orbital angular momentum is also conserved. Remarkably, the model of spin-conversing scattering is commonly used in numerous scattering experiments performed with STM on spin-orbit–coupled surfaces [74–76, 78, 79]. However, applying this model to the observed scattering events indicates a conventional Rashba state for the s, p_z- as well as the p_x, p_y-derived state as shown in Fig. 7.22(c). This indication is in conflict with the findings of DFT calculations, which predict an unconventional spin topology for the p_x, p_y-derived state for the isostructural alloys Bi/Cu(111) [32], Bi/Ag(111) [24, 30], and Pb/Ag(111) [24]. Assuming unconventional p_x, p_y-derived states

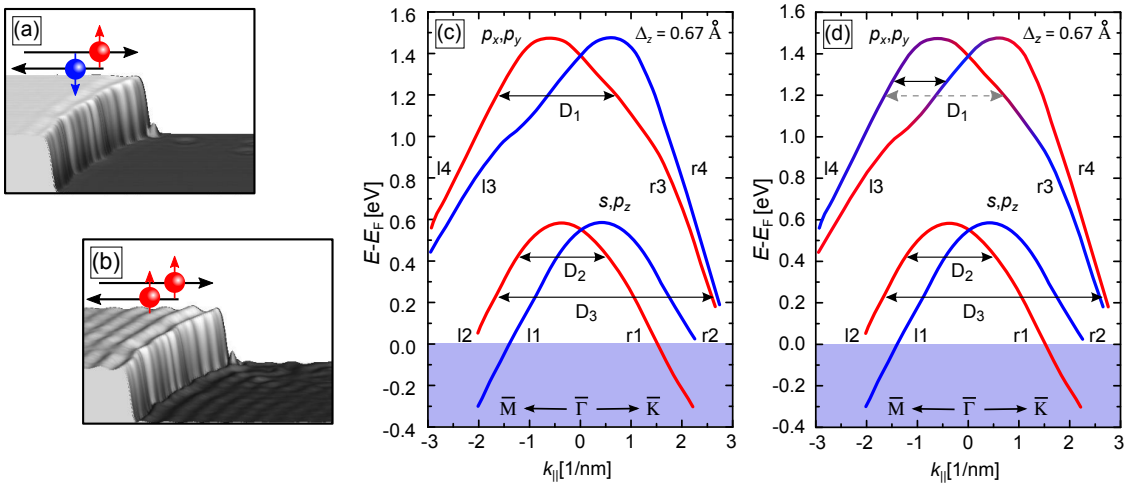

Figure 7.22: (a-b) An intuitive understanding of spin-dependent scattering [17]. Due to the orthogonality of antiparallel aligned spins spin-flip scattering leads to a vanishing interference (a). Only parallel spin polarizations contribute a constructive interference pattern on the surface (b). (c) The observed scattering vectors D_1, D_2, and D_3 lead to a conventional Rashba model within the model of spin-conservation for the Pb/Ag(111) surface. (d) Theoretically predicted unconventional spin texture in the p_x, p_y-derived state. A possible scattering channel for D_1 would give the indicated forwardscattering (black arrow) with a decreased scattering vector (grey arrow indicates the experimentally observed D_1).

according to the theoretically predicted spin polarization as shown in Fig. 7.22(d) should enable a forward scattering process as indicated with the black arrow. The resulting scattering vector should remain roughly constant with $q^* = 2k_0$ above E_F and can therefore be clearly distinguished from the observed scattering D_1 (indicated with the dashed grey arrow). However, such a constant scattering event has not been observed in the energy range of the p_x, p_y-derived state. Furthermore within this model D_1 connects bands with an antiparallel spin orientation which should lead to a vanishing interference.

In order to resolve this apparent contradiction between experiment and theory further DFT calculations have been performed, which consider the orbital angular momentum and lead to the second interpretation.[9]

Fig. 7.23(a) shows the calculated spin-resolved band structure of the Pb-derived states around E_F for a Pb relaxation of $\Delta_z = 0.67$ Å. It is clearly seen that the s, p_z states with a band onset at about 0.5 eV show a strong Rashba-type spin polarization (as well as the p_z states at 2.5 eV), while the p_x, p_y-derived bands, the band onset of which is at 1.5 eV, exhibit a more complex spin texture. In particular around the $\overline{\Gamma}$-point the polarization decreases rapidly and even exhibits a reversal of the spin direction at some k-points. As the p_x, p_y bands show no direct crossing with the s, p_z-bands (in contrast to the Bi/Ag(111) case and the Pb/Ag(111) with stronger relaxation), for larger k-values the spin direction

[9]The DFT calculations have been performed by Dr. G. Bihlmayer, Peter Grünberg Institut and Institute of Advanced Simulation, Forschungszentrum Jülich and JARA, 52425 Jülich, Germany

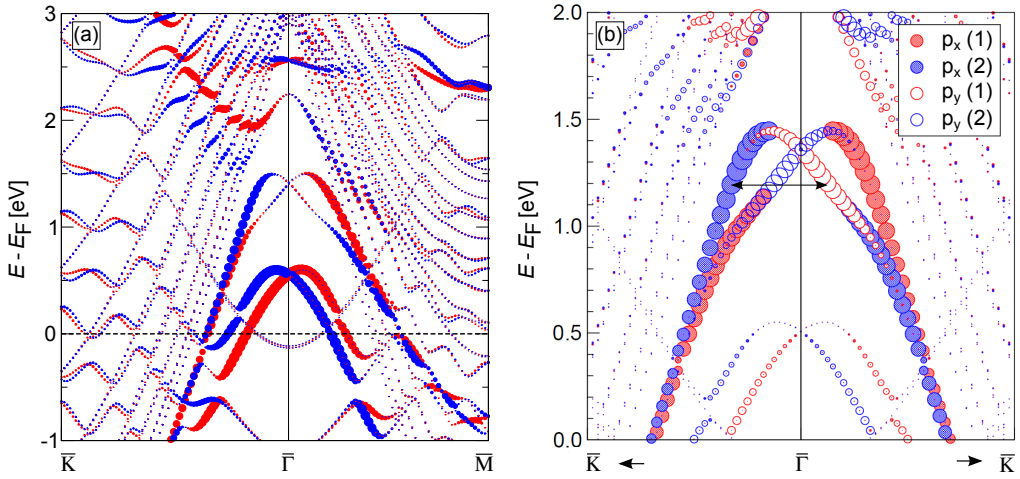

Figure 7.23: (a) Calculated band structure of the $(\sqrt{3}\times\sqrt{3})$Pb/Ag(111)$R30°$ surface alloy on a nine-layer Ag(111) film. The Pb relaxation is fixed at $\Delta_z = 0.67$ Å. Red and blue colours indicate the spin polarization with respect to a spin-quantization axis that is perpendicular to the k-vector and surface normal. (b) Spin- and orbital-resolved band structure of the $(\sqrt{3}\times\sqrt{3})$Pb/Ag(111)$R30°$ surface alloy. Open and full circles show contributions from p_x and p_y orbitals, respectively. The size of the symbols in (a) and (b) indicates the degree of spin polarization. The arrow indicates the experimentally observed D_1 scattering which is assigned as $\vec{J}$-conserving scattering channel.

reverses again and increases to larger momentum values.

To shed light on the origin of this loss of spin polarization near the $\overline{\Gamma}$-point the spin- and orbital-resolved band structure is shown in Fig. 7.23(b) focusing on the p_x and p_y states. Apparently, near the Brillouin zone the states consist of a mixture of p_x with one spin-orientation and p_y states of the opposite spin orientation. It is well known from hole-states in semiconductors that spin-orbit coupling at small momenta can lead to the formation of orbital-moment–carrying states (p_x, p_y) [164], while Rashba-type spin-orbit coupling dominates at larger k-values and forces the spin direction in-plane. Additionally, crystal-field effects decouple the p_x and p_y states according to the momentum direction.

Although an apparent decrease of spin polarization for the p_x, p_y states at small k-values is clearly visible in Fig. 7.23, the origin of this reduction can not be directly identified. In principle, also an increased out-of–plane component of the spin moment may lead to the same behaviour. This possibility was checked and no significant spin component along the surface normal was found, but rather a mixture of strongly in-plane polarized p_x and p_y orbitals with opposite spin polarization. Although the total spin polarization is dramatically reduced near the center of the Brillouin zone, the scattering from k to k, i.e. between time-reversal partners, is still prohibited by time reversal symmetry [87].

Finally, why is the intra-band scattering—as indicated by the arrow in Fig. 7.23(b)— allowed, despite the fact that initial and final states are dominantly of opposite spin character? The answer can be neither found in the conservation of the spin angular momentum $\vec{S}$ nor the orbital momentum $\vec{L}$, but in the conservation of the total momentum, $\vec{J} = \vec{L} + 1/2\vec{S}$.

Therefore a transfer of spin angular momentum $\vec{S}$ has to be compensated by an equivalent transfer of orbital momentum, $\vec{L}$. To check for possible constructive spin-flip scattering events the spin-orbit coupling Hamiltonian can be written as

$$H_{\mathrm{SOC}} = \xi \vec{L} \cdot \vec{S} = \xi l_z s_z + \frac{\xi}{2}(l^+ s^- + l^- s^+). \tag{7.3.3}$$

The first term represents the diagonal part of the matrix in Eq. (5.2.4) and represents spin-conservation, whereas the spin-flip part is represented by the second term (off-diagonal) containing the ladder operators $l^{+/-}$ and $s^{-/+}$, which ascent or descent the orbital and spin character, respectively [165].
Including the spin-conserving part of the H_{SOC} the interference expectation value can be written as

$$|\Psi|^2 \propto \langle \Psi_{\mathrm{i}} | \xi l_z s_z | \Psi_{\mathrm{f}} \rangle \,. \tag{7.3.4}$$

This term represents exactly the spin-conserving model that has been given before. But including the spin-flip part of H_{SOC} leads to

$$|\Psi|^2 \propto \langle \Psi_{\mathrm{i}} | \frac{\xi}{2}(l^+ s^- + l^- s^+) | \Psi_{\mathrm{f}} \rangle \,. \tag{7.3.5}$$

Due to the product of ladder operators ($l^{+/-} s^{-/+}$) the braket is only non-zero for spin-flip transitions that are accompanied by a simultaneous flip of angular orbital momentum. Loosely speaking, if $\Delta\vec{J} = \Delta\vec{L} + 1/2\Delta\vec{S} = 0$, a 180° reversal of spin $\vec{S}$ needs to be compensated by a 90° rotation of the orbital moment, i.e. from a p_x to a p_y orbital or vice versa.
Indeed, the scattering process indicated by the black arrow in Fig. 7.23(b) connects p_x to p_y orbitals of opposite spin and is therefore allowed according to Eq. (7.3.5). For the scattering within the s, p_z- derived band with equal spin-polarizations for initial and final states Eq. (7.3.4) is non-zero and allows for constructive interference.
A forward scattering process, as could be imagined in the $PbAg_2$ surface alloy between different bands of the same spin, can be excluded since it involves scattering from a p_x to a p_y orbital without a spin-flip and is neither allowed by Eq. (7.3.4) nor Eq. (7.3.5).
The interpretation of scattering events in terms of spin polarization of the involved bands can not be drawn from a plot of the spin polarization of the states alone (see Fig. 7.23(a)), since it is not directly possible to conclude about allowed or forbidden quasi-particle scattering events in systems with mixed orbital symmetries. Only in a simple case, i.e. when the involved states do not carry orbital moments (s, p_z, d_{z^2}), the Rashba picture of spin polarization holds and selection rules can be directly inferred. In the case of the Bi(110) surface analyzed in this way [74] this was meaningful, since the surface states of this surface are of p_z character. In the present system, however, such assignments are misleading, since—in addition to the spin—also the orbital character has to be taken into account.

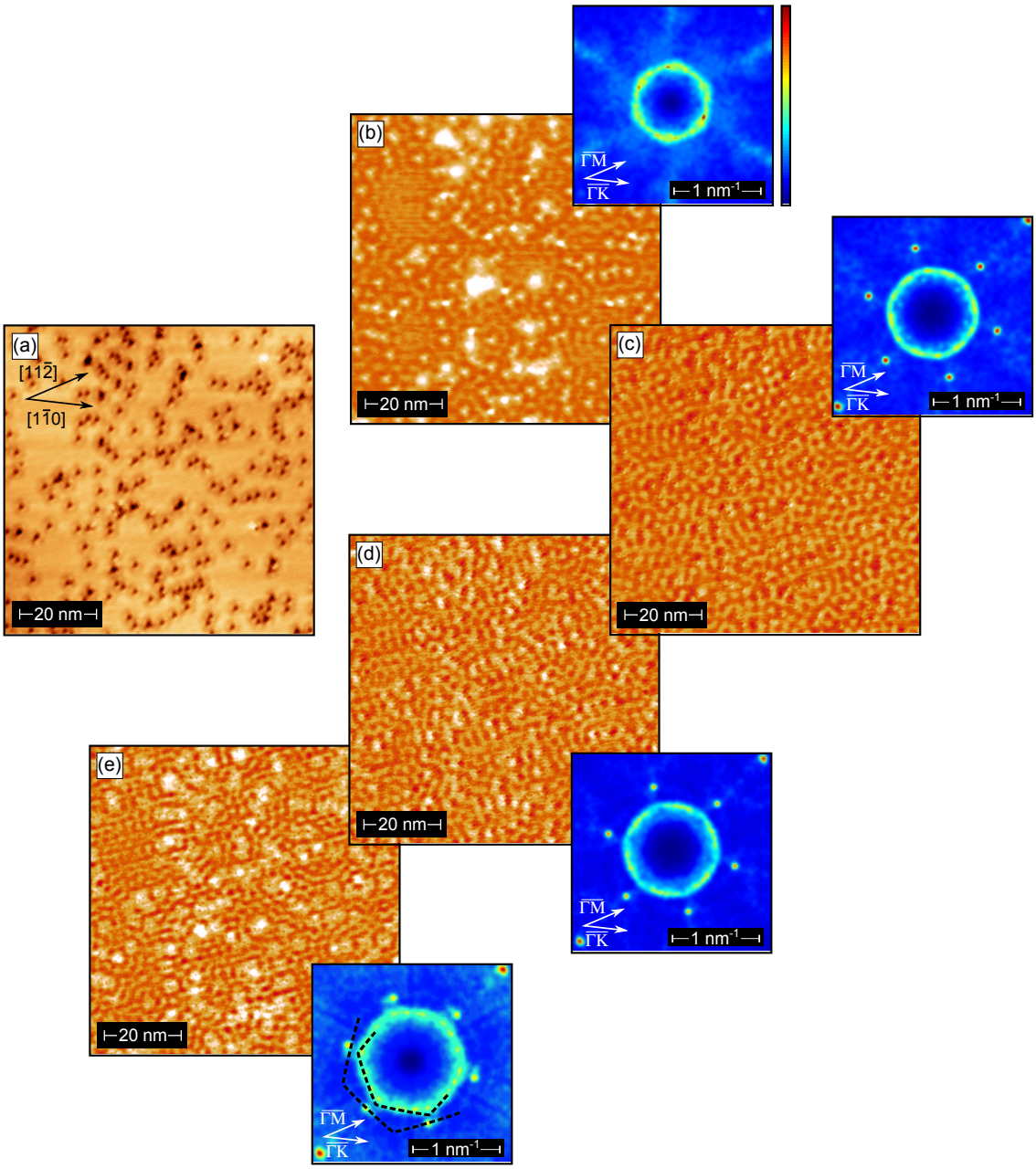

Figure 7.24: (a) $60 \times 60\,\mathrm{nm}^2$ Constant-current image of the $(\sqrt{3} \times \sqrt{3})$ Pb/Ag(111)$R30°$ surface alloy on a large terrace, the surface defects serve exclusively as scattering centers. (b) $\mathrm{d}I/\mathrm{d}U$ map measured at $U = 1087\,\mathrm{mV}$, (c) $U = +37\,\mathrm{mV}$,(d) $U = -63\,\mathrm{mV}$, and (e) $U = -263\,\mathrm{mV}$. All $\mathrm{d}I/\mathrm{d}U$ maps feature strong quasi-particle interferences. The insets of (b)-(e) show the corresponding symmetrized 2D-FFTs. The visible scattering events in the 2D-FFTs depict an anisotropic dispersion along $\overline{\Gamma K}$ and $\overline{\Gamma M}$ and show an excellent compliance to step edge scattering (see text for details).

7.3.4 Quasi-particle interferences on defects

Eventually the approach of step edge scattering is investigated and verified. Using step edges as scattering potentials confines the scattering—it bisects the 2D Brillouin zone—and could therefore lead to different results. In order to verify the approach of step edge scattering a series of quasi-particle interference maps is repeated on a flat surface in the same energy range. Figure 7.24 presents a $\mathrm{d}I/\mathrm{d}U$ series on a terrace. Figure 7.24 (a) shows the topography of the investigated area, step edges are at least 50 nm away from the surface area to suppress the influence of step edges. Figure 7.24(b-e) show $\mathrm{d}I/\mathrm{d}U$ maps, the insets show the corresponding symmetrized 2D-FFTs of the maps. In Fig. 7.24(b) ($U = 1087\,\mathrm{mV}$) the 2D-FFT depicts a hexagonally shaped frame pointing with the cusps into the $\overline{\Gamma\mathrm{M}}$ directions, which is—within the error bars—in perfect agreement to the observed intra-band scattering between the p_x, p_y-derived state for step edge scattering in Fig. 7.20(d) ($U = 1037\,\mathrm{eV}$). The sp_z- and p_x, p_y-derived bands coexist in the energy range of Fig. 7.24(c-e) ($U = +37\,\mathrm{mV}$, $U = -63\,\mathrm{mV}$, and $U = -263\,\mathrm{mV}$, respectively) and the 2D-FFT maps reveal the evolution of a hexagonally shaped frame pointing into $\overline{\Gamma\mathrm{K}}$ directions. This scattering can be assigned as intra-band scattering within the s, p_z- derived band. The size and orientation of the observed scattering events agree again excellent with the step edge scattering data in Fig. 7.19(d-e). Remarkably, also the second faint signal

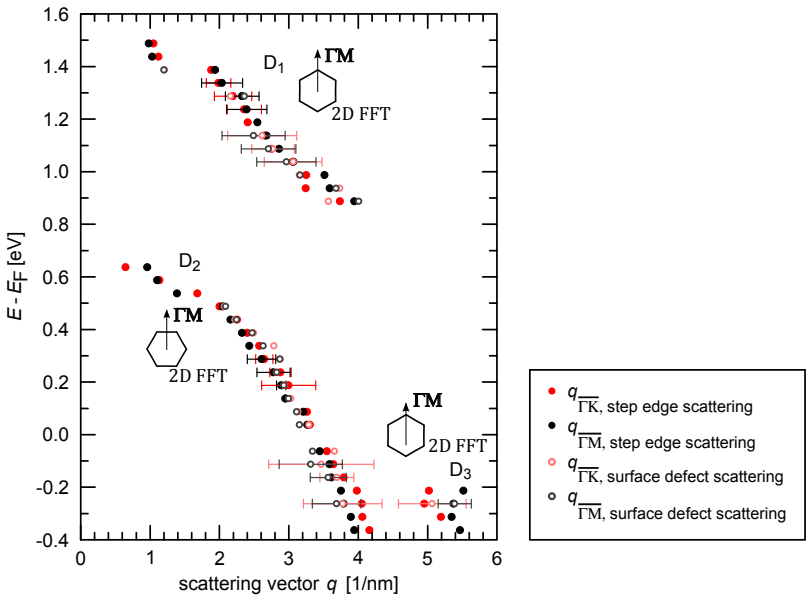

Figure 7.25: Dispersion of scattering vectors q as obtained by step edge scattering (red and black) and surface defect scattering (salmon and grey). The error bars are shown only partially for more clarity, all omitted error bars are comparable in size or smaller. As can be seen within in the accuracy of the data points the results obtained by step edge scattering and surface defect scattering show an excellent agreement. Due to the smaller scattering potential the surface defect scattering shows slightly less scattering events, but all scattering events D_1, D_2, and D_3 are observed.

in the 2D-FFT of Fig. 7.19(e) is visible in Fig. 7.24(e) (both maps have the same setpoint $U = -263\,\mathrm{meV}$). It is attenuated even more compared to the step edge scattering. This can be addressed to the fact, that step edges provide larger scattering potentials compared to defect scattering resulting in stronger reflections on the potential barrier and thus stronger interferences.

The extracted scattering vectors $q(E)$ of the quasi-particle interference maps recorded for step edge scattering and defect scattering are displayed in Fig. 7.25. The step edge scattering data are represented by filled circles in red ($\overline{\Gamma\mathrm{K}}$ direction) and black ($\overline{\Gamma\mathrm{M}}$ direction) and the defect scattering data are indicated with empty circles in salmon ($\overline{\Gamma\mathrm{K}}$ direction) and grey ($\overline{\Gamma\mathrm{M}}$ direction). Some exemplary error bars are shown, the others are omitted for more clarity within the plot. All omitted error bars are comparable in size or smaller. Obviously the two data sets have exactly the same characteristic within the accuracy of the data. It confirms that the step edge scattering does not influence the observed scattering events in this case. The benefit of step edges is as discussed above the higher scattering potential leading to enhanced quasi-particle interferences, which allows to detect the signals with higher accuracy.

Summarizing the $(\sqrt{3} \times \sqrt{3})$ Pb/Ag(111)$R30°$ surface has been investigated by means of STM/STS, ARPES, and DFT calculations in this section. Tunneling spectroscopy shows two characteristically shaped peaks in the empty density of states. These peaks are fit by thermally broadened van-Hove-like singularities and identified as signatures of Rashba-split bands. Tunneling spectroscopy and quasi-particle interferences allowed to reconstruct its band structure. Combining ARPES and STM allowed to assign scattering vectors in the occupied energy range, revealing inter-band as well as intra-band scattering events.

The scattering events can be interpreted by two different models, whereas the spin-conserving model led to a contradiction between indicated spin polarization and theoretically predicted topology. DFT calculations revealed that in order to evaluate the interference pattern of quasi-particle maps besides the spin also the orbital momentum of the involved electronic states has to be considered. Namely, constructive interferences for spin-flip scattering events may be allowed as long as the total momentum $\vec{J}$ can be conserved if it is accompanied by a corresponding change of angular momentum.

In conclusion STM measurements are not sensitive to distinguish between a spin-conserving scattering within states of pure symmetry or a $\vec{J}$-conserving scattering event of states with mixed orbital symmetries. Very recently a photoemission and inverse photoemission study reported about the same insensitivity for their experiments [166], which makes it impossible so far to give a secure statement of spin polarizations in spin-orbit–coupled systems with these methods.

Eventually the use of step edges as scatter potentials is approved by the comparison to defect scattering, which are absolutely compatible within the accuracy of the data.

7.4 The Rashba type spin-split surface of Bi/Ag(111)

Different to the $(\sqrt{3} \times \sqrt{3})$ Pb/Ag(111)$R30°$, which exhibits a mostly unoccupied band structure, the $(\sqrt{3} \times \sqrt{3})$ Bi/Ag(111)$R30°$ bands shift down in energy, since Bi has one p electron more than Pb. As a result the s, p_z-derived band is completely occupied, but the onset of the p_x, p_y-derived band is still in the unoccupied energy range (see Fig. 5.5). The electronic structure of the $(\sqrt{3} \times \sqrt{3})$ Bi/Ag(111)$R30°$ surface has been subject of numerous investigations [24, 27, 30, 33] and general consensus between experimental and theoretical works on the dispersion of the electronic bands has been reached, but the spin texture of the unoccupied energy range gives still rise to open questions.
Recently Hirayama *et al.* [29] observed pronounced oscillations in the unoccupied energy range which clearly showed an energy dispersion for the p_x, p_y-derived Rashba bands between the Rashba energy E_{R_1} and E_{F} indicating a conventional Rashba splitting within simple spin-conserving scattering. They observed no quantum interferences between E_{R_1} and E_1 which was interpreted to be a direct consequence of a conventional spin structure (see Fig. 7.29(a)), which—according to Ref. [29]—leads to forbidden backscattering between E_1 and the Rashba energy E_{R_1}. This observation stands in contradiction to the Pb/Ag(111) results presented in the previous section where scattering was clearly observed for the p_x, p_y-derived bands as well as for the s, p_z- derived band between the respective values for E_0 and E_{R}. Consequently, this issue needs further investigation. Also the p_x, p_y band onset was determined at about $(E - E_{\mathrm{F}}) = 0.6\,\mathrm{eV}$ in Ref. [29] with a rather blunt spectrum, that didn't feature the strong Rashba-type peak-shape in the DOS. However, the exact band positions, splitting strengths, quasi-particle interferences and spin polarization will be investigated in the following.

7.4.1 Spectroscopy

The $(\sqrt{3} \times \sqrt{3})$ Bi/Ag(111)$R30°$ surface alloy was prepared as described in Sec. 7.1.2. Figure 7.26 shows an averaged STS spectrum of the $(\sqrt{3} \times \sqrt{3})$ Bi/Ag(111)$R30°$ surface alloy, the blue lines represent fits to the data. Two asymmetric peaks can be identified, that can clearly be assigned to the s, p_z- (left side, occupied states) and the p_x, p_y-derived (right side, empty states) Rashba states [24, 30]. The intensity of the observed peaks is about one order of magnitude more intense than in Ref. [29]. The distinctly stronger STS signal might be addressed to the different measurement temperature (4.8 K vs. 77 K), a lower modulation amplitude, and/or a better surface quality as compared to the surface in Ref. [29] which was prepared on a 10 ML thick Ag(111) film on Si(111). This yielded in comparably small terrace sizes less than 25 nm, which were additionally disturbed by screw dislocations.
In order to extract information about the band onsets and splitting strengths the peaks in the averaged STS spectrum in Fig. 7.26 were fit according to the procedure described in Sec. 7.3.1. The agreement of the fit with the experimental data is particularly good for the

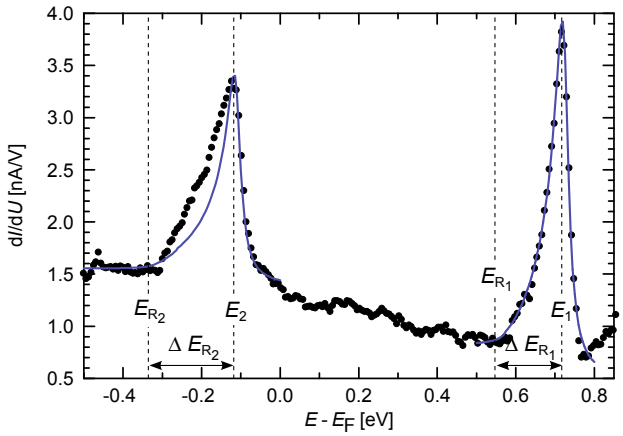

Figure 7.26: Tunneling spectrum (black dots) of the $(\sqrt{3} \times \sqrt{3})$ Bi/Ag(111)$R30°$ surface alloy. Two Rashba-type peaks are identified at $E_1 = (725 \pm 5)\,\mathrm{meV}$ with $\Delta E_{\mathrm{R}_1} = (150 \pm 10)\,\mathrm{meV}$ and $E_2 = -(110 \pm 5)\,\mathrm{meV}$ with $\Delta E_{\mathrm{R}_2} = (220 \pm 10)\,\mathrm{meV}$ (set point: $I_{\mathrm{set}} = 1\,\mathrm{nA}$). The blue lines represent fits to the peaks (see text for details).

p_x, p_y-derived band with $E_1 = (725 \pm 5)\,\mathrm{meV}$ with $\Delta E_{\mathrm{R}_1} = (150 \pm 10)\,\mathrm{meV}$. This value is considerably larger than the previously reported band onset of about $E_1 = 600\,\mathrm{meV}$ [29]. The overall agreement is also reasonable for the s, p_z- derived Rashba band, where the fit results in $E_2 = -(110 \pm 5)\,\mathrm{meV}$ and $\Delta E_{\mathrm{R}_2} = (220 \pm 10)\,\mathrm{meV}$ in agreement with earlier ARPES and STS data [23, 25, 100]. The energy distance between both Rashba band onsets amounts to $\Delta = 835\,\mathrm{meV}$ which is in good agreement to the theoretically predicted band structure with $\Delta_{\mathrm{DFT}} \approx 800\,\mathrm{meV}$ [24].
However, the fitting procedure for the s, p_z-derived states can not reproduce the shoulder which appears at the left flank of the peak. It was reproducible for different tips and samples and its origin can be addressed to the gap opening at the hybridization point of the two Rashba bands (see Fig. 7.28(b) and 7.29(a-b)). Without spin-orbit coupling the pure spin states of both bands were orthogonal and the bands could cross. Since the spin-orbit coupling in the Bi/Ag alloy is indeed strong, considerable spin-mixing occurs, resulting in the opening of a hybridization gap [24, 30]. This leads to a reduced band velocity and thereby enhances the DOS [167].

7.4.2 Quasi-particle interferences on step edges and ARPES

To obtain the energy dispersion a series of $\mathrm{d}I/\mathrm{d}U$ maps in the bias range between $-400\,\mathrm{meV}$ up to $+800\,\mathrm{meV}$ is performed (increment $50\,\mathrm{meV}$). Figure 7.27(a) shows the topography of the investigated sample area. It features atomically flat terraces which are separated by three step edges with different crystallographic directions. The arrows indicate the crystallographic directions relative to the Bi overlayer which are rotated by 30° with respect to the Ag(111) substrate, i.e. $\overline{\Gamma\mathrm{K}}_{\mathrm{Bi}} \parallel \overline{\Gamma\mathrm{M}}_{\mathrm{Ag}}$ and $\overline{\Gamma\mathrm{M}}_{\mathrm{Bi}} \parallel \overline{\Gamma\mathrm{K}}_{\mathrm{Ag}}$. Quasi-particle interference

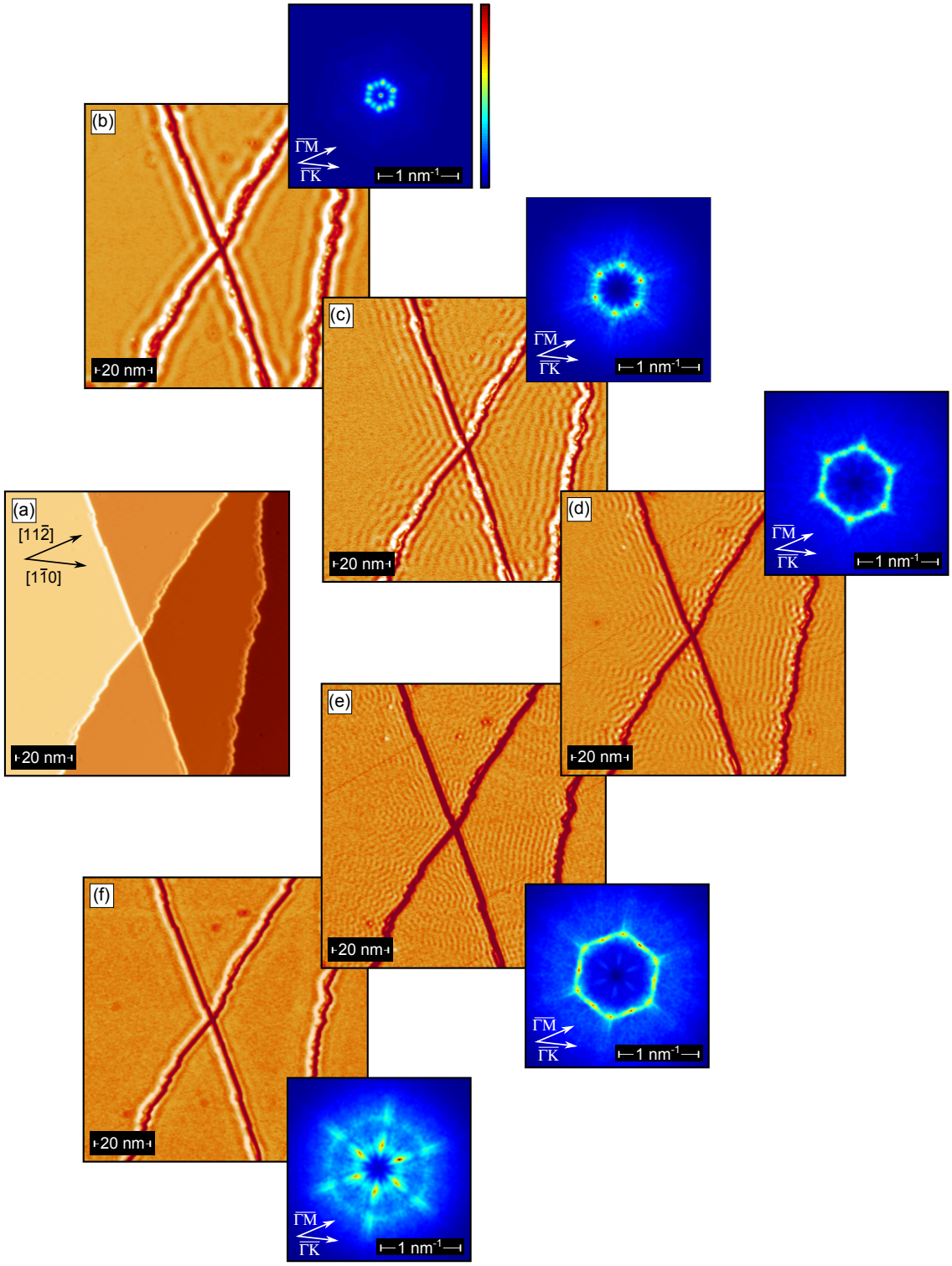

Figure 7.27: (a) $100\times100\,\mathrm{nm}^2$ constant-current image of the $(\sqrt{3}\times\sqrt{3})$ Bi/Ag(111)$R30°$ surface alloy with 4 different terraces heights. (b) $\mathrm{d}I/\mathrm{d}U$ map measured at $U = +587\,\mathrm{mV}$, (c) $U = +387\,\mathrm{mV}$,(d) $U = +187\,\mathrm{mV}$,(e) $U = +37\,\mathrm{mV}$, and (f) $U = -313\,\mathrm{mV}$. The insets of (b)-(f) show the corresponding symmetrized 2D-FFTs. (see text for details).

maps are shown in Fig. 7.27(b-f) for representative energies. Standing waves parallel to step edges are clearly visible for the maps in (b-e). Figures 7.27(b) and (c) show the interference patterns measured at $U = +587\,\mathrm{meV}$ and $U = +387\,\mathrm{meV}$, i.e. below and above the Rashba energy E_{R_1} of the upper Rashba band, respectively. Although the pattern above E_{R_1} is far less structured than the one below in both cases standing waves parallel to step edges are clearly visible. The 2D-FFT maps show clearly hexagonal frames with cusps pointing into $\overline{\Gamma\mathrm{M}}$ directions for both energies.

This observation is in contrast to Ref. [29], where the absence of an interference pattern above E_{R_1} was interpreted in terms of forbidden backscattering of a Rashba-split surface state. At this point it is important to note that the involved electrons occupy Bloch states. Therefore, k refers to the crystal momentum rather than the electron momentum and k itself is no longer suitable to determine if backscattering is allowed or not. Instead, the band velocity for Bloch states is defined as $v_n(E) = \frac{1}{\hbar}\nabla_k E_n(k)$ and one would expect that backscattering can occur between sections with positive and negative slope ∇_k, i.e. positive and negative band velocity. In contrast to the observations reported in Ref. [29] this is indeed possible below and above the Rashba energy.

Decreasing the energy in Fig. 7.27(d-e) shows, that the wavelengths of the observed interference patterns shrink and subsequently the scattering vectors q expand in the corresponding 2D-FFT maps, which indicates a hole-like band. A clear dispersion can be seen in the maps (b)-(e), which is the energy range where only the p_x, p_y-derived state exists. Comparing the 2D-FFT maps of (b)-(e) an evolution in the hexagonal warping can be clearly seen in accordance to the k^3 proportionality in Eq. (5.4.2). The $\mathrm{d}I/\mathrm{d}U$ map in Fig. 7.27(f) is recorded at $U = -313\,\mathrm{mV}$, which is considerably below the s, p_z-band onsets. Although the $\mathrm{d}I/\mathrm{d}U$ map shows only the faint impression of interference, the 2D-FFT map reveals obviously two coexisting scattering vectors. The shapes shows a faint warping with cusps pointing into $\overline{\Gamma\mathrm{M}}$ direction. It should be noted that the enhanced intensity spots stem from scattering perpendicular to step edges and their sixfold appearance is an artefact of the symmetrization as discussed in Sec. 7.3.

All extracted $q(E)$ values are displayed in Fig. 7.28(a). Clearly, an energy dispersion $q(E)$ can be observed for both Rashba bands. Three different scattering channels can be identified, labeled D_1, D_2, and D_3, respectively. The illustrated hexagon represents the shapes of the p_x, p_y scattering events as observed in the quasi-particle maps. The data measured along the $\overline{\Gamma\mathrm{K}}$ and $\overline{\Gamma\mathrm{M}}$ directions are plotted in red and black, respectively and red and black lines depict corresponding fits to the data.

Scattering within the p_x, p_y-derived band (labeled D_1 in Fig. 7.28) starts at about $+700\,\mathrm{meV}$. In the energy range between the Rashba energy E_{R_1} of the p_x, p_y-derived band and E_{F} the data are fully consistent with the data presented in Ref. [29]. Assuming an intra-band scattering and fitting the D_1 signal to a parabolic dispersion yields $E_1 = (737 \pm 20)\,\mathrm{meV}$ for the p_x, p_y-derived state. A linear term was included in the fit since a pure parabolic fit did not match to the dispersion characteristic. However, this value is in agreement with the STS data presented in Fig. 7.26. The effective mass is determined by the parabolic

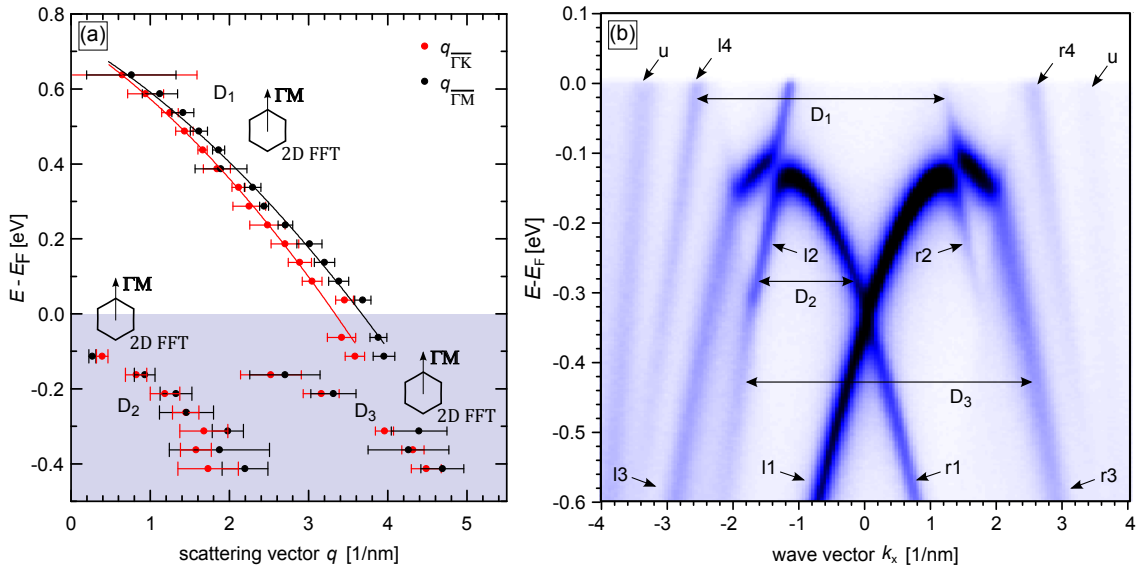

Figure 7.28: (a) Dispersion of scattering vectors q as extracted from the series of quasi-particle interference maps shown in Fig. 7.27. Data measured along the $\overline{\Gamma K}$ and $\overline{\Gamma M}$ directions are plotted in red and black, respectively. Respective lines are the results of fits of intra-band scattering events.(b) The electronic structure of $(\sqrt{3} \times \sqrt{3})$Bi/Ag/Au(111)$R30°$ as determined by ARPES, adapted from Ref. [100].The measured band structure along $\overline{\Gamma M}$ consists of three surface bands labeled by r1-r3 (l1-l3) at positive (negative) wave vectors and a Ag(111) umklapp bulk band u.

contribution of the fit to $m^*_{\overline{\Gamma M}} = -(0.46 \pm 0.10)\, m_e$ and $m^*_{\overline{\Gamma K}} = -(0.39 \pm 0.09)\, m_e$. Due to the hybridization between s, p_z- and p_x, p_y-derived states, the interpretation of the interference patterns observed for energies below $-100\,$meV is more complex with the two different scattering channels D_2 and D_3. Assuming intra-band scattering within the s, p_z-derived band for D_2 would lead to $m^*_{\overline{\Gamma K}} = (-0.11 \pm 0.01)\, m_e$ and $m^*_{\overline{\Gamma M}} = (-0.15 \pm 0.01)\, m_e$ which is far below values determined by ARPES measurements. Ignoring the hybridization a parabolic fit for the branches l3/r3 and r1/l1, which are originally the s, p_z-derived branches, leads to an effective mass $m^* = -0.35\, m_e$ [23, 31]. In order to compare the scattering events D_2 and D_3 in the occupied electronic band structure of Bi/Ag(111) an ARPES measurement of Bi/Ag/Au(111) is shown in Fig. 7.28(b). Within the accuracy of the data the Bi/Ag/Au(111) and Bi/Ag(111) provide the same band dispersion despite the fact that Bi/Ag/Au(111) exhibits a larger hybridization gap opening[10]. However, the band structure can be seen more clearly in the Bi/Ag/Au(111) data.

The comparison to ARPES allows to assign the scattering signals in the occupied energy range with the D_2 signal as inter-band scattering between l2 and r1 or respectively r2 and l1. As a result the scattering vector between l2 and r1 becomes very short and the resulting dispersion suggests a much smaller effective electron mass which is no longer representative for electrons in the s, p_z-derived bands.

[10]Private correspondence with Dr. H. Bentmann.

The D_3 signal can be clearly distinguished from the D_1 signal comparing their distinctly different sizes around $(E - E_F) \approx -(100 - 200)$ meV. The D_3 scattering can be identified in the ARPES measurement in Fig. 7.28(b) as an inter-band scattering between l2 and r3 or l3 and r2. Interestingly, the D_1 signal disappears at the moment when D_2 and D_3 appear. This does not necessarily mean that the intra-band scattering D_1 does not occur but it might be addressed to the exponential damping of states with non-zero $k_{||}$ as discussed in Eq. (2.1.20). As a result the scattering vectors D_2 and D_3 may dominate the tunneling current and lead to a stronger intensity in the FFT which may eventually bury the D_1 signal which features a much larger scattering vector. Indeed, intra-band scattering within the p_x, p_y-derived band could be observed simultaneously with inter-band scatterings between p_x, p_y and sp_z states in a recent study [35] on $(\sqrt{3} \times \sqrt{3})$Bi/Cu(111)$R30°$, which features a band dispersion similar to $(\sqrt{3} \times \sqrt{3})$Pb/Ag(111)$R30°$ without hybridization.

7.4.3 Spin polarization and DFT calculations

After the identification of the scattering channels the spin polarization of the involved bands is discussed. Similar to the discussion in Sec. 7.3 the description begins with a model that discusses the role and importance of spin-conservation.
In a spin-conservation scenario in Fig 7.29(a) the observed inter-band scattering events D_2 and D_3 agree very well with the predicted spin texture in the occupied energy range in

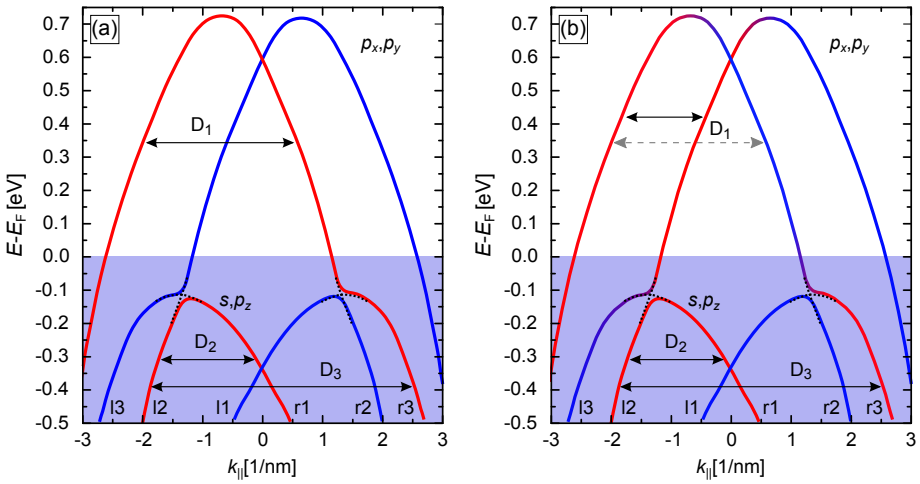

Figure 7.29: (a) The assumption of spin-conserving scattering of the observed scattering events indicates a conventional p_x, p_y-derived Rashba state in contradiction to DFT calculations [24]. The observed inter-band scattering events confirm the predicted hybridization gap between p_x, p_y- and s, p_z- derived band. The interpretation of the intra-band scattering as spin-conserving in the occupied states is in agreement to the predicted spin texture in Fig. 5.5. (b) The predicted unconventional spin texture in the p_x, p_y-derived state. A possible scattering channel for D_1 would give the indicated forwardscattering (black arrow) with a decreased length compared to the experimentally observed D_1 (grey arrow).

Fig. 7.29(b) with the change of spin polarization around the hybridization gap. The D_2 scattering connects l2 and r1 or r2 and l1 branches and D_3 connects l2 and r3 or l3 and r2 branches, thus both scattering events connect states with parallel spin orientations.
The intra-band scattering D_1 leads to the indication of a conventional spin texture for the p_x, p_y-derived state (presented in Fig. 7.29(a))—in contradiction to the predicted unconventional spin topology. Within the model of an unconventional spin texture in Fig. 7.29(b) a forward scattering process with $q = 2k_0 = \text{const.}$ should be observed rather than the observed intra-band D_1 scattering, indicated with the respectively black and grey arrows. The experimental data for the p_x, p_y scattering provide the same characteristics for the Bi/Ag(111) alloy as previously observed for Pb/Ag(111) in Sec. 7.3. In order to resolve this obvious systematic contradiction between experiment and theory DFT calculations have been performed for the Bi/Ag(111) surface that include an analysis of the orbital character accordingly to the Pb/Ag(111) case[11]. Fig. 7.30(a) shows the calculated spin-resolved band structure of the Bi-derived states around E_F. It is clearly visible that the s, p_z states with a band onset at about E_F show a strong Rashba-type spin polarization. Due to the hybridization the branches that originally belonged to the s, p_z- derived bands are connected to the p_x, p_y branches and vice versa (see the dashed lines in Fig. 7.29). Subsequently the spin texture of the p_x, p_y- and s, p_z- derived bands is quite complex in the occupied energy range. The p_x, p_y-derived bands change spin polarization around E_F

[11] The DFT calculations have been performed by Dr. G. Bihlmayer, Peter Grünberg Institut and Institute of Advanced Simulation, Forschungszentrum Jülich and JARA, 52425 Jülich, Germany

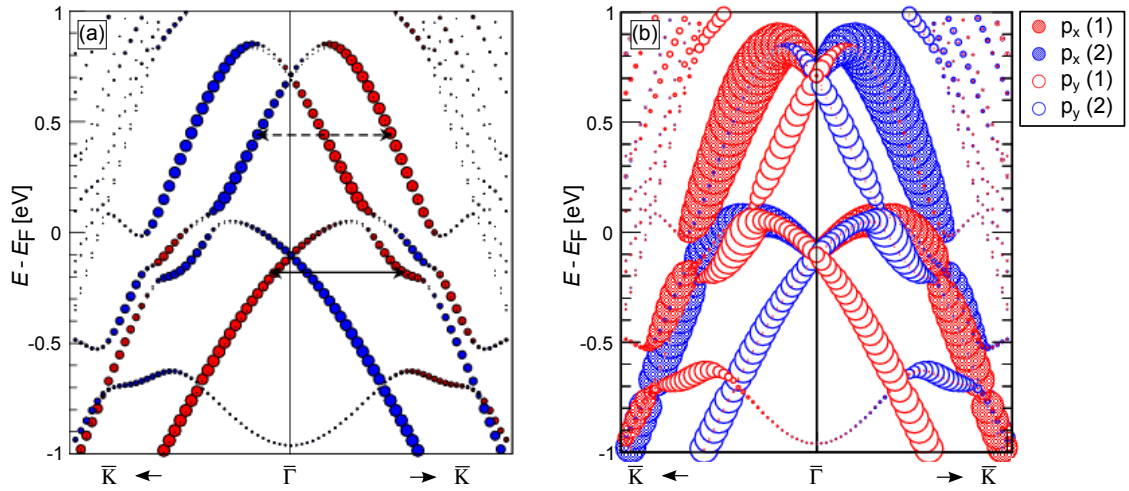

Figure 7.30: (a) Calculated band structure of the $(\sqrt{3} \times \sqrt{3})$ Bi/Ag(111)$R30°$ surface alloy on an eight-layer Ag(111) stack, terminated with $(\sqrt{3} \times \sqrt{3})$ Bi/Ag(111)$R30°$ on both sides. Red and blue colours indicate the spin polarization with respect to a spin-quantization axis that is perpendicular to the k-vector and surface normal. (b) Spin- and orbital-resolved band structure of the $BiAg_2$ surface alloy. Open and full circles show contributions from p_x and p_y orbitals, respectively. The size of the symbols in (a) and (b) indicates the degree of spin polarization.

and the s, p_z- derived bands change their spin polarization around $(E - E_F) = -200\,\text{meV}$. The p_x, p_y spin texture in the unoccupied range shows an unconventional polarization with a loss of spin polarization around the $\overline{\Gamma}$-point. This loss of spin polarization near the $\overline{\Gamma}$-point can be explained by the spin- and orbital-resolved band structure shown in Fig. 7.30(b) focusing on the p_x and p_y states. A mixture of p_x with one spin orientation and p_y states of the opposite spin orientation can be found around the center of the Brillouin zone, which is similar to the Pb/Ag(111) band structure discussed in Sec. 7.3 [164]. The second possibility for a decreased in-plane spin polarization—an increased out-of–plane spin component—was also checked and found to be not significant. In the same manner as for Pb/Ag(111) scattering between time-reversal partners from k to $-k$ is still prohibited by time reversal symmetry [87].
Using the spin-orbit Hamiltonian

$$H_{\text{SOC}} = \xi \vec{L} \cdot \vec{S} = \xi l_z s_z + \frac{\xi}{2}(l^+ s^- + l^- s^+) \tag{7.4.1}$$

the three different scattering events are checked for spin-conserving or spin-flip scattering. The D_1 scattering process connects p_x to p_y orbitals of opposite spin and therefore the spin-flip term

$$|\Psi|^2 \propto \langle \Psi_\text{i} | \frac{\xi}{2}(l^+ s^- + l^- s^+) | \Psi_\text{f} \rangle \tag{7.4.2}$$

is non-zero and allows for a constructive interference. The scattering event D_2 can be explained as spin- and orbital momentum-conserving scattering in Fig. 7.30(b) connecting equal orbitals with parallel spin alignment, therefore the spin-conserving term

$$|\Psi|^2 \propto \langle \Psi_\text{i} | \xi l_z s_z | \Psi_\text{f} \rangle \tag{7.4.3}$$

is non-zero for D_2. The D_3 scattering event appears more complex. In the representation of Fig. 7.30(b) D_3 connects p_x and p_y orbitals with equal spin polarizations, which is neither allowed by Eq. (7.4.2) nor by Eq. (7.4.3) as none of these terms allows for constructive interference with equal spins and different orbitals.
The origin of the scattering event can be found in Fig. 7.31 which gives a more detailed representation for all involved p orbitals, namely p_z (a), p_x (b) and p_y (c). The open and full circles distinguish different spin polarizations in (a)-(c) and the symbol sizes indicate the degree of orbital character. Now, with the full detailed presentation a connection between l2 and r3 branches (or l3 to r2) can be explained by spin-flip scattering. Looking at the l3 and r3 branches, which originally stem from the s, p_z- derived bands, a significant p_z character can be seen in (a). The p_x orbitals in (b) do not allow for constructive interference, since D_3 connects p_z and p_x orbitals with equal spin alignments but different orbital character, which does not yield a constructive interference according to Eq. (7.4.2) and Eq. (7.4.3). Close inspection in (c) indicates a significant p_y character for the r2 and l2 branches, which have an opposite spin polarization compared to the l3 and r3 branches in (a). Consequently the D_3 scattering is identified as spin-flip scattering accompanied by a change from p_z to a p_y orbital character.

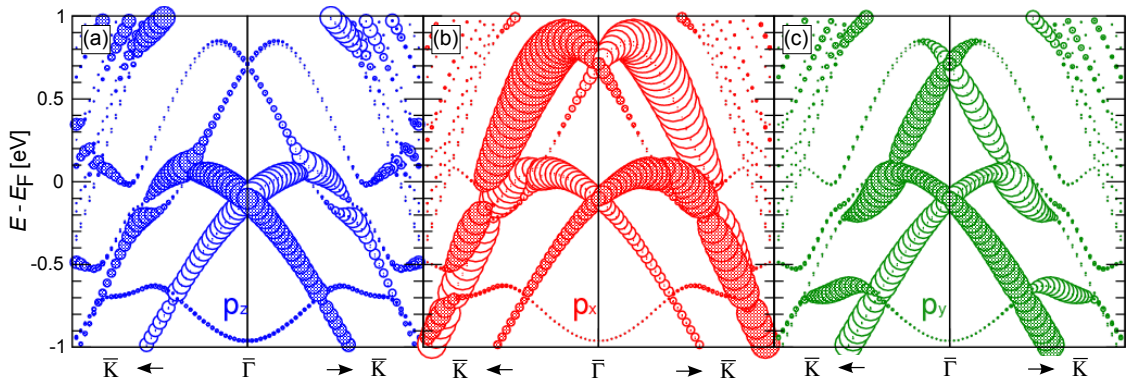

Figure 7.31: Spin- and orbital-resolved band structure of the $(\sqrt{3} \times \sqrt{3})$ Bi/Ag(111)$R30°$ surface alloy separately illustrated for p_z (a), p_x (b) and p_y (c). Open and full circles distinguish the different spin directions in (a-c). The size of the symbols in (a) and (b) indicates the degree of orbital character.

In summary the experimentally observed Rashba bands of the $(\sqrt{3} \times \sqrt{3})$Bi/Ag(111)$R30°$ surface showed a good agreement to earlier experiments and DFT calculations. The STS measurements confirmed the existence of a hybridization gap around the band onset of the s, p_z-derived band due to the shoulder, which is superimposed on the Rashba peak of the s, p_z-derived band.

Quasi-particle experiments could observe intra-band interferences in the complete unoccupied energy range within the p_x, p_y-derived bands—in contrast to an earlier study, which reported about forbidden backscattering between E_1 and E_{R_1} [29]. The finding of scattering in that energy range emphasizes the fact, that the electrons are Bloch electrons and their velocity is not determined by the k value but the respective band slope. The intra-band scattering allowed to reconstruct the qualitative dispersion of the p_x, p_y-derived band.

In the occupied energy range two coexisting scattering events were found which were both assigned as inter-band scattering events between the p_x, p_y- and s, p_z- derived bands, therefore the band dispersion of the s, p_z-derived band could not be extracted from quasi-particle interferences in the occupied energy range. However, the band structure of the s, p_z-derived band is fully occupied and accessible by ARPES measurements.

The interpretation of the observed scattering events in a spin-conserving model could explain the observed inter-band scattering events in the occupied energy range, but indicated—in contradiction to DFT calculations—a conventional spin texture for the p_x, p_y-derived band. Including the orbital character in DFT calculations could then solve this problem enabling constructive spin-flip scattering for the p_x, p_y-derived states by a simultaneous change of the orbital angular momentum, which conserves the total momentum $\vec{J}$. Interestingly the intra-band scattering event D_3, which could be interpreted as spin-conserving scattering in the first model was also identified as a spin-flip scattering event. This leads to the conclusion that an interpretation of quasi-particle interferences in spin-orbit–coupled materials only considering the spin polarization may lead to misleading interpretations as it neglects their

spin-orbit–coupled nature, where the spin is not a good quantum number, but $\vec{J}$. Further this section confirmed clearly that STM measurements are not sensitive to distinguish between scattering within states of pure symmetries or mixed orbital symmetries. Some scattering events (D_3) can be even interpreted successful in both models.

8 Summary and Outlook

The structural and electronic properties of Pb and Bi deposited on Ag(111) have been investigated in this work.

Section 7.1 describes the growth of Pb and Bi on Ag(111). The $(\sqrt{3}\times\sqrt{3})$ Pb/Ag(111)$R30°$ surface alloy has been found to suffer from comparably high number of defects compared to the isostructural $(\sqrt{3}\times\sqrt{3})$ Bi/Ag(111)$R30°$ surface. For coverages higher than $1/3\,\mathrm{ML}_{\mathrm{Ag(111)}}$ the surface undergoes a dealloying process, which results in the formation of patches of a pure Pb(111) overlayer exhibiting a characteristical moiré pattern. These findings are in agreement with previous studies.

The moiré pattern has been proven to exist up to Pb layer thicknesses of $\approx 70\,\mathrm{ML}$, additionally the surface featured an odd-even contrast in layer thickness, that allowed to detect buried Ag step edges and a precise determination of layer thicknesses.

The $(\sqrt{3}\times\sqrt{3})$ Bi/Ag(111)$R30°$ surface has been found to grow with a very high quality. The surface undergoes a dealloying process above $1/3\,\mathrm{ML}_{\mathrm{Ag(111)}}$ to a pure rectangular Bi ribbon phase, that is slightly less dense than the Bi(110) surface. In principal this finding is in agreement with earlier works, but the origin of the striped phase has been discussed controversely. The striped phase has been confirmed as commensurate (3012) phase in this work and a moiré origin, that would arise from an incommensurate phase, could be excluded.

Subsequently, at coverages exceeding $1\,\mathrm{ML}_{\mathrm{Bi(110)}}$ pure Bi(110) films are obtained, which provide a strongly anisotropic ribbon growth reaching lengths up to $1\,\mu\mathrm{m}$. The Bi(110) domains grow along three crystallographic equivalent orientations due to the threefold symmetry of the Ag(111) substrate and exhibits an additional 180° rotational degree of freedom for each orientation. All domains feature a striped modulation, which is most probably a 1D relaxation to reduce stress in the film.

In section 7.2 electronic QWSs of Pb films were investigated and the quantum character has been verified for large film thicknesses of $\approx 100\,\mathrm{ML}$. The assignment of layer thickness has been achieved by the comparison of experimentally and theoretically determined QWS solutions. A model for the dispersion has been given, which is able to explain the evolution from plateau-like STS signatures of lower QWS solutions to peak-shaped STS signals for higher QWS solutions. Quasi-particle interference maps of the QWS bands confirmed the free-electron-like character around the center of the 2D Brillouin zone.

The Rashba-split surface states of Pb/Ag(111) and Bi/Ag(111), which are the main part of this work, have been investigated by means of STM in sections 7.3 and 7.4. Tunneling spectroscopy and quasi-particle interference mapping were able to characterize two

Rashba-split surface states in the Pb/Ag(111) surface alloy. Tunneling spectroscopy showed two characteristically shaped peaks in the empty density of states which were identified as signatures of Rashba-split bands. Sensing the complete relevant energy range in STS enlightened the band structure, which was so far discussed contradictory in literature.
The combination of ARPES and quasi-particle interference mapping not only allowed the reconstruction of the band structure of Pb/Ag(111) in the occupied and empty states but also made the clear assignment of quasi-particle interference scattering vectors possible. It has been shown that both intra- and inter-band scattering events occur on the Pb/Ag(111) surface.
The interpretation of the observed scattering channels could be carried out in two interpretations, which led to two different spin polarizations for the p_x, p_y-derived state. The spin-conserving interpretation led to the indication of a conventional Rashba spin texture in contradiction to DFT calculations, that predicted unconventional Rashba states. In order to resolve the apparent contradiction more sophisticated DFT calculations were performed by collaborators at the FZ Jülich, which besides the spin also considered the orbital momentum of the involved electronic states. It turned out that constructive spin-flip scattering events may be allowed if they are accompanied by a corresponding change of angular momentum, which conserves the total momentum $\vec{J}$.
The isostructural Rashba-split Bi/Ag(111) surface has been characterized in a similar way with STS measurements, that led to a good agreement with the predicted band positions in DFT calculations. The observed quasi-particle interferences were able to reconstruct the band dispersion in the empty states. By the observation of scattering between the band onset and Rashba energy for both Rashba-split states an earlier study could be disproved, that claimed a forbidden backscattering in that energy range. Careful analysis of scattering patterns below the Fermi level revealed the coexistence of two scattering vectors. The consideration of ARPES allowed to assign the two scattering channels as inter-band scattering events. A spin-conserving interpretation of the scattering within the p_x, p_y-derived bands led to the same contradiction between experiment and theory as in the Pb/Ag(111) case. Again the issue could be resolved within extended DFT calculations as $\vec{J}$-conserving scattering events with a simultaneous spin and orbital flip. Misleadingly, the spin-conserving approach initially indicated a good compliance between experiment and theory in the occupied energy range. However, under the constraint of $\vec{J} = \text{const.}$ one of the pretended spin-conserving scattering events could be identified as a spin-flip scattering channel.
This work reveals the existence of constructive quasi-particle interferences for spin-flip scattering events. It also demonstrates that STM measurements are not able to distinguish between spin-conserving scattering within states of pure symmetry or a $\vec{J}$-conserving scattering event within states of mixed orbital symmetries. The same statement for photoemission as well as inverse photoemission experiments has been presented in a very recent study [166], concluding that a secure spin polarization interpretation for spin-orbit–coupled materials is not possible with these experimental methods so far. Summarizing, an interpretation

within a spin-conserving approach has turned out to be insufficient for spin-orbit–coupled materials.
In this new light the various quasi-particle interference experiments on spin-orbit–coupled surfaces should be treated carefully, e.g. on topological insulators a lot of studies have been performed in the last years [75, 76, 78, 79]. The scattering events in those studies have always been interpreted within in the spin-conserving model and in order to verify this approach the orbital character of those systems should be analyzed.

For future measurements the deposition of single magnetic impurities on top of the Rashba surfaces of Pb/Ag(111) as well as Bi/Ag(111) could yield interesting new results. Very recently a study about Bi_2Te_3 could show [79], that depending on the exact choice of the deposited atoms—cobalt or manganese—new scattering channels could be observed .
One could also consider spin-polarized STM experiments on Pb/Ag(111) and Bi/Ag(111) surfaces, since it is not clear a priori what to expect from this experiment. I consider two different scenarios:
In scenario 1 the tip is only sensitive to the wave functions that provide a parallel alignment to the tip. Therefore spin-flip interferences should vanish as they contain two antiparallel spin orientations. In this scenario spin-conserving scattering should not be influenced if the polarization direction of the surface wave functions agrees with the tip polarization. For each spin-conserving intra-band scattering exist two equal scattering vectors, e.g. one that connects "up" polarized branches and another one that connects branches with the corresponding antiparallel "down" polarization. One of these vectors will be cut away in this scenario, but since they are equal in length, the scattering itself should be still visible.
In scenario 2 the tip probes the complete braket $\langle\Psi|H|\Psi\rangle$, not sensitive to the individual bra or ket vector. The embedded Hamiltonian may induce spin-orbit–flips as it is intrinsically the case for H_{SOC} or spin-flips induced by magnetic impurities on the surface. In this scenario the use of a spin-polarized tip should not influence the observed scattering channels at all.
Although scattering events provide simple physics at the first glance, the underlying mechanisms are complicated and intriguing. Hopefully, it is possible to shed more light on scattering experiments as well as on SOC systems with the suggested experiments in the future.

Appendix

Deriving a formulation for the DOS

The DOS is defined as

$$\rho(E) = \frac{1}{V}\sum_{j,\vec{k}} \delta(E - E_j(\vec{k})). \tag{8.0.1}$$

counting the number of states per volume V, E_j depends generally on k. Periodic conditions yield

$$k = \frac{2\pi}{L} \cdot n, n \in \mathbb{Z} \tag{8.0.2}$$

and

$$\Delta n = 1 = \Delta k \frac{L}{2\pi} \tag{8.0.3}$$

is valid for neighbouring k. Expanding Eq. (8.0.1) with Eq. (8.0.3) leads to

$$\rho(E) \quad = \quad \frac{1}{V}\sum_{j,k_1..k_d} \frac{L^d}{(2\pi)^d}\Delta k_1 \cdot \Delta k_2 \cdot ...\Delta k_d \tag{8.0.4}$$

With $V = L^d$ and the thermodynamic limit

$$\lim_{N\to\infty, V\to\infty} \frac{1}{V}\sum_{k_1..k_d} \to \frac{1}{(2\pi)^d}\int \mathrm{d}^d k \tag{8.0.5}$$

follows

$$\rho(E) = \sum_j \frac{1}{(2\pi)^d}\int_{BZ} \mathrm{d}^d k\, \delta(E - E_j(\vec{k})). \tag{8.0.6}$$

The integration over $\mathrm{d}^d k$ has to be evaluated in curvilinear coordinates

$$S \quad := \quad \{k|E = \text{const.}\} \tag{8.0.7}$$

$$\mathrm{d}^d k = dk_\perp \mathrm{d}^{d-1} S \qquad \mathrm{d}^{d-1} S := \text{surface element of S.} \tag{8.0.8}$$

This leads to

$$\rho(E) = \sum_j \frac{1}{(2\pi)^d}\int_{BZ \bigcap S} \mathrm{d}k_\perp \mathrm{d}^{d-1} S\, \delta(E - E_j(\vec{k})). \tag{8.0.9}$$

The integral over $\mathrm{d}k_\perp$ can be expressed with

$$\mathrm{d}E = (\vec{\nabla}_{\vec{k}} E(\vec{k}))\mathrm{d}\vec{k} = |\vec{\nabla}_{\vec{k}} E(\vec{k})|\mathrm{d}k_\perp \tag{8.0.10}$$

and using the delta distribution in the integral results in

$$\rho(E) = \sum_j \frac{1}{(2\pi)^d} \int_{BZ \bigcap S} \mathrm{d}^{d-1} S \, \frac{1}{|\vec{\nabla}_{\vec{k}} E(\vec{k})|_{E=E_j}}. \tag{8.0.11}$$

For a surface state with $d = 2$ follows

$$\rho(E) = \sum_j \frac{1}{(2\pi)^2} \int_{BZ \bigcap S} \mathrm{d}S \frac{1}{|\vec{\nabla}_{\vec{k}} E(\vec{k})|_{E=E_j}}. \tag{8.0.12}$$

List of Figures

List of own publications

► L. El-Kareh, P. Sessi, T. Bathon, and M. Bode, Quantum Interference Mapping of Rashba-Split Bloch States in Bi/Ag(111), Phys. Rev. Lett. **110**, 176803 (2013).

► L. El-Kareh, P. Mehring, V. Caciuc, N. Atodiresei, A. Beimborn, S. Blügel, and C. Westphal, Self-assembled monolayers of methylselenolate on the Au(111) surface: A combined STM and DFT study, Surface Science, (2014).

► L. El-Kareh, G. Bihlmayer, A. Buchter, H. Bentmann, S. Blügel, F. Reinert, and M. Bode, A combined experimental and theoretical study of Rashba-split surface states on the $(\sqrt{3}\times\sqrt{3})$ Pb/Ag(111)$R30^\circ$ surface, New Journal of Physics **16**, 045017 (2014).

► S. Fiedler, L. El-Kareh, S. V. Eremeev, O. E. Tereshchenko, C. Seibel, P. Lutz, K. A. Kokh, E. V. Chulkov, T. V. Kuznetsova, V. I. Grebennikov, M. Bode, and F. Reinert, Defect and structural imperfection effects on the electronic properties of BiTeI surfaces, New Journal of Physics **16**, 075013 (2014).

Bibliography

[1] G. Dresselhaus, Spin-orbit coupling effects in zinc blende structures, Phys. Rev. **100**, 580 (1955). (cited on page 7)

[2] Y. A. Bychkov and E. I. Rashba, Oscillatory effects and the magnetic susceptibility of carriers in inversion layers, Journal of Physics C: Solid State Physics **17**, 6039 (1984). (cited on pages 7, 37, and 38)

[3] S. A. Wolf *et al.*, Spintronics: A spin-based electronics vision for the future, Science **294**, 1488 (2001). (cited on page 7)

[4] I. Žutić, J. Fabian, and S. Das Sarma, Spintronics: Fundamentals and applications, Rev. Mod. Phys. **76**, 323 (2004). (cited on page 7)

[5] S. Bader and S. Parkin, Spintronics, Annual Review of Condensed Matter Physics **1**, 71 (2010). (cited on page 7)

[6] S. Datta and B. Das, Electronic analog of the electro-optic modulator, Applied Physics Letters **56**, 665 (1990). (cited on page 7)

[7] J. Nitta, T. Akazaki, H. Takayanagi, and T. Enoki, Gate control of spin-orbit interaction in an inverted $In_{0.53}Ga_{0.47}As/In_{0.52}Al_{0.48}As$ heterostructure, Phys. Rev. Lett. **78**, 1335 (1997). (cited on page 7)

[8] T. Koga, J. Nitta, H. Takayanagi, and S. Datta, Spin-filter device based on the Rashba effect using a nonmagnetic resonant tunneling diode, Phys. Rev. Lett. **88**, 126601 (2002). (cited on page 7)

[9] M. Ohno and K. Yoh, Datta-das-type spin-field-effect transistor in the nonballistic regime, Phys. Rev. B **77**, 045323 (2008). (cited on page 7)

[10] G. A. Nemnes, A. Manolescu, and V. Gudmundsson, Reduction of ballistic spin scattering in a spin-FET using stray electric fields, Journal of Physics: Conference Series **338**, 012012 (2012). (cited on page 7)

[11] S. Matityahu, A. Aharony, O. Entin-Wohlman, and S. Tarucha, Spin filtering in a Rashba–Dresselhaus–Aharonov–Bohm double-dot interferometer, New Journal of Physics **15**, 125017 (2013). (cited on page 7)

[12] E. Cappelluti, C. Grimaldi, and F. Marsiglio, Topological change of the Fermi surface in low-density Rashba gases: Application to superconductivity, Phys. Rev. Lett. **98**, 167002 (2007). (cited on page 7)

[13] S. LaShell, B. A. McDougall, and E. Jensen, Spin splitting of an Au(111) surface state band observed with angle resolved photoelectron spectroscopy, Phys. Rev. Lett. **77**, 3419 (1996). (cited on pages 7, 37, 41, and 43)

[14] F. Reinert, G. Nicolay, S. Schmidt, D. Ehm, and S. Hüfner, Direct measurements of the L-gap surface states on the (111) face of noble metals by photoelectron spectroscopy, Phys. Rev. B **63**, 115415 (2001). (cited on pages 7, 31, 32, 37, and 41)

[15] G. Nicolay, F. Reinert, S. Hüfner, and P. Blaha, Spin-orbit splitting of the L-gap surface state on Au(111) and Ag(111), Phys. Rev. B **65**, 033407 (2001). (cited on pages 7, 31, 32, 37, 41, V, and VI)

[16] F. Reinert, Spin–orbit interaction in the photoemission spectra of noble metal surface states, Journal of Physics: Condensed Matter **15**, S693 (2003). (cited on pages 7, 37, 42, and 43)

[17] L. Petersen and P. Hedegård, A simple tight-binding model of spin–orbit splitting of sp-derived surface states, Surface Science **459**, 49 (2000). (cited on pages 7, 37, 38, 42, 52, 97, and XIV)

[18] G. Bihlmayer, Y. Koroteev, P. Echenique, E. Chulkov, and S. Blügel, The Rashba-effect at metallic surfaces, Surface Science **600**, 3888 (2006). (cited on pages 7, 37, 38, and 42)

[19] M. Heide, G. Bihlmayer, P. Mavropoulos, A. Bringer, and S. Blügel, Spin-orbit driven physics at surfaces., Psi-k Newsletter (2006). (cited on pages 7, 37, 38, 39, 41, and 42)

[20] O. Krupin *et al.*, Rashba effect at magnetic metal surfaces, Phys. Rev. B **71**, 201403 (2005). (cited on pages 7, 42, and 43)

[21] F. Forster, A. Bendounan, F. Reinert, V. Grigoryan, and M. Springborg, The Shockley-type surface state on Ar covered Au(111): High resolution photoemission results and the description by slab-layer DFT calculations, Surface Science **601**, 5595 (2007). (cited on pages 7, 42, and 43)

[22] H. Bentmann and F. Reinert, Enhancing and reducing the Rashba-splitting at surfaces by adsorbates: Na and Xe on Bi/Cu(111), New Journal of Physics **15**, 115011 (2013). (cited on pages 7, 42, and 43)

[23] C. R. Ast *et al.*, Giant spin splitting through surface alloying, Phys. Rev. Lett. **98**, 186807 (2007). (cited on pages 7, 43, 46, 47, 49, 71, 104, 107, and VII)

[24] G. Bihlmayer, S. Blügel, and E. V. Chulkov, Enhanced Rashba spin-orbit splitting in Bi/Ag(111) and Pb/Ag(111) surface alloys from first principles, Phys. Rev. B **75**, 195414 (2007). (cited on pages 7, 41, 43, 44, 45, 46, 47, 60, 88, 96, 103, 104, 108, VII, and XVI)

[25] C. R. Ast *et al.*, Local detection of spin-orbit splitting by scanning tunneling spectroscopy, Phys. Rev. B **75**, 201401 (2007). (cited on pages 7, 37, 43, 45, 46, 50, 52, 59, 71, 88, 89, 95, and 104)

[26] C. R. Ast *et al.*, Spin-orbit split two-dimensional electron gas with tunable Rashba and Fermi energy, Phys. Rev. B **77**, 081407 (2008). (cited on pages 7 and 43)

[27] F. Meier, H. Dil, J. Lobo-Checa, L. Patthey, and J. Osterwalder, Quantitative vectorial spin analysis in angle-resolved photoemission: Bi/Ag(111) and Pb/Ag(111), Phys. Rev. B **77**, 165431 (2008). (cited on pages 7, 43, 46, 47, 48, 49, 88, 95, 103, and VIII)

[28] I. Gierz *et al.*, Structural influence on the Rashba-type spin splitting in surface alloys, Phys. Rev. B **81**, 245430 (2010). (cited on pages 7, 43, 46, 63, and 88)

[29] H. Hirayama, Y. Aoki, and C. Kato, Quantum interference of Rashba-type spin-split surface state electrons, Phys. Rev. Lett. **107**, 027204 (2011). (cited on pages 7, 43, 52, 103, 104, 106, and 111)

[30] H. Bentmann, S. Abdelouahed, M. Mulazzi, J. Henk, and F. Reinert, Direct observation of interband spin-orbit coupling in a two-dimensional electron system, Phys. Rev. Lett. **108**, 196801 (2012). (cited on pages 7, 43, 46, 96, 103, and 104)

[31] H. Bentmann *et al.*, Origin and manipulation of the Rashba splitting in surface alloys, EPL (Europhysics Letters) **87**, 37003 (2009). (cited on pages 7, 43, 46, 96, and 107)

[32] H. Mirhosseini *et al.*, Unconventional spin topology in surface alloys with Rashba-type spin splitting, Phys. Rev. B **79**, 245428 (2009). (cited on pages 7, 43, 47, 60, and 96)

[33] I. Gierz, F. Meier, J. H. Dil, K. Kern, and C. R. Ast, Tuning the spin texture in binary and ternary surface alloys on Ag(111), Phys. Rev. B **83**, 195122 (2011). (cited on pages 7, 8, 43, and 103)

[34] L. Moreschini *et al.*, Influence of the substrate on the spin-orbit splitting in surface alloys on (111) noble-metal surfaces, Phys. Rev. B **80**, 035438 (2009). (cited on pages 7, 43, and 96)

[35] M. Steinbrecher, H. Harutyunyan, C. R. Ast, and D. Wegner, Rashba-type spin splitting from interband scattering in quasiparticle interference maps, Phys. Rev. B **87**, 245436 (2013). (cited on pages 7, 43, 52, 53, and 108)

[36] D. Pacilé *et al.*, Electronic structure of an ordered Pb/Ag(111) surface alloy: Theory and experiment, Phys. Rev. B **73**, 245429 (2006). (cited on pages 7, 43, 44, 45, 88, 95, and VII)

[37] T. Hirahara *et al.*, Manipulating quantum-well states by surface alloying: Pb on ultrathin Ag films, Phys. Rev. B **78**, 035408 (2008). (cited on pages 7, 43, and 88)

[38] L. Moreschini *et al.*, Assessing the atomic contribution to the Rashba spin-orbit splitting in surface alloys: Sb/Ag(111), Phys. Rev. B **79**, 075424 (2009). (cited on pages 7, 43, and 96)

[39] F. Meier *et al.*, Interference of spin states in photoemission from Sb/Ag(111) surface alloys, Journal of Physics: Condensed Matter **23**, 072207 (2011). (cited on pages 7 and 43)

[40] H. Mirhosseini, A. Ernst, S. Ostanin, and J. Henk, Tuning independently the Fermi energy and spin splitting in Rashba systems: Ternary surface alloys on Ag(111), Journal of Physics: Condensed Matter **22**, 385501 (2010). (cited on page 8)

[41] G. Binnig, H. Rohrer, C. Gerber, and E. Weibel, Tunneling through a controllable vacuum gap, Applied Physics Letters **40**, 178 (1982). (cited on page 11)

[42] G. Binning, H. Rohrer, Ch. Gerber, and E. Weibel, Surface Studies by Scanning Tunneling Microscopy, Phys. Rev. Lett. **49**, 57 (1982). (cited on page 11)

[43] G. Binnig, H. Rohrer, C. Gerber, and E. Weibel, 7×7 reconstruction on Si(111) resolved in real space, Phys. Rev. Lett. **50**, 120 (1983). (cited on page 11)

[44] R. Wiesendanger, *Scanning Probe Microscopy and Spectroscopy* (Cambridge University Press, Cambridge, 1994). (cited on pages 11 and 16)

[45] J. Bardeen, Tunneling from a Many-Particle Point of View, Phys. Rev. Lett. **6**, 57 (1961). (cited on pages 11 and 13)

[46] J. Tersoff and D. Hamann, Theory and Application for the Scanning Tunneling Microscope, Phys. Rev. Lett. **50**, 1998 (1983). (cited on pages 11 and 13)

[47] J. Tersoff and D. R. Hamann, Theory of the scanning tunneling microscope, Phys. Rev. B **31**, 805 (1985). (cited on pages 11, 13, 15, and 89)

[48] C. J. Chen, Theory of scanning tunneling spectroscopy, Journal of Vacuum Science & Technology A **6**, 319 (1988). (cited on page 11)

[49] V. A. Ukraintsev, Data evaluation technique for electron-tunneling spectroscopy, Phys. Rev. B **53**, 11176 (1996). (cited on page 11)

[50] D. Bonnel, *Scanning Probe Microscopy and Spectroscopy - Theory, Techniques, and Applications* (Wiley-VCH, 2001). (cited on pages 11 and 16)

[51] M. Ternes, *Scanning tunneling spectroscopy at the singe atom scale*, PhD thesis, École polytechnique fédérale de Lausanne, 2006. (cited on pages 11 and 21)

[52] SRS Stanford Research Systems, *MODEL SR830 DSP Lock-In-Amplifier*, 2011. (cited on pages 11 and 19)

[53] S. Kahle, *Magnetic Properties of Individual Molecules Studied by Scanning Tunneling Microscopy*, PhD thesis, Universität Konstanz, 2013. (cited on page 11)

[54] Y. Kuk, P. J. Silverman, and H. Q. Nguyen, Study of metal surfaces by scanning tunneling microscopy with field ion microscopy, Journal of Vacuum Science & Technology A **6**, 524 (1988). (cited on page 15)

[55] V. M. Hallmark, S. Chiang, J. F. Rabolt, J. D. Swalen, and R. J. Wilson, Observation of atomic corrugation on Au(111) by scanning tunneling microscopy, Phys. Rev. Lett. **59**, 2879 (1987). (cited on page 15)

[56] P. H. Lippel, R. J. Wilson, M. D. Miller, C. Wöll, and S. Chiang, High-resolution imaging of copper-phthalocyanine by scanning-tunneling microscopy, Phys. Rev. Lett. **62**, 171 (1989). (cited on page 15)

[57] J. Wintterlin *et al.*, Atomic-resolution imaging of close-packed metal surfaces by scanning tunneling microscopy, Phys. Rev. Lett. **62**, 59 (1989). (cited on page 15)

[58] C. J. Chen, Origin of atomic resolution on metal surfaces in scanning tunneling microscopy, Phys. Rev. Lett. **65**, 448 (1990). (cited on pages 15 and 63)

[59] C. J. Chen, *Introduction to scanning tunneling microscopy* (Oxford University Press, 2008). (cited on pages 15, 16, and 21)

[60] M. F. Crommie, C. P. Lutz, and D. M. Eigler, Imaging standing waves in a two-dimensional electron gas, Nature **363**, 524 (1993). (cited on pages 20 and 33)

[61] J. Klein, A. Léger, M. Belin, D. Défourneau, and M. J. L. Sangster, Inelastic-electron-tunneling spectroscopy of metal-insulator-metal junctions, Phys. Rev. B **7**, 2336 (1973). (cited on page 21)

[62] J. Kliewer *et al.*, Dimensionality effects in the lifetime of surface states, Science **288**, 1399 (2000). (cited on pages 22, 23, 33, and 52)

[63] C. Davisson and L. H. Germer, Diffraction of electrons by a crystal of nickel, Phys. Rev. **30**, 705 (1927). (cited on page 24)

[64] W. Shockley, On the surface states associated with a periodic potential, Phys. Rev. **56**, 317 (1939). (cited on pages 29, 30, and V)

[65] A. Zangwill, *Physics at surfaces* (Cambridge University Press, 1988). (cited on pages 29, 30, 31, and V)

[66] B. Feuerbacher, B. Fitton, and W. R.F., editors, *Photoemission and the Electronic Properties of Surfaces* (John Wiley & Sons Ltd., 1978). (cited on page 30)

[67] I. Tamm, über eine mögliche Art der Elektronenbindung an Kristalloberflächen, Physik. Zeits. Sowjetunion **1** (1932). (cited on page 31)

[68] P. O. Gartland and B. J. Slagsvold, Transitions conserving parallel momentum in photoemission from the (111) face of copper, Phys. Rev. B **12**, 4047 (1975). (cited on page 31)

[69] P. Heimann, H. Neddermeyer, and H. F. Roloff, Ultraviolet photoemission for intrinsic surface states of the noble metals, Journal of Physics C: Solid State Physics **10**, L17 (1977). (cited on page 31)

[70] A. Tamai *et al.*, Spin-orbit splitting of the shockley surface state on Cu(111), Phys. Rev. B **87**, 075113 (2013). (cited on pages 32 and 42)

[71] L. Petersen, P. Laitenberger, E. Lægsgaard, and F. Besenbacher, Screening waves from steps and defects on Cu(111) and Au(111) imaged with STM: Contribution from bulk electrons, Phys. Rev. B **58**, 7361 (1998). (cited on page 33)

[72] L. Bürgi, O. Jeandupeux, H. Brune, and K. Kern, Probing hot-electron dynamics at surfaces with a cold scanning tunneling microscope, Phys. Rev. Lett. **82**, 4516 (1999). (cited on pages 33 and 92)

[73] P. Wahl, M. A. Schneider, L. Diekhöner, R. Vogelgesang, and K. Kern, Quantum coherence of image-potential states, Phys. Rev. Lett. **91**, 106802 (2003). (cited on pages 33 and 92)

[74] J. I. Pascual *et al.*, Role of spin in quasiparticle interference, Phys. Rev. Lett. **93**, 196802 (2004). (cited on pages 33, 77, 96, and 99)

[75] T. Zhang *et al.*, Experimental demonstration of topological surface states protected by time-reversal symmetry, Phys. Rev. Lett. **103**, 266803 (2009). (cited on pages 33, 34, 37, 38, 49, 92, 96, and 115)

[76] P. Roushan *et al.*, Topological surface states protected from backscattering by chiral spin texture, Nature **460**, 1106 (2009). (cited on pages 33, 34, 49, 92, 96, and 115)

[77] K. Schouteden, P. Lievens, and C. Van Haesendonck, Fourier-transform scanning tunneling microscopy investigation of the energy versus wave vector dispersion of electrons at the Au(111) surface, Phys. Rev. B **79**, 195409 (2009). (cited on page 33)

[78] M. Nurmamat *et al.*, Unoccupied topological surface state in Bi_2Te_2Se, Phys. Rev. B **88**, 081301 (2013). (cited on pages 33, 49, 92, 96, and 115)

[79] P. Sessi *et al.*, Visualizing spin-dependent bulk scattering and breakdown of the linear dispersion relation in Bi_2Te_3, Phys. Rev. B **88**, 161407 (2013). (cited on pages 33, 34, 49, 92, 96, and 115)

[80] J. J. Sakurai, *Advanced Quantum Mechanics* (Addison-Wesley Publishing Company, 1967). (cited on page 37)

[81] M. Bode *et al.*, Chiral magnetic order at surfaces driven by inversion asymmetry, Nature **447**, 190 (2007). (cited on pages 37 and 38)

[82] B. Zimmermann, M. Heide, G. Bihlmayer, and S. Blügel, First-principles analysis of a homochiral cycloidal magnetic structure in a monolayer Cr on W(110), Phys. Rev. B **90**, 115427 (2014). (cited on pages 37 and 38)

[83] M. König *et al.*, Quantum spin hall insulator state in HgTe quantum wells, Science **318**, 766 (2007). (cited on pages 37 and 38)

[84] Y. L. Chen *et al.*, Experimental realization of a three-dimensional topological insulator, Bi_2Te_3, Science **325**, 178 (2009). (cited on pages 37, 38, and 49)

[85] L. Fu, Hexagonal warping effects in the surface states of the topological insulator Bi_2Te_3, Phys. Rev. Lett. **103**, 266801 (2009). (cited on pages 37, 38, 48, and 49)

[86] J. E. Moore, The birth of topological insulators, Nature **464**, 194 (2010). (cited on pages 37 and 38)

[87] X.-L. Qi and S. Zhang, The quantum spin hall effect and topological insulators, Physics Today **63**, 33 (2010). (cited on pages 37, 38, 98, and 110)

[88] S. H. Mirhosseini, *Ab initio investigations of the Rashba spin-orbit coupling in the electronic structure of surfaces*, PhD thesis, Martin-Luther-Universität Halle-Wittenberg, 2010. (cited on pages 37 and 50)

[89] D. R. Winkler, *Spin–Orbit Coupling Effects in Two-Dimensional Electron and Hole Systems* (Springer, 2003). (cited on page 37)

[90] F. Schwabl, *Quantenmechanik* (Springer, Berlin, 2007). (cited on pages 37 and 38)

[91] L. Thomas, The motion of the spinning electron, Nature **117**, 514 (1926). (cited on page 38)

[92] O. Krupin, *Dichroism and Rashba effect at magnetic crystal surfaces of rare-earth metals*, PhD thesis, Freie Universität Berlin, 2004. (cited on page 38)

[93] S. D. Kevan and R. H. Gaylord, High-resolution photoemission study of the electronic structure of the noble-metal (111) surfaces, Phys. Rev. B **36**, 5809 (1987). (cited on page 41)

[94] I. Gierz, *Investigation of Two-Dimensional Electron Gases with Angular Resolved Photoemission Spectroscopy*, PhD thesis, École polytechnique fédérale de Lausanne, 2011. (cited on pages 41 and 44)

[95] P. Linstrom and W. Mallard, editors, *NIST Chemistry WebBook, NIST Standard Reference Database Number 69* (National Institute of Standards and Technology, Gaithersburg MD, retrieved 2014). (cited on page 42)

[96] M.A. Van Hove *et al.*, The surface reconstructions of the (100) crystal faces of iridium, platinum and gold: I. Experimental observations and possible structural models, Surf. Sci. **103**, 189 (1981). (cited on page 43)

[97] J. V. Barth, H. Brune, G. Ertl, and R. J. Behm, Scanning tunneling microscopy observations on the reconstructed Au(111) surface: Atomic structure, long-range superstructure, rotational domains, and surface defects, Phys. Rev. B **42**, 9307 (1990). (cited on page 43)

[98] N. Takeuchi, C. T. Chan, and K. M. Ho, Au(111): A theoretical study of the surface reconstruction and the surface electronic structure, Phys. Rev. B **43**, 13899 (1991). (cited on page 43)

[99] S. Narasimhan and D. Vanderbilt, Elastic stress domains and the herringbone reconstruction on Au(111), Phys. Rev. Lett. **69**, 1564 (1992). (cited on page 43)

[100] H. Bentmann, *Spin-Bahn-Kopplung in Grenzschichten: Mikroskopische Zusammenhänge und Strategien zur Manipulation*, PhD thesis, Julius-Maximilians-Universität Würzburg, 2012. (cited on pages 46, 47, 48, 104, 107, VII, VIII, and XV)

[101] J. Premper, M. Trautmann, J. Henk, and P. Bruno, Spin-orbit splitting in an anisotropic two-dimensional electron gas, Phys. Rev. B **76**, 073310 (2007). (cited on pages 48, 49, and VIII)

[102] F. Meier, H. Dil, J. Lobo-Checa, L. Patthey, and J. Osterwalder, Erratum: Quantitative vectorial spin analysis in angle-resolved photoemission: Bi/Ag(111) and Pb/Ag(111) [phys. rev. b 77, 165431 (2008)], Phys. Rev. B **79**, 089902 (2009). (cited on page 47)

[103] S. Vajna *et al.*, Higher-order contributions to the Rashba-Bychkov effect with application to the Bi/Ag(111) surface alloy, Phys. Rev. B **85**, 075404 (2012). (cited on page 48)

[104] J. Henk, A. Ernst, and P. Bruno, Spin polarization of the L-gap surface states on Au(111), Phys. Rev. B **68**, 165416 (2003). (cited on page 49)

[105] M. Hoesch *et al.*, Spin structure of the Shockley surface state on Au(111), Phys. Rev. B **69**, 241401 (2004). (cited on page 49)

[106] J. Henk, M. Hoesch, J. Osterwalder, A. Ernst, and P. Bruno, Spin–orbit coupling in the L-gap surface states of Au(111): Spin-resolved photoemission experiments and first-principles calculations, Journal of Physics: Condensed Matter **16**, 7581 (2004). (cited on page 49)

[107] L. El-Kareh, P. Sessi, T. Bathon, and M. Bode, Quantum interference mapping of Rashba-split Bloch states in Bi/Ag(111), Phys. Rev. Lett. **110**, 176803 (2013). (cited on pages 52 and 90)

[108] L. El-Kareh *et al.*, A combined experimental and theoretical study of Rashba-split surface states on the $(\sqrt{3} \times \sqrt{3})$ Pb/Ag(111) $R30°$ surface, New Journal of Physics **16**, 045017 (2014). (cited on pages 52 and 92)

[109] J. Sakurai, *Modern quantum mechanics* (Addison-Wesley Publishing Company, 1994). (cited on page 52)

[110] P. M. Echenique and J. B. Pendry, The existence and detection of Rydberg states at surfaces, Journal of Physics C: Solid State Physics **11**, 2065 (1978). (cited on page 55)

[111] N. V. Smith, N. B. Brookes, Y. Chang, and P. D. Johnson, Quantum-well and tight-binding analyses of spin-polarized photoemission from Ag/Fe(001) overlayers, Phys. Rev. B **49**, 332 (1994). (cited on page 55)

[112] A. M. Shikin, O. Rader, G. V. Prudnikova, V. K. Adamchuk, and W. Gudat, Quantum well states of sp- and d-character in thin Au overlayers on W(110), Phys. Rev. B **65**, 075403 (2002). (cited on pages 55 and 56)

[113] M. A. Mueller, T. Miller, and T.-C. Chiang, Determination of the bulk band structure of Ag in Ag/Cu(111) quantum-well systems, Phys. Rev. B **41**, 5214 (1990). (cited on page 56)

[114] M. Becker, *Scanning Tunneling Spectroscopy of Pb Thin Films*, PhD thesis, Christian-Albrechts-Universität zu Kiel, 2010. (cited on pages 56, 57, 64, 65, 67, 81, 82, 83, 84, and 85)

[115] A. Nuber, *Intrinsische und extrinsische Einflüsse auf zweidimensionale elektronische Zustände*, PhD thesis, Julius-Maximilians-Universität Würzburg, 2011. (cited on page 56)

[116] W. B. Su *et al.*, Correlation between quantized electronic states and oscillatory thickness relaxations of 2D Pb islands on Si(111)-(7×7) surfaces, Phys. Rev. Lett. **86**, 5116 (2001). (cited on pages 57 and 81)

[117] M. Hupalo *et al.*, Uniform-height island growth of Pb on Si(111) $-$ Pb($\sqrt{3} \times \sqrt{3}$) at low temperatures, Phys. Rev. B **64**, 155307 (2001). (cited on pages 57 and 81)

[118] J. H. Dil, J. W. Kim, S. Gokhale, M. Tallarida, and K. Horn, Self-organization of Pb thin films on Cu(111) induced by quantum size effects, Phys. Rev. B **70**, 045405 (2004). (cited on pages 57, 79, and 81)

[119] B. Wu and Z. Zhang, Stability of metallic thin films studied with a free electron model, Phys. Rev. B **77**, 035410 (2008). (cited on pages 57 and 81)

[120] N. Miyata *et al.*, Electronic transport properties of quantum-well states in ultrathin Pb (111) films, Phys. Rev. B **78**, 245405 (2008). (cited on pages 57, 58, and 81)

[121] Y. Guo *et al.*, Superconductivity modulated by quantum size effects, Science **306**, 1915 (2004). (cited on pages 57 and 81)

[122] D. Eom, S. Qin, M.-Y. Chou, and C. K. Shih, Persistent superconductivity in ultrathin Pb films: A scanning tunneling spectroscopy study, Phys. Rev. Lett. **96**, 027005 (2006). (cited on pages 57 and 81)

[123] S. Qin, J. Kim, Q. Niu, and C.-K. Shih, Superconductivity at the two-dimensional limit, Science **324**, 1314 (2009). (cited on pages 57 and 81)

[124] Y.-F. Zhang *et al.*, Band structure and oscillatory electron-phonon coupling of Pb thin films determined by atomic-layer-resolved quantum-well states, Phys. Rev. Lett. **95**, 096802 (2005). (cited on pages 57 and 81)

[125] Y. Qi *et al.*, Atomic-layer-resolved local work functions of Pb thin films and their dependence on quantum well states, Applied Physics Letters **90**, (2007). (cited on pages 57 and 81)

[126] X. Zhang, A. Zhao, K. Wang, and X. Xiao, Kondo effect of single Co atoms adsorbed on Pb/Si(111) nanoislands, Phys. Rev. B **78**, 035431 (2008). (cited on pages 57 and 81)

[127] F. Schulte, A theory of thin metal films: Electron density, potentials and work function, Surface Science **55**, 427 (1976). (cited on page 57)

[128] I. B. Altfeder, V. Narayanamurti, and D. M. Chen, Imaging subsurface reflection phase with quantized electrons, Phys. Rev. Lett. **88**, 206801 (2002). (cited on pages 57, 58, and 81)

[129] M. H. Upton, T. Miller, and T.-C. Chiang, Unusual band dispersion in Pb films on Si(111), Phys. Rev. B **71**, 033403 (2005). (cited on pages 57, 58, and 83)

[130] J. H. Dil, J. W. Kim, T. Kampen, K. Horn, and A. R. H. F. Ettema, Electron localization in metallic quantum wells: Pb versus In on Si(111), Phys. Rev. B **73**, 161308 (2006). (cited on pages 57 and 58)

[131] Y. Sun *et al.*, Van hove singularities as a result of quantum confinement: The origin of intriguing physical properties in Pb thin films, Nano Research **3**, 800 (2010). (cited on pages 57, 58, 83, 85, and IX)

[132] S. He *et al.*, Band structure and Fermi surface of atomically uniform lead films, New Journal of Physics **12**, 113034 (2010). (cited on pages 57 and 58)

[133] S. Pan, Q. Liu, F. Ming, K. Wang, and X. Xiao, Interface effects on the quantum well states of Pb thin films, Journal of Physics: Condensed Matter **23**, 485001 (2011). (cited on page 57)

[134] M. C. Yang *et al.*, Phase contribution of image potential on empty quantum well states in Pb islands on the Cu(111) surface, Phys. Rev. Lett. **102**, 196102 (2009). (cited on pages 57 and 58)

[135] A. Zugarramurdi, N. Zabala, V. M. Silkin, A. G. Borisov, and E. V. Chulkov, Lifetimes of quantum well states and resonances in Pb overlayers on Cu(111), Phys. Rev. B **80**, 115425 (2009). (cited on page 57)

[136] M. Becker and R. Berndt, Scattering and lifetime broadening of quantum well states in Pb films on Ag(111), Phys. Rev. B **81**, 205438 (2010). (cited on pages 57, 58, 67, and 85)

[137] Y. Jia *et al.*, Strong quantum size effects in Pb(111) thin films mediated by anomalous Friedel oscillations, Phys. Rev. Lett. **105**, 066101 (2010). (cited on page 57)

[138] J. Dalmas *et al.*, Ordered surface alloy formation of immiscible metals: The case of Pb deposited on Ag(111), Phys. Rev. B **72**, 155424 (2005). (cited on pages 59, 61, 62, 63, and 88)

[139] G. Wittich, *Scanning Tunneling Microscopy and Spectroscopy at Low Temperatures: Development of a 1 K-Instrument and Local Characterization of Heterogenous Metal Systems*, PhD thesis, Universität Konstanz, 2005. (cited on pages 59, 61, 62, 64, and 65)

[140] C. R. Ast *et al.*, Orbital selective overlayer-substrate hybridization in a Pb monolayer on Ag(111), Phys. Rev. B **73**, 245428 (2006). (cited on pages 59 and 65)

[141] C. Kato, Y. Aoki, and H. Hirayama, Scanning tunneling microscopy of Bi-induced Ag(111) surface structures, Phys. Rev. B **82**, 165407 (2010). (cited on pages 59, 71, 72, and 73)

[142] K. H. L. Zhang *et al.*, Observation of a surface alloying-to-dealloying transition during growth of Bi on Ag(111), Phys. Rev. B **83**, 235418 (2011). (cited on pages 59, 71, 72, 73, 74, 76, 77, and XI)

[143] H. L. Zhang, W. Chen, X. S. Wang, J. Yuhara, and A. T. S. Wee, Growth of well-aligned Bi nanowire on Ag(111), Applied Surface Science **256**, 460 (2009). (cited on pages 59, 76, 77, 78, and 79)

[144] K. J. Rawlings, M. J. Gibson, and P. J. Dobson, The epitaxial growth of lead and thallium on (111) silver and copper, Journal of Physics D: Applied Physics **11**, 2059 (1978). (cited on page 61)

[145] K. Takayanagi, D. Kolb, K. Kambe, and G. Lehmpfuhl, Deposition of monolayer and bulk lead on Ag(111) studied in vacuum and in an electrochemical cell, Surface Science **100**, 407 (1980). (cited on pages 61 and 65)

[146] K. Morgenstern, G. Rosenfeld, and G. Comsa, Local correlation during ostwald ripening of two-dimensional islands on Ag(111), Surface Science **441**, 289 (1999). (cited on page 64)

[147] C. Nagl, O. Haller, E. Platzgummer, M. Schmid, and P. Varga, Submonolayer growth of Pb on Cu(111): Surface alloying and de-alloying, Surface Science **321**, 237 (1994). (cited on page 65)

[148] A. Crepaldi *et al.*, Combined ARPES and STM study of Pb/Au(111) moiré structure: One overlayer, two symmetries, Phys. Rev. B **87**, 115138 (2013). (cited on page 65)

[149] A. D. Novaco and J. P. McTague, Orientational epitaxy—the orientational ordering of incommensurate structures, Phys. Rev. Lett. **38**, 1286 (1977). (cited on page 65)

[150] T. Wiederholt, H. Brune, J. Wintterlin, R. Behm, and G. Ertl, Formation of two-dimensional sulfide phases on Al(111): an STM study, Surface Science **324**, 91 (1995). (cited on page 65)

[151] F. Jona, Low-energy electron diffraction study of surfaces of antimony and bismuth, Surface Science **8**, 57 (1967). (cited on page 75)

[152] P. Hofmann, The surfaces of bismuth: Structural and electronic properties, Progress in Surface Science **81**, 191 (2006). (cited on page 75)

[153] J. Sun *et al.*, Structural determination of the Bi(110) semimetal surface by leed analysis and ab initio calculations, Phys. Rev. B **74**, 245406 (2006). (cited on pages 76, 77, and XI)

[154] P. Hofmann, J. E. Gayone, G. Bihlmayer, Y. M. Koroteev, and E. V. Chulkov, Electronic structure and Fermi surface of Bi(100), Phys. Rev. B **71**, 195413 (2005). (cited on page 77)

[155] K.-F. Braun, S. Fölsch, G. Meyer, and K.-H. Rieder, Observation of charge-density wave domains on the Cr(110) surface by low-temperature scanning tunneling microscopy, Phys. Rev. Lett. **85**, 3500 (2000). (cited on page 77)

[156] T. Nagao *et al.*, Nanofilm allotrope and phase transformation of ultrathin Bi film on Si(111)7 × 7, Phys. Rev. Lett. **93**, 105501 (2004). (cited on pages 77 and 79)

[157] V. Fournée *et al.*, Quantum size effects in metal thin films grown on quasicrystalline substrates, Phys. Rev. Lett. **95**, 155504 (2005). (cited on page 79)

[158] V. Yeh, L. Berbil-Bautista, C. Z. Wang, K. M. Ho, and M. C. Tringides, Role of the metal/semiconductor interface in quantum size effects: Pb /Si(111), Phys. Rev. Lett. **85**, 5158 (2000). (cited on page 79)

[159] F. Ying-Shuang *et al.*, Modifying quantum well states of Pb thin films via interface engineering, Chinese Physics Letters **27**, 066804 (2010). (cited on page 81)

[160] E. Chulkov, V. Silkin, and P. Echenique, Image potential states on metal surfaces: Binding energies and wave functions, Surface Science **437**, 330 (1999). (cited on page 82)

[161] N. D. Lang, Spectroscopy of single atoms in the scanning tunneling microscope, Phys. Rev. B **34**, 5947 (1986). (cited on page 89)

[162] S. Crampin, J. Kröger, H. Jensen, and R. Berndt, Phase coherence length and quantum interference patterns at step edges, Phys. Rev. Lett. **95**, 029701 (2005). (cited on page 92)

[163] P. Echenique *et al.*, Decay of electronic excitations at metal surfaces, Surface Science Reports **52**, 219 (2004). (cited on page 92)

[164] R. Winkler, Spin polarization of quasi-two-dimensional hole systems, Phys. Rev. B **71**, 113307 (2005). (cited on pages 98 and 110)

[165] H. Zhang *et al.*, Engineering quantum anomalous hall phases with orbital and spin degrees of freedom, Phys. Rev. B **87**, 205132 (2013). (cited on page 99)

[166] S. N. P. Wissing *et al.*, Ambiguity of experimental spin information from states with mixed orbital symmetries, Phys. Rev. Lett. **113**, 116402 (2014). (cited on pages 102 and 114)

[167] M. Bode *et al.*, Magnetization-direction-dependent local electronic structure probed by scanning tunneling spectroscopy, Phys. Rev. Lett. **89**, 237205 (2002). (cited on page 104)

Danksagung

Ich möchte an dieser Stelle allen danken, die mir während meiner Dissertation mit Rat und Tat zur Seite standen und zum Gelingen dieser Arbeit beigetragen haben.

Zunächst bedanke ich mich bei Herrn Prof. Dr. Bode für die Aufnahme in seiner Arbeitsgruppe und die Möglichkeit meine Dissertation in der Experimentellen Physik II anzufertigen. Bei fachlichen und technischen Fragen konnte ich mich stets an ihn wenden und habe oft wertvolle Gedankenanstöße erhalten. Auch danke ich für das interessante und vielschichtige Arbeiten während der letzten Jahre, das weit über die reine Thematik von Rashba aufgespaltenen Oberflächen hinausging und meine Kenntnisse so in verschiedenste Richtungen erweitert hat.

Priv.-Doz. Dr. Jörg Schäfer danke ich für die Bereitschaft die Tätigkeit als Zweitgutachter zu übernehmen.

Dr. Gustav Bihlmayer hat die in dieser Arbeit präsentierten DFT Rechnungen zu den Rashbasystemen Bi/Ag(111) Pb/Ag(111) durchgeführt, deren Ergebnis eine zweite Interpretation der Quasiteilcheninterferenz möglich gemacht haben und die Interpretation von Quasiteilcheninterferenz völlig neu beleuchtet, auch dafür danke ich. Mit Dr. Hendrik Bentmann hatte ich einige anregende Diskussionen, die mir bei der Deutung der Bi/Ag(111) Messdaten halfen, die chronologisch die erste Messung darstellen.

Jeanette Kemmer und Tobias Mauerer danke ich für die angenehme Atmosphäre im Büro während der letzten Jahre.
Meinem Studienfreund Sebastian Knoche möchte ich für seine stete Hilfsbereitschaft bei einigen Syntaxproblemen und auch mathematischen und theoretischen Fragestellungen danken. Thomas Bathon, Dr. Markus Scholz und Sebastian Fiedler danke ich für das Korrekturlesen meiner Arbeit. Markus hat mir auch insbesondere im Bereich der PES mit seinem Fachwissen weitergeholfen.

Auf die Hilfe von Sebastian Fiedler, Thomas Bathon, Stefan Wilfert, Tobias Mauerer, Jens Kügel und Oliver Storz und konnte ich mich immer verlassen. Mit Thomas und Dr. Paolo Sessi habe ich mir in den letzten Jahre die UHV Kammer geteilt.

Mein besonderer Dank gilt den Mitarbeitern der Mechanikwerkstatt, die hervorragende

Arbeit leisten und auch bei spontanen Einsätzen im Labor sofort zur Stelle waren.

Nichtzuletzt danke ich Sebastian und meiner kompletten Familie, die ständig und bedingungslos immer für mich da gewesen sind und mir in anstrengenden Phasen immer den Rücken gestärkt haben.

Eidesstattliche Erklärung

gemäß §5, Abs. 2, Satz 2, 3, 4 und 6 der
Promotionsordnung der
Fakultät für Physik und Astronomie der
Julius-Maximilians-Universität Würzburg

Hiermit erkläre ich an Eides statt, dass ich die vorliegende Dissertation eigenständig, d.h. insbesondere selbstständig und ohne Hilfe einer kommerziellen Promotionsberatung angefertigt und keine anderen als die von mir angegebenen Quellen und Hilfsmittel benutzt habe und dass ich die Gelegenheit zum Promotionsvorhaben nicht kommerziell vermittelt bekommen habe und insbesondere nicht eine Person oder Organisation eingeschaltet habe, die gegen Entgelt Betreuer bzw. Betreuerinnen für die Anfertigung von Dissertationen sucht.

Hiermit erkläre ich zudem, dass ich die Regeln der Universität Würzburg über gute wissenschaftliche Praxis eingehalten habe und dass ich die Dissertation in gleicher oder anderer Form nicht bereits in einem anderen Prüfungsfach vorgelegt habe.

Würzburg, den 16.12.2014

Lydia El-Kareh